Hot spin carriers in cold semiconductors

Time and spatially resolved magneto-optical Kerr effect spectroscopy of optically induced electron spin dynamics in semiconductor heterostructures

Dissertation zur Erlangung des
naturwissenschaftlichen Doktorgrades
der Julius-Maximilians-Universität Würzburg

vorgelegt von

Tobias Henn

aus Kirchheim unter Teck

Würzburg 2014

Eingereicht am: 16. Oktober 2014

bei der Fakultät für Physik und Astronomie

1. Gutachter: Prof. Dr. W. Ossau

2. Gutachter: Prof. Dr. L. W. Molenkamp

3. Gutachter: Prof. Dr. M. Oestreich

der Dissertation

Vorsitzender: Prof. Dr. F. Reinert

1. Prüfer: Prof. Dr. W. Ossau

2. Prüfer: Prof. Dr. L. W. Molenkamp

3. Prüfer: Prof. Dr. R. Oppermann

im Promotionskolloquium

Tag des Promotionskolloqiums: 25. Februar 2015

Doktorurkunde ausgehändigt am: ... ...

Parts of this thesis have already been published:

Henn, T., Kiessling, T., Reuter, D., Wieck, A. D., Biermann, K., Santos, P. V., and Ossau, W.: *Time and spatially resolved electron spin detection in semiconductor heterostructures by magneto-optical Kerr microscopy*, Feature Article in special issue "Semiconductor Spintronics", physica status solidi (b), DOI:10.1002/pssb.201350192 (2014).

Henn, T., Quast, J.-H., Kiessling, T., Reuter, D., Wieck, A. D., Ossau, W., and Molenkamp, L. W.: *Hot electron spin diffusion in n-type GaAs*, part of "Focus Point on Quantum Spintronics and Related Phenomena", European Physical Journal Plus 129, 118 (2014).

Henn, T., Kiessling, T., Reuter, D., Wieck, A. D., Ossau, W., and Molenkamp, L. W.: *Picosecond real-space imaging of electron spin diffusion in GaAs*, Physical Review B 88, 195202 (2013). Editors' Suggestion.

Henn, T., Kiessling, T., Biermann, K., Santos, P. V., Ossau, W., and Molenkamp, L. W.: *Ultrafast supercontinuum fiber-laser based pump-probe scanning magneto-optical Kerr effect microscope for the investigation of electron spin dynamics in semiconductors at cryogenic temperatures with picosecond time and micrometer spatial resolution*, Review of Scientific Instruments 84, 123903 (2013).

Henn, T., Heckel, A., Beck, M., Kiessling, T., Reuter, D., Wieck, A. D., Ossau, W., and Molenkamp, L. W.: *Hot carrier effects on the magneto-optical detection of electron spins in GaAs*, Physical Review B 88, 085303 (2013).

Quast, J.-H., **Henn, T.**, Kiessling, T., Reuter, D., Wieck, A. D., Ossau, W., and Molenkamp, L. W.: *Hot carrier effects on lateral electron spin diffusion in n-type GaAs*, Physical Review B 87, 205203 (2013).

Further publications under participation of the author:

Bieker, S., **Henn, T.**, Kiessling, T., Ossau, W., Molenkamp, L. W.: *Spatially resolved thermodynamics of the partially ionized exciton gas in GaAs*, submitted to Physical Review Letters.

Bieker, S., **Henn, T.**, Kiessling, T., Ossau, W., Molenkamp, L. W.: *Relaxation and radiative decay kinetics of free excitons in nearly defect-free bulk GaAs*, submitted to Physical Review X.

Bieker, S., **Henn, T.**, Kiessling, T., Ossau, W., Molenkamp, L. W.: *Excitonic ring formation in ultrapure bulk GaAs*, Physical Review B 90, 201305(R) (2014). Rapid Communication.

Münzhuber, F., **Henn, T.**, Kiessling, T., Ossau, W., Molenkamp, L. W., Gieseking, B., Astakhov, G. V., and Dyakonov, V.: *Exciton decay dynamics controlled by impurity occupation in strongly Mn-doped and partially compensated bulk GaAs*, Physical Review B 90, 125203 (2014).

Kiessling, T., Quast, J.-H., Kreisel, A., **Henn, T.**, Ossau, W., and Molenkamp, L. W.: *Spatially resolved photocarrier energy relaxation in low-doped bulk GaAs*, Physical Review B 86, 161201(R) (2012). Rapid Communication.

Moffet, R. C., Furutani, H., Rödel, T. C., **Henn, T. R.**, Sprau, P. O., Laskin, A., Uematsu, M., and Gilles, M. K.: *Iron speciation and mixing in single aerosol particles from the Asian continental outflow*, Journal of Geophysical Research 117, D07204 (2012).

Moffet, R. C., **Henn, T.**, Laskin, A., and Gilles, M. K.: *Automated Chemical Analysis of Internally Mixed Aerosol Particles Using X-ray Spectromicroscopy at the Carbon K-Edge*, part of special issue "Atmospheric Analysis as Related to Climate Change", Analytical Chemistry 82, 7906 (2010).

Pratt, K. A., Twohy, C. H., Murphy, S. M., Moffet, R. C., Heymsfield, A. J., Gaston, C. J., Demott, P. J., Field, P. R., **Henn, T. R.**, Rogers, D. C., Gilles, M. K., Seinfeld, J. H., and Prather, K. A.: *Observation of playa salts as nuclei in orographic wave clouds*, Journal of Geophysical Research 115, D15301 (2010).

Moffet, R. C., **Henn, T. R.**, Tivanski, A. V., Hopkins, R. J., Desyaterik, Y., Kilcoyne, A. L. D., Tyliszczak, T., Fast, J., Barnard, J., Shutthanandan, V., Cliff, S. S., Perry, K. D., Laskin, A., and Gilles, M. K.: *Microscopic characterization of carbonaceous aerosol particle aging in the outflow from Mexico City*, Atmospheric Chemistry and Physics 10, 961 (2010).

Contents

Chapter 1

Introduction

With central processing units, memory devices, and network switches operating at inconceivable speeds and capacities, today's solid state electronics enables data processing, storage, and communication capabilities which are unprecedented in human history. Having followed the trajectory initially observed by Moore [1] and Dennard [2] for 50 consecutive years, the ongoing miniaturization of semiconductor electronic devices and the accompanying decrease in device power consumption has reliably driven the progress of information technology for decades. However, this development will come to an end in the near future [3, 4].

With the fabrication of 14 nm feature sizes commercially available today, semiconductor electric circuits are rapidly approaching length scales at which detrimental quantum effects severely affect device performance [5]. Moreover, with the advent of mobile computing applications and the rise of green computing ideals, the focus of attention has shifted towards low power consumption and instant-on architectures which are difficult to implement using available technology.

To overcome these challenges, spin transport electronics, or spintronics, was conceived at the turn of the millennium as a new paradigm for information storage and processing [6–9]. The basic idea behind this paradigm is conceptually simple. While conventional semiconductor electronics relies on electric charge as the carrier of information, spintronics aims to either replace or supplement the role of charge by the electron spin degree of freedom. This approach promises numerous advantages including nonvolatility, higher data processing speed, a reduction of electric power consumption, and improved integration densities compared with conventional semiconductor devices [8].

The realization of practical semiconductor spintronic applications, however, has proved extremely challenging [10]. The implementation of spintronic devices demands for the precise control of the injection, storage, manipulation, transfer, and detection of electron spin coherence in solid state systems. A prerequisite for the mastery of these operations is the development of a coherent understanding of the fundamental processes that govern electron spin decoherence, relaxation, and transport in semiconductors.

Spin-sensitive magneto-optical spectroscopy has emerged as a particularly successful technique for the exploration of electron spin dynamics in solid state systems. Magneto-optical spectroscopy arguably is the most widely used tool for the investigation of spin

phenomena in direct band gap semiconductors. Taking advantage of the spin selectivity of the optical interband transitions in zincblende-type crystals, spin polarized electrons are excited by above-bandgap illumination of the sample with a circularly polarized pump laser. In its simplest form, magneto-optical spectroscopy then infers the state of the electron spin system by using the degree of circular polarization of the photoluminescence (PL) as a tracer for the electron spin polarization. Photoluminescence spectroscopy, however, depends on the simultaneous presence of conduction band electrons and valence band holes and is therefore limited to time and length scales on the order of the minority carrier lifetime and the ambipolar charge diffusion length.

A more sophisticated approach, magneto-optical Kerr effect (MOKE) spectroscopy, eludes these limitations by deducing the electron spin polarization from a measurement of the change of the major axis of optical polarization, the Kerr rotation, of a second probe laser which is reflected from the sample surface [11]. Using fast pulsed laser sources and strong focussing optics, pump-probe MOKE microscopy allows for the investigation of the electron spin system with femtosecond time and micrometer spatial resolution with ultra-high sensitivity down to the single-spin level.

Pump-probe MOKE spectroscopy has been used in a wide range of beautiful experiments to study electron and hole spin transport and relaxation processes in bulk semiconductors, semiconductor heterostructures, quantum wells (QWs), and quantum dots (QDs). Notable applications of MOKE and the closely related Faraday rotation microscopy [12] include the first observation of electron spin lifetimes in excess of 100 ns [13] and spin drift over macroscopic distances exceeding 100 µm in bulk n-GaAs [14], the study of optically excited electron spin packets subject to electric, magnetic, and strain fields [15], the optical investigation of electrical spin injection in n-GaAs channels [16], the detection of current-induced electron spin polarization in strained nonmagnetic semiconductors [17], the first observation of the spin Hall effect in bulk [18] and low-dimensional semiconductors [19], the magneto-optical read-out of single electron spins in QDs [20, 21], and direct real-space mapping of the formation of a persistent spin helix in a two-dimensional electron system [22].

The majority of these magneto-optical experiments have been performed at liquid helium temperatures. It is well established – but perhaps not widely appreciated – that under conditions typically found in such experiments, in semiconductors the electron temperature T_e can significantly exceed the lattice temperature T_L as a result of the deposition of excess energy in the electron system by above-bandgap optical excitation [23–28]. This effect is most pronounced at very low lattice temperatures for which the energetic coupling between the electron system and the lattice is weak [29]. Moreover, the optical power densities for which an overheating of the electron system is observed easily fall below typical excitation intensities in pump-probe MOKE microscopy which result from the necessity to strongly focus the pump laser to achieve high spatial resolution while exciting a detectable electron spin polarization. At low lattice temperatures, pump-induced carrier heating therefore is inherent to the nonresonant optical spin excitation in two-color MOKE microscopy and virtually cannot be avoided.

Surprisingly, the significance of this photocarrier heating for both the electron spin dynamics and the magneto-optical electron spin detection has been widely overlooked in the pioneering works on spatially resolved Kerr spectroscopy. With the present thesis *Hot spin carriers in cold semiconductors* we intend to close this gap by providing a comprehensive investigation of hot carrier effects in low-temperature pump-probe MOKE microscopy.

We establish in this thesis that the influence of hot photocarriers on electron spin MOKE microscopy is twofold. We demonstrate that the presence of hot electrons strongly affects both the fundamental aspect of pump-probe Kerr microscopy, the correct magneto-optical electron spin detection, and the subject of investigation, the electron spin transport processes.

We have developed a new ultrafast supercontinuum fiber-laser based pump-probe scanning MOKE microscope which allows to investigate the electron spin dynamics with picosecond time and micrometer spatial resolution. Using this instrument, we focus our work on two particularly important model systems which are archetypal for the magneto-optical investigation of semiconductor spin phenomena, bulk n-doped gallium arsenide (GaAs) and GaAs-based QWs grown along the non-conventional crystallographic [110] direction.

The surprising discovery of 100 ns low-temperature spin relaxation times in bulk n-GaAs doped close to the metal-insulator-transition [13] and the experimental proof that it is possible to transfer spin polarized electrons in semiconductors over macroscopic distances [14] provided the ignition for the field of semiconductor spintronics. Attracted by the potential applications made possible by these findings, the majority of the early MOKE microscopy work has focused on the n-GaAs system [15, 16, 30–34].

Likewise, the observation of nanosecond spin dephasing times at room temperature in (110) GaAs QWs [35] constitutes a next crucial step towards the implementation of practical spintronic devices. Such sufficiently long dephasing times combined with their comparatively high electron mobilities make two-dimensional electron gases (2DEGs) embedded in (110) QWs promising candidates for conducting channels in spintronic device concepts [36]. Moreover, (110) QWs are particularly interesting for the investigation of the fundamentals of electron spin dephasing in semiconductors. In (110) QWs a reduction of symmetry with respect to the bulk material leads to the suppression of the usually dominant Dyakonov-Perel electron spin dephasing [37] which then is superseded by other relaxation mechanisms. Gallium arsenide (110) QWs therefore provide a valuable testbed for the theoretical understanding of electron spin relaxation processes and are extensively investigated by magneto-optical spectroscopy [38–46].

For both systems we demonstrate the strong impact of hot carrier effects on the low-temperature magneto-optical electron spin detection and the spin transport properties.

Outline

The aim of the present work is to provide a comprehensive investigation of hot carrier effects in low-temperature pump-probe MOKE microscopy of the electron spin diffusion in semiconductors. The outline of this thesis is as follows:

Chapter 2 is the first of a series of three chapters that introduce the fundamentals of semiconductor spin physics, hot carrier energy relaxation, and the magneto-optical electron spin detection. We here review the electronic states and their optical excitations in bulk semiconductors and QWs and describe the optical injection of spin polarized electrons by the absorption of circularly polarized light.

In chapter 3 we introduce the Larmor precession and spin quantum beats, electron spin relaxation and dephasing, and electron spin diffusion. These phenomena are the hallmarks of optically induced electron spin dynamics in semiconductors. We describe how two particularly important parameters, the electron spin relaxation time and the electron spin diffusion coefficient, are obtained from time- and spatially resolved observations of these processes. We conclude by introducing the photoinduced magneto-optical Kerr effect, the experimental probe which we later use for the electron spin detection.

In chapter 4 we discuss the optical excitation of hot photocarriers and their thermalization and energy relaxation by carrier-carrier and carrier-phonon scattering. We then introduce the electron-acceptor PL thermometry technique which we later use for spatially resolved electron temperature spectroscopy.

In chapter 5, the first of two chapters concerned with general experimental methods and materials, we describe our optical instrumentation. We provide a detailed characterization of our ultrafast supercontinuum fiber-laser based pump-probe scanning MOKE microscope and briefly describe our microphotoluminescence experiment.

In chapter 6 we introduce the samples that are investigated in this thesis. For each specimen we provide a description of the sample structure and use standard PL spectroscopy to identify the optical transitions which are relevant to the following MOKE microscopy measurements.

In chapter 7 we present our continuous-wave (cw) MOKE microscopy results. We first establish that a thermal gradient in the electron system, a byproduct of the optical spin injection by the pump laser, locally disturbs the interrelationship between the

electron spin polarization and the experimentally observed Kerr rotation. Because of this disturbance, cw MOKE microscopy using an arbitrary probe wavelength in general, and contrary to common belief, does not correctly reveal the true local electron spin density. We demonstrate different ways to overcome this limitation and to correctly measure the electron spin profile.

We next consider the influence of hot carriers on the steady-state electron spin diffusion process. Owing to the high kinetic energy of the photoexcited electrons, the spin transport properties observed in optical spectroscopy studies may strongly deviate from the intrinsic properties of the examined system. We present a modified spin diffusion model which is capable of separating the intrinsic spin diffusivity from the hot electron contribution and thereby allows us to obtain spin transport parameters of the undisturbed system. Using a combination of Hanle-MOKE spin relaxation time measurements and steady-state MOKE microscopy we determine the intrinsic temperature dependence of the electron spin diffusion coefficient of a bulk n-GaAs sample.

In chapter 8 we demonstrate that our newly developed supercontinuum MOKE microscope is operational for time-resolved spectroscopy. We therefore first study the coherent spin transfer across a semiconductor heterointerface. We show that our two-color instrumentation allows us to selectively excite and probe the electron spin polarization in a bulk GaAs layer and a modulation-doped QW in a complex semiconductor heterostructure. We quantitatively analyze two-color Kerr rotation transients and obtain important parameters such as effective g-factors, spin relaxation times, and the average electron capturing time from the surrounding barriers into the QW.

We then present a first example of our picosecond-resolved MOKE imaging technique that allows us to directly observe the time-evolution of optically excited electron spin packets in real-space with high spatial and temporal resolution. Using this technique we determine the temperature dependence of the electron spin diffusion coefficient of a 2DEG in a (110) QW.

In chapter 9 we return to our investigation of hot carrier effects. We use time-resolved MOKE microscopy to study the transient low-temperature electron spin diffusion in bulk GaAs. We directly measure the time dependence of the electron spin diffusion coefficient from the momentary expansion rate of the spin packet. We find that the spin diffusion coefficient is strongly reduced with increasing time. Quantitative analysis and comparison with our previous cw spectroscopy data demonstrates that this decrease is caused by the transient cooling of the hot photocarriers.

We conclude by summarizing in chapter 10 the main results of this thesis.

Part I

Fundamentals and Theory

Chapter 2

Electronic states and optical transitions

This is the first of three chapters that provide an introduction to the the fundamentals of electron spin physics in semiconductor heterostructures and their magneto-optical spectroscopy. We here summarize the quantum mechanical description of the electronic states in direct band gap semiconductors and establish the selection rules and the polarization of the optical interband transitions between these states.

To keep this work self-contained, we first briefly review the basic properties of the electronic states in bulk zincblende-type semiconductors, the cubic crystal system GaAs belongs to. We focus on the description of the electron and hole states close to the Brillouin zone center which are most relevant to the magneto-optical electron spin spectroscopy. After establishing the symmetry properties of the electronic states in bulk GaAs, we next describe the influence of spatial confinement, realized by the epitaxial growth of semiconductor heterostructures, on the electron and hole wave functions.

In the second part of the chapter we review the quantum mechanical treatment of the optical interband transitions in bulk and low-dimensional semiconductors. We detail how the symmetry properties of the electron and hole wave functions govern the allowed optical transitions and their polarization and introduce the concept of optical spin injection, the above-bandgap excitation of spin polarized conduction band electrons by circularly polarized light.

2.1 Electronic states in bulk zincblende-type semiconductors and quantum wells

2.1.1 Crystal structure of gallium arsenide

We first recall the basic crystalline properties of the material system under investigation, GaAs. Gallium arsenide is a III-V binary semiconductor composed to equal parts of gallium (Ga) and arsenic (As) ions. Similar to the majority of III-V semiconductors, GaAs crystallizes in the cubic zincblende structure.

The zincblende structure shown in Fig. 1 (a) consist of two face-centered cubic (fcc) sublattices which are populated by the Ga and As ions, respectively. The room temperature lattice constant of the cubic unit cell of GaAs is $a_0 = 5.65\,\text{Å}$ [49]. The fcc

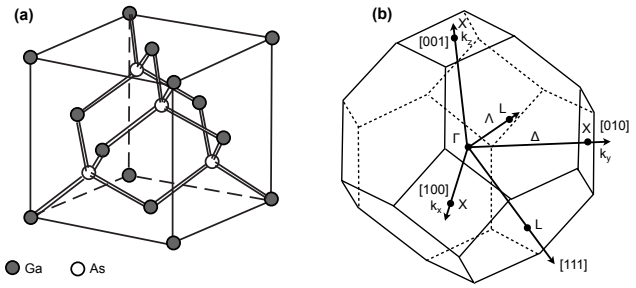

Figure 1: (a) The GaAs cubic unit cell. Adapted from [47]. **(b)** First Brillouin zone of the fcc Bravais lattice of GaAs. The high-symmetry Γ, *L*, and *X* points in **k**-space are found at the Brillouin zone center and at the intersections of the ⟨100⟩ and ⟨111⟩ axes with the zone boundary. Adapted from [48].

sublattices are displaced by $(\sqrt{3}/4)a_0$ against each other along the cube main diagonal [111] direction, i.e. each Ga ion is tetrahedrally surrounded by four As ions and vice versa [50]. The tetrahedral chemical bonds are derived from sp^3 hybridized orbitals formed by the *s* and *p* valence electrons of the neighboring ions and are, as is typical for most III-V compound semiconductors, of mainly covalent nature.

The first Brillouin zone of GaAs, a truncated octahedron, is shown in Fig. 1 (b). The high-symmetry Γ, *L*, and *X* points in **k**-space are found at the Brillouin zone center and at the intersections of the ⟨100⟩ and ⟨111⟩ axes with the zone boundary.

We describe in the following how the symmetry of the semiconductor crystal structure governs both the allowed optical excitations and important aspects of the electron spin dynamics. The tetrahedral symmetry of the GaAs lattice is directly reflected by the electronic wave functions which, in combination with the action of spin-orbit coupling, enables optical spin excitation. Moreover, in contrast to elemental semiconductors with diamond structure (e.g. germanium and silicon), the GaAs crystal structure lacks inversion symmetry. This absence of inversion symmetry gives rise to the Dyakonov-Perel spin relaxation mechanism which is usually dominant in n-doped bulk GaAs (compare section 3.1.2).

2.1.2 Electronic band structure of gallium arsenide

We next briefly review the electronic band structure of GaAs. Inspection of the band diagram shown in Fig. 2 (a) reveals that GaAs is a direct band gap semiconductor. Using double group notation, the degenerate energy maxima of the highest occupied Γ_7 and Γ_8 valence bands (VBs) and the minimum of the lowest unoccupied Γ_6 conduction band (CB) coincide at the Brillouin zone center $\mathbf{k} = 0$. The fundamental energy gap between the Γ_6 conduction band and the Γ_8 valence bands is $E_{\mathrm{gap}} = 1.519\,\mathrm{eV}$ at liquid helium temperature [51]. The Γ_7 valence band is shifted by $\Delta_{\mathrm{SO}} = 0.34\,\mathrm{eV}$ towards lower energies by spin-orbit interaction.

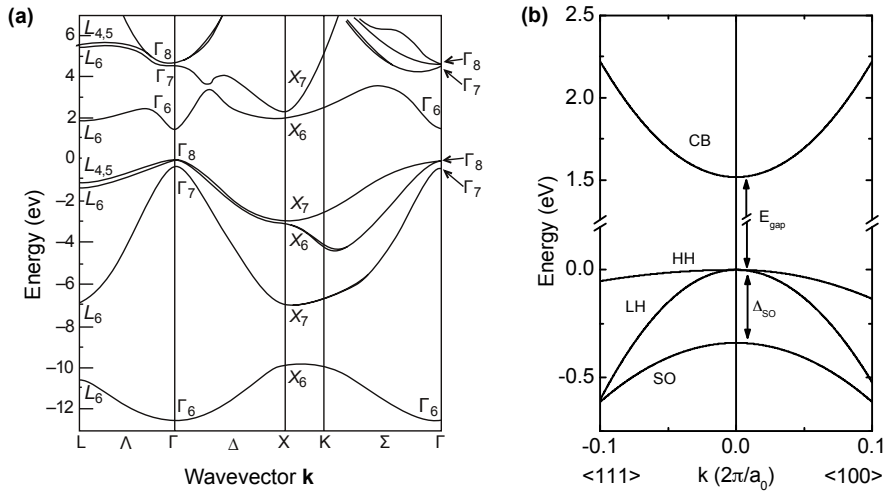

Figure 2: (a) Electronic band structure of GaAs calculated by the empirical pseudopotential method. The zero point of the energy scale is taken to coincide with the top of the valence band. The symmetries of the respective bands are denoted using double group notation. Adapted from [47]. **(b)** Conduction and valence band dispersion along the high symmetry <001> and <111> axes in the vicinity of the Γ point obtained from a standard $\mathbf{k} \cdot \mathbf{p}$ calculation [52]. Note the strong valence band warping.

The optical properties of GaAs in the visible and near-infrared spectral range are governed by electric dipole interband transitions. The transitions which are relevant for the present work take place in the Brillouin zone center between the Γ_6 conduction and Γ_8 valence bands. In the following we first consider the atomistic origin of the participating electronic states. We then provide a quantum mechanical description of the possible optical transitions and discuss the associated selection rules which govern the optical spin injection.

From a tight-binding perspective, the Γ_6 CB states are derived from antibonding σ orbitals and possess *s*-type symmetry. The Γ_7 and Γ_8 VBs are formed from bonding π orbitals and the associated hole states are of *p*-type symmetry [47]. The otherwise sixfold degeneracy of the valence bands is lifted by spin-orbit coupling as detailed below. Each of the three hole subbands and the conduction band are twofold degenerate at the Γ point. As discussed in detail in section 3.1.2, this degeneracy is lifted for $\mathbf{k} \neq 0$ by the Dresselhaus effect. The Dresselhaus effect arises as a consequence of the absence of inversion symmetry in zincblende-type semiconductors and leads to an additional energetic splitting of the electronic states, the bulk inversion asymmetry splitting [53].

2.1.3 Symmetry and wave functions

We now turn to a more formal quantum mechanical description of the electronic states in zincblende semiconductors. For the following discussion we first neglect spin-orbit interaction. As a starting point for the construction of the electron and hole wave functions we use the stationary one-electron Schrödinger equation:

$$H_0\psi = \left(\frac{\mathbf{p}^2}{2m_0} + V(\mathbf{r})\right)\psi = E\psi \tag{2.1}$$

for the motion of an electron of mass m_0 in a potential $V(\mathbf{r})$. Here $\mathbf{p}$ denotes the momentum operator and E is the energy of the respective eigenstate $|\psi\rangle$ of the Hamilton operator H_0.

For a spatially periodic crystal potential $V(\mathbf{r}) = V(\mathbf{r}+\mathbf{R}_j)$, where $\mathbf{R}_j$ is an arbitrary Bravais lattice vector, the solutions of Eq. (2.1) are Bloch functions of the form:

$$\psi_{n,\mathbf{k}}(\mathbf{r}) = e^{i\mathbf{k}\cdot\mathbf{r}}u_{n,\mathbf{k}}(\mathbf{r}) \tag{2.2}$$

The wave vector $\mathbf{k}$ is restricted to the first Brillouin zone and n denotes the band index. The lattice periodic functions $u_{n,\mathbf{k}}(\mathbf{r}) = u_{n,\mathbf{k}}(\mathbf{r}+\mathbf{R}_j)$ share the translation invariance of the Bravais crystal lattice.

While explicit expressions for $u_{n,\mathbf{k}}(\mathbf{r})$ in general are not available, important properties of the lattice periodic part of the Bloch functions can be deduced from symmetry arguments. From Neumann's principle, the symmetry group of any physical property of a crystal will include the symmetry elements of the point group of the crystal lattice [54]. As a consequence, each Bloch function associated with a high symmetry point in the first Brillouin zone is invariant under the same transformations as the respective point in $\mathbf{k}$-space. We will in the following use this property to deduce expressions for the conduction and valence band states at the Γ point, i.e. at $\mathbf{k} = 0$.

The point group of zincblende-type semiconductors is T_d [55]. Group theory shows that the CB function $u^c(\mathbf{k} = 0, \mathbf{r})$ transforms in the same way as the atomic s wave function under symmetry operations that map a tetrahedron onto itself. Similar symmetry considerations can be applied to the valence band hole states. At $\mathbf{k} = 0$ the threefold degenerate valence band states can be chosen as eigenfunctions of the $\hat{z}$-component of the orbital momentum operator L_z with magnetic quantum numbers $m_L = \{0, \pm 1\}$ [47].

It is convenient for the following discussion to choose a basis of valence band wave functions which transform similar to the atomic p_x, p_y, and p_z orbitals under operations of the point group T_d. Following the usual convention, the lattice periodic parts of these conduction and valence band functions are denoted as $|S\rangle$, $|X\rangle$, $|Y\rangle$, and $|Z\rangle$ [47].

We next consider the influence of spin-orbit interaction on the electron and hole wave functions. Spin-orbit interaction is a relativistic effect which stems from the magnetic moment $\boldsymbol{\mu} = -(g\mu_B/\hbar)\mathbf{S}$ of the electron spin $\mathbf{S}$. Here g is the Landé g-factor, $\hbar$ is the reduced Planck constant, and μ_B is the Bohr magneton. The Hamiltonian of the spin-orbit interaction can be derived from a series expansion of the Dirac equation up to

terms of order $(1/c^2)$ as [56]:

$$H_{\mathrm{SO}} = \frac{\hbar}{4c^2 m_0^2} (\nabla V \times \mathbf{p}) \cdot \boldsymbol{\sigma} \tag{2.3}$$

with the speed of light c. The three components of $\boldsymbol{\sigma}$ are the spin-1/2 Pauli matrices [57].

For GaAs which contains the heavy As anion, the influence of spin-orbit interaction on the electronic states close to the Brillouin zone center is rather strong. This is seen from the comparatively large value of the spin orbit splitting $\Delta_{\mathrm{SO}} = 0.34\,\mathrm{eV}$. Moreover, and most important for the polarization of the electric dipole interband transitions, the symmetries of the valence band hole wave functions are strongly changed by spin-orbit interaction.

When including H_{SO} in the Schrödinger equation Eq. (2.1), the lattice periodic functions $|X\rangle$, $|Y\rangle$, and $|Z\rangle$ are no longer eigenfunctions of the total Hamilton operator. Instead, when treating H_{SO} as a perturbation, the eigenfunctions of the Hamiltonian including H_{SO} can be chosen to be eigenstates of the total orbital momentum operator $\mathbf{J} = \mathbf{L} + \mathbf{S}$ with quantum numbers $J = \{1/2, 3/2\}$ [58]. The resulting basis functions are known as the angular momentum representation [59]. The new eigenfunctions of the Hamiltonian including H_{SO} are linear combinations of product states of the $|S\rangle$, $|X\rangle$, $|Y\rangle$, and $|Z\rangle$ orbital wave functions with the two eigenfunctions of the spin operator $\mathbf{S} = (\hbar/2)\boldsymbol{\sigma}$, the spinors $|\uparrow\rangle$ and $|\downarrow\rangle$ [60]. Explicit expressions for these linear combinations are given in Table 2.1. For the arbitrary phase of the normalization constants we follow the convention of Ref. [48]. The wave functions listed in Table 2.1 are used in the following sections to evaluate the relative strength and the polarization of optical interband transitions.

2.1.4 Electron and hole dispersion near the Γ point

In the preceding section we have constructed the conduction and valence band wave functions at the Γ point. At $\mathbf{k} = 0$, the Γ_8 valence band states are degenerate as shown in Fig 2 (a). For finite $\mathbf{k}$ this degeneracy is lifted by spin-orbit coupling. Moving away from the Brillouin zone center, the Γ_8 states with $J = 3/2$ are split into the $J_z = \pm 1/2$ light hole (LH) and the $J_z = \pm 3/2$ heavy hole (HH) bands. The Γ_7 valence band with $J = 1/2$ and $J_z = \pm 1/2$ is termed the split-off (SO) hole band.

For small wave vectors $|\mathbf{k}| \ll (2\pi/a_0)$ close to the Brillouin zone center, the parabolic energy dispersion relation:

$$E_c(\mathbf{k}) = \frac{\hbar^2 k^2}{2m_e^*} \tag{2.4}$$

of the GaAs conduction band is isotropic with an effective electron mass $m_e^* = 0.067 m_0$ [52]. This isotropy reflects the spherical symmetry of the s-type orbitals from which the Γ_6 band is derived.

Table 2.1: Angular momentum representation of the conduction and valence band wave functions at the Γ point in zincblence-type semiconductors [59]. J and m_J denote the quantum numbers of the total angular momentum operator **J** and the projection of the total angular momentum J_z along the z-axis. Symmetries are denoted using the double group notation.

Symmetry	$\lvert J, m_J\rangle$	Wave function
Γ_6	$\lvert 1/2, 1/2\rangle$	$\lvert S\uparrow\rangle$
	$\lvert 1/2, -1/2\rangle$	$\lvert S\downarrow\rangle$
Γ_7	$\lvert 1/2, 1/2\rangle$	$\frac{1}{\sqrt{3}}\lvert (X+iY)\downarrow\rangle + \frac{1}{\sqrt{3}}\lvert Z\uparrow\rangle$
	$\lvert 1/2, -1/2\rangle$	$-\frac{1}{\sqrt{3}}\lvert (X-iY)\uparrow\rangle + \frac{1}{\sqrt{3}}\lvert Z\downarrow\rangle$
Γ_8	$\lvert 3/2, 3/2\rangle$	$\frac{1}{\sqrt{2}}\lvert (X+iY)\uparrow\rangle$
	$\lvert 3/2, 1/2\rangle$	$\frac{1}{\sqrt{6}}\lvert (X+iY)\downarrow\rangle - \frac{\sqrt{2}}{\sqrt{3}}\lvert Z\uparrow\rangle$
	$\lvert 3/2, -1/2\rangle$	$-\frac{1}{\sqrt{6}}\lvert (X-iY)\uparrow\rangle - \frac{\sqrt{2}}{\sqrt{3}}\lvert Z\downarrow\rangle$
	$\lvert 3/2, -3/2\rangle$	$\frac{1}{\sqrt{2}}\lvert (X-iY)\downarrow\rangle$

For the parabolic conduction band dispersion Eq. (2.4), the electron density of states $g(E_c)$ per unit crystal volume is [59]:

$$g(E_c)\,dE_c = \frac{1}{2\pi^2}\left(\frac{2m_e^*}{\hbar^2}\right)^{3/2}\sqrt{E_c}\,dE_c \tag{2.5}$$

where we have considered the twofold spin degeneracy of the conduction band.

For the GaAs Γ_8 valence bands, deviations from an isotropic parabolic dispersion are present even for small wave vectors close to the Γ point, a phenomenon known as valence band warping. Analytical expressions for the anisotropic HH and LH dispersions for small **k** can be derived from a standard 8-band $\mathbf{k}\cdot\mathbf{p}$ calculation as [47]:

$$E_{hh}(\mathbf{k}) = -Ak^2 - \left[B^2k^4 + C^2\left(k_x^2k_y^2 + k_y^2k_z^2 + k_z^2k_x^2\right)\right]^{1/2} \tag{2.6}$$

$$E_{lh}(\mathbf{k}) = -Ak^2 + \left[B^2k^4 + C^2\left(k_x^2k_y^2 + k_y^2k_z^2 + k_z^2k_x^2\right)\right]^{1/2} \tag{2.7}$$

The constants A, B, and C are related to the well-known Kohn-Luttinger parameters $\gamma_1 = 6.98$, $\gamma_2 = 2.06$, and $\gamma_3 = 2.93$ of GaAs [52] as [47]:

$$\left(\hbar^2/2m_0\right)\gamma_1 = -A \tag{2.8}$$

$$\left(\hbar^2/2m_0\right)\gamma_2 = -B/2 \tag{2.9}$$

$$\left(\hbar^2/2m_0\right)\gamma_3 = \left[\left(B^2/4\right) + \left(C^2/12\right)\right]^{1/2} \tag{2.10}$$

For a given direction, the HH and LH valence band dispersions close to the Γ point are parabolic as shown in Fig. 2 (b). The valence band curvature and the associated

effective heavy and light hole masses m^*_{hh} and m^*_{lh}, however, depend strongly on the specific direction of $\mathbf{k}$. The strongest difference in the effective hole masses is observed for wave vectors pointing along the <100> and <111> axes.

In section 2.2.1 we show that for interband transitions the wave vector of the participating initial electronic states is conserved, i.e. optical transitions are vertical in the $E(\mathbf{k})$ diagram. The anisotropy of the GaAs valence bands therefore has direct consequences for the energy distribution of conduction band electrons which are excited by monochromatic light. In GaAs, the strong valence band warping leads to a broadening of the initial energy distribution of optically excited conduction band electrons [27].

2.1.5 Electronic states in quantum wells

In addition to studying spin phenomena in bulk semiconductors we also investigate spin transport in low-dimensional semiconductor systems. The QWs examined in this thesis consist of alternating layers of GaAs and aluminium gallium arsenide ($Al_xGa_{1-x}As$) alloys. The GaAs/$Al_xGa_{1-x}As$ interface is of type-I [61] and the band gap energies are $E_{\text{gap}}^{\text{GaAs}} < E_{\text{gap}}^{Al_xGa_{1-x}As}$ [52]. When a layer of GaAs is placed between two $Al_xGa_{1-x}As$ barriers, both the conduction band electrons and the valence band holes therefore are confined to the GaAs layer. The position dependence of the conduction and valence band edges along the growth-axis of such a type-I QW structure is schematically shown in Fig. 3 (a). When the GaAs layer thickness L_z is thin enough to be comparable to the de Broglie wavelength $\lambda = h/p$ of the electrons or holes, spatial confinement strongly modifies the electronic states [54]. If the growth axis of the heterostructure is chosen to be the z-axis, the motion of electrons and holes is unrestricted within the QW plane. The movement along the z-axis, however, becomes quantized.

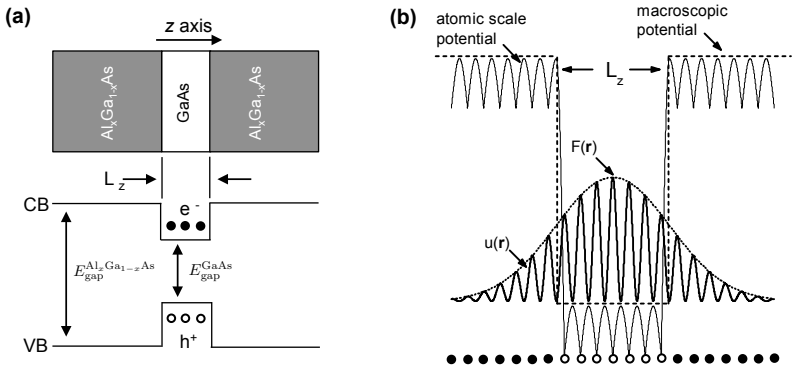

Figure 3: (a) Top: schematic of a type-I GaAs/$Al_xGa_{1-x}As$ single QW structure. Bottom: schematic of the conduction and valence band edges along the growth axis. The electrons and holes are confined to the GaAs layer of width L_z. Adapted from [54]. **(b)** Envelope wave approximation for electronic quantum well states. The wave function is a product of the slowly varying envelope function $F(\mathbf{r})$ and the lattice periodic function $u(\mathbf{r})$. The influence of the individual atomic potentials on the envelope wave function is approximated by a finite rectangular potential well. Adapted from [59].

We next review the new symmetry properties which are imposed on the electronic wave functions by the QW confinement potential. These symmetries are important for the optical selection rules introduced in the following sections. For the sake of simplicity we focus on the effects of quantum confinement on the conduction band states. We note that the description of the QW hole states is conceptually similar. The quantitative treatment of the in-plane hole energy dispersion, however, is significantly more complex because of the strong valence band mixing in GaAs QWs [23, 47].

For the $Al_xGa_{1-x}As/GaAs/Al_xGa_{1-x}As$ layer structure shown in Fig. 3 (a), the global translation invariance of the bulk crystal potential $V(\mathbf{r}) = V(\mathbf{r}+\mathbf{R}_j)$ is broken along the QW growth axis z. Therefore the Schrödinger equation Eq. (2.1) can no longer be solved by a simple Fourier analysis which for the bulk crystal leads to the Bloch functions Eq. (2.2) [62]. A common approach to overcoming this difficulty is the envelope wave approximation (EWA) which was first introduced for the description of semiconductor defect states [58].

The basic ideas underlying the EWA are illustrated in Fig. 3 (b). Following the EWA procedure we decompose the full crystal potential of the $GaAs/Al_xGa_{1-x}As$ heterostructure into a lattice-periodic atomic-scale potential and a macroscopic confinement potential $V_{\mathrm{con}}(z)$ which follows the CB edge. For the description of the QW electron states $|\psi\rangle$ we use the Bloch functions Eq. (2.2) as a complete set of orthonormal basis functions [59]:

$$\psi(\mathbf{r}) = \int A(\mathbf{k}) e^{i\mathbf{k}\cdot\mathbf{r}} u(\mathbf{k},\mathbf{r}) d^3\mathbf{k} \approx u(0,\mathbf{r}) \int A(\mathbf{k}) e^{i\mathbf{k}\cdot\mathbf{r}} d^3\mathbf{k} \equiv F(\mathbf{r}) u(\mathbf{r}) \tag{2.11}$$

where $A(\mathbf{k})$ denotes the set of expansion coefficients. We further assume in Eq. (2.11) that the lattice periodic part of the Bloch functions only weakly depends on $\mathbf{k}$, i.e. $u(\mathbf{k},\mathbf{r}) \approx u(0,\mathbf{r})$. In the envelope wave approximation, QW wave functions therefore are products of the lattice periodic function $u(\mathbf{r})$ and a slowly varying envelope function $F(\mathbf{r})$. Using the separation ansatz [63]:

$$F(\mathbf{r}) = e^{i\mathbf{k}\cdot\mathbf{r}_\parallel} \chi_c(z) u(\mathbf{r}) \tag{2.12}$$

where the coordinate vector $\mathbf{r}_\parallel$ is restricted to the QW plane, we arrive at the Schrödinger equation:

$$\left(-\frac{\hbar^2}{2m_e^*} \frac{\partial^2}{\partial z^2} + V_{\mathrm{conv}}(z) \right) \chi_c(z) = E_z^c \chi(z) \tag{2.13}$$

for the envelope function $\chi_c(z)$.

Treating $V_{\mathrm{conv}}(z)$ as a finite potential well as shown in Fig. 3 (b), the restriction of the electron motion along the z-axis leads to a set of bound QW states $\chi_c^n(z)$ with quantum numbers $n = \{1,2,3\ldots\}$ and discrete energy eigenvalues [57] which, to a first approximation, depend on the GaAs effective conduction band mass as:

$$E_{z,n}^c \sim \frac{1}{m_e^*} \tag{2.14}$$

A similar procedure can be used to obtain the solutions for the heavy hole and light hole QW envelope functions χ_{hh} and χ_{lh}. Since $m^*_{lh} < m^*_{hh}$, it is seen from Eq. (2.14) that the quantum confinement lifts the bulk heavy hole-light hole degeneracy at zero in-plane wave vector $\mathbf{k}_{\|} = 0$.

Exemplary conduction and valence band envelope functions for a finite potential well are schematically shown in Fig. 4. Most important for the optical selection rules in QWs, for a symmetric confinement potential $V_{\mathrm{con}}(z)$ the envelope functions have alternating odd and even parity with respect to the QW center. The associated probability density $|\chi^n(z)|^2$ exhibits $(n-1)$ nodes [57].

2.2 Optical interband transitions and matrix elements

We next briefly summarize the quantum mechanical treatment of the interaction of electromagnetic waves with the electronic states of semiconductors. Choosing the Coulomb gauge [64], we therefore describe the electric field $\mathbf{E} = -\frac{1}{c}\left(\frac{\partial \mathbf{A}}{\partial t}\right)$ and the magnetic field $\mathbf{B} = \nabla \times \mathbf{A}$ by the vector potential $\mathbf{A}(\mathbf{r},t)$.

We consider the interaction with a monochromatic electromagnetic plane wave with wave vector $\mathbf{q}$ and frequency $(\omega/2\pi)$ described by the vector potential:

$$\mathbf{A}(\mathbf{r},t) = A \cdot \hat{\mathbf{e}} \cdot \left(e^{i(\omega t - \mathbf{q}\cdot\mathbf{r})} + \text{c.c.}\right) \tag{2.15}$$

where c.c. denotes the complex conjugate. The amplitude $A = E/q$ is proportional the electric field amplitude E. The polarization state of the wave is defined by the complex unit vector $\hat{\mathbf{e}}$.

We account for the additional electromagnetic field by replacing the momentum operator $\mathbf{p}$ by the minimal-coupling term $\mathbf{p} + (e\mathbf{A}/c)$ in the Schrödinger equation Eq. (2.1). Neglecting contributions which arise from the spin-orbit term Eq. (2.3) and dropping terms $\mathcal{O}(A^2)$, the one-electron Hamiltonian then is [47]:

$$H = H_0 + \frac{e}{m_0 c}\mathbf{A}(\mathbf{r},t)\cdot\mathbf{p} \equiv H_0 + H_{\mathrm{eR}} \tag{2.16}$$

We use perturbation theory to treat the influence of the second term of the Hamilton operator in Eq. (2.16). The time-harmonic perturbation described by the electron-radiation interaction Hamiltonian H_{eR} induces transitions between the conduction and valence band states of the unperturbed Hamiltonian H_0 [47]. From the Fermi Golden Rule, the transition rate $\tilde{P}_{if}$ between an initial state $|i\rangle$ with energy E_i and a final state $|f\rangle$ with energy E_f is [57]:

$$\tilde{P}_{if} = \frac{2\pi}{\hbar}\left|\langle f|H_{\mathrm{eR}}|i\rangle\right|^2 \delta(E_f - E_i - \hbar\omega) \tag{2.17}$$

2.2.1 Interband transitions in bulk semiconductors

We first consider optical transitions between the Γ_6 conduction band and the Γ_7 and Γ_8 valence band states in bulk semiconductors. From Eqs. (2.15), (2.16), and (2.17) we therefore evaluate the matrix elements:

$$|\langle c|\,\mathbf{A}\cdot\mathbf{p}\,|v\rangle|^2 \tag{2.18}$$

for the bulk conduction and valence band Bloch functions:

$$|c\rangle = u^c_{\mathbf{k}_c}(\mathbf{r})e^{i\mathbf{k}_c\mathbf{r}} \tag{2.19}$$

$$|v\rangle = u^v_{\mathbf{k}_v}(\mathbf{r})e^{i\mathbf{k}_v\mathbf{r}} \tag{2.20}$$

with wave vectors $\mathbf{k}_c$ and $\mathbf{k}_v$. The explicit expression for the matrix element Eq. (2.18) in position-space representation is:

$$|\langle c|\,\mathbf{A}\cdot\mathbf{p}\,|v\rangle|^2 \sim \left|\int u^{c*}_{\mathbf{k}_c} e^{i(\mathbf{q}-\mathbf{k}_c)\mathbf{r}}\,(\hat{\mathbf{e}}\cdot\mathbf{p})\,u^v_{\mathbf{k}_v} e^{i\mathbf{k}_v\mathbf{r}}\,d^3r\right|^2 \tag{2.21}$$

When applying $\mathbf{p} = (\hbar/i)\nabla$, the integral in Eq. (2.21) splits in the sum of two terms. From the orthogonality of the functions $u^c_{\mathbf{k}_c}$ and $u^v_{\mathbf{k}_v}$, the first term vanishes. By writing $\mathbf{r} = \mathbf{R}_j + \mathbf{r}'$, where $\mathbf{r}'$ lies within one unit cell and $\mathbf{R}_j$ is an arbitrary Bravais lattice vector, we transform the integration over the whole crystal to an infinite sum of integrals which cover a single crystal unit cell [47].

Using the periodicity of the functions $u^{c,v}$ we find that the matrix element Eq. (2.21) is only non-zero if the wave vectors of the conduction and valence band states fulfill the condition:

$$\mathbf{k}_c = \mathbf{q} \pm \mathbf{k}_v \tag{2.22}$$

As a consequence of the translation symmetry of the semiconductor crystal, the total wave vector of the photon and the participating initial state is conserved in optical transitions.

Following the above procedure, the remaining step for the evaluation of the transition matrix element involves an integration over the volume of a single unit cell. Using Eq. (2.22), this integration is further reduced to [47]:

$$\int\limits_{\substack{\text{unit}\\ \text{cell}}} u^{c*}_{\mathbf{k}_v+\mathbf{q}}\,(\hat{\mathbf{e}}\cdot\mathbf{p})\,u^v_{\mathbf{k}_v}\,d^3\mathbf{r}, \tag{2.23}$$

For electromagnetic waves with frequencies in the visible and near-infrared spectral range, the wave vector $|\mathbf{q}| \ll (2\pi/a_0)$ is much smaller than the size of the Brillouin zone. To further simplify Eq. (2.23), we therefore expand the conduction band wave function $u^c_{\mathbf{k}_v+\mathbf{q}}$ into a Taylor series in $\mathbf{q}$:

$$u^c_{\mathbf{k}_v+\mathbf{q}} = u^c_{\mathbf{k}_v} + \mathbf{q}\cdot\nabla_{\mathbf{k}}u^c_{\mathbf{k}} + \mathcal{O}(q^2) \tag{2.24}$$

For the small wave vectors $\mathbf{q} \approx 0$ we drop the $\mathbf{q}$-dependent terms in Eq. (2.24), i.e. the interband transition rate $\tilde{P}_{if} \sim |\langle c|\,\hat{\mathbf{e}}\cdot\mathbf{p}\,|v\rangle|^2$. This approximation is the well known electric dipole approximation and implies [47]:

$$\mathbf{k}_c = \mathbf{k}_v \tag{2.25}$$

i.e. optical dipole interband transitions are "vertical" or direct in $\mathbf{k}$-space. Using the dipole approximation, we finally obtain the electric dipole transition matrix element:

$$|\langle c|\,\hat{\mathbf{e}}\cdot\mathbf{p}\,|v\rangle|^2 = \left|\int\limits_{\substack{\text{unit}\\ \text{cell}}} u^{c*}_{\mathbf{k}}(\hat{\mathbf{e}}\cdot\mathbf{p})u^{v}_{\mathbf{k}}\,d^3\mathbf{r}\right|^2 = |\langle u_c|\,\hat{\mathbf{e}}\cdot\mathbf{p}\,|u_v\rangle|^2 \equiv |P_{cv}|^2 \tag{2.26}$$

In the following section 2.3 we calculate the polarization and the relative strength of the optical interband transitions by evaluating $|P_{cv}|^2$ for the conduction and valence band wave functions listed in Table 2.1. Before doing so, however, we first briefly consider the influence of quantum confinement on optical interband transitions.

2.2.2 Interband transitions in quantum wells

The treatment of optical dipole-transitions in QWs follows the procedure outlined above for the bulk case with the main difference that the transitions take place between the envelope wave states:

$$|c\rangle = u^{c}_{\mathbf{k}_c}(\mathbf{r})e^{i\mathbf{k}_{c,\|}\cdot\mathbf{r}}\chi_c(z) \tag{2.27}$$

$$|v\rangle = u^{v}_{\mathbf{k}_v}(\mathbf{r})e^{i\mathbf{k}_{v,\|}\cdot\mathbf{r}}\chi_v(z) \tag{2.28}$$

The electric dipole transitions between conduction and valence band QW states are governed by the matrix elements [59]:

$$|P_{cv}|^2 = |\langle c|\,\hat{\mathbf{e}}\cdot\mathbf{p}\,|v\rangle|^2 = |\langle u_c|\,\hat{\mathbf{e}}\cdot\mathbf{p}\,|u_v\rangle|^2\,|\langle\chi_c|\,\chi_v\rangle|^2 \tag{2.29}$$

and the spatial phase-matching condition:

$$\mathbf{k}_{c,\|} = \mathbf{k}_{v,\|} \tag{2.30}$$

which implies that the in-plane wave vector $\mathbf{k}_\|$ of the initial QW state is conserved.

A comparison between Eqs. (2.26) and (2.29) reveals that the polarization of the interband transitions in QWs determined by the matrix element $|\langle u_c|\,\hat{\mathbf{e}}\cdot\mathbf{p}\,|u_v\rangle|^2$ is similar to the bulk case. The reduction of the translation invariance by the QW confinement potential and the associated symmetry of the envelope functions, however, leads for symmetric QWs to the additional dipole selection rule:

$$|\langle\chi_c|\,\chi_v\rangle|^2 \approx \delta_{n_c,n_v} \tag{2.31}$$

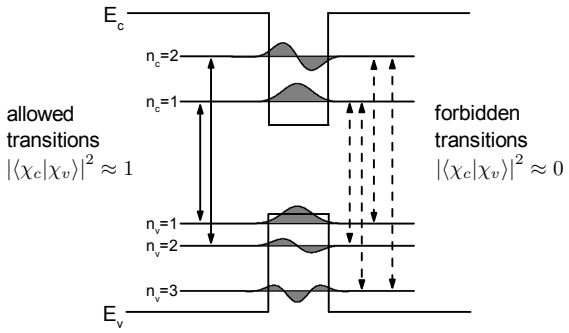

Figure 4: Allowed (solid arrows) and forbidden (dashed arrows) electric dipole transitions in a symmetric rectangular quantum well. Gray shaded curves illustrate conduction and valence band envelope wave functions $\chi_{c,v}$. For transitions involving initial and final envelope states with different quantum numbers $n_{c,v}$ the matrix element Eq. (2.29) vanishes. Adapted from [59].

where the Kronecker delta δ_{n_c,n_v} is zero unless transitions take place between QW subbands with the same quantum number $n_c = n_v$ [59]. This condition is partially relaxed by the difference in effective masses and confinement potential heights for the conduction and valence band states. However, for symmetric QWs dipole transitions in any case can only take place between electron and hole subbands of the same parity, for which $(n_c + n_v)$ is an even integer. The QW interband transitions are labeled according to the quantum numbers of the participating subbands as (1E-1HH), (1E-1LH), etc. Some dipole allowed and forbidden transitions between different QW electron and hole states are schematically illustrated in Fig. 4.

2.3 Dipole selection rules and optical spin injection

We next introduce the concept of optical spin injection, i.e. the optical excitation of an ensemble of spin polarized electrons, which is the very foundation of pump-probe magneto-optical spectroscopy. We therefore consider the absorption of $\sigma^{\pm}$ right and left circularly polarized light described by the polarization vectors $\hat{\mathbf{e}} = 1/\sqrt{2}\,(\hat{\mathbf{x}} \pm i\hat{\mathbf{y}})$. We deduce the polarization dependence of the interband transitions and their relative strengths from Eq. (2.26). To obtain the selection rules we evaluate the dipole matrix elements:

$$\left|P_{cv}^{\pm}\right|^2 = \left|\langle u_c|\, p_x \pm i p_y\, |u_v\rangle\right|^2 \tag{2.32}$$

for the possible permutations of the conduction and valence band wave functions $|J, m_J\rangle$ listed in Table 2.1.

From symmetry considerations, the only non-zero matrix elements of the components p_i of the momentum vector operator $\mathbf{p}$ between the basis functions $|S\rangle$, $|X\rangle$, $|Y\rangle$, and

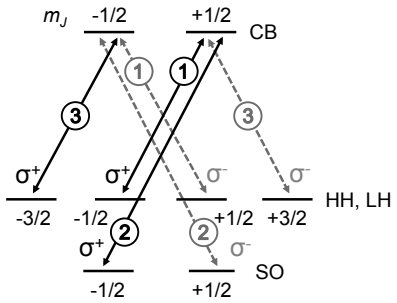

Figure 5: Optical spin injection in bulk zincblende-type semiconductors. Solid (dashed) arrows represent dipole-allowed transitions for the absorption of σ^+ (σ^-) right (left) circularly polarized light. The numbers in circles indicate the relative strength of the respective transition at $\mathbf{k} = 0$. Adapted from [60].

$|Z\rangle$ are [27, 47, 48]:

$$\langle S|\, p_x\, |X\rangle = \langle S|\, p_y\, |Y\rangle = \langle S|\, p_z\, |Z\rangle \equiv \Pi \tag{2.33}$$

From Eq. (2.33) and Table 2.1 we therefore obtain the dipole selection rules:

$$\Delta L = \pm 1 \quad \text{and} \quad \Delta m_J = \pm 1 \tag{2.34}$$

for the absorption of circularly polarized light. The dipole selection rules Eq. (2.34) reflect the conservation of total angular momentum: the absorption of a photon with angular momentum projection $\pm\hbar$ along the propagation direction $\hat{z}$ results in the creation of an electron-hole pair with an equal total angular momentum projection $(m_{J,e} + m_{J,h})\hbar = \pm\hbar$.

We next calculate the relative strength of the dipole-allowed transitions between the $|3/2, -3/2\rangle$ HH and $|3/2, -1/2\rangle$ LH and the $|1/2, \pm 1/2\rangle$ CB states for the absorption of σ^+ light as:

$$\frac{\left|\langle 3/2, -3/2|\, \hat{p}_x + i\hat{p}_y\, |1/2, -1/2\rangle\right|^2}{\left|\langle 3/2, -1/2|\, \hat{p}_x + i\hat{p}_y\, |1/2, +1/2\rangle\right|^2} = \frac{3}{1} \tag{2.35}$$

Analogous calculations yield the relative strengths of the remaining allowed transitions which are summarized in Fig. 5.

The above considerations are strictly valid only at the Brillouin zone center. Since the lattice periodic functions $u(\mathbf{k}, \mathbf{r}) \approx u(0, \mathbf{r})$ depend only weakly on $\mathbf{k}$, the relative transition strengths listed in Fig. 5, however, remain a good approximation for all excitation energies in the vicinity of the band gap.

We have arrived at the important result that illumination of bulk zincblende-type semiconductors with circularly polarized light with photon energies $E_0 < \hbar\omega < E_0 + \Delta_{\mathrm{SO}}$ excites $|\downarrow\rangle$ and $|\uparrow\rangle$ conduction electrons with a maximum ratio of $3/1$. This phenomenon

is known as optical spin injection or optical orientation [65]. The optical orientation technique allows for the precise preparation of the conduction band electron spin polarization in semiconductors. It today is the most important and widely used experimental method for the creation of spin polarized electrons in zincblende-type semiconductors. The photoinduced dynamics of the electron spin polarization following the optical excitation are the subject of chapter 3.

The net electron spin polarization S_z along the z-axis is defined as [60]:

$$S_z = \frac{n_\uparrow - n_\downarrow}{n_\uparrow + n_\downarrow} \tag{2.36}$$

It is a measure for the difference in the densities $n_{\uparrow,\downarrow}$ of electrons which are polarized parallel ($m_J = +1/2$) or antiparallel ($m_J = -1/2$) to the propagation direction of the exciting light. From the above considerations, for resonant optical spin injection in bulk GaAs the theoretical limit for the maximum attainable polarization at the moment of excitation is $S_{z,\max} = 1/2$.

A more realistic treatment takes into account that at low temperatures optical absorption is governed by Coulomb-correlated electron-hole pairs, i.e. excitons, whose wave function consist of electron and hole states with $k \lesssim 1/a_B^*$, where a_B^* is the exciton effective Bohr radius. Due to the strong HH-LH coupling for $k > 0$, the Coulomb interaction induces an additional mixing of single-particle states with different S_z [66]. Therefore, a reduction of the maximum attainable degree of optically excited spin orientation is expected. At low lattice temperatures electron spin polarizations close to 50 %, however, still are experimentally observed for nearly resonant excitation [67]. A moderate decrease of the spin excitation efficiency is observed with increasing excitation energy [68]. When the photon energy is tuned above $E_0 + \Delta_{\mathrm{SO}}$, $|\uparrow\rangle$ and $|\downarrow\rangle$ electrons are excited with equal probability and we expect $S_z \approx 0$.

The polarization of QW interband transitions is similar to that of bulk GaAs. However, in QWs the degeneracy between the Γ_8 valence band states at $\mathbf{k}_\parallel = 0$ is lifted by the different confinement energies for the HH and LH envelope functions. A maximum spin polarization of $S_{z,\max} \approx 1$ can therefore be experimentally achieved in QWs when the excitation energy is tuned between the fundamental (1E-1HH) and (1E-1LH) transitions [66, 69, 70].

Chapter 3

Optically induced electron spin dynamics in semiconductors

In the preceding chapter we have introduced the optical orientation technique which allows for the all-optical excitation of spin polarized carriers in semiconductors. We next discuss three phenomena which are the hallmarks of optically induced electron spin dynamics in semiconductors, i.e. Larmor precession and spin quantum beating, electron spin relaxation and dephasing, and electron spin diffusion. We describe how two particularly important parameters, the electron spin relaxation time τ_s and the electron spin diffusion coefficient D_s, are deduced from time and spatially resolved observations of these processes. We conclude by introducing the photoinduced magneto-optical Kerr effect, the experimental probe that allows for the optical detection of the spatiotemporal dynamics of electron spins in semiconductors.

3.1 Electron spin relaxation and dephasing

3.1.1 Larmor precession, electron spin decoherence, dephasing, and relaxation

To introduce the concept of spin decoherence, dephasing, and relaxation we consider a spin-1/2 particle in an external magnetic field $\mathbf{B} = B\hat{\mathbf{z}}$ pointing along the z-axis. The magnetic moment associated with the spin of a free electron is [57]:

$$\boldsymbol{\mu} = -\frac{g\mu_B}{\hbar}\mathbf{S} \tag{3.1}$$

where $\mu_B = (e\hbar/2m_0)$ is the Bohr magneton. For a free electron the Landé factor is $g \approx 2.002$. For electrons in a solid, the g-factor is modified by spin-orbit-interaction with the lattice ion potential [71]. The magnetic moment of a crystal Bloch state can be characterized by Eq. (3.1) in terms of an effective g-factor g^* which can significantly differ in magnitude and sign from the Landé g-factor. For conduction band electrons in bulk GaAs, the commonly accepted low-temperature value is $g^* = -0.44$ [72].

The Hamiltonian for the electron spin in the external magnetic field is [57]:

$$H_{\text{spin}} = -\boldsymbol{\mu} \cdot \mathbf{B} = \omega_L S_z \tag{3.2}$$

with the Larmor frequency $\omega_L = \gamma B$, which is proportional to the the gyromagnetic ratio $\gamma = g^* \mu_B / \hbar$. We denote the eigenstates of the Hamiltonian Eq. (3.2) as $|\uparrow\rangle$ and $|\downarrow\rangle$. The eigenenergies of these states are:

$$E_{\uparrow,\downarrow} = \pm\frac{1}{2}\hbar\omega_L = \pm\frac{1}{2}g^*\mu_B B \tag{3.3}$$

The energy difference $\Delta E_{\uparrow,\downarrow} = g^* \mu_B B$ is termed the Zeeman energy splitting.

We next consider the time evolution of an arbitrary spin state:

$$|\psi(0)\rangle = \cos\left(\frac{\theta}{2}\right) e^{-i\varphi/2}|\uparrow\rangle + \sin\left(\frac{\theta}{2}\right) e^{i\varphi/2}|\downarrow\rangle \tag{3.4}$$

which at $t = 0$ is a superposition of the spin-up and spin down states. The angle θ describes the relative amplitude of the two eigenstates of Eq. (3.2) while φ defines the initial phase relation between the $|\uparrow\rangle$ and $|\downarrow\rangle$ components.

In the absence of external influences from the environment, the time evolution of $|\psi(t)\rangle = U(t)|\psi(0)\rangle$ is governed by the time evolution operator [56]:

$$U(t) = \exp(-iH_{\text{spin}}t/\hbar) = \exp(-iS_z\omega_L t/\hbar) \tag{3.5}$$

This time evolution of a pure spin state under the influence of H_{spin} alone is termed spin coherence [5]. For the initial state Eq. (3.4), the time dependence of the expectation values for the spin components S_i along the three cartesian coordinate axis are [57]:

$$\langle\psi(t)|S_z|\psi(t)\rangle = \frac{\hbar}{2}\cos(\theta) \tag{3.6}$$

$$\langle\psi(t)|S_x|\psi(t)\rangle = \frac{\hbar}{2}\sin(\theta)\cos(\varphi + \omega_L t) \tag{3.7}$$

$$\langle\psi(t)|S_y|\psi(t)\rangle = \frac{\hbar}{2}\sin(\theta)\sin(\varphi + \omega_L t) \tag{3.8}$$

The expectation value $\langle S_z\rangle$ is time-independent. For $\langle S_x\rangle$ and $\langle S_y\rangle$, however, a sinusoidal time dependence results from a change in the relative phase of the Zeeman-split states $|\uparrow\rangle$ and $|\downarrow\rangle$, a phenomenon commonly referred to as spin quantum beats [73]. This is the quantum mechanical description of the Larmor precession of the electron's magnetic moment in an external magnetic field [74].

For an electron spin in a semiconductor, interaction with the environment will lead to a perturbation of the coherent time evolution described by Eqs. (3.6) - (3.8). The effect of the interaction with the environment is to destroy the spin coherence , i.e. to give rise to spin decoherence and relaxation. Spin relaxation and decoherence in general can be understood as a result of the action of random time-fluctuating magnetic fields on the electron spin state. These randomly fluctuating fields can be external fields or internal effective fields which arise from spin-orbit interaction.

The two important parameters which characterize these randomly fluctuating fields are the root-mean-square amplitude $\langle\Omega\rangle$ and correlation time τ_c during which the field may be considered constant [75]. Spin relaxation and decoherence results from precession in these random magnetic fields with an average precession frequency ($\langle\Omega\rangle/2\pi$). After a time τ_c, the direction and amplitude of the field change randomly and spin precession around the new direction of the field proceeds. After a number of such steps, the initial coherence of the spin state is completely lost.

For a more quantitative definition of spin decoherence and relaxation we introduce the two times T_1 and T_2 which describe the decay of the longitudinal and transverse spin components with respect to an external field $\mathbf{B}$. The spin lifetime or relaxation time T_1 characterizes the time scale over which a change in the relative occupation between $|\uparrow\rangle$ and $|\downarrow\rangle$ occurs. The spin coherence time T_2 defines the time over which the coherent phase relation between both states is lost [75]. While this loss of phase relation does not take additional energy, a change in the population of the Zeeman states requires energy dissipation, typically by a change of the kinetic energy of the electron or scattering with phonons.

The above discussion concerns the relaxation and decoherence of a single electron spin. In our magneto-optical spectroscopy experiments we observe the net spin polarization of a large ensemble of electrons. The time evolution of an ensemble spin polarization $\mathbf{S}$ which is uniform in space (i.e. for which diffusive processes are not relevant) in an external magnetic field $\mathbf{B} = B_0\hat{\mathbf{z}} + \mathbf{B}_1(t)$ is commonly described in terms of the phenomenological Bloch equations [76]:

$$\frac{\partial}{\partial t}S_x = \gamma(\boldsymbol{S}\times\boldsymbol{B})_x - S_x/T_2^* \tag{3.9}$$

$$\frac{\partial}{\partial t}S_y = \gamma(\boldsymbol{S}\times\boldsymbol{B})_y - S_y/T_2^* \tag{3.10}$$

$$\frac{\partial}{\partial t}S_z = \gamma(\boldsymbol{S}\times\boldsymbol{B})_z - \left(S_z - S_z^0\right)/T_1 \tag{3.11}$$

Here S_z^0 is the equilibrium electron spin polarization in the static field $\mathbf{B}_0$. The loss of the ensemble electron spin coherence is determined by the spin dephasing time [75]:

$$\frac{1}{T_2^*} = \frac{1}{T_2} + \frac{1}{T_2^{\text{inh}}} \tag{3.12}$$

The inhomogeneous spin relaxation time T_2^{inh} arises from spatial and temporal fluctuations in the precession frequencies of the individual spins of the ensemble, e.g. due to spatial variations of the local external magnetic field or slight differences in the g-factor for conduction band electrons in different $\mathbf{k}$-states [60]. Similar considerations apply to the relaxation of the longitudinal ensemble spin polarization component along the static external field direction $\mathbf{B}_0$, which is described by the relaxation time T_1.

In crystals with cubic symmetry, $T_1 = T_2$ for magnetic fields which satisfy $\gamma B \ll (1/\tau_c)$ [60]. For electron spins in semiconductors, the correlation time τ_c usually is either given by the momentum scattering time τ_p^*, or by the average time between the interaction of electrons with phonons or holes. Since the relevant time scales for these processes are typically smaller than a picosecond, $T_1 = T_2$ holds for fields up to several tesla, which are much higher than the external fields used in this work. For the following discussions we therefore assume the equality of the spin relaxation and dephasing times and denote them by the symbol τ_s and use both terms interchangeably.

3.1.2 Microscopic origin of electron spin relaxation

The investigation of the microscopic origin of electron spin relaxation in solid state environments has been a major focus of spintronics research for several decades. Extensive reviews on electron spin relaxation are given e.g. in Refs. [37, 60, 65, 71, 77–79]. We here restrict ourself to a brief introduction of the four most important microscopic mechanisms, Elliot-Yafet, Bir-Aronov-Pikus, Dyakonov-Perel, and hyperfine interaction, which are required for a qualitative understanding of the electron spin relaxation in the GaAs-based heterostructures investigated in this work. The physical ideas behind these spin relaxation mechanisms are illustrated conceptually in Fig. 6.

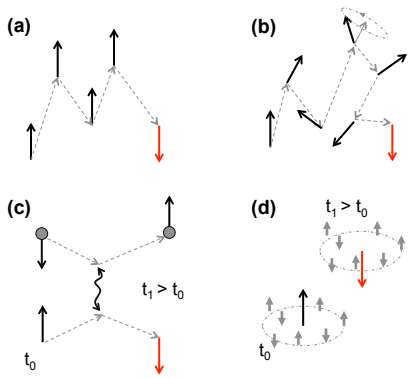

Figure 6: Microscopic origin of conduction band electron spin relaxation in semiconductors. **(a)** Elliot-Yafet mechanism: Conduction band states with $\mathbf{k} \neq 0$ are not spin eigenstates. An electron spin flip can take place when the electron scatters from phonons or impurities. **(b)** Dyakonov-Perel mechanism: Electron spins precess in $\mathbf{k}$-dependent Dresselhaus effective internal magnetic fields. The precession frequency and field orientation change randomly with each scattering event. **(c)** Bir-Aronov-Pikus mechanism: The electron-hole exchange interaction can lead to a spin flip-flop process between a conduction band electron and valence band hole. **(d)** Hyperfine interaction: The spins of donor-bound electrons precess in the randomly oriented fluctuating hyperfine field of nuclear spins of the lattice ions. Reprinted from [80], original adapted from [71].

Elliot-Yafet mechanism

The Elliot-Yafet (EY) mechanism is due to the fact that conduction band electron (and valence band hole) states are not spin eigenstates. Spin-orbit interaction induced by the periodic lattice ion potential leads to a coupling of spin-up and spin-down states from different energy bands which share the same wave vector $\mathbf{k}$. The respective Bloch states can be written as [60]:

$$\psi_{n,\mathbf{k}\uparrow}(\mathbf{r}) = e^{i\mathbf{k}\cdot\mathbf{r}}\left[a_{n,\mathbf{k}}(\mathbf{r})\,|\uparrow\rangle + b_{n,\mathbf{k}}(\mathbf{r})\,|\downarrow\rangle\right] \tag{3.13}$$

$$\psi_{n,\mathbf{k}\downarrow}(\mathbf{r}) = e^{i\mathbf{k}\cdot\mathbf{r}}\left[a^{*}_{n,-\mathbf{k}}(\mathbf{r})\,|\downarrow\rangle - b^{*}_{n,-\mathbf{k}}(\mathbf{r})\,|\uparrow\rangle\right] \tag{3.14}$$

As first noticed by Elliot, because of this admixture of opposite spin components in the Bloch states Eqs. (3.13) and (3.14), ordinary spin-independent scattering by impurities or phonons can couple spin-up and spin-down electrons and give rise to spin relaxation [79]. Moreover, as pointed out later by Yafet, the modulation of the lattice ion-induced spin-orbit interaction by phonons can directly couple $|\uparrow\rangle$ and $|\downarrow\rangle$ states and mediate spin-flip processes.

From perturbation theory, the spin-orbit coupling induced mixing of opposite spin components from remote Bloch bands is inversely proportional to the energy separation ΔE between the unperturbed states at given $\mathbf{k}$ [60]:

$$|b(\mathbf{k})| \approx \lambda_{\mathrm{SO}}(\mathbf{k})/\Delta E(\mathbf{k}) \tag{3.15}$$

Here λ_{SO} is the matrix element of the spin-orbit Hamiltonian H_{SO} [compare Eq.(2.3)] between two states from different Bloch bands with same wave vector $\mathbf{k}$. For the comparatively large band gap E_{gap} of GaAs the coupling of spin-down valence band states to spin-up conduction band states (and vice versa) is weak, i.e. $|b| \ll 1$ and $|a|$ is close to unity. Therefore, Elliot-Yafet relaxation is inefficient for conduction band electrons in GaAs. In contrast, $|\uparrow\rangle$ and $|\downarrow\rangle$ components are completely mixed for the GaAs hole states listed in Table 2.1. The initial orientation of the total angular momentum of the hole therefore is typically completely lost after a single scattering event. Hole spin relaxation in bulk GaAs therefore happens extremely fast on the time scale of the hole momentum scattering time, i.e. in the sub-ps domain [81]. In our magneto-optical spectroscopy experiments the hole spin system therefore is virtually unpolarized and the observed Kerr rotation is exclusively due to the electron spin polarization.

Bir-Aronov-Pikus mechanism

The Bir-Aronov-Pikus (BAP) mechanism is an electron spin dephasing mechanism which is possible in the presence of holes. The Hamiltonian for the direct exchange interaction between electrons and holes is [37]:

$$H_{\mathrm{BAP}} = A\,\mathbf{S}\cdot\mathbf{J}\,\delta(\mathbf{r}) \tag{3.16}$$

where A is proportional to the exchange integral between conduction and valence band states [60], $\mathbf{r}$ is the relative position, and $\mathbf{S}$ and $\mathbf{J}$ are the spin and total angular momentum operators for the electron and hole, respectively.

The direct exchange interaction Hamiltonian Eq. (3.16) between electrons and holes can induce a simultaneous flip of the electron and hole spin states during an electron-hole scattering event. While the total angular momentum is conserved in such spin flip-flop processes, the exchange interaction can mediate a transfer of a non-equilibrium electron spin polarization to the hole system [37]. The consecutive rapid loss of the hole spin orientation by the EY mechanism acting in combination with the BAP exchange scattering therefore can lead to a fast relaxation of the electron spin polarization.

The BAP mechanism is believed to be the dominant electron spin relaxation channel for strongly p-doped samples where in thermal equilibrium residual unpolarized holes are present. BAP scattering has been observed to lead to sub-nanosecond electron spin relaxation times in moderately doped p-GaAs [82]. Moreover, the creation of holes is an inevitable byproduct of the optical spin excitation in magneto-optical pump-probe spectroscopy experiments. Therefore, under the condition of optical orientation, the BAP mechanism can also contribute to electron spin relaxation in nominally undoped or n-doped samples if other relaxation mechanisms are suppressed [37]. This situation is found e.g. in (110) QWs (compare below), where BAP relaxation with optically created holes is significant for the dephasing of the out-of-plane electron spin component [83].

Hyperfine interaction

Hyperfine interaction (HFI), the interaction between the magnetic moments of the electron spin and lattice nuclei, can lead to an efficient dephasing of localized, e.g. donor-bound, electrons. In GaAs, all lattice nuclei carry the magnetic moment of $I = 3/2$ nuclear spins [60]. From a typical Bohr radius $a_B^* \approx 50\,\text{Å}$ of a hydrogenic donor wave function [47], the wave function of a localized electron in GaAs is spread over a large number $N \approx 10^5$ of lattice sites. Mean-squared fluctuations in the nuclear spin orientation lead to a hyperfine field which is comparable to the combined action of $\sqrt{N} \approx 300$ nuclear spins. On average, for donor-bound electrons in GaAs this hyperfine field is equivalent to an effective field of $\approx 5.4\,\text{mT}$ [84]. Larmor precession in the randomly oriented fluctuating magnetic fields of their respective environment leads to a fast dephasing of the spin polarization of an ensemble of localized electrons. Furthermore, for static optical orientation of bound electrons, HFI leads to a transfer of spin polarization from the electron ensemble to the lattice nuclei, the Overhauser effect [65].

The spin relaxation rate by HFI increases with the correlation time τ_c, the average time bound electrons spend at the localization sites. HFI is therefore important in low-doped samples at low lattice temperatures [67], where the wave function overlap between different donor-bound electrons is small and thermal excitations of bound electrons to the conduction band are suppressed. Here electrons on average are confined to an individual donor site for long times and HFI-induced spin relaxation is strong. For itinerant conduction band electrons, however, τ_c is very small and spin relaxation by HFI is suppressed by motional narrowing. In HFI relaxation dominated samples, providing a dilute background of mobile conduction band electrons e.g. by by slightly raising the sample temperature [30] or by weak above-bandgap illumination therefore can lead to a strong increase of the electron spin relaxation time by up to two orders of

magnitude [84].

Dyakonov-Perel mechanism

We last turn to the Dyakonov-Perel (DP) mechanism. From Kramers theorem, the combined action of time reversal and space inversion symmetry mandates a twofold spin degeneracy $E_{c,\uparrow}(\mathbf{k}) = E_{c,\downarrow}(\mathbf{k})$ of the electron Bloch states [53]. In GaAs, space inversion symmetry is broken by the presence of two distinct ions in the basis of the zincblende-type lattice and the Kramers degeneracy is lifted, i.e. $E_{c,\uparrow}(\mathbf{k}) \neq E_{c,\downarrow}(\mathbf{k})$. Moreover, in semiconductor heterostructures space inversion symmetry also can be broken e.g. by asymmetric QW confinement potentials along the growth axis.

For conduction band electrons, the $\mathbf{k}$-dependent lifting of the spin degeneracy of the Bloch states is described by an intrinsic effective internal magnetic field $\mathbf{B}(\mathbf{k})$. In non-centrosymmetric crystal structures this effective spin-orbit coupling field arises from the electric fields in the crystal unit cell. In the reference frame of the moving electrons these fields appear as magnetic fields, thereby coupling the electron spin with the wave vector $\mathbf{k}$ [85]. The contribution to the Hamiltonian for the one-electron Schrödinger equation Eq. (2.1) from the internal effective field is [37, 78]:

$$H_{\mathrm{SOI}} = \frac{\hbar}{2}\boldsymbol{\sigma} \cdot \boldsymbol{\Omega}(\mathbf{k}) \tag{3.17}$$

The requirement to reflect the breaking of spatial inversion symmetry mandates that $\boldsymbol{\Omega}_i(\mathbf{k})$ is odd in $\mathbf{k}$. For the bulk inversion asymmetry (BIA) of the zincblende-type lattice, an analytical expression for the precession frequency vector $\boldsymbol{\Omega}(\mathbf{k})$ to the lowest order in $\mathbf{k}$ has been derived by Dresselhaus as [86]:

$$\boldsymbol{\Omega}_{\mathrm{BIA}}(\mathbf{k}) = 2\gamma_D/\hbar \left[k_x \left(k_y^2 - k_z^2\right), k_y \left(k_z^2 - k_x^2\right), k_z \left(k_x^2 - k_y^2\right)\right] \tag{3.18}$$

where γ_D is the Dresselhaus spin splitting parameter [65].

For heterostructures, the symmetry of the Dresselhaus field strongly depends on the growth direction $\hat{z}$ of the QW. Neglecting terms which are cubic in the in-plane momentum component $\mathbf{k}_{\|}$, the Dresselhaus field in a GaAs QW grown on a (001) surface has the form [37]:

$$\boldsymbol{\Omega}_{[001]}(\mathbf{k}) = \frac{\beta}{\hbar}\left[-k_x, k_y, 0\right] \tag{3.19}$$

where $\beta = \gamma_D \langle k_z^2 \rangle$ with the expectation value $\langle k_z^2 \rangle$ of the envelope wave function. For QWs grown along the crystallographic [110] direction, the k-linear approximation for the Dresselhaus field is [37]:

$$\boldsymbol{\Omega}_{[110]}(\mathbf{k}) = \frac{2\beta}{\hbar}\left[0, 0, k_x\right] \tag{3.20}$$

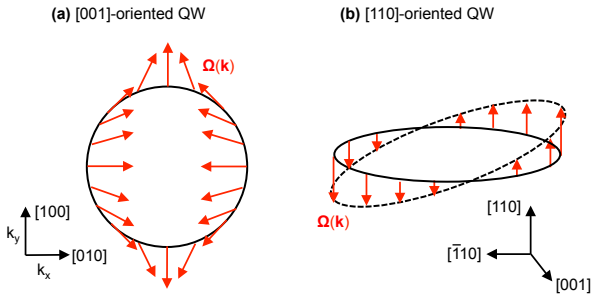

Figure 7: Dresselhaus spin-orbit fields in QWs. Red arrows represent the amplitude and direction of $\mathbf{\Omega}(\mathbf{k})$ for electrons with a given wave vector amplitude k (black circle) in QWs grown on **(a)** [001]- and **(b)** [110]-oriented substrates. Adapted from [37] and [60].

where we have introduced new coordinates $\hat{x} \parallel [1\bar{1}0]$, $\hat{y} \parallel [00\bar{1}]$, and $\hat{z} \parallel [110]$. Schematic diagrams of the Dresselhaus fields $\mathbf{\Omega}_{[001]}$ and $\mathbf{\Omega}_{[110]}$ are shown in Fig. 7.

From comparison with the Zeeman Hamiltonian Eq. (3.2), the effective internal field causes Larmor precession of the electron spin around the axis $\mathbf{\Omega}(\mathbf{k})$. For an ensemble of spin polarized conduction band electrons, the precession frequency and direction differs for each individual electron. Moreover, from the point of view of a single electron spin, the precession frequency and axis change after each scattering event which takes the electron to a new $\mathbf{k}$-state. As noticed by Dyakonov and Perel, this precession in the momentum-dependent Dresselhaus field can lead to the rapid dephasing of the electron spin ensemble.

The correlation time τ_c for the precession in the random fluctuating internal magnetic field is the average momentum scattering time τ_p^* between changes in the $\mathbf{k}$-state of the electron. In general $\tau_p^* < \tau_p$, since the transport scattering time τ_p is only very weakly influenced by electron-electron scattering via umklapp processes, while ordinary Coulomb scattering still randomizes both electrons' $\mathbf{k}$ vectors [87]. Depending on the average Dresselhaus precession frequency $\langle\Omega\rangle$ and τ_p^*, two limiting cases can be observed for the DP relaxation mechanism.

For $\langle\Omega\rangle\tau_p^* \gtrsim 1$, the weak scattering or quasi-collision-free regime, electron spins on average precess more than a full cycle about the Dresselhaus field before a scattering event changes the electrons' $\mathbf{k}$ vector. Here the initial coherent spin dynamics following pulsed excitation can become oscillatory rather than exponentially decaying as observed in ultrahigh-mobility 2DEGs in modulation-doped GaAs QWs [87, 88]. The initial electron spin polarization is completely lost after a single scattering event takes place, i.e. [37, 60]:

$$\tau_s \approx \tau_p^* \tag{3.21}$$

For $\langle\Omega\rangle\tau_p^* \ll 1$, the collision-dominated or strong scattering regime usually associated with the DP mechanism, electron spins on average only precess by a small angle $\delta\phi = \langle\Omega\rangle\tau_p^*$ before scattering randomizes the precession frequency and axis. From

random-walk theory, the spin relaxation time, defined as the time where, on average, the electron spin precession angle reaches unity, is [60]:

$$\frac{1}{\tau_s} \approx \langle \Omega^2 \rangle \tau_p^* \tag{3.22}$$

It is interesting to note that in the collision dominated regime frequent scattering indeed increases the spin relaxation time.

For bulk zincblende-type semiconductors, from Eq. (3.18) the average precession frequency $\langle \Omega_{\mathrm{BIA}} \rangle \sim k^3$. Since the average electron wave vector $\langle k \rangle$ increases with the electron concentration n, the DP relaxation mechanism becomes very efficient for highly n-doped degenerate samples. In bulk GaAs, the DP mechanism therefore is usually the dominant spin relaxation mechanism for $n \geq 2 \times 10^{16}\,\mathrm{cm}^{-3}$. For $n \approx 1 \times 10^{16}\,\mathrm{cm}^{-3}$, however, DP relaxation at low temperatures is still rather weak while dephasing by HFI is strongly suppressed by motional narrowing. It is this donor concentration regime for which exceptionally long spin relaxation times in excess of 100 ns are observed in bulk GaAs [67].

An interesting situation arises when electron spins are optically oriented along the growth axis of (110) QWs. Here for all $\mathbf{k}$ the electron spin is parallel to the Dresselhaus spin-orbit field [compare Fig. 7 (b) and Eq. (3.20)], i.e. precession of S_z around $\mathbf{\Omega}_{[110]}$ is not possible. From theory, the vanishing of the in-plane components of $\mathbf{\Omega}_{[110]}$ is not restricted to the k-linear approximation but is strictly valid to all orders of the electron wave vector [89]. Therefore, DP relaxation is effectively suppressed for the out-of-plane component of the electron spin, and spin relaxation is expected to become strongly anisotropic. Indeed, up to a tenfold increase of the spin relaxation time for out-of-plane oriented spins as compared to in-plane electron spin components has been observed experimentally in (110) GaAs QWs [35, 38, 45].

3.2 Spin dynamics in transverse magnetic fields

We next introduce three different manifestations of optically induced electron spin dynamics in transverse magnetic fields. We limit the discussion to the case of isotropic spin relaxation rates and effective g-factors. Details on optically induced electron spin dynamics in anisotropic systems are given e.g. in Refs. [45, 90, 91].

Depending on the excitation mode (pulsed or cw) and the ratio of the spin relaxation time τ_s and the period t_{rep} between consecutive pulses of the pump pulse train, one observes spin quantum beats, resonant spin amplification, and the depolarization of a steady-state electron spin polarization with increasing transverse fields, the Hanle effect. The major characteristics of these phenomena are schematically illustrated in Fig. 8.

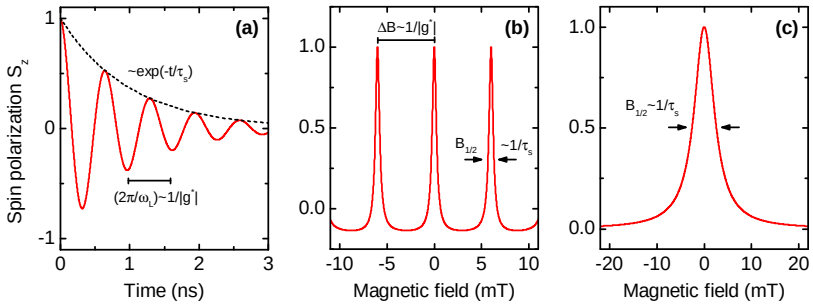

Figure 8: Schematics of different manifestations of optically induced electron spin dynamics in transverse magnetic fields. **(a)** Spin quantum beats following pulsed excitation. The spin polarization S_z exhibits an exponentially decaying sinusoidal time dependence due to the combined action of spin relaxation and Larmor precession in the external field. **(b)** Resonant spin amplification. The spin polarization S_z at a fixed delay shortly before the arrival of the following pump pulse periodically changes with the applied magnetic field. Maxima in S_z are observed when the Larmor precession period is commensurable with the pulse-to-pulse interval of the excitation laser. **(c)** Hanle effect for cw excitation. Depolarization of the steady-state electron spin density is observed when the in-plane magnetic field amplitude is increased.

3.2.1 Spin quantum beats

We first consider pulsed excitation of spin polarized electrons with **S** initially oriented along the sample normal $\hat{z}$. For the case $\tau_s \ll t_{\mathrm{rep}}$ the spin relaxation time is substantially shorter than the pulse-to-pulse interval and S_z completely vanishes before the arrival of the following pump pulse. The momentary spin polarization therefore is entirely due to only the last of the previous pump pulses. Application of a transverse in-plane magnetic field B_{xy} leads to Larmor precession of the ensemble spin polarization (compare section 3.1.1). From the Bloch Eqs. (3.9) - (3.11), the time dependence of the $\hat{z}$-component of the ensemble spin polarization is:

$$S_z(t) = S_z^0 \cos(\omega_L t) \exp(-t/\tau_s) \tag{3.23}$$

Here S_z^0 is the spin polarization at the moment of excitation. From a measurement of the Larmor precession period $(2\pi/\omega_L) = h/(|g^*|\mu_B B_{xy})$ the absolute value of the effective electron g-factor g^* is readily obtained. Moreover, the spin relaxation time τ_s can be extracted from the exponentially decaying amplitude envelope of the sinusoidally oscillating spin quantum beats $S_z(t)$.

3.2.2 Resonant spin amplification

Typical repetition rates of pulsed laser sources used for time-resolved magneto-optical spectroscopy are in the range of 10 MHz to 100 MHz which corresponds to pulse-to-pulse intervals t_{rep} of 10 ns to 100 ns. An interesting situation arises when $\tau_s \gtrsim t_{\mathrm{rep}}$, a condition commonly encountered e.g. for the long-lived spin polarizations in n-doped bulk GaAs [67] and cadmium telluride (CdTe) QWs [92]. In this case S_z excited

by previous pump pulses is not fully relaxed and temporally overlaps with the spin polarization generated by the following pulses.

When the electron spins precess in weak external magnetic fields, S_z contributions originating from different pump pulses can interfere either destructively or constructively. If the precession period $(2\pi/\omega_L)$ is commensurable with the pulse-to-pulse interval t_{rep}, the momentary polarization of the resident carriers is aligned parallel to the newly photocreated electron spins. As a result the observed spin polarization is greatly enhanced, a condition termed resonant spin amplification (RSA) [13].

In the RSA regime, the electron spin polarization is [91]:

$$S_z\left[\Delta t, \omega_L(B_{xy})\right] = \frac{S_z^0}{2} e^{-(t_{\mathrm{rep}}+\Delta t)/\tau_s} \frac{e^{t_{\mathrm{rep}}/\tau_s}\cos\left[\omega_L(t_{\mathrm{rep}}+\Delta t)\right] - \cos\left(\omega_L \Delta t\right)}{\cosh\left(t_{\mathrm{rep}}/\tau_s\right) - \cos\left(\omega_L t_{\mathrm{rep}}\right)} \tag{3.24}$$

Here $\Delta t \in [-t_{\mathrm{rep}}, 0)$ is the delay before the arrival of the next pump pulse. When measuring $S_z(B_{xy})$ shortly before the arrival of the following pump pulse, a series of sharp peaks is observed when B_{xy} is swept. The peaks in S_z correspond to magnetic fields for which electron spins precess integer multiples of 2π rad during the pulse-to-pulse interval t_{rep}. The RSA peak width is inversely correlated with the spin relaxation time [45]. From a fit of Eq. (3.24) to a RSA peak, τ_s can be extracted [91]. From the peak-to-peak separation ΔB_{xy} the absolute value of the g-factor is obtained as:

$$|g^*| = \frac{h}{t_{\mathrm{rep}} \mu_B \Delta B_{xy}} \tag{3.25}$$

Moreover, destructive interference allows to suppress the electron spin polarization in such a way that $S_z = 0$ at the arrival of each pump pulse. The electron spin dynamics observed after the pump pulse then is only due to a single excitation. Destructive RSA therefore can be used to avoid repetition-rate artifacts and can significantly simplify the quantitative analysis of time-resolved electron spin diffusion processes.

3.2.3 Hanle effect

For cw optical excitation, spin injection, relaxation, and precession take place simultaneously. An increase of the transverse magnetic field amplitude B_{xy} leads to a decrease of the steady-state ensemble polarization S_z. This is the Hanle effect well known from atomic physics. The dependence of the out-of-plane spin polarization on the transverse field is [65]:

$$S_z(B_{xy}) = \frac{S_z(0)}{1 + (B_{xy}/B_{1/2})^2} \tag{3.26}$$

where $S_z(0)$ is the steady-state spin polarization in the absence of external fields. Here $B_{1/2} = \hbar/(g^* \mu_b T_s)$ is the transverse magnetic field for which the observed spin polarization is reduced with respect to $S_z(0)$ by a factor of two. If g^* of the system is known, the electron spin lifetime T_s is readily obtained from a measurement of the Hanle effect using optical spin orientation and MOKE or polarization resolved PL spectroscopy.

In n-type semiconductors, BAP scattering and recombination with photocreated holes are additional extrinsic electron spin decay channels which lead to a reduction of the observed spin lifetime T_s with respect to the intrinsic spin relaxation time τ_s of the undisturbed system [93]. This reduction of T_s is most significant in material systems which exhibit exceptionally long spin relaxation times, for which the recombination rate with photocreated holes becomes comparable to the spin relaxation rate. Here the spin lifetime depends on the optical pump density g_z as [91]:

$$T_s^{-1} = \tau_s^{-1}\,(1 + g_z/g_0) \tag{3.27}$$

By measuring a series of Hanle curves Eq. (3.26) and extrapolating $B_{1/2}(g_z)$ to zero pump power, the intrinsic spin relaxation time τ_s can be determined from Eq. (3.27).

3.3 Electron spin diffusion

In the previous section 3.2 we have described how the spin relaxation time can readily be obtained from different magneto-optical spectroscopy experiments which involve spin precession in external magnetic fields. In contrast, the determination of electron spin transport properties by optical spectroscopy is more challenging. The two most widely used techniques for the optical investigation of electron spin transport are transient spin grating (TSG) spectroscopy [94–98] and MOKE or Faraday rotation microscopy [15, 32,68,99]. Both approaches involve the optical excitation of a spatially varying electron spin polarization. TSG spectroscopy is only capable of observing the amplitude decay of an transient electron spin grating which results from to the combined action of spin relaxation and diffusion. Magneto-optical Kerr effect microscopy, however, allows for time-resolved real space imaging of the diffusive spreading of electron spin packets. Moreover, cw MOKE microscopy can be used to measure steady-state electron spin polarization profiles.

For both techniques drift-diffusion models are commonly employed to analyze the spatiotemporal dynamics of the electron spin polarization. From a comparison between the experimental observations and the diffusion models, important parameters such as the electron spin diffusion coefficient D_s and the related electron spin mobility μ_s are obtained. The spin mobility μ_s describes the drift velocity of an electron spin packet in response to an applied electric field, and D_s determines the speed of the diffusive spreading of the packet [95]. Taken together with the relaxation time τ_s, these quantities determine the time and length scale available for the manipulation and transport of a non-equilibrium electron spin distribution. For that reason, the spin relaxation time and diffusion coefficient are key figures of merit which characterize a semiconductor's prospects for spin-based electronic applications [60,71,100]. The reliable measurement of D_s is therefore an integral task for pump-probe MOKE microscopy experiments.

In the following section we introduce the electron spin diffusion model which we subsequently use for the quantitative analysis of our MOKE microscopy measurements. We first present the general form of the diffusion equation. We then introduce simplifications to the diffusion equation which are appropriate for our experimental geometry

and the samples examined in the present work. For cw and pulsed excitation we present analytical solutions for the respective steady-state and time-dependent electron spin polarization profiles. We discuss for both cases how D_s can be extracted from MOKE microscopy measurements.

3.3.1 Spin diffusion equation

Optically excited electron spin diffusion in semiconductors is commonly described in terms of a diffusion equation. The partial differential vector equation for the three cartesian components S_i of the electron spin polarization $\mathbf{S} = (S_x, S_y, S_z)$ in the presence of a static homogeneous external magnetic field is [15, 32, 71, 101]:

$$\frac{\partial}{\partial t}\mathbf{S}(\mathbf{r},t) = \nabla_r \left[D_s(\mathbf{r},t)\nabla_r \mathbf{S}(\mathbf{r},t)\right] - \tau_s^{-1}\mathbf{S}(\mathbf{r},t) + g^*\mu_B\hbar^{-1}\left[\mathbf{B}\times\mathbf{S}(\mathbf{r},t)\right] + \mathbf{g}(\mathbf{r},t) \quad (3.28)$$

The first term on the right hand side of Eq. (3.28) describes the diffusion of the electron spin polarization. The electron spin diffusion current density [102]:

$$\mathbf{j}_{s,i}(\mathbf{r},t) = -D_s(\mathbf{r},t)\left[\nabla_r S_i(\mathbf{r},t)\right] \quad (3.29)$$

is related to the spatial gradient of the respective spin polarization component S_i by the electron spin diffusion coefficient (or diffusivity) D_s. Equation (3.29) is Fick's first law for electron spin diffusion. The second term in Eq. (3.28) is due to electron spin relaxation and the third term describes electron spin precession in the static external magnetic field. The excitation of electron spin polarization by optical spin injection is accounted for by the source term $\mathbf{g}(\mathbf{r},t)$.

For arbitrary sample geometries and spatially varying diffusion coefficients no analytical solutions for Eq. (3.28) are available. However, a number of simplifications are possible for the MOKE microscopy measurements presented in this work. Local optical spin injection is performed by a focused pump laser with a Gaussian spatial intensity profile (compare section 5.1.3). The pump laser is focused at normal incidence on the sample surface and only excites electron spins S_z oriented along the sample normal $\hat{z}$. If applied, the external magnetic field B_{xy} lies in the sample plane.

Spin diffusion in the examined samples takes place either in 2DEGs which are confined to the QW plane or in thin bulk samples with layer thicknesses $d \ll L_s$ which are substantially smaller than the spin diffusion length $L_s \equiv \sqrt{D_s\tau_s}$. In both cases spin diffusion can be treated as a two-dimensional problem [15, 32]. Moreover, in all examined samples D_s is isotropic with respect to the in-plane crystal axes. Therefore the spin polarization profile $S_z(r)$ is radially symmetric and does only depend on the radial distance r to the excitation spot center. In polar coordinates, the diffusion equation Eq. (3.28) therefore simplifies to [99, 103]:

$$\frac{\partial}{\partial t}\tilde{S}(r,t) = \frac{1}{r}\frac{\partial}{\partial r}\left(D_s r\frac{\partial \tilde{S}}{\partial r}\right) - \tau_s^{-1}\tilde{S} + i\omega_L\tilde{S} + g_z(r,t) \quad (3.30)$$

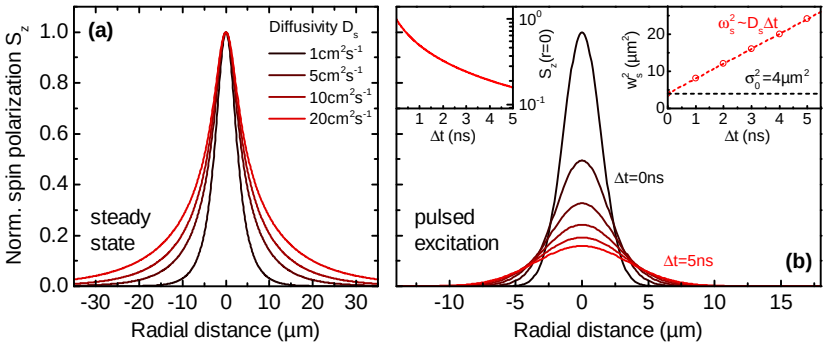

Figure 9: Electron spin diffusion model. **(a)** Steady state electron spin polarization profiles $S_z(r)$ for different diffusion coefficients D_s. The excitation spot $(1/e)$ half width is $\sigma_0 = 2\,\mu\text{m}$ and $\tau_s = 100\,\text{ns}$. **(b)** Spin polarization profile $S_z(r)$ for increasing delays Δt after pulsed excitation calculated from Eq. (3.30) for $D_s = 10\,\text{cm}^2\,\text{s}^{-1}$ and $\tau_s = 100\,\text{ns}$. Left inset: Spin polarization transient $S_z(\Delta t, r = 0)$ at the center of excitation (log. scale). Note the non-exponential decay. Right inset: Squared $(1/e)$ half width $w_s^2(\Delta t)$ of the spin polarization profile. The dashed line indicates the width σ_0^2 of the excitation source.

In Eq. (3.30) we have introduced the complex spin polarization $\tilde{S} \equiv S_z + iS_{xy}$ to describe the out-of-plane and in-plane spin components S_z and S_{xy} by a single scalar field [101].

In the following we present analytical solutions to Eq. (3.30) for the steady-state spin polarization profile resulting from cw excitation and for the time-resolved diffusion of an electron spin packet created by pulsed optical excitation. Some important properties of these solutions are illustrated in Fig. 9.

Continuous-wave excitation and steady-state solution

We first consider the case of a spatially uniform diffusion coefficient D_s. For cw excitation by a point source $g_z(r) = g_0\delta(r)$, the steady-state Green's function solutions s_z and s_{xy} of Eq. (3.30) for the electron spin polarization components are [32]:

$$s_z(r) = \text{Re}\left[K_0\left(r\sqrt{\frac{1}{D_s\tau_s} + i\frac{\omega_L}{D_s}}\right)\right] \tag{3.31}$$

$$s_{xy}(r) = \text{Im}\left[K_0\left(r\sqrt{\frac{1}{D_s\tau_s} + i\frac{\omega_L}{D_s}}\right)\right] \tag{3.32}$$

where K_0 is the zeroth-order modified Bessel function. The electron spin polarization profile which results from optical excitation by a Gaussian pump laser profile:

$$g_z(r) = g_{z,0}\exp\left(-r^2/\sigma_0^2\right) \tag{3.33}$$

with an $(1/e)$ spot size half width σ_0 is obtained by convolution of Eqs. (3.31) and (3.32) with the source term Eq. (3.33). The resulting profiles $S_z(r)$ in the absence of

external magnetic fields B_{xy} are illustrated in Fig. 9 (a) for a range of numerical values of D_s which are characteristic for low-temperature spin diffusion in bulk n-GaAs.

For spatially varying diffusion coefficients, analytical solutions for the spin diffusion equation are not available. However, Eq. (3.30) can be solved numerically for arbitrary $D_s(r)$, e.g. by the finite element method (FEM). If τ_s is independently determined from Hanle-MOKE measurements, the electron spin diffusion coefficient D_s can be obtained by fitting the solution of Eq. (3.30) to experimentally observed electron spin polarization profiles $S_z(r)$.

Pulsed excitation and time-dependent solution

We next consider the time-dependent solution of the diffusion equation Eq. (3.30) for a spatially uniform diffusion coefficient and zero magnetic field. For a focussed pump laser with a Gaussian spatial intensity profile the time evolution of the spin polarization after a short excitation pulse is [99, 103, 104]:

$$S_z(\Delta t, r) = \frac{\sigma_0^2 S_{z,0}}{\sigma_0^2 + 4D_s\Delta t} \exp\left(\frac{-r^2}{w_s^2}\right) \exp\left(\frac{-\Delta t}{\tau_s}\right) \tag{3.34}$$

with a time-dependent squared $(1/e)$ half width:

$$w_s^2(\Delta t) = \sigma_0^2 + 4D_s\Delta t \tag{3.35}$$

and an initial Gaussian $(1/e)$ half width σ_0. For $B_{xy} > 0$, Larmor precession leads to a periodic modulation of $S_z(\Delta t, r)$ described by an additional factor $\cos(\omega_L \Delta t)$. Exemplary spin diffusion profiles calculated from Eq. (3.34) for increasing Δt are shown in Fig. 9 (b). From Eq. (3.34) it is seen that diffusion leads to a non-exponential decay of the spin polarization $S_z(\Delta t, r = 0)$ at the pump spot center. This is shown in the left inset of Fig. 9 (b).

For cw excitation the shape of the stationary spin polarization profile results from the combined action of spin relaxation and diffusion [31, 32]. Steady-state MOKE microscopy therefore relies on complementary measurements of the spin relaxation time for the determination of spin diffusion coefficients. In contrast, for short pulsed excitation, spin propagation and relaxation are completely decoupled. The spatial shape of the spin polarization profile is completely determined by the action of diffusion, while spin relaxation only modifies the overall amplitude of the spin packet [105]. Unlike cw spectroscopy, the observation of $S_z(\Delta t, r)$ by time-resolved MOKE microscopy therefore allows for a direct measurement of the spin diffusion coefficient while eluding the additional characterization of the spin lifetime.

For a constant spin diffusivity which does not change with Δt, we expect from Eq. (3.35) a linear dependence of w_s^2 on the pump-probe delay with a slope of $4D_s$. This is illustrated in the right inset of Fig. 9 (b). A measurement of the Gaussian width $w_s(\Delta t)$ of the spin packet therefore directly yields the spin diffusivity

$$D_s = \frac{1}{4}\frac{\partial}{\partial \Delta t}\left[w_s^2(\Delta t)\right] \tag{3.36}$$

For a Gaussian spin packet, Eq. (3.36) is also valid for a time-dependent spin diffusion coefficient where $D_s(\Delta t)$ is determined from the momentary slope of the tangent to the $w_s^2(\Delta t)$ curve [103].

3.4 Photoinduced magneto-optical Kerr effect

We conclude this chapter by introducing the photoinduced magneto-optical Kerr effect, the very phenomenon which we employ to optically detect the electron spin polarization in semiconductors. The MOKE is the change of the polarization state of light which is reflected from the surface of a magnetized solid. It is closely related to other magneto-optical effects including circular dichroism and the Faraday effect. In the context of electron spin spectroscopy, we specifically refer to the photoinduced MOKE [106, 107] to denote that the sample magnetization is optically induced by aligning the magnetic moments of the electron spins by optical spin injection.

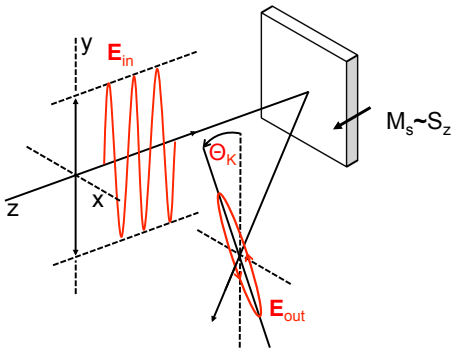

Figure 10: Schematic of the polar MOKE. The major axis of polarization of linearly polarized light is rotated by the Kerr angle θ_K, when the light is reflected at normal incidence from a sample with an out-of-plane magnetization $M_s \sim S_z$. The polarization state is changed from linear to elliptical polarization. The ratio of the minor to the major axis of polarization is the tangent of the Kerr ellipticity ϕ_K. Note that the nonzero angle of incidence shown here is for the purpose of graphical representation only. Adapted from [80].

Depending on the relative orientation of the sample surface, the magnetization vector, and the plane which contains the wave vector of the incident and reflected light, one distinguishes the longitudinal, equatorial, and polar Kerr effect [108]. The polar geometry, which is used exclusively in this work, is illustrated schematically in Fig. 10. Here the light is reflected at normal incidence from the sample surface. Symmetry dictates that the change of the polarization state is only sensitive to the magnetization component which is parallel to the wave vector of the incident light, i.e. the magnetization which is pointing along the sample normal $\hat{z}$.

The Kerr rotation θ_K is the angle included between the initial linear polarization axis of the incident light and the major axis of polarization of the reflected light beam. The

tangent of the Kerr ellipticity is defined as the ratio of the minor and major axes of the polarization ellipse of the reflected light (compare also Fig. 17).

In the following we provide a macroscopic description of the photoinduced MOKE. We describe how a measurement of the Kerr rotation θ_K of a linearly polarized probe laser can be used to obtain information on the electron spin polarization. A microscopic model which relates the observed Kerr rotation to electron spin-induced changes in the excitonic optical properties of semiconductors is presented later in section 7.1.3, where we quantitatively analyze experimentally observed Kerr rotation spectra, i.e. the dependence of the Kerr rotation on the probe laser wavelength.

3.4.1 Macroscopic description of the polar MOKE

The origin of all magneto-optical effects can be traced to differences in the interaction of photons of positive and negative optical helicity with magnetic solids. The Kerr rotation θ_K of a linearly polarized probe laser results from a difference in the complex dielectric functions $\tilde{\varepsilon}^{\pm}(\hbar\omega)$ for $\sigma^{\pm}$ left and right circularly polarized light with photon energy $E_{\text{probe}} = \hbar\omega$. For the following description of the polar MOKE we therefore decompose the linearly polarized probe laser beam in two left and right circularly polarized modes of equal amplitude E_{in} [109]. For propagation along the z-axis, the electric field vectors of these modes are:

$$\mathbf{E}_{\pm}(z,t) = \text{Re}\left[E_{\text{in}} e^{i(\omega t - 2\pi\tilde{n}^{\pm} z/\lambda_0)}(\hat{\mathbf{x}} \pm i\hat{\mathbf{y}})\right] \tag{3.37}$$

with the vacuum wavelength $\lambda_0 = (hc/E_{\text{probe}})$ and the complex refractive index:

$$\tilde{n}^{\pm} = n_{\pm} - i\,\kappa_{\pm} \tag{3.38}$$

where $n_{\pm}$ and $\kappa_{\pm}$ are the real index of refraction and the absorption.

The Kerr rotation stems from the influence of the sample magnetization on the dielectric tensor $\tilde{\epsilon}$. In the case of the photoinduced MOKE, the magnetization $M_s \sim S_z$ is due to the magnetic moments of the electron spins which are aligned by optical orientation. For cubic crystals and the electron spin polarization S_z pointing along the z-axis, the dielectric tensor is of the form:

$$\tilde{\epsilon}(S_z) = \begin{pmatrix} \tilde{\varepsilon}_{xx} & \tilde{\varepsilon}_{xy} & 0 \\ -\tilde{\varepsilon}_{xy} & \tilde{\varepsilon}_{xx} & 0 \\ 0 & 0 & \tilde{\varepsilon}_{zz} \end{pmatrix} \tag{3.39}$$

From symmetry, the off-diagonal tensor elements:

$$\tilde{\varepsilon}_{xy}(S_z) = -\tilde{\varepsilon}_{xy}(-S_z) \tag{3.40}$$

are odd functions of the electron spin polarization. The complex index of refraction for the $\sigma^{\pm}$ polarization modes Eq. (3.37) is related to the components of the dielectric tensor Eq. (3.39) as [108]:

$$\tilde{n}_{\pm}^2 = \tilde{\varepsilon}^{\pm} = \tilde{\varepsilon}_{xx} \pm i\tilde{\varepsilon}_{xy} \tag{3.41}$$

The Kerr rotation results from the difference in the phase jumps $\Delta^{\pm}$ of the complex amplitude reflection coefficients [110]:

$$r_{\pm} = |r_{\pm}|e^{i\Delta_{\pm}} = \frac{n_{\pm} - i\,\kappa_{\pm} - 1}{n_{\pm} - i\,\kappa_{\pm} + 1} \tag{3.42}$$

The explicit expression for the phase jumps under normal incidence for the circular polarization modes is [109]:

$$\Delta^{\pm} = \arctan\left(-\frac{2\kappa^{\pm}}{n^{\pm 2} + \kappa^{\pm 2} - 1}\right) \tag{3.43}$$

From Eq (3.43) we can directly relate, without any approximations [109], the Kerr rotation:

$$\theta_K = -\frac{1}{2}\left(\Delta^{+} - \Delta^{-}\right) \tag{3.44}$$

to the respective dielectric functions via the well-known relation $\tilde{n}^{\pm} = (\tilde{\varepsilon}^{\pm})^{1/2}$ for the complex index of refraction. From Eq. (3.44) it is seen that the polar Kerr rotation θ_K indeed is a direct measure of the difference in phase angle delays of the circularly polarized plane wave components of the reflected light [111].

The symmetry of Eq. (3.40) for the dielectric tensor dictates that the Kerr rotation in polar geometry is an odd function of the spin polarization, i.e. $\theta_K(S_z) = -\theta_K(-S_z)$ [109]. Expanding θ_K in powers of S_z and dropping higher order contributions $\mathcal{O}(S_z^3)$, a linear dependence of the Kerr rotation on the electron spin polarization:

$$\theta_K = \alpha S_z \tag{3.45}$$

is generally assumed. The constant of proportionality α is termed the magneto-optical coefficient.

From Eq. (3.45), a systematic variation of the temporal delay Δt between short pump and probe laser pulses or the relative distance r between focused pump and probe laser beams and measurement of $\theta_K(\Delta t, r)$ is expected to reflect the time evolution and spatial dependence of the optically induced electron spin polarization $S_z(\Delta t, r)$. This is the fundamental working principle of pump-probe MOKE microscopy of the electron spin dynamics in semiconductors.

Chapter 4

Photocarrier heating and electron energy relaxation

Although the main focus of this thesis is on the electron spin dynamics, we will provide in the following a rather detailed discussion of hot electron excitation and photocarrier energy relaxation for two reasons. First, the very fact that optical excitation can lead to a heating of the electron system has been known for 45 years [23]. The investigation of carrier energy relaxation has been an important field of optical spectroscopy for decades, on which a significant amount of literature and previous work exists. Parts of the magneto-optical spectroscopy and spintronics community, however, seemingly have been unaware of these results or have ignored hot carrier effects in the interpretation of their experimental results. Second, an understanding of the temperature dependence of the electron-phonon relaxation rates, which are responsible for the cooling of the carrier system, is important for the understanding of the experimental results presented later in this work.

In this chapter we will introduce the most important aspects of photoinduced electron heating by above-bandgap optical excitation and the photocarrier energy relaxation by phonon emission. We also describe electron-acceptor photoluminescence thermometry, the experimental probe which allows for the spatially resolved measurement of the local electron temperature in semiconductors and which we use in a later part of this thesis.

4.1 Nonresonant optical excitation

We first consider the fundamental aspect of photocarrier heating, the nonresonant optical excitation of electron-hole pairs. We limit the discussion to the case of moderate excitation energies $E_{\mathrm{gap}} < \hbar\omega_{\mathrm{exc}} < E_{\mathrm{gap}} + \Delta_{\mathrm{SO}}$ which is relevant to magneto-optical pump-probe spectroscopy. For excitation with such comparatively low excess energies $\Delta E_{\mathrm{exc}} = \hbar\omega_{\mathrm{exc}} - E_{\mathrm{gap}}$, in GaAs the possible interband transitions are restricted to take place in the close vicinity of the Brillouin zone center. Here the CB, HH, and LH dispersions $E(\mathbf{k})$ are well described by Eqs. (2.4), (2.6), and (2.7).

Nonresonant optical excitation creates electron-hole pairs whose total kinetic energy equals the difference between the photon energy and the semiconductor band gap. From Eq. (2.25), the wave vector conservation $\mathbf{k}_c = \mathbf{k}_v$ mandates that optical transitions are "vertical" or direct in $\mathbf{k}$-space. The fraction E_c^{ini} of the total excess energy ΔE_{exc} which

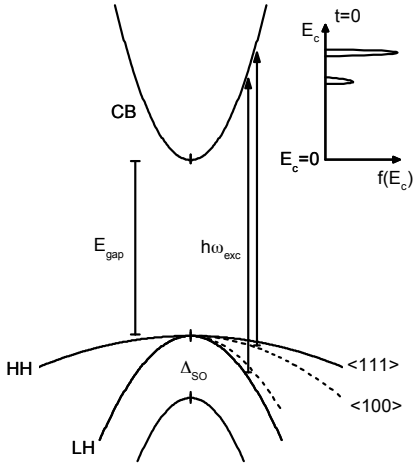

Figure 11: Nonresonant optical excitation in zincblende-type semiconductors. The absorption of monochromatic light with photon energy $E_{\mathrm{gap}} < \hbar\omega_{\mathrm{exc}} < E_{\mathrm{gap}} + \Delta_{\mathrm{SO}}$ creates two initial CB electron populations which originate from the HH and LH transitions. Both initial electron energy distributions $f(E_c^{\mathrm{ini}})$ are broadened by the valence band warping. Adapted from [25].

is transferred to the excited electron therefore is directly related to the curvature of the conduction and valence bands. For optical transitions between parabolic bands with effective masses m_e^* and $m_{\mathrm{hh,lh}}^*$, the initial electron excess energy is [26]:

$$E_c^{\mathrm{ini}} = \left(\hbar\omega_{\mathrm{exc}} - E_{\mathrm{gap}}\right) / \left(1 + m_e^*/m_{\mathrm{hh,lh}}^*\right) \tag{4.1}$$

In GaAs, $m_e^* \ll m_{\mathrm{hh,lh}}^*$ and therefore most of the excitation excess energy is transferred to the electron.

Because of the different hole masses, the above-bandgap excitation with monochromatic light initially creates two distinct conduction band electron populations which originate from the HH and LH valence bands. Moreover, since the effective LH and HH masses depend on the direction of $\mathbf{k}$ (compare section 2.1.3), the initial electron energy distribution functions $f(E_c^{\mathrm{ini}})$ are broadened by the valence band anisotropy [25, 27]. This situation is illustrated in Fig. 11. In GaAs, the width of the two initial conduction band electron distributions is $\lesssim 10\,\%$ of the respective $\langle E_c^{\mathrm{ini}} \rangle$ [24, 25, 27].

The optical spin injection in two-color MOKE microscopy typically involves excitation excess energies $\Delta E_{\mathrm{exc}} \approx 40\,\mathrm{meV} - 60\,\mathrm{meV}$ [15, 30, 33, 68, 83, 101]. For the low lattice temperatures $T_L \lesssim 10\,\mathrm{K}$ at which most MOKE microscopy experiments are performed, the mean initial electron excess energy:

$$\langle E_c^{\mathrm{ini}} \rangle \gg k_B T_L \tag{4.2}$$

exceeds the thermal energy scale $k_B T_L$ of the lattice by approximately two orders of magnitude. Even for very weak excitation powers, a substantial amount of excess energy

is deposited in the electron system by above-bandgap illumination. The creation of a hot[1] electron gas, which is not in thermal equilibrium with the lattice, is therefore inherent to the optical spin excitation technique and virtually cannot be avoided in low-temperature two-color MOKE microscopy.

4.2 Different regimes of photocarrier relaxation

Hot carrier effects arise both in cw steady-state and transient spectroscopy measurements involving pulsed excitation. In the following discussion we first focus on the conceptually simpler transient case, where the different stages of excitation, thermalization, and relaxation take place in a sequential, though temporally overlapping, order. After establishing the main ideas for the transient case we discuss the steady-state situation for cw excitation, for which all of the above processes occur simultaneously.

For both cases we mainly focus on the dynamics of the conduction band electron system in bulk semiconductors, which are most relevant for the electron temperature spectroscopy in bulk n-type GaAs presented later in this thesis. The general aspects of thermalization and relaxation, however, apply qualitatively similar to the dynamics of hot valence band holes and hot exciton gases in bulk semiconductors as well as to the carrier relaxation dynamics in QWs. Extensive reviews on carrier relaxation in these systems are given e.g. in Refs. [27, 28, 112].

In the following sections we introduce the different scattering mechanisms which are responsible for the photocarrier thermalization, i.e. the establishment of a Maxwell-Boltzmann or Fermi-Dirac energy distribution of the carrier ensemble, and the energy relaxation, i.e. the cooling of the photocarriers down to the lattice temperature. Before describing the relevant processes in detail, we follow Ref. [28] and first briefly sketch out the temporally overlapping stages of transient thermalization and energy relaxation following pulsed optical excitation.

After short pulsed optical excitation and losing the initial coherence, the semiconductor is in the non-thermal regime in which the distribution function of the excited electron-hole pairs or excitons cannot be characterized by a temperature. Next, carrier-carrier scattering leads to an efficient redistribution of energy within the carrier system. This process typically establishes a thermal carrier distribution within a couple of picoseconds. The energy distribution of the excited carriers is then described by a carrier temperature which typically exceeds the lattice temperature. In general, this temperature can differ for individual carrier subsystems, e.g. excitons, electrons and holes.

Concurrent with and following the thermalization, energy relaxation of the hot photocarriers takes place by slower electron-phonon scattering processes which mediate the transfer of electron excess energy and momentum to the crystal lattice. At low T_L, these relaxation processes can take from several 100 ps [28] up to 100 ns [113] to cool

[1] By “hot” we refer to every carrier distribution which satisfies Eq. (4.2), i.e. distributions with mean kinetic energies which exceed the thermal energy scale $k_B T_L$ of the lattice. In contrast, we refer to a thermalized carrier ensemble only if the energy distribution function can be completely characterized by a temperature.

the carrier system down to the lattice temperature. Following this energy relaxation, the semiconductor finally enters the isothermal regime, in which all charge carriers, phonons, and excitons are described by the same temperature. This isothermal regime differs from the thermal equilibrium insofar, as cold excess photocarriers may still be present which ultimately recombine either radiatively or non-radiatively.

4.3 Photocarrier thermalization

Following pulsed optical excitation, two competing relaxation paths are possible for the initial, hot, non-thermal electron distribution. These processes are the rapid relaxation towards the conduction band bottom by fast emission of optical phonons [24, 114] and the energy exchange with other charge carriers by Coulomb scattering.

Coulomb scattering can take place either with other photoexcited hot electrons or, if present, with initially cold electrons which belong to an intrinsic background population. In both cases electron-electron scattering effectively randomizes the initial carrier energy distribution within a few scattering events [115] and leads to a fast redistribution of the excess energy among the electron ensemble.The total excess energy deposited in the electron system is conserved by such carrier-carrier Coulomb scattering processes. From the point of view of the hot photocarriers, however, scattering with initially cold intrinsic electrons represents an efficient relaxation mechanism.

The redistribution of excess energy among the carriers by Coulomb scattering rapidly drives the electron ensemble in a thermalized energy distribution. The time scale τ_{therm} on which this thermalization takes place strongly depends on the specific experimental conditions. From a detailed comparison [116] between theory [115, 117] and experimental data [118, 119] it is found that at moderate densities $n_e \lesssim 1 \times 10^{17}\,\text{cm}^{-3}$ the electron-electron scattering rate $\Gamma_{\text{e,e}}$ in bulk GaAs depends on the electron concentration as:

$$\Gamma_{\text{e,e}} \sim n_e^{2/3} \tag{4.3}$$

The efficiency of the Coulomb scattering strongly decreases with decreasing electron density. Therefore, a strong dependence of τ_{therm} on the photocarrier density and the background doping density is expected. Indeed, a systematic decrease of the thermalization time τ_{therm} with n_e has been observed in a number of time-resolved PL spectroscopy experiments. Reported thermalization time constants for bulk GaAs range from ultrafast values $\tau_{\text{therm}} = 100\,\text{fs}$ at $n_e = 1 \times 10^{17}\,\text{cm}^{-3}$ [120] up to $\tau_{\text{therm}} \gtrsim 2\,\text{ns}$ at very low excitation densities $n_e \lesssim 1 \times 10^{13}\,\text{cm}^{-3}$ [24]. Most relevant for the time-resolved measurements presented later in this work is the observation of an upper bound $\tau_{\text{therm}} \lesssim 15\,\text{ps}$ at low lattice temperatures $T_L = 10\,\text{K}$ for excitation densities $n_e \geq 4 \times 10^{14}\,\text{cm}^{-3}$ by Snoke et al. [115, 118]. From this observation we conclude that the electron ensemble is always thermalized on the time scales relevant to our transient MOKE microscopy measurements which span several hundred picoseconds.

Following the brief thermalization period τ_{therm} after the initial photoexcitation, the electron ensemble of a non-degenerate semiconductor is described by a Boltzmann distribution function [121]:

$$f(E_c) \sim \exp\left(-\frac{E_c}{k_B T_e}\right) \tag{4.4}$$

For the parabolic dispersion relation Eq. (2.4), the mean kinetic energy $\langle E_c \rangle$ of the thermalized CB electron ensemble is related to the electron temperature T_e as:

$$\langle E_c \rangle = \frac{3}{2} k_B T_e \tag{4.5}$$

The phonon scattering processes which eventually lead to a cooling of the hot electron ensemble with temperature T_e down to the lattice temperature T_L are described in the following section.

4.4 Conduction band electron energy relaxation

In GaAs, polar coupling through the electric field of the lattice polarization and deformation potential coupling through strain-induced energy changes of the band edges are the two distinct physical mechanisms which give rise to electron-phonon interaction [25]. Similar to the case of optical electric dipole transitions (compare section 2.2.1), phonon scattering processes between initial conduction band states $|\mathbf{k}_i\rangle$ with energy E_i and final states $|\mathbf{k}_f\rangle$ with energy E_f are governed by wave vector and energy conservation [122]:

$$E_f = E_i \pm \hbar\omega_{\mathbf{q}} \quad \text{and} \quad \mathbf{k}_f = \mathbf{k}_i \pm \mathbf{q} \tag{4.6}$$

where $\hbar\omega_{\mathbf{q}}$ is the energy of the phonon with wave vector $\mathbf{q}$.

For the moderate electron excess energies considered here, electron-one phonon scattering can only involve phonon states close to the Brillouin zone center. For conduction band electrons in GaAs, the accessible phonons are the longitudinal acoustic (LA) and transverse acoustic (TA) modes with comparatively small energies $\hbar\omega_{\mathbf{q}} \lesssim 3\,\text{meV}$ [27] and the longitudinal optical (LO) mode whose energy is approximately constant. From the small LA and TA energies it is seen that acoustic phonon scattering is rather inefficient at cooling hot electrons.

At the Brillouin zone center, the LO phonon energy is $\hbar\omega_{\text{LO}} = 36.8\,\text{meV}$ [26]. Because of this large LO phonon energy, the rapid cascade emission of LO phonons potentially allows for a rapid decrease of the initial electron excess energy after pulsed excitation. However, LO phonon emission is only energetically accessible for carriers with sufficiently high kinetic energies $E_c \geq \hbar\omega_{\text{LO}}$. The efficiency of the LO phonon cascade relaxation therefore exhibits a delicate oscillatory dependence on the excitation excess energy [114, 123].

In the presence of cold background carriers, electron-electron scattering and LO phonon cascade emission are competing mechanisms whose relative efficiency determines the fraction of the initial photocarrier excess energy $\langle E_c^{\text{ini}} \rangle$ which is transferred

to the thermalized electron ensemble. From Eq. (4.3), a larger fraction of the initial excess energy is expected to be retained within the electron system for higher carrier densities [26]. Experimentally, at $T_L = 10\,\mathrm{K}$ for $\langle E_c^{\mathrm{ini}} \rangle \approx 300\,\mathrm{meV}$ a critical background carrier density $n_c^* = 8 \times 10^{16}\,\mathrm{cm}^{-3}$ has been determined for which the scattering rate of a single hot electron with the background electron plasma equals the LO phonon emission rate [124].

We now turn to a more quantitative description of the electron-phonon scattering rates in bulk GaAs. We limit our discussion to the case of a non-degenerate[2] Maxwellian electron ensemble with temperature T_e. The three relevant scattering processes are deformation-potential (dp) and piezoelectric (pe) scattering with acoustic phonons and polar-optical (op) scattering with LO phonons [27].

Analytical expressions for the average conduction band electron excess energy loss rates due to one electron-one phonon scattering processes as a function of the electron and lattice temperatures have been derived by Ulbrich in his seminal work Ref. [24] as:

$$\left\langle \frac{dE_c}{dt} \right\rangle_{\mathrm{dp}} = -\left(\frac{(8)(2)^{1/2} E_1^2 m_e^{*5/2} (k_B T_e)^{3/2}}{\pi^{3/2} \hbar^4 \rho} \right) \left(\frac{T_e - T_L}{T_e} \right) \tag{4.7}$$

$$\left\langle \frac{dE_c}{dt} \right\rangle_{\mathrm{pe}} = -\left(\frac{64\pi^{1/2} e^2 e_{14}^2 m_e^{*3/2} a (k_B T_e)^{1/2}}{2^{1/2} \hbar^2 (4\pi\varepsilon_0)^2 \kappa_0^2 \rho} \right) \left(\frac{T_e - T_L}{T_e} \right) \tag{4.8}$$

$$\begin{aligned} \left\langle \frac{dE_c}{dt} \right\rangle_{\mathrm{op}} &= -(2m_e^*)^{1/2} (\hbar\omega_{\mathrm{LO}})^{3/2} \left(\frac{e}{\hbar} \right)^2 \frac{\left(\kappa_\infty^{-1} - \kappa_0^{-1} \right)}{(4\pi\varepsilon_0)} \\ &\quad \times \left[\exp\left(-\frac{\hbar\omega_{\mathrm{LO}}}{k_B T_e} \right) - \exp\left(-\frac{\hbar\omega_{\mathrm{LO}}}{k_B T_L} \right) \right] \end{aligned} \tag{4.9}$$

Here $\kappa_0 = 12.5$ and $\kappa_\infty = 10.9$ are the low- and high-frequency dielectric constants, $e_{14} = 0.16\,\mathrm{C\,m}^{-2}$ is the piezoelectric coupling constant, $a \approx 0.4$ is a dimension-less factor, $E_1 = 6.3\,\mathrm{eV}$ is the deformation-potential and $\rho = 5.32\,\mathrm{g\,cm}^{-3}$ is the volumetric mass density of GaAs [49].

Similar expressions can be obtained for the phonon emission energy loss rates of valence band holes. Because of the effective mass dependence of the scattering rates, the energy loss for the heavier holes is expected to significantly exceed the electron energy loss rates. Moreover, for the p-type symmetry of the holes states, not only polar optical Fröhlich interaction, but also non-polar interaction with optical phonons contributes to the loss rates. These enhancements of the hole loss rates, however, are partially compensated by the anisotropic valence band dispersion relation. As a net result, the hole energy loss rates are approximately a factor of 2.5 higher than the electron-phonon scattering rates in GaAs [28].

Figure 12 (a) shows theoretical average energy loss rates $\langle dE_c/dt \rangle$ versus electron temperature T_e calculated from Eqs. (4.7) - (4.9) for a lattice temperature $T_L = 8\,\mathrm{K}$. As

[2] Calculations for a degenerate electron gas indicate only minor differences for the average electron excess energy loss rates [125].

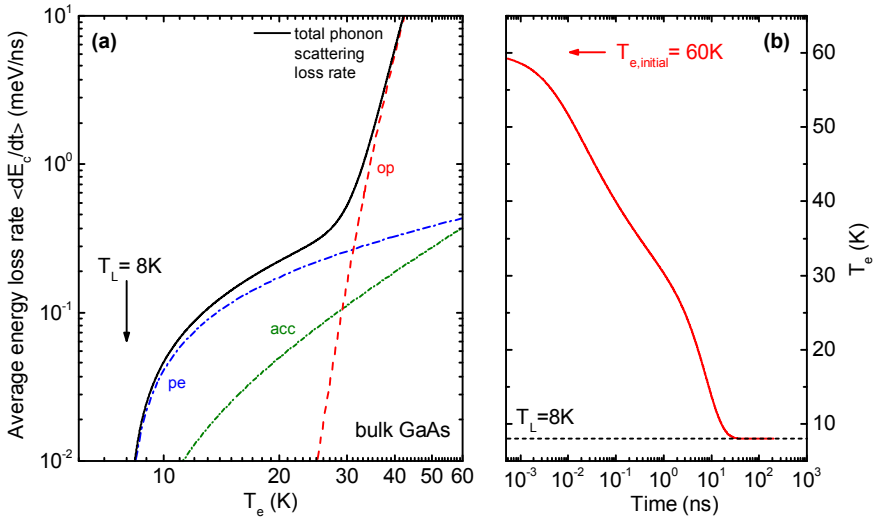

Figure 12: (a) Average energy loss rate $\langle dE_c/dt \rangle$ per electron versus electron temperature T_e for a thermalized Maxwell-Boltzmann distributed conduction band electron ensemble in bulk GaAs at $T_L = 8\,\mathrm{K}$. The dashed curves show the individual contributions of the polar-optical (op, red), piezoelectric (pe, blue) and acoustic-deformation potential (dp, green) one electron-one phonon scattering processes. The solid black line is the total average energy loss rate. Calculated after Ref. [24]. **(b)** Transient cooling of hot electrons in GaAs. The time dependence $T_e(t)$ is calculated from Eq. (4.10) for an initial electron temperature $T_{e,\mathrm{initial}} = 60\,\mathrm{K}$ using the phonon loss rates of (a). The dashed line indicates the lattice temperature $T_L = 8\,\mathrm{K}$. Note the logarithmic time axis.

expected from the preceding discussion, for high electron temperatures polar-optical scattering is the dominant energy relaxation channel. For $T_e \lesssim 30\,\mathrm{K}$, however, the fraction of electrons with $E_c > \hbar\omega_{\mathrm{LO}}$ in the high-energy tail of the Maxwellian distribution rapidly collapses and the LO phonon energy loss rate quickly diminishes for decreasing electron temperatures. The remaining piezoelectric and deformation-potential acoustic phonon scattering are rather inefficient at cooling the hot electrons, i.e. the coupling between the electron system and the lattice becomes weak. At low lattice temperatures, the deposition of very small amounts of excess energy by nonresonant photoexcitation can therefore already lead to a significant heating of the electron system [24, 126].

Following pulsed excitation and the initial thermalization processes, from Eq. (4.4) and Eqs. (4.7) - (4.9) the time evolution of the electron temperature is governed by the energy loss equation:

$$\frac{dT_e(t)}{dt} = \frac{2}{3k_B}\left(\left\langle\frac{dE_c(T_e)}{dt}\right\rangle_{\mathrm{dp}} + \left\langle\frac{dE_c(T_e)}{dt}\right\rangle_{\mathrm{pe}} + \left\langle\frac{dE_c(T_e)}{dt}\right\rangle_{\mathrm{op}}\right) \tag{4.10}$$

From Eq. (4.10) the theoretical cooling curve $T_e(t)$ of the electron ensemble down to lattice temperature can be calculated if the initial electron temperature $T_{e,\mathrm{initial}}$ is known.

In Fig. 4.10 (b) we exemplarily show the time dependence $T_e(t)$ of the electron temperature which we calculate from Eq. (4.10) for $T_{e,\mathrm{initial}} = 60\,\mathrm{K}$ and a lattice temperature $T_L = 8\,\mathrm{K}$. For $T_e \gtrsim 30\,\mathrm{K}$, LO phonon emission mediates a very fast initial decrease of the electron excess temperature. For smaller T_e, however, the electron cooling significantly slows down because of the collapse of the LO phonon scattering rate. The lattice temperature is only reached after very long times $t \gtrsim 30\,\mathrm{ns}$. We will later compare experimentally obtained electron cooling data to the calculation presented above.

4.5 Continuous-wave excitation and steady-state electron temperature

For cw excitation electron-hole-pair creation, thermalization, and energy relaxation take place simultaneously. For $n_e \gtrsim 10^{14}\,\mathrm{cm}^{-3}$, photoexcited electrons scatter quasi-instantaneously with other electrons and thermalize rapidly. The photocarrier excess energy is continuously redistributed among the electron ensemble and the optical excitation acts as a sustained power source for the electron system.

The steady-state electron temperature can be deduced from power-balance considerations. The electron temperature adjusts such that the power transferred to the electron distribution by nonresonant optical excitation is equal to the total power loss $\langle dE/dt \rangle_{\mathrm{tot}}$ of the electron system to the lattice which is given by the sum of Eqs. (4.7) - (4.9).

The electron generation rate by optical excitation is [24]:

$$g = P_{\mathrm{exc}} \left(\hbar\omega_{\mathrm{exc}} V\right)^{-1} \tag{4.11}$$

where P_{exc} is the total absorbed light power and V is the excitation volume. The average energy transferred to the electron system per excited electron-hole pair is $\langle E_c^{\mathrm{ini}} \rangle F(n_e)$. Here $F(n_e) \approx n_e/(n_e + n_c^*) \leq 1$ is a dimensionless factor which increases monotonically with the electron density [23]. The factor $F(n_e)$ considers the relative efficiency of the initial LO phonon cascade relaxation and the energy transfer to the electron system by Coulomb scattering. For the critical electron density $n_e = n_c^*$, initial LO phonon emission and electron-electron scattering occur with equal probability.

The steady-state electron temperature is obtained from the power balance equation [24]:

$$\left\langle \frac{dE_c(T_e)}{dt} \right\rangle_{\mathrm{tot}} = \langle E_c^{\mathrm{ini}} \rangle F(n_e)\, g\, n_e^{-1} \tag{4.12}$$

At low lattice temperatures, for a given excitation energy the electron temperature T_e is expected to increase with the optical excitation power. A strong heating of the electron system is expected for rather low P_{exc} because of the very weak electron-lattice coupling by acoustic phonons. For $T_e \approx 30\,\mathrm{K}$, however, the drastic increase of $\langle dE_c/dt \rangle_{\mathrm{tot}}$ by LO phonon emission limits the rise of T_e. The electron temperature therefore is expected to saturate slightly above $T_e \gtrsim 30\,\mathrm{K}$.

This dependence of $T_e(P_{\mathrm{exc}})$ is indeed observed in Fig. 13 (a) where we show the electron temperature in bulk semi-insulating GaAs as a function of excitation intensity

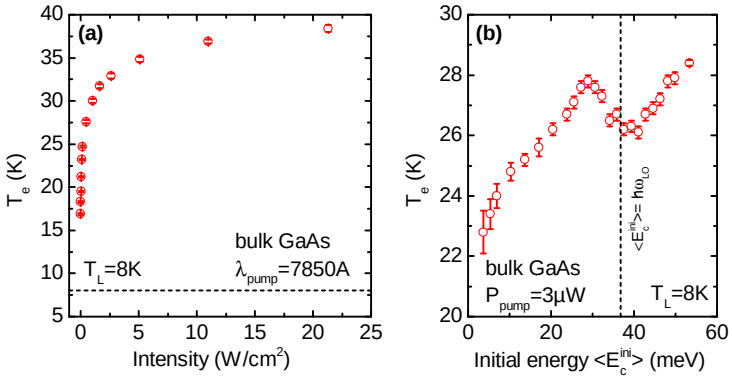

Figure 13: (a) Electron temperature T_e in bulk semi-insulating GaAs as a function of excitation intensity. The excitation wavelength $\lambda_{\text{pump}} = 7850\,\text{Å}$ corresponds to a mean electron excess energy $\langle E_c^{\text{ini}} \rangle \approx 50\,\text{meV}$. The dashed line indicates the lattice temperature $T_L = 8\,\text{K}$. **(b)** Dependence of T_e on the average electron excess energy $\langle E_c^{\text{ini}} \rangle$ for the same sample. The dashed line indicates the LO phonon energy $\hbar\omega_{\text{LO}} = 36.8\,\text{meV}$.

at a lattice temperature of 8 K. The spectroscopic technique which we use to experimentally deduce the electron temperature is described in the following section. The excitation wavelength $\lambda_{\text{pump}} = 7850\,\text{Å}$ used for the measurement corresponds to a mean electron excess energy of $\langle E_c^{\text{ini}} \rangle \approx 50\,\text{meV}$. Note that for this comparatively low excess energy a strong photocarrier heating is still observed even at vanishingly low excitation densities $\ll 1\,\text{W}\,\text{cm}^{-2}$.

From Eq. (4.12) an increase of the electron temperature is expected for increasing electron excess energies $\langle E_c^{\text{ini}} \rangle$. This is demonstrated in Fig. 13 (b) where we measure T_e as a function of the optical excitation energy.[3] However, deviations from the monotonic increase of T_e with increasing excitation excess energy are observed. When $\langle E_c^{\text{ini}} \rangle \approx \hbar\omega_{\text{LO}}$, the initial LO phonon relaxation is particularly efficient at reducing the total excess energy transferred to the electron system. The fast LO emission of the newly excited photocarriers then is reflected by a dip in the $T_e(\langle E_c^{\text{ini}} \rangle)$ curve. This local minimum does not appear as a sudden drop in $T_e(\hbar\omega_{\text{exc}})$, but is smeared out by the spectral broadening of the initial electron energy distribution function $f(E_c^{\text{ini}})$ caused by the valence band warping (compare section 4.1).

4.6 Photoluminescence thermometry

We conclude this chapter by describing how the conduction band electron energy distribution $f(E_c)$ can be directly inferred from the PL of the electron-to-neutral acceptor

[3] Contrary to the data shown in Fig. 13 (a) which are obtained for homogeneous illumination of the sample, the $T_e(\hbar\omega_{\text{exc}})$ measurement of Fig. 13 (b) is performed with a focused pump laser with 3.8 µm diameter. The difference in excitation conditions prevents a direct comparison between both data sets. For further details on the sample and experimental conditions see Ref. [127].

(e,A^0) free-to-bound transition. We describe how the electron temperature T_e is readily obtained from a quantitative line shape analysis of this (e,A^0) transition. Such photoluminescence thermometry measurements are later used in this work for the interpretation of our cw MOKE microscopy measurements.

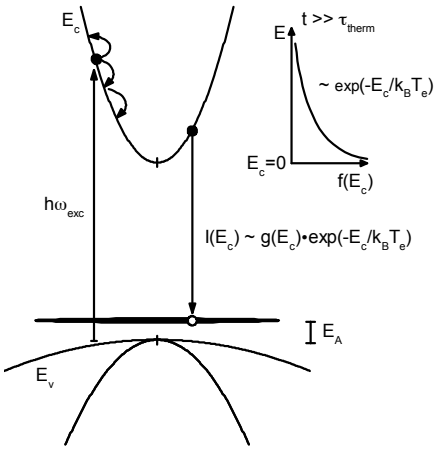

Figure 14: Electron-acceptor photoluminescence thermometry. Conduction band electrons recombine radiatively with neutral acceptor states with binding energy E_A. The line shape of the free-to-bound (e,A^0) transition reflects the density of occupied states $N(E_c) = f(E_c) \cdot g(E_c)$ of the electron system. Adapted from [25].

As one of the many possible recombination paths, CB electrons can recombine radiatively with holes which are bound to acceptor states [128]. The shallow hydrogenic acceptor impurity states which are relevant for this work are formed by substitutional group IV impurities on As sites [129]. This electron-to-neutral acceptor (e,A^0) transition takes place between the conduction band continuum states and the discrete bound acceptor state with fixed binding energy E_A.

Neglecting the minor $\mathbf{k}$-dependence of the transition matrix element between the conduction band states and the acceptor envelope wave function, the (e,A^0) PL line shape $I(\hbar\omega)$ directly reflects the electron distribution $N(E_c)$ [130, 131]. For the bulk density of states Eq. (2.5) of the parabolic conduction band and a Boltzmann-distributed electron ensemble the (e,A^0) PL line shape therefore is:

$$I(\hbar\omega) \sim \sqrt{\hbar\omega - E_{\mathrm{gap}} + E_A}\, \exp\left(-\frac{\hbar\omega - E_{\mathrm{gap}} + E_A}{k_B T_e}\right) \tag{4.13}$$

A quantitative analysis of the (e,A^0) PL line shape using Eq. (4.13) directly yields the electron temperature T_e.

Part II

Methods and materials

Chapter 5

Optical instrumentation

5.1 Pump-probe MOKE microscopy setup

5.1.1 Design considerations

Depending on the subject of investigation, the use of either pulsed or cw laser sources is advantageous for different MOKE spectroscopy experiments. In general, time-resolved pump-probe spectroscopy is ideally suited for the observation of comparatively fast spin relaxation phenomena which take place on the sub-nanosecond time scale. These phenomena include e.g. the electron spin relaxation in narrow GaAs QWs and the hole spin dephasing in bulk semiconductors and low-dimensional systems. Moreover, as we will demonstrate in this work, picosecond real-space imaging of electron spin propagation by time-resolved MOKE microscopy is a particularly valuable tool for the direct measurement of electron spin diffusion coefficients. The goal of achieving high temporal resolution, however, mandates the use of ultrafast laser sources. Mode-locked femtosecond Ti:sapphire (Ti:Sa) laser systems are therefore commonly used for time-resolved Kerr rotation (TRKR) spectroscopy. While offering unrivaled time resolution, a potential drawback of these laser sources is their spectrally broad emission with typical line widths on the order of $\approx$10-20 meV [106].

In contrast, cw spectroscopy enables MOKE measurements with extremely high energy resolution. For the visible and near-infrared (NIR) spectral range, actively stabilized, tunable, single-frequency sources with line widths in the single-kHz regime have been demonstrated both in the form of traditional solid state lasers [132, 133] and semiconductor diode laser systems [134], and commercial sub-100 kHz systems are readily available. Such spectrally narrow laser sources allow to address the spin polarization of specific electron sub-ensembles in semiconductors, e.g. to selectively probe the spin polarization of free and donor-bound carriers or the excited and ground states in low-dimensional systems. Since a temporal synchronization of the steady-state pump and probe laser sources is not required, the implementation of cw two-color pump-probe schemes is comparatively easy. Moreover, cw MOKE microscopy can be used to image the steady-state electron spin polarization resulting from electrical spin injection, e.g. from ferromagnetic contacts. Finally, cw Hanle-MOKE measurements are particularly well suited to determine the exceptionally long spin relaxation times e.g. found in bulk n-doped GaAs or in modulation-doped CdTe QWs.

Because of the complementarity of both approaches, the versatility of the hybrid Kerr microscope presented in this work is greatly enhanced by the possibility to study low-temperature electron spin transport in semiconductor systems by means of cw and time-resolved MOKE microscopy. The instrument is specifically designed such that it allows for the rapid change between the pulsed and cw configuration without the necessity to carry out any changes to the optical setup. The instrument is unique in its ability to provide both cw and picosecond pump-probe MOKE imaging of electron spins with nearly diffraction-limited spatial resolution in a single Kerr microscopy setup.

For cw spectroscopy we follow the common approach of using two independent Ti:Sa lasers as the continuously tunable pump and probe laser sources. For time-resolved measurements with pulsed excitation and detection, however, we choose a novel approach which mitigates some potential disadvantages of the typical use of a single, mode-locked Ti:Sa laser.

In the traditional form of degenerate time-resolved pump-probe spectroscopy the pulsed pump and probe lasers are obtained from the same laser source, i.e. the excitation and detection wavelengths are equal. In semiconductors an appreciable Kerr rotation signal is only observed in the vicinity of the excitonic optical resonances. The necessity to detect the small spin-induced polarization signals therefore limits the excitation energies accessible by degenerate MOKE spectroscopy. However, a strong influence of the excitation energy on the electron spin dynamics due to pump-induced carrier heating and the resulting electron temperature gradients is expected both for bulk semiconductors and QWs. It is therefore desirable to independently control the pump and probe wavelengths in MOKE spectroscopy experiments to enable the systematic investigation of the interrelationship between charge, spin, and heat transport in the electron system of semiconductor heterostructures.

In the past this has been achieved by elaborate synchronization of the pulse trains of two independent mode-locked Ti:Sa laser systems [11, 135, 136]. We here present a new approach to time-resolved two-color MOKE microscopy which is based on an ultrafast ‘white light’ supercontinuum fiber-laser source.

The use of pulsed supercontinuum sources for optical spectroscopy is a new development which has gained significant traction only within the last few years. Supercontinuum sources are today widely used for chemical analysis by coherent anti-Stokes Raman spectroscopy (CARS) [137], for the creation of precise frequency standards using frequency combs [138], and most notably for bio-imaging applications including stimulated emission depletion (STED) microscopy [139] and optical coherence tomography (OCT) [140]. We are, however, to our knowledge the first to apply a supercontinuum source to time-resolved pump-probe scanning MOKE microscopy. Building on our experience that we have gathered in the development of a general purpose pump-probe Kerr microscope during the last years, we are convinced that we have arrived at a rather sophisticated – yet easy to implement – solution which we intend to share with the spintronics community. In the following we therefore give a particularly detailed

description and characterization of our instrument to provide a comprehensive, self-contained documentation of a state-of-the art approach towards two-color picosecond Kerr microscopy.

The three main advantages of our instrument for time-resolved spectroscopy are (i) the ability to independently tune the excitation and detection energy while avoiding the necessity to synchronize two separate picosecond laser systems, (ii) access to the whole visible and near-infrared spectral range for the investigation of a wide range of different semiconductor material systems while maintaining a high repetition rate, and (iii) a significant reduction of the complexity and the costs involved in the development of a picosecond two-color Kerr microscope due to the utilization of a single robust and comparatively inexpensive femtosecond fiber-laser source.

The aim to investigate the spatio-temporal dynamics of optically induced electron spin packets imposes challenging requirements on the experimental setup: Typical spin diffusion lengths in semiconductors are of the order of several micrometers [15, 32]. In bulk n-GaAs long spin relaxation times exceeding 100 ns are routinely observed [13, 67, 141]. Spin relaxation in QWs, however, is much faster and typically happens on time scales of the order of hundred picoseconds [35, 37, 142]. Time-resolved real-space imaging of electron spin diffusion processes therefore requires an instrument which allows to investigate electron spins with micrometer spatial and picosecond time resolution at cryogenic temperatures. The pump-probe MOKE microscope presented here meets these requirements and is capable of measuring optically induced electron spin diffusion for sample temperatures between 8 K-300 K with < 3 ps time and $< 2\,\mu$m spatial resolution.

5.1.2 Instrumentation

A schematic diagram of the experimental setup is shown in Fig. 15. To minimize disturbances by dynamic changes in the ambient environment we operate the Kerr microscope in a climate-controlled laboratory where we stabilize the temperature and relative humidity within $\pm 0.2\,^{\circ}$C and below 35 %, respectively. The instrument is built on an optical table equipped with an active vibration isolation system. The detrimental effects of turbulent air currents on the polarization state of the pump and probe lasers are reduced by enclosing the entire setup with a laminar flow box.

Access to sample temperatures between 8 K and 300 K is provided by an Oxford MicrostatHe narrow tail liquid helium flow optical cryostat which enables the use of short focal length focussing optics. The cryostat is mounted on a mechanical 3-axis stage for lateral scanning of the sample position and focussing of the pump and probe laser beams.

The sample is yieldably clamped to a copper holder which is mounted in vacuum on

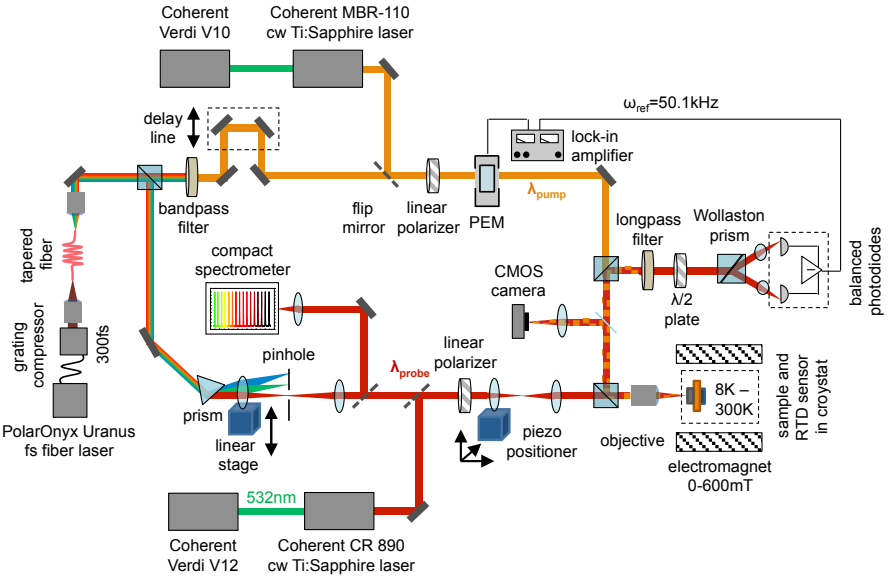

Figure 15: Schematic of the two-color pump-probe MOKE microscope. The main optical components of the Kerr microscope are the supercontinuum generation, the instrumentation for the independent spectral filtering of the pulsed pump and probe laser, additional Ti:sapphire lasers for cw spectroscopy, the focussing and raster-scanning optics for the local optical electron spin excitation and detection and the manipulation of the probe laser position, and the balanced photoreceiver lock-in Kerr rotation detection scheme for the measurement of the small spin-dependent changes of the probe laser polarization.

the coldfinger of the cryostat. Care is taken to avoid a strain-induced **k**-dependent splitting of the conduction band spin states which affects the electron spin dynamics [15]. A calibrated Cernox resonant tunneling diode (RTD) temperature sensor is attached to the backside of the copper holder for accurate measurements of the sample temperature. The cryostat is placed between the poles of an electromagnet which allows for the application of external in-plane magnetic fields of up to 600 mT in Voigt geometry. A calibrated Hall sensor is used to monitor the magnetic field at the sample position.

The main optical components of the pump-probe MOKE microscope are the supercontinuum generation, the instrumentation for the independent spectral filtering of the pump and probe laser, two additional Ti:sapphire lasers for cw spectroscopy, the focussing and raster-scanning optics for the local optical electron spin excitation and detection and the manipulation of the probe laser position, and the balanced photoreceiver lock-in detection scheme for the measurement of the small spin-induced changes of the probe laser polarization. A detailed description of each component is given in the following.

Supercontinuum generation

The generation of the 'white light' supercontinuum from which we derive the pulsed pump and probe laser beams is based on nonlinear frequency conversion of a short near-infrared laser pulse in a tapered optical fiber. For the optical pumping of the fiber we use the output of a mode-locked PolarOnyx Uranus 1030 high power femtosecond laser which provides pulses with a central wavelength of $\approx 1030\,\mathrm{nm}$. The repetition rate of the pump laser system is 36.4 MHz which corresponds to a 27.5 ns pulse-to-pulse interval. The time-averaged output power of the pump laser is 3 W. After exiting the pump laser, a grating compressor is used to reduce the output pulse length to $\lesssim 300\,\mathrm{fs}$.

The pump pulses are coupled into the tapered fiber by an infinity corrected Olympus 10x plan achromat objective (numerical aperture NA = 0.25) which is mounted on a 3-axis fiber launch system. A Faraday isolator is placed in the pump beam path in front of this objective to prevent unintentional back-reflection of pump light into the laser cavity. Owing to the high peak intensities achieved by the strong femtosecond pump laser in the thin tapered fiber, a variety of nonlinear effects including soliton fission, stimulated Raman and Brillouin scattering, four-wave-mixing, and self-phase modulation lead to a strong spectral broadening of the pump pulses [143]. Depending on specific parameters such as fiber waist diameter, excitation pulse duration, pump wavelength, and peak pulse power this spectral broadening results in the creation of a smooth supercontinuum which can extend from $\approx 400\,\mathrm{nm} - 1600\,\mathrm{nm}$ [144, 145].

The configuration of the instrument described here is optimized for the investigation of GaAs-based semiconductor heterostructures. We therefore use a comparatively thick fiber with a 4 µm waist diameter which leads to supercontinuum creation with appreciable spectral weight in the vicinity of the relevant 800 nm spectral region. The maximum time-averaged power transmitted through the fiber is $\approx 875\,\mathrm{mW}$. A typical spectrum of the output of the supercontinuum source is shown in Fig. 16 (a) on a logarithmic scale. While the supercontinuum in the present configuration is limited to wavelengths $\gtrsim 520\,\mathrm{nm}$, access to higher photon energies can be obtained by using a thinner fiber.

After exiting the fiber the supercontinuum light is collimated by a second, infinity corrected, fiber launch mounted Olympus 4x plan achromat microscope objective (NA = 0.1). The supercontinuum output is extremely sensitive to small changes of the pump laser input coupling into the fiber. To enhance the temporal stability of the supercontinuum we therefore further suppress the influence of environmental fluctuations by placing the entire supercontinuum generation unit in an additional plexiglass housing.

We use a broadband anti-reflection coated 70:30 beamsplitter to divide the supercontinuum beam in two components. We obtain the pulsed probe and pump lasers from these two beams by performing individual spectral filtering, where we use the 70 % transmitted component for the probe laser.

Spectral filtering of the pulsed pump and probe lasers

The spectral position of the excitonic Kerr resonance depends on the semiconductor material, the sample temperature, and in the case of low-dimensional systems on the confinement energy. While it is often sufficient to operate the pump laser at fixed above-bandgap wavelengths, MOKE microscopy requires a continuously tunable probe laser to allow for a versatile investigation of different semiconductor heterostructures.

To meet this requirement in time-resolved measurements we have implemented a prism-based spectral filtering scheme for the pulsed probe laser. The probe beam is horizontally dispersed by a N-SF14 glass prism. A high-dispersion glass type is used to enhance the angular spread of the individual spectral components of the supercontinuum to achieve a high spectral resolution. To minimize reflection losses, the prism is operated under the condition of minimum deviation. The 59.6° apex angle of the prism is designed such that the incident and exit angles are made Brewster's angle for wavelengths between $\approx 700 - 900\,\mathrm{nm}$. The lossless transmitted horizontal polarization component of the initially unpolarized supercontinuum is subsequently used as the linearly polarized probe laser beam as described below.

Following the prism, the dispersed probe beam is focused by a $f = 100\,\mathrm{mm}$ lens on a 50 µm pinhole. In the focal plane of the lens, the angular dispersion introduced by the prism translates to a lateral displacement of the focus position of different wavelength components of the supercontinuum. The focussing lens is mounted on a PI miCos LS-65 linear stage which allows for horizontal scanning of the lens position with sub-micrometer resolution and uni-directional repeatability. Variation of the lens position allows for a selection of the desired wavelength component from the supercontinuum by the pinhole.

For the combination of the N-SF14 glass prism and the $f = 100\,\mathrm{mm}$ focussing lens, the lateral wavelength dispersion of the superontinuum in the pinhole plane is $\approx 1\,\text{Å}\,\mu\mathrm{m}^{-1}$ in the spectral vicinity of 800 nm. Precise tuning of the probe wavelength therefore requires a rather fine computer-controlled manipulation of the lens displacement with micrometer accuracy. After passing the pinhole, the transmitted spectral component is collimated by a second $f = 60\,\mathrm{mm}$ lens. By manipulating the position of the first lens while keeping the pinhole position fixed, the probe wavelength can be tuned without changing the beam direction after the second lens.

In Fig. 16 we demonstrate the continuous tuning of the probe laser over a wide spectral range between 520 nm and 820 nm by systematic variation of the scanning lens position. For each lens position we measure the probe laser spectrum with a compact CCD spectrometer which can be introduced in the probe beam path after the filtering instrumentation by temporarily inserting a flip mirror.

We determine the energy resolution of the prism filter by measuring the full-width at half maximum (FWHM) of the probe laser spectrum as a function of the central wavelength λ_{probe}. In Fig. 16 (b) we show that no systematic variation of the probe laser linewidth with increasing λ_{probe} is observed. The FWHM stays approximately constant over the whole examined wavelength range. The mean value of the FWHM is 3.9 meV

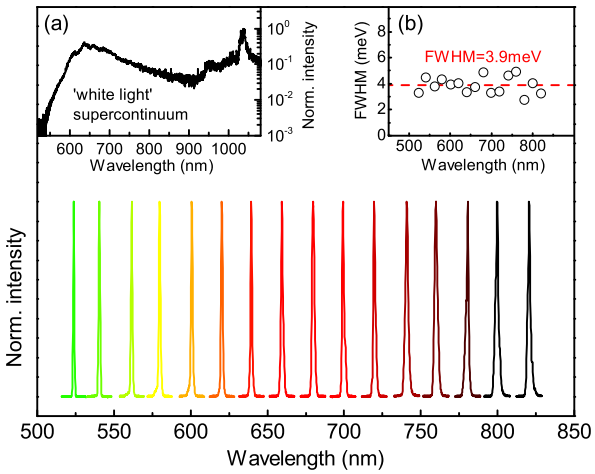

Figure 16: Spectra of the continuously tunable probe laser obtained by dispersive filtering of the white-light supercontinuum. **Inset (a)** Typical output spectrum of the pulsed fiber-laser source (4 µm fiber waist diameter, 875 mW time-averaged total output power). **Inset (b)** Spectral width (FWHM) of the probe laser as a function of central laser wavelength. The red dashed line indicates the mean FWHM of 3.9 meV.

and the FWHM never exceeds 5 meV. If necessary, the spectral resolution of the prism filter can be improved by using a smaller pinhole and a higher dispersion glass type; however this leads to a reduction of the available probe laser power.

The pump laser wavelength is selected by passing the supercontinuum through a standard optical bandpass filter. A broad selection of high-quality dielectric bandpass filters which cover the whole visible and near-infrared spectral range is commercially available. Depending on the material system under investigation, filters with appropriate central wavelengths and passband widths can be introduced in the pump laser beam path.

A synchronized pair of conventional mechanical delay lines is placed in the pump beam path to introduce a variable time delay Δt between the pump and probe pulses. The PI miCos LS-110 linear stages each have a travel range of 305 mm with 50 nm resolution and uni-directional repeatability. The present configuration provides a maximum delay of 4 ns which can be extended by multi-pass operation of the delay lines.

Continuous-wave Ti:sapphire laser sources

For cw two-color MOKE spectroscopy, two independent Ti:sapphire lasers can be used in the Kerr microscope as the pump and probe laser beams by simply changing the position of two flip mirrors. Both Ti:Sa lasers are pumped at 532 nm with 10 W by two frequency-doubled, diode-pumped neodymium-doped yttrium orthovanadate

($Nd:YVO_4$) Coherent Verdi V10 and V12 solid state lasers. The pump laser for MOKE spectroscopy is provided by a Coherent MBR-110 ring-cavity Ti:Sa laser which can be tuned between 775 nm and 840 nm. A continuously tunable Coherent CR 890 linear-cavity Ti:Sa laser which provides access to wavelengths between 770 nm and 900 nm is used as the MOKE probe laser source. The CR 890 Ti:Sa is particularly well suited for high-resolution Kerr spectroscopy since is does not exhibit mode hopping during wavelength tuning. Its wavelength therefore can be tuned with sub-0.1 Å resolution and repeatability. We use computer-controlled stepping motors to automatically vary the configuration of intra-cavity Lyot filters to set the calibrated wavelengths of both Ti:Sa systems.

Focussing and raster-scanning optics

The diffraction limit for the spatial resolution Δ of conventional far-field optical microscopy is determined by the wavelength λ and the numerical aperture NA of the focussing objective [110]:

$$\Delta \geq \frac{1}{2}\frac{1.22\lambda}{\mathrm{NA}} \tag{5.1}$$

Achieving micrometer spatial resolution in the near-infrared and visible range therefore requires the use of high NA focussing optics with short focal distances. To minimize aberrations in the spatially resolved electron spin detection it is further desirable to utilize high-quality room-temperature microscope objectives which must be operated outside the cryostat. Spatial constraints therefore dictate to use short working distance optical cryostats and the utilization of the same microscope objective for the focusing of both the pump and probe laser beam.

We use an infinity-corrected Mitutoyo 50x plan apochromatic long working-distance microscope objective ($f = 4\,\mathrm{mm}$, $\mathrm{NA} = 0.42$) to focus the pump and probe beams on the sample surface. The moderate numerical aperture of the objective is chosen for quasi-normal-incidence focussing of the pump and probe beams with negligible photon angular momentum along the sample in-plane directions [146]. To scan the probe with respect to the fixed pump beam position, we introduce a pair of $f = 4\,\mathrm{mm}$ aspheric lenses arranged in confocal geometry in the probe beam path. The first lens is mounted on a PI P-611.3 Nanocube 3-axis piezo positioner which offers 100 µm travel range with nanometer resolution along each axis.

Manipulation of the relative position of the aspheric lens pair changes the probe laser's angle of incidence on the microscope objective aperture. This directly translates to a change of the focus position of the probe beam on the sample surface (compare Fig. 18). Since the focal lengths of the microscope objective and the aspheric lenses are equal, lateral scanning of the piezo-mounted lens directly results in a translation of the probe laser beam position at the sample surface by the same distance. The Kerr microscope therefore offers a $100 \times 100\,\mu\mathrm{m}^2$ field of view.

After reflection from the sample surface the pump and probe lasers are collected by the same microscope objective. Polarization retaining beamsplitters are used to steer

the pump and probe beams to the Kerr rotation detection optics and to a CMOS camera which is placed in the focal plane of a $f = 75\,\mathrm{mm}$ lens. The CMOS camera is used to monitor the focussing of both lasers and the positioning of the probe beam. We additionally use the CMOS camera for the determination of the spatial resolution of the MOKE microscope as described below.

Optical spin excitation

We employ the standard optical orientation technique introduced in section 2.3 for the electron spin excitation by the pump laser. We use a Hinds Instruments PEM-100 photoelastic quartz modulator (PEM) [147] to periodically modulate the pump polarization between σ^+ left and σ^- right circular polarization at a frequency $(\omega_{\mathrm{ref}}/2\pi) = 50.1\,\mathrm{kHz}$. Before entering the PEM, the linear polarization of the pump laser is therefore adjusted to $+45°$ to the horizontal by a high-quality Glan-Thompson polarizer. The fast axis of the PEM is oriented horizontally and the retardation is set to $(\lambda/4)$ for the respective pump wavelength. After passing the PEM, the modulated pump beam is focused on the sample surface and locally excites electrons with a net spin polarization S_z oriented along the sample normal $\hat{z}$.

The benefit of the PEM modulation is twofold. First, the fast, sinusoidal change of the electron spin orientation prevents the unintentional polarization of nuclear spins by transfer of angular momentum from the electron to the lattice system (compare section 3.1.2). Second, the periodic modulation of the pump laser polarization enables lock-in detection of the small Kerr rotation signals.

Lock-in Kerr rotation detection

The spatially resolved electron spin detection in our experiments is based on the polar MOKE. In the presence of spin polarized electrons, the probe laser state is changed from the initially linear to elliptical polarization after reflection from the sample surface (compare section 3.4). In the polar geometry of our setup, the major axis of polarization is rotated by the Kerr angle θ. The ratio of the major and minor axis of polarization is determined by the tangent of the Kerr ellipticity ϕ as indicated schematically in Fig. 17.

The magnitude of Kerr rotations observed in pump-probe MOKE microscopy experiments on non-magnetic semiconductors is typically well below 1 mrad. To facilitate the detection of the small polarization signals we employ a balanced photoreceiver lock-in detection scheme [106, 148]. Before entering the focussing optics, the probe laser is set to vertical linear polarization by a Glan-Thompson polarizer. After reflection from the sample surface, the elliptical polarization state of the probe laser induced by the polar MOKE is described by the Jones vector [149]:

$$\mathbf{E}_{\mathrm{out}} = E_0 \begin{pmatrix} \cos(\theta)\cos(\phi) - i\sin(\theta)\sin(\phi) \\ \sin(\theta)\cos(\phi) + i\cos(\theta)\sin(\phi) \end{pmatrix} \tag{5.2}$$

After being collected by the microscope objective, the major axis of polarization of the reflected probe beam is rotated by 45° by a Soleil-Babinet compensator. The com-

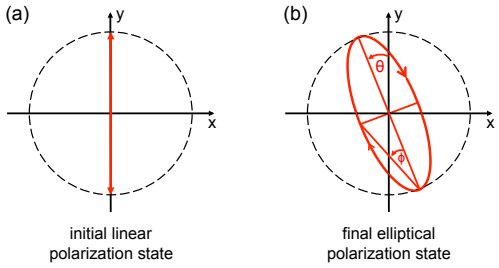

Figure 17: Probe laser polarization states in our MOKE spectroscopy measurements. **(a)** Initial vertical linear polarization. **(b)** Elliptical polarization after reflection from the sample surface. The major axis of polarization is rotated by the Kerr angle θ, the ratio of the major and minor axis of polarization is the tangent of the Kerr ellipticity ϕ.

pensator therefore is set to $(\lambda/2)$ retardation and the fast axis is tilted by 22.5° to the vertical.

We use a Wollaston prism to split the probe laser into two separate, linearly polarized beams carrying the $\hat{x}$ (horizontal) and $\hat{y}$ (vertical) polarization components which are focused on two separate photodiodes of a balanced photodetector. A high-transmission Semrock RazorEdge ultra-steep longpass filter (transition width $\lesssim 5\,\mathrm{meV}$) with an appropriate cut-off wavelength is placed in front of the Wollaston prism to prevent the collinear, modulated pump laser from entering the detector.

The custom-built balanced photodetector is specifically optimized for raster-scanning microscopy to achieve highest possible spatial homogeneity in the detection efficiency. We therefore employ large-area Hamamatsu Photonics silicon photodiodes to compensate for the small lateral displacement of the probe beam focus position on the diode surface caused by the raster-scanning of the probe beam position.

The two probe beam components evoke photocurrents which are proportional to the respective beam intensity:

$$I_{x,y} = |\,(\mathbf{E}_{\mathrm{out}})_{x,y}\,|^2 \tag{5.3}$$

A high-sensitivity transimpedance amplifier with a $1 \times 10^7\,\mathrm{V\,A^{-1}}$ gain is used to generate a voltage signal which is proportional to the photocurrent difference:

$$V_{\mathrm{out}} = g_{\mathrm{LI}}\,(I_x - I_y) \tag{5.4}$$

The conversion coefficient g_{LI} considers the wavelength-dependent quantum efficiency of the photoreceiver diodes and the modulation frequency dependent transimpedance amplifier gain. Using Eq. (5.2) we obtain:

$$V_{\mathrm{out}} = g_{\mathrm{LI}}\left(|E_0|^2/2\right) \times \Big(\sin\left[2(\theta-\phi)\right] + \sin\left[2(\theta+\phi)\right]\Big) \tag{5.5}$$

The periodic modulation of the optical spin excitation by the PEM leads to a sinusoidal time dependence of the Kerr rotation and ellipticity, i.e. $\theta(t) = \theta_K \sin(\omega_{\mathrm{ref}} t)$ and

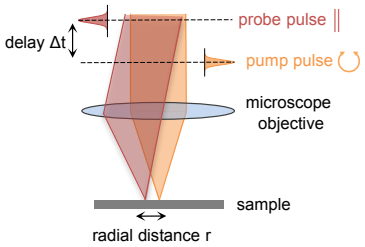

Figure 18: Schematic illustration of the working principle of time-resolved real space imaging of electron spin diffusion by pump-probe MOKE microscopy. The focussed probe beam is repeatedly raster-scanned with respect to the pump spot position and the local Kerr rotation $\theta_K(\Delta t, r)$ is measured as a function of the pump-probe delay Δt. This procedure yields full information on the spatio-temporal dynamics of the electron spin polarization $S_z(\Delta t, r)$.

$\phi(t) = \phi_K \sin(\omega_{\text{ref}} t)$. The photodetector output voltage can be expanded in terms of odd harmonics of the PEM frequency ω_{ref} using the Jacobi-Anger identity [150]:

$$\sin(z\sin(x)) = 2\sum_{n=0}^{\infty} J_{2n+1}(z)\sin((2n+1)x) \tag{5.6}$$

where J_k denotes the Bessel function of kth order.

Combining Eqs. (5.5) and (5.6) we obtain an explicit expression for the time dependence of the detector output voltage:

$$\begin{aligned} &V_{\text{out}}(t) = \\ &g_{\text{LI}} |E_0|^2 \sum_{n=0}^{\infty} \Big(J_{2n+1}\left[2(\theta_k - \phi_k)\right] + J_{2n+1}\left[2(\theta_k + \phi_k)\right] \Big) \\ &\times \quad \sin\left[(2n+1)\omega_{\text{ref}} t\right] \end{aligned} \tag{5.7}$$

The detector voltage $V_{\text{out}}(t)$ is demodulated at the fundamental PEM frequency by a Stanford Research SR530 lock-in amplifier. The lock-in output voltage V_{LI} is proportional to the ω_{ref} frequency component of the input signal, i.e. the lock-in is only sensitive to the $n = 0$ term of the series in Eq. (5.7). Furthermore, since $|\theta_K| \ll 1$ and $|\phi_K| \ll 1$, the approximation $J_1(x) \approx \frac{x}{2}$ can be used [150]. The lock-in output voltage is therefore a direct measure of the local Kerr rotation, i.e.:

$$V_{\text{LI}} = 2 g_{\text{LI}} |E_0|^2 \theta_K \tag{5.8}$$

The conversion coefficient g_{LI} can be determined from an independent calibration procedure described below. Following this calibration, absolute values of the local Kerr rotation are directly obtained from the lock-in measurement.

Finally, as illustrated in Fig. 18, by repeatedly raster-scanning the probe with respect to the pump spot position and measuring the local Kerr rotation $\theta_K(\Delta t, r)$ as a function

of the pump-probe delay Δt and the relative pump-probe distance r, full information on the spatio-temporal dynamics of the electron spin polarization $S_z(\Delta t, r)$ is obtained[4]. This is the working principle of time-resolved real-space imaging of electron spins by pump-probe MOKE microscopy.

5.1.3 Instrument characterization

Supercontinuum stability and available output power

While offering great experimental flexibility, potential drawbacks of the use of supercontinuum laser sources for pump-probe spectroscopy are the limited power after narrow spectral filtering and the susceptibility of the spectral distribution of the supercontinuum output to temporal fluctuations. By carefully minimizing environmental fluctuations and using a sufficiently strong pump laser, both challenges can be overcome and supercontinuum sources can be successfully applied to MOKE microscopy.

In our instrument the total tapered fiber output power of 875 mW and the supercontinuum spectral width of ≈ 1000 nm suggest an average spectral power density of $\lesssim 1\,\mathrm{mW\,nm^{-1}}$. However, as shown in Fig. 16 (b), the actual spectral power density strongly varies with wavelength. Moreover, temporal drift of the coupling of the pump laser into the supercontinuum fiber can cause detrimental fluctuations of the total available output power and the spectral power density distribution of the supercontinuum.

To validate the absence of such fluctuations and to demonstrate the operability of our Kerr microscope we first characterize the long-term stability of the supercontinuum source. We therefore show in Fig. 19 a representative time trace of the total supercontinuum output power which we measure with a calibrated thermopile sensor over an extended time period of 2 hours. Within this observation window we measure a mean total output power of 875 mW which fluctuates only very weakly with a relative standard deviation (RSD) of 0.3 %.

To further quantify the spectral stability of the supercontinuum source we additionally measure with a calibrated semiconductor sensor time traces of the individual pump and probe beam powers after the spectral filtering schemes described above. For the individual pump and probe beam stability measurements we use a pump laser wavelength $\lambda_{\mathrm{pump}} = 780$ nm and tune the central probe laser wavelength to $\lambda_{\mathrm{probe}} = 820$ nm. From the time traces shown in Fig. 19 we determine a mean pump power of 403 µW (1.3 % RSD) and probe laser power of 288 µW (2.4 % RSD). Compared to the pump laser, the spectrally more narrow probe laser is slightly stronger affected by the weak fluctuations of the spectral supercontinuum power distribution.

Overall we observe a high temporal stability of the fiber laser source, demonstrating the viability of our supercontinuum approach for pump-probe MOKE microscopy. Careful inspection of the partial time trace shown in the inset of Fig. 19 further reveals that a major component of the weak probe power drift is periodic in the $t_{\mathrm{AC}} \approx 20$ min

[4] For pulsed excitation, the lock-in integration time is typically chosen such that for each spatial position and pump-probe delay the reported signal is the average of $\approx 2 \times 10^8$ pulses.

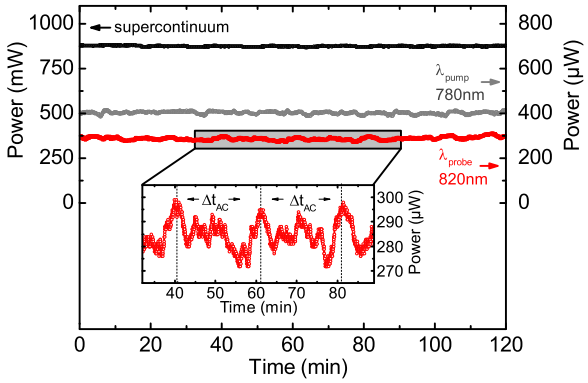

Figure 19: Time traces of the total supercontinuum output power (black) and the pump (gray) and probe (red) beams after narrow spectral filtering. Dashed lines in the inset indicate the cooling cycle period Δt_{AC} of the laboratory climate control (see text).

cooling cycle period of the laboratory climate control. If necessary the pump and probe power stability therefore can potentially be further improved by increasing the laboratory temperature stability or by the additional use of inexpensive commercial liquid crystal laser amplitude stabilizers.

After passing the polarization modulation, focussing, and raster-scanning optics, the available pump and probe power arriving at the sample surface are $P_{\text{pump}} \approx 6\,\mu\text{W}$ and $P_{\text{probe}} \approx 12\,\mu\text{W}$. Despite the comparatively low absolute value of the pump power, the strong focussing of the pump beam allows for high-density optical injection of spin-polarized photocarriers. When using the maximum available pump power, photocarrier densities exceeding $1 \times 10^{17}\,\text{cm}^{-3}$ for bulk GaAs and $1 \times 10^{12}\,\text{cm}^{-2}$ for GaAs-based QW samples are obtained.[5] Moreover, the probe power of $\approx 2\,\mu\text{W}$ which finally arrives at the balanced photoreceiver yields Kerr rotation output voltage amplitudes on the order of 1 mV which are readily detected by standard lock-in amplifiers.

Spatial resolution

We determine the spatial resolution of the instrument from CMOS camera images of the focused pump and probe spots. The square pixel size of the camera is $d_{\text{CMOS}} = 5.3\,\mu\text{m}$. For the $(75\,\text{mm}/4\,\text{mm})$ ratio of the focal lengths of the camera lens and the microscope objective, one pixel corresponds to a distance of 0.28 µm on the sample surface.

From Eq. (5.1) the diffraction limit for the attainable spatial resolution depends on the laser wavelength λ. We here characterize the spatial resolution for a central pump

[5] Photocarrier densities are calculated for a pump spot area of $3\,\mu\text{m}^2$, a sample reflectance $R = 0.3$, a pump wavelength of 780 nm, and a pump pulse energy of 0.14 pJ (corresponding to a 5 µW time-averaged pump power at a repetition rate of 36.4 MHz). For the bulk sample we consider absorption in a 1 µm epilayer with a penetration depth of 0.7 µm at $\lambda = 780\,\text{nm}$ [151]. For the QW we assume an absorption coefficient of $1 \times 10^4\,\text{cm}^{-1}$ and the 20 nm QW width of the samples examined in this work.

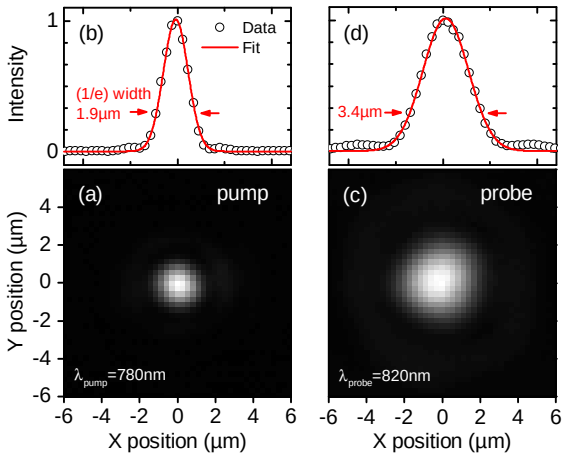

Figure 20: Characterization of the spatial resolution of the Kerr microscope for the time-resolved measurement configuration using the supercontinuum source. **(a,c)** CMOS camera images of the focused pump and probe laser spots. **(b,d)** Normalized intensity profiles of the pump and probe laser obtained from line cuts through the CMOS camera images. Red solid lines are Gaussian fits from which we determine the spatial resolution of the instrument.

wavelength $\lambda_{\text{pump}} = 780\,\text{nm}$ and a probe wavelength $\lambda_{\text{probe}} = 820\,\text{nm}$ which are subsequently used in the majority of measurements presented in this work.

We first consider the spatial resolution for the time-resolved measurement configuration using the supercontinuum source. In Figs. 20 (a,c) we show CMOS camera images of the focused pump and probe spots. Line cuts through the center of the radial symmetric intensity profiles are shown in Figs. 20 (b) for the pump and (d) for the probe spot. The intensity profiles $I(r)$ are well described by Gaussians:

$$I(r) = I_0 \times \exp\left(-\frac{r^2}{\Delta^2}\right) \tag{5.9}$$

where I_0 is the maximum intensity and Δ the $(1/e)$ half width of the spots. Gaussian fits of the intensity profiles shown in Figs. 20 (b,d) yield $\Delta_{\text{pump}} = 0.95\,\mu\text{m}$ and $\Delta_{\text{probe}} = 1.7\,\mu\text{m}$ for the pump and probe beam. The increased probe spot width is mainly caused by the additional passage of the two aspheric scanning lenses. We have verified that the determination of spot widths from CMOS camera images yields identical results as the conventional knife-edge scan technique [68].

The net optical resolution Δ of the microscope is determined by the convolution of both intensity profiles. From the convolution of the Gaussian intensity profiles we obtain a spatial resolution:

$$\Delta_{\text{tr}} = \sqrt{\Delta_{\text{probe}}^2 + \Delta_{\text{pump}}^2} = 1.9\,\mu\text{m} \tag{5.10}$$

for the time-resolved instrument configuration. Following a similar approach, we also determine the spatial resolution of the Kerr microscopy setup for the cw configuration using the Ti:Sa lasers. We here measure the spatial extent of the focused pump and probe laser spots as $\Delta_{\text{pump}} = 0.7\,\mu\text{m}$ and $\Delta_{\text{probe}} = 1.2\,\mu\text{m}$. From convolution the net optical resolution of the setup for cw microscopy is therefore:

$$\Delta_{\text{cw}} = 1.4\,\mu\text{m} \tag{5.11}$$

The higher spatial resolution for the cw configuration stems from a slightly more ideal illumination of the focussing microscope objective aperture by the Ti:Sa laser beams. In principle, the spatial resolution for the time-resolved configuration could be further enhanced by optimizing the pulsed pump and probe beam diameters using additional beam expanders at the cost of introducing additional complexity to the setup.

Time resolution

Dispersion in the tapered fiber leads to a significant prolongation of the initial $\lesssim 300\,\text{fs}$ infrared pump pulse. As a result the total duration of the supercontinuum pulse is of the order of 5 ps. However, as revealed by cross-correlation frequency-resolved optical gating (XFROG) characterization [152], the temporal width of the arrival time distribution of individual spectral components of a supercontinuum with bandwidths comparable to our filtered pump and probe laser beams is typically of the order of 500 to 1500 fs [143, 153]. From this consideration we expect an overall time resolution of $\approx$ 2-3 ps for our pump-probe MOKE microscope.

The comparatively weak intensities of the filtered pump and probe beams impede auto-correlation and XFROG measurements of the respective pulse lengths for the direct determination of the time resolution of our instrument. As an alternative we determine an upper bound for the time resolution by observing the very fast initial rise of the transient Kerr rotation signal following the pulsed optical spin excitation. This approach has the advantage of being available in situ, i.e. it does not require any modification of the experimental setup or additional equipment, and considers all optical components of the Kerr microscope in its operational configuration which could potentially impair the time resolution of the instrument.

In Fig. 21 we show a typical time trace of the Kerr rotation $\theta_K(\Delta t)$ which we measure on a MBE-grown GaAs epilayer (200 nm layer thickness; grown on (001)-oriented semi-insulating GaAs substrate) for short delays between −4 ps and 4 ps. The sample temperature is $T_L = 8\,\text{K}$. For the detection of the Kerr rotation transient the probe laser is tuned to the bulk GaAs excitonic resonance at $\lambda_{\text{probe}} = 820\,\text{nm}$. The pump wavelength is $\lambda_{\text{pump}} = 780\,\text{nm}$.

Following the pulsed excitation at $\Delta t = 0\,\text{ps}$ we observe a very steep rise of the Kerr rotation $\theta_K(\Delta t)$. This experimentally observed Kerr rotation transient is a convolution of the actual step-like rise of the Kerr rotation with the temporal pump and probe pulse profiles. To determine the time resolution of our MOKE microscope we therefore

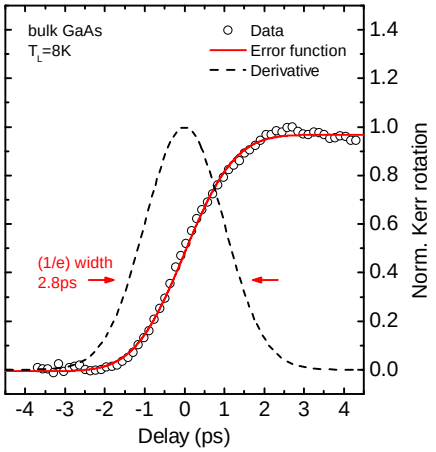

Figure 21: Characterization of the time resolution of our pump-probe MOKE microscope. Transient Kerr rotation $\theta_K(\Delta t)$ measured in a GaAs MBE epilayer at $T_L = 8\,\mathrm{K}$ (black markers). The red solid line is a Gaussian error function fit from which we deduce the instruments time resolution. The black dashed line shows the normalized derivative of the fit to visualize the temporal width of the error function fit.

describe the resolution-limited observation of the initial Kerr rotation transient by a Gaussian error function:

$$\theta_K(\Delta t) = \theta_{K,\max}\left[1+\mathrm{erf}\left(\frac{\Delta t}{w_t}\right)\right]/2 \tag{5.12}$$

where $\theta_{K,\max}$ is the maximum Kerr rotation amplitude. The error function width w_t describes the experimentally observed finite Kerr rotation rise time. In Fig. 21 we show a fit of the model Eq. 5.12 from which we obtain:

$$w_t = (2.8 \pm 0.1)\,\mathrm{ps} \tag{5.13}$$

This temporal width w_t is a direct measure of an upper bound of our instrumental time resolution, since the experimentally observed rise time of the excitonic Kerr rotation transient not only depends on the pump and probe pulse lengths, but also includes the finite time of to the built-up of the excitonic Kerr rotation in the sample.

Absolute Kerr angle calibration for continuous-wave spectroscopy

In the later course of this work we use cw MOKE microscopy to quantitatively measure the local Kerr rotation angle $\theta_K(r)$. We therefore carry out an additional calibration procedure to enable direct measurements of θ_K using the lock-in detection scheme described in section 5.1.2. We have conceived a calibration technique which evokes a sinusoidal photoreceiver signal whose amplitude can be related to a known variable reference angle. From this calibration measurement we determine the conversion coefficient g_{LI} which from Eq. (5.8) directly relates the lock-in output voltage V_{LI} to the

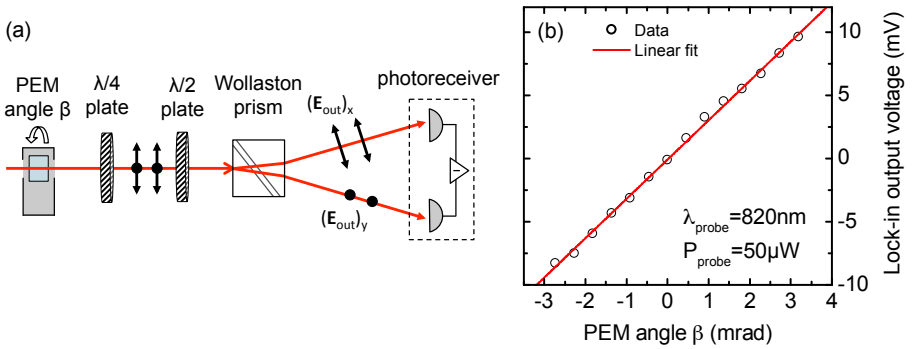

Figure 22: Calibration procedure for quantitative lock-in measurements of absolute Kerr rotation angles. **(a)** Schematic of the calibration setup. The vertically polarized probe laser is passed through a PEM whose fast axis is tilted by a small variable angle β with respect to the horizontal. The peak phase retardation of the PEM is $\delta_0 = \pi$. The PEM is followed by a $(\lambda/4)$ wave plate with vertical fast axis and a Soleil-Babinet compensator set to half-wave retardation (drawn as $(\lambda/2)$ plate). The fast axis of the compensator is tilted by 22.5° to the vertical. The vertical and horizontal polarization components of the modulated probe beam are split by a Wollaston prism and detected by the balanced photoreceiver. **(b)** Lock-in output voltage V_{out} as a function of the PEM tilt angle β (open markers) together with a linear fit (red line).

product of the probe laser power and the absolute value of the Kerr rotation angle.

The calibration scheme is specifically implemented such that the calibration signal can be demodulated on the fundamental PEM frequency $(\omega_{\text{ref}}/2\pi)$. It is important to employ a calibration procedure which involves lock-in demodulation on the same frequency which is subsequently used for the actual Kerr rotation measurements: The bandwidth of transimpedance amplifiers commonly used in MOKE spectroscopy experiments is typically $\lesssim 100\,\text{kHz}$, i.e. it is comparable to the second harmonic of the PEM modulation frequency. A comparatively low bandwidth is purposefully used to suppress the unintentional amplification of high frequency noise components which are detrimental to the Kerr rotation measurement. However, the conversion coefficient g_{LI} therefore depends on ω_{ref} and significantly decreases for higher modulation frequencies. It is therefore essential to perform the calibration for the identical modulation frequency later used in the actual MOKE measurements.

A schematic of the calibration setup is shown in Fig. 22 (a). The vertically polarized probe laser is passed through a PEM whose fast axis is tilted with respect to the horizontal by a small variable angle β. The PEM is attached to a mechanical mount which allows for precise manipulation of the tilt angle β by a micrometer screw.

The peak phase retardation of the PEM is set to $\delta_0 = \pi$. The PEM is followed by a NIR broadband $(\lambda/4)$ wave plate with a vertically oriented fast axis and a Soleil-Babinet compensator set to half-wave retardation. Similar to the MOKE measurement configuration, the fast axis of the compensator is tilted by 22.5° to the vertical. The

horizontal and vertical polarization components of the probe beam are split by the Wollaston prism and their intensity difference is detected by the balanced photoreceiver.

The time dependence of the modulated polarization state of the probe laser after passing the Soleil-Babinet compensator is:

$$\mathbf{E}_{\text{out}} = \frac{E_0}{\sqrt{2}} \begin{pmatrix} e^{i\beta}\left[i\cos(\beta) + e^{i\delta}\sin(\beta)\right] \\ e^{-i\beta}\left[i\cos(\beta) - e^{i\delta}\sin(\beta)\right] \end{pmatrix} \tag{5.14}$$

where $\delta = \delta_0 \sin(\omega_{\text{ref}} t)$ is the momentary PEM retardation phase. The time-dependent photoreceiver output voltage $V_{\text{out}} = g_{\text{LI}}(I_x - I_y)$ is:

$$V_{\text{out}}(t) = g_{\text{LI}} |E_0|^2 \sin(2\beta) \sin\Big(\delta_0 \sin[\omega_{\text{ref}} t]\Big) \tag{5.15}$$

Finally, using the Jacobi-Anger expansion Eq. (5.6), we obtain for lock-in demodulation on the fundamental PEM frequency $(\omega_{\text{ref}}/2\pi)$ and small calibration angles $|\beta| \ll 1$, i.e. for $\sin(2\beta) \approx 2\beta$:

$$V_{\text{LI}} = \Big(4 g_{\text{LI}} |E_0|^2 J_1(\pi)\Big)\, \beta \tag{5.16}$$

To determine the conversion coefficient g_{LI} we measure the lock-in output voltage V_{LI} as a function of the PEM tilt angle β. To precisely replicate the conditions subsequently used in the MOKE measurements we carry out the calibration using the full MOKE microscopy configuration. We therefore place the additional PEM and $(\lambda/4)$ wave plate in the probe beam path directly in front of the Soleil-Babinet compensator. The probe beam is focussed on the surface of the sample which is kept at room temperature (thereby acting as a passive mirror), and the calibration measurement is performed using the reflected probe laser beam. The result of the calibration procedure is shown in Fig. 22 (b) for $\lambda_{\text{probe}} = 820\,\text{nm}$ and a probe power of $50\,\mu\text{W}$ which are later used for our spatially resolved cw MOKE measurements. From the slope of a linear fit we determine from Eq. (5.16) the conversion coefficient as:

$$g_{\text{LI}} = (54.7 \pm 0.1)\,\mu\text{V}\,\text{mrad}^{-1}\,\mu\text{W}^{-1} \tag{5.17}$$

Under typical experimental conditions used for our cw MOKE spectroscopy measurements, we are able to detect Kerr rotation changes which correspond to lock-in output voltage differences $\Delta V_{\text{out}} \approx 10\,\mu\text{V}$. Using Eqs. (5.8) and (5.17) we therefore can estimate an angular resolution:

$$\Delta\theta_K \lesssim 2 \times 10^{-6}\,\text{rad} \tag{5.18}$$

of our Kerr microscope for cw MOKE spectroscopy with a $50\,\mu\text{W}$ focussed probe beam.

5.2 Microphotoluminescence setup

Photoluminescence spectroscopy allows for an efficient and reliable identification and determination of the energetic position of the excitonic resonances which are relevant

for the subsequent MOKE electron spin detection. We therefore routinely use standard cw PL spectroscopy for an auxiliary pre-characterization of our samples before performing Kerr microscopy measurements. In the course of this work we additionally use microphotoluminescence (μ-PL) spectroscopy for the measurement of the local steady-state electron temperature profile $T_e(r)$ under cw optical excitation. In the following we provide a short overview of the employed PL instrumentation and briefly describe the fundamental working principle of spatially resolved PL detection.

5.2.1 Instrumentation

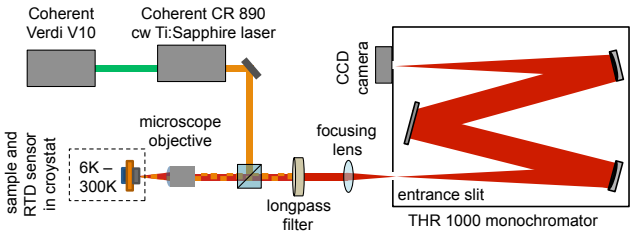

Figure 23: Schematic of the microphotoluminescence (μ-PL) spectroscopy setup. The setup is operated in confocal geometry, i.e. a magnified image of the PL emitted from the sample surface is formed in the entrance slit plane of the monochromator. When operating the monochromator in diffraction-less zero-order mode this image directly translates on the CCD array detector. When using the standard first-order diffraction mode, wavelength dispersion only affects the horizontal direction while the spatial information along the vertical axis, i.e. parallel to the entrance slit, is retained.

A schematic diagram of the main components of our μ-PL setup is shown in Fig. 23. Tunable optical excitation is provided by the same Coherent CR 890 Ti:Sa which we also use for cw MOKE spectroscopy. The Ti:Sa laser beam is therefore routed to the remote PL laboratory either using a single-mode optical fiber or in standard free-space configuration (omitted in Fig. 23). When using the free-space configuration the pointing stability of the laser is actively controlled by a TEM Messtechnik Aligna automated laser beam alignment and stabilization system.

The sample is clamped on the cold finger of a Cryovac Konti-Cryostat-Mikro liquid He flow optical microscopy cryostat. The sample temperature can be varied from 5 K to 300 K and is monitored by a calibrated Cernox RTD sensor attached next to the sample. The laser is focused by a Mitutoyo 20x plan apochromatic microscope objective ($f = 10\,\mathrm{mm}$, NA $= 0.4$) on the sample surface. The luminescence is collected by the same microscope objective and focussed by a $f = 250\,\mathrm{mm}$ lens on the entrance slit of a Jobin Yvon THR 1000 monochromator. An additional dielectric longpass filter is used to suppress backscattering of the laser light into the spectrometer. The luminescence is analyzed by the 1000 mm focal length Czerny-Turner spectrometer which is equipped with a NIR-blazed $1200\,\mathrm{mm}^{-1}$ grating and a liquid nitrogen-cooled Princeton Instruments CCD-array detector. The spectrometer is calibrated using characteristic Kr and

Xe gas emission lines.

5.2.2 Spatially resolved photoluminescence detection

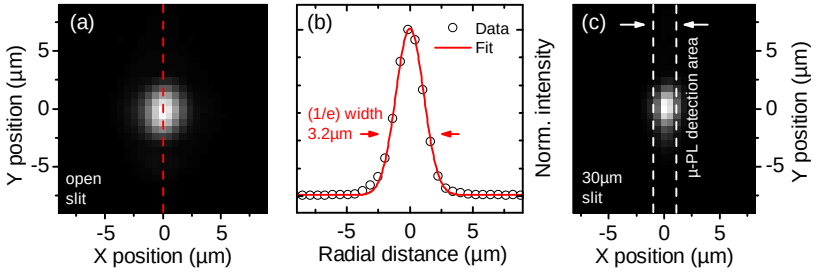

Figure 24: Characterization of the pump laser spot size for μ-PL spectroscopy. Axis labels correspond to distances on the sample surface. **(a)** Zero-order mode CCD camera image of the focused laser spot with open monochromator entrance slit. **(b)** Vertical line cut of the laser spot intensity profile (open markers) with Gaussian fit (red line) as indicated in (a). **(c)** Zero-order CCD image of the focused pump laser spot with monochromator entrance slit closed to 30 µm. The vertical dashed lines indicate the horizontal width of the μ-PL detection area.

The setup is operated in confocal geometry, i.e. an image of the PL emitted from the sample surface is formed in the entrance slit plane of the monochromator. When operating the spectrometer in diffraction-less zero-order mode, this image directly translates on the CCD array detector. In Fig. 24 (a) we show a CCD camera image of the focused laser spot which we record with a completely opened monochromator entrance slit. For the $(250\,\text{mm}/10\,\text{mm}) = (\times 25)$ magnification factor of the PL setup and the 15 µm square pixel size of the sensor, one CCD pixel corresponds to a distance of 0.6 µm on the sample surface. We therefore directly determine the pump spot size from a Gaussian fit to the vertical intensity profile shown in Fig. 24 (b). The $(1/e)$ half width:

$$\Delta_{\text{PL}} = 1.6\,\mu\text{m} \tag{5.19}$$

of the excitation laser spot closely coincides with the net optical resolution $\Delta_{\text{cw}} = 1.4\,\mu\text{m}$ of the cw MOKE microscope configuration. This allows for a direct comparison of results obtained from μ-PL spectroscopy and cw Kerr microscopy.

For μ-PL spectroscopy the setup is aligned such that the image of the focused pump spot is centered on the monochromator entrance slit. The entrance slit is closed to a width of 30 µm, i.e. below the horizontal extent of the magnified pump spot image. The CCD camera then detects a narrow vertical line cut of the PL image as illustrated in Fig. 24 (c). When using the monochromator in standard first-order mode, wavelength dispersion only affects the horizontal direction while the full spatial information along the vertical axis, i.e. parallel to the entrance slit, is retained. Individual rows of the CCD array sensor then contain PL spectra emitted from specific sample positions while individual columns correspond to PL intensity profiles emitted at different wavelengths.

Chapter 6

Samples

In this chapter we introduce the samples which are investigated in the present work. We describe four samples, two bulk n-doped GaAs epilayers and two GaAs-based QW structures. The bulk GaAs samples were provided by D. Reuter and A. D. Wieck.[6] The QW samples were grown by K. Biermann and P. V. Santos.[7] In the following we first provide for each sample a description of the heterostructure layer sequence. We then use standard cw PL spectroscopy to identify the optical transitions which are relevant to the following MOKE microscopy measurements.

6.1 Bulk n-GaAs samples

Sample 11889 is a 1 µm n-type GaAs epilayer grown by molecular beam epitaxy (MBE) on a (001)-oriented GaAs substrate. The sample structure consists of a 50 nm undoped GaAs buffer layer, a ten-period GaAs/AlAs superlattice with a period of 5 nm GaAs + 5 nm AlAs, followed by a second 50 nm undoped GaAs layer and the 1 µm Si-doped n-GaAs layer. The superlattice is grown to getter segregating unintentional impurities from the substrate. It also confines the photoexcited carriers to the top 1 µm GaAs layer by suppressing diffusion into the substrate. The room temperature electron density and mobility of the epilayer are $n = 1.4 \times 10^{16}\,\mathrm{cm}^{-3}$ and $\mu = 5500\,\mathrm{cm}^2\,\mathrm{V}^{-1}\,\mathrm{s}^{-1}$ as determined by standard van-der-Pauw characterization. We found that additional above-bandgap illumination of the sample does not significantly change the charge mobility at room temperature. The donor concentration is chosen such that the expected low-temperature electron spin relaxation times are maximal for bulk GaAs [84] to facilitate the following MOKE microscopy measurements. We note that this sample is intentionally chosen to be very similar in both layer thickness and donor concentration to bulk GaAs samples which have been the subject of numerous previous spatially resolved Kerr and Faraday rotation spectroscopy studies [14–16, 30–33, 68].

Sample 12464 also is a MBE-grown 1 µm n-type GaAs epilayer. In contrast to sample 11889, here the layer under investigation is buried between two n-doped $Al_xGa_{1-x}As$ barriers to avoid a possible charge carrier depletion resulting from the direct transition from the epilayer surface to the vacuum. Growth of sample 12464 is initiated on a

[6] Institut für angewandte Festkörperphysik, Ruhr-Universität Bochum, 44780 Bochum, Germany
[7] Paul-Drude-Institut für Festkörperelektronik, 10117 Berlin, Germany

(001)-oriented GaAs substrate by an undoped 5 nm GaAs layer, followed by 100 nm of Si-doped $Al_{0.34}Ga_{0.66}As$ and an additional intrinsic 100 nm $Al_{0.34}Ga_{0.66}As$ layer. The following 1 µm thick Si-doped bulk GaAs epilayer is covered by the same AlGaAs barrier sequence grown in reverse order. Both $Al_xGa_{1-x}As$ barriers restrict the motion of the spin polarized electrons to the investigated epilayer by inhibiting diffusion of the photocarriers into the substrate. The top barrier is followed by 200 nm of GaAs and 10 nm of AlAs. The sample is capped by an additional 10 nm GaAs layer to prevent oxidation of the $Al_xGa_{1-x}As$. The room temperature electron density and mobility of the n-GaAs layer have been determined by van-der-Pauw characterization as $n = 9.4 \times 10^{15}\,\mathrm{cm}^{-3}$ and $\mu = 6200\,\mathrm{cm}^2\,\mathrm{V}^{-1}\,\mathrm{s}^{-1}$. Again, at room temperature no significant change of the mobility is observed when illuminating the sample.

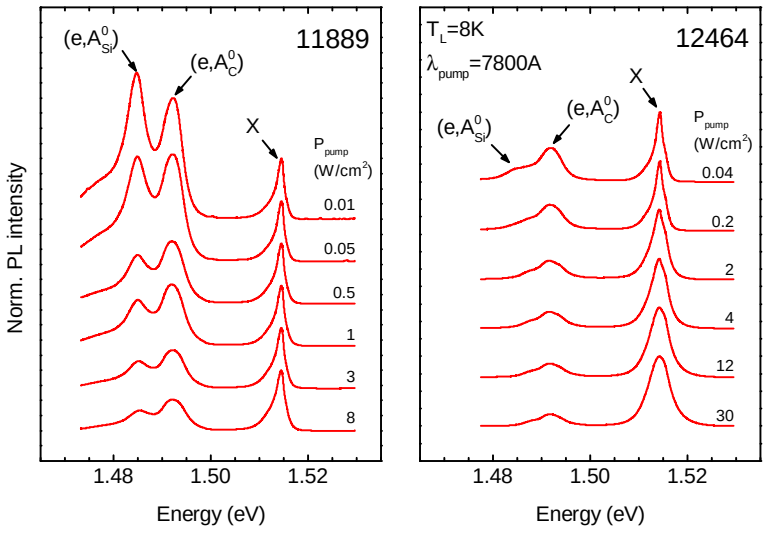

Figure 25: Pump power dependence of the cw PL spectra of the bulk n-GaAs samples 11889 (left) and 12464 (right) measured at $T_L = 8\,\mathrm{K}$. The excitation wavelength is $\lambda_{\mathrm{pump}} = 7800\,\text{Å}$. Text labels indicate the excitonic (X) and defect-related (e,A^0) transitions.

In Fig. 25 we show cw PL spectra of both bulk GaAs samples measured at $T_L = 8\,\mathrm{K}$ for different excitation densities. The excitation wavelength is $\lambda_{\mathrm{pump}} = 7800\,\text{Å}$. For both samples three distinct PL bands are observed. The high energy peak (X) centered at $\approx 1.515\,\mathrm{eV}$ is due to the recombination of excitonic complexes [154]. It consists of PL originating from the recombination of free excitons [(FX), 1.513-1.515 eV)], neutral donor-bound excitons [(D^0,X), 1.5141 eV], and excitons bound to charged donors [(D^+,X), 1.5133 eV] [49]. These transitions are not resolved as individual peaks because of the comparatively high defect density of the samples. However, from the energetic position of the PL maximum we infer that for the excitation densities employed in this work the majority of the excitonic PL originates from (D^0,X) recombination. This assignment, consistent with the strong Si n-doping of the sample, is corroborated by

additional polarization-resolved PL measurements where we observe a strong decrease of the PL circular polarization degree in the spectral vicinity of the excitonic PL intensity maximum (not shown here). This vanishing of the zero-field circular polarization degree is characteristic of the spin singlet state formed by the two electrons which constitute the (D^0,X) complex [67].

At lower photon energies we observe for both samples two distinct PL bands which are related to recombination of holes bound to neutral shallow acceptors [154]. The first peak at 1.493 eV is due to the recombination of free conduction band electrons with carbon acceptor-bound holes, the (e,A^0_{C}) transition [49]. At a slightly lower photon energy of 1.485 eV we observe the (e,A^0_{Si}) transition which involves the $\mathrm{Si}_{\mathrm{As}}$ acceptor [49]. Observation of this transition, again, is expected from the amphoteric Si dopant used for the n-doping of the bulk GaAs samples. Additionally, for both electron-acceptor transitions a low-energy shoulder is observed. This shoulder stems from the (D^0,A^0) recombination of Si donor-bound electrons with acceptor-bound holes which occurs at 1.4892 eV and 1.4816 eV for the carbon and silicon acceptor, respectively [49]. The relative decrease of the defect-related PL intensity with respect to the excitonic luminescence with increasing excitation density observed in Fig. 25 is caused by saturation of the finite number of acceptor states for higher photocarrier densities.

6.2 Quantum well samples

Sample M4_2661 is an intentionally undoped 5x GaAs multiple quantum well (MQW) structure. We have chosen a MQW structure for our MOKE microscopy investigation to enhance the absorption of pump light for below-barrier optical spin injection and to facilitate the detection of the expected small Kerr rotation signals. MBE growth was initiated on a (110)-oriented GaAs substrate by a 200 nm GaAs buffer layer. The buffer is followed by a 500 nm $\mathrm{Al}_{0.15}\mathrm{Ga}_{0.85}\mathrm{As}$ layer and a series of five intrinsic GaAs QWs, each with a width of 20 nm. The QWs are embedded in 64 nm wide $\mathrm{Al}_{0.15}\mathrm{Ga}_{0.85}\mathrm{As}$ barriers. The sample is capped by 120 nm of $\mathrm{Al}_{0.15}\mathrm{Ga}_{0.85}\mathrm{As}$ followed by a top 2 nm GaAs layer.

In Fig. 26 (a) we show PL spectra of sample M4_2661 which we measure at $T_L = 8\,\mathrm{K}$ for different pump intensities. The excitation wavelength is $\lambda_{\mathrm{pump}} = 7850\,\text{Å}$. For very low excitation powers the PL spectrum is dominated by the (1E-1HH) electron-heavy hole transition which occurs between 1.521-1.524 eV. With increasing pump power we additionally observe the first (1E-1LH) electron-light hole transition at 1.528 eV. At high excitation densities, additional PL occurs around ≈ 1.514 eV which originates from the GaAs substrate or the bulk GaAs buffer layer.

Careful inspection of the PL spectrum for the lowest excitation power reveals a fine-structure of the (1E-1HH) transition. In Fig. 26 (a) we identify three individual transitions labeled A to C. Peak A observed at the highest energy of 1.524 eV is attributed to the recombination of free heavy hole excitons. Peaks B and C at 1.523 eV

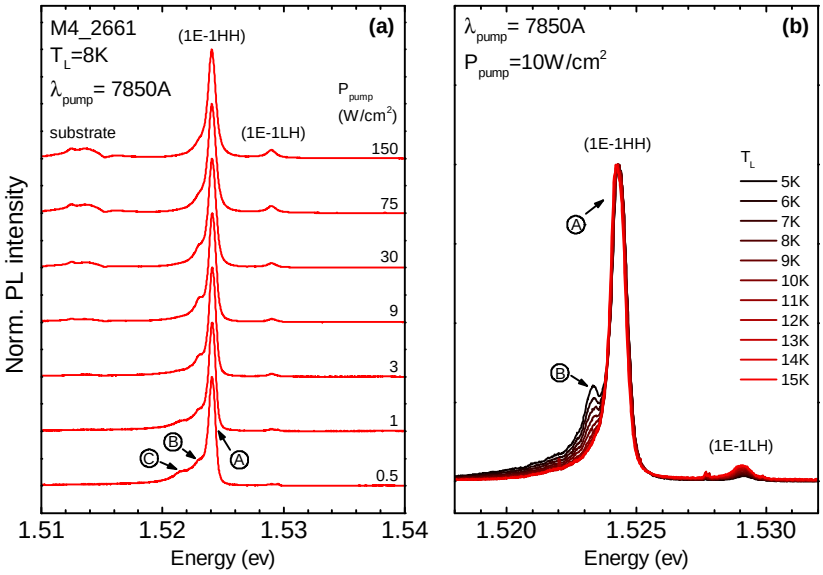

Figure 26: Continuous-wave PL spectra of sample M4_2661. **(a)** Pump power dependence measured at $T_L = 8\,\mathrm{K}$. The excitation wavelength is $\lambda_{\mathrm{pump}} = 7850\,\text{Å}$. Text labels A to C indicate different transitions in the fine structure of the (1E-1HH) PL. **(b)** Rapid quenching of the PL of transition B with increasing lattice temperature T_L.

and 1.521 eV might result from the recombination of localized or defect-bound excitons which saturate with increasing excitation density.

For peak B, however, an alternative transition is more likely. In our MOKE studies presented later we find that the (110) QW sample exhibits very long out-of-plane electron spin lifetimes $T_s^z \gtrsim 20\,\mathrm{ns}$ [compare Fig. 47 (b)]. This observation strongly suggests the presence of a dilute 2DEG in the nominally undoped QWs. For low excitation densities peak B therefore might result from the recombination of negatively charged trions (X^-) which can form from optically excited neutral excitons in the presence of excess electrons [155–157]. Refs. [158, 159] report trion binding energies $E_b^{X^-} = 1.3\,\mathrm{meV}$ for GaAs QWs of identical widths as our sample. This binding energy coincides with the separation between the exciton peak A and peak B observed in our PL measurements.

Our interpretation that transition B originates from the (X^-) negative trion recombination is corroborated by the PL measurements shown in Fig. 26 (b) where we investigate the dependence of the QW PL on the lattice temperature for a moderate excitation density of $10\,\mathrm{W\,cm^{-2}}$. At low $T_L = 5\,\mathrm{K}$ we observe peak B as a strong transition on the low-energy side of the (1E-1HH) PL. The luminescence from peak B, however, rapidly diminishes with increasing temperature and completely vanishes for $T_L \gtrsim 15\,\mathrm{K}$. At this temperature $k_B T_L \gtrsim E_b^{X^-}$, i.e. the thermal energy exceeds the trion binding energy and the trion becomes unstable. A similar temperature dependent quench of the trion luminescence has been reported previously for GaAs QWs [160, 161] which further

substantiates or assignment.

As a side note we additionally observe the expected increase of the relative intensity of the (1E-1LH) luminescence with increasing T_L. This rise of the (1E-1LH) PL stems from the growing thermal occupation of the first light hole valence subband with increasing temperature.

Sample M4_2807 is a MBE-grown heterostructure which contains a high mobility 2DEG embedded in a symmetric modulation-doped 20 nm wide GaAs QW. The QW is confined on both sides by short-period GaAs/AlAs superlattices. The sample design is optimized for the investigation of electron spin dynamics in a degenerate two-dimensional electron system with very high elastic mean free paths. The complex sample structure results from the aim to achieve the highest possible electron mobilities in a symmetric QW system.

Growth is initiated on a (001)-oriented GaAs substrate by a 500 nm GaAs buffer layer, followed by 137 nm $Al_{0.4}Ga_{0.6}As$, 200 nm GaAs, and 50 nm AlAs. Grown on top are 100 nm beryllium-doped GaAs (Be concentration 5×10^{15} cm^{-3}), 455 nm $Al_{0.4}Ga_{0.6}As$, 2.7 nm GaAs, 1.8 nm AlAs, 2.4 nm GaAs, and 1.8 nm AlAs. The bottom Si-delta doping film with a Si sheet density of 1.7×10^{12} cm^{-2} is grown in the center of the last GaAs layer, in a distance of ≈ 100 nm to the QW center.

The above layers are followed by the first 83.6 nm wide GaAs/AlAs short-period superlattice. The superlattice consists of alternating layers of 2.7 nm thick GaAs and AlAs layers of variable thickness which gradually decreases from 1.8 nm to 0.7 nm. The 2DEG is confined to the following 20 nm undoped GaAs layer which is topped by an identical short-period superlattice grown in reverse order. This top superlattice is followed by 1.8 nm AlAs and a 2.4 nm GaAs layer which contains the top Si delta-doping film with a Si sheet density of 1.9×10^{12} cm^{-2}.

Growth of the sample is finished by an additional 50 nm $Al_{0.4}Ga_{0.6}As$ layer, two periods of 2 nm thick GaAs layers which both at their center contain Si delta-doping films with a Si sheet density of 1.5×10^{12} cm^{-2}, and a top 1 nm GaAs capping layer.

The temperature dependence of the electron density and the charge mobility of the 2DEG have been determined by standard Hall characterization. The charge mobility is $\mu_c = 1 \times 10^6$ cm^2 V^{-1} s^{-1} at 4.2 K and monotonically decreases to 8×10^3 cm^2 V^{-1} s^{-1} at room temperature. The electron density $n_s = 2.2 \times 10^{11}$ cm^{-2} is constant within $\pm 5\,\%$ over the whole examined temperature range.

In Fig. 27 (a) we show cw PL spectra of sample M4_2807 which we measure at $T_L = 5$ K for different excitation densities. Contrary to our previous PL measurements on the MQW sample M4_2661, we here choose a short pump wavelength $\lambda_{\text{pump}} = 4440$ Å which excites electron-hole pairs in the GaAs/AlAs superlattice barrier. These photocarriers relax into the QW where they recombine radiatively. We use above-barrier excitation because for sample M4_2807 the absorption in the QW volume for below-barrier excitation is very weak which aggravates the observation of the 2DEG luminescence.

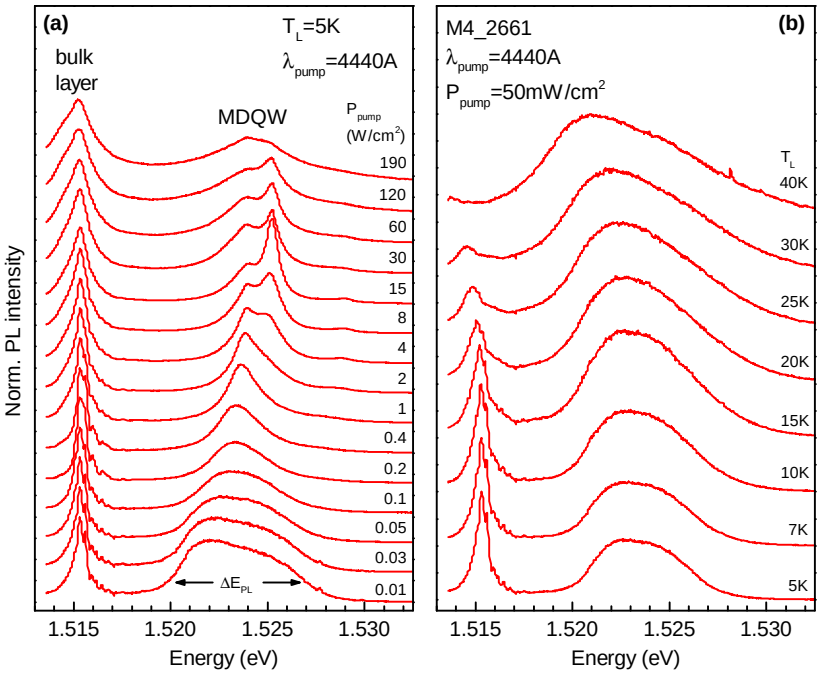

Figure 27: Continuous-wave PL spectra of sample M4_2807. **(a)** Pump power dependence measured at $T_L = 8\,\mathrm{K}$. The excitation wavelength is $\lambda_{\mathrm{pump}} = 4400\,\text{Å}$, i.e. photocarriers are excited above the GaAs/AlAs short-period superlattice band gap. **(b)** Photoluminescence spectra for different lattice temperatures T_L.

In undoped QWs the absorption and luminescence properties are dominated by the excitonic resonances which occur as sharp peaks in the optical spectra (compare Fig. 26). In strongly modulation-doped QWs (MDQWs), however, exciton formation is suppressed because of screening of the Coulomb interaction between photocreated electron-hole pairs and phase space filling effects [162, 163]. Instead, the PL of n-MDQWs can be understood qualitatively in terms of band-band-transitions which occur between photocreated holes which relax to the valence band maximum and the CB electron states which are filled up to the level defined by the Fermi energy E_F.

For very weak excitation we observe in Fig. 27 (a) the broad PL spectrum which is characteristic of strongly modulation-doped QWs [157, 164, 165]. The additional low-energy PL observed around 1.515 eV is attributed to excitonic transitions in the bulk 100 nm GaAs layer of the MBE heterostructure[8]. The spectral width $\Delta E_{PL} \approx 7\,\mathrm{meV}$

[8] In analogy to Ref. [166] we observe signatures of exciton center-of-mass quantization in the high-energy flank of the bulk GaAs PL peak (not shown here). This observation suggests that the bulk PL signal is mainly due to radiative recombination in the thin 100 nm GaAs layer enclosed in two AlAs and $Al_xGa_{1-x}As$ barriers.

of the QW PL band which occurs between $\approx 1.520\,\mathrm{eV}$ and $1.527\,\mathrm{eV}$ is in good agreement with the electron Fermi energy $E_F = (\hbar^2 \pi n_s)/m_e^* = 7.8\,\mathrm{meV}$ which we calculate for the electron density n_s obtained from the Hall measurement and an effective mass $m_e^* = 0.067 m_0$. The high energy part of the PL directly reflects the occupation of the CB electronic states in the vicinity of the Fermi edge and allows for the optical determination of the electron temperature of the 2DEG [37, 157]. The expected broadening of the electron Fermi distribution with increasing T_e is observed in Fig. 27 (b) where we show the QW PL for low excitation densities at different lattice temperatures up to 40 K.

With increasing excitation density a marked transition of the QW PL occurs. We first observe a slight decrease of the Fermi energy as a redshift of the high-energy PL cutoff. Next, a first PL peak develops at 1.5240 eV. When further increasing the excitation density, a second sharp PL peak appears at 1.5255 eV which dominates the PL spectrum for moderate excitation densities. The appearance of this peak is correlated with the observation of an additional weak luminescence signal at 1.5290 eV. For very high excitation densities the QW PL again evolves into a broad, comparatively structureless band.

The observed changes in the PL spectrum are suggestive of a strong optically induced change in the MDQW 2DEG density, i.e. of optical gating [167]. We propose that the transformation of the PL line shape is due to different capturing efficiencies for electrons and holes from the superlattice barriers into the QW. We suppose that the hole capturing process is more efficient, i.e. that above-barrier illumination preferentially creates holes in the QW. The reduced electron capture efficiency is due to the potential barrier for electrons in the CB formed by the modulation doping. An increase of the excitation power then leads to a reduction of the 2DEG density due to recombination of the resident electrons with the photocreated holes. This process effectively transfers electrons from the 2DEG back into to doping layer [168].

For low excitation densities the decrease of the electron density leads to the observed shift of the PL Fermi edge towards lower energies. When further decreasing the electron density by raising the excitation power, the negatively charged trion (X^-) becomes stable which we observe as the low-energy peak at 1.5240 eV. For higher excitation, the density of photocreated holes approaches the total electron density and neutral exciton formation is favored. In this case the PL spectrum is dominated by the heavy hole exciton luminescence which we observe at 1.5255 eV. The weak luminescence signal at 1.5290 eV is attributed to the light hole exciton. The origin of the observed broadening of the MDQW PL at very high excitation densities is not clear, but might possibly be due to electron-hole plasma recombination.

Part III

Results and discussion

Chapter 7

Continuous-wave spectroscopy

In this chapter we present our experimental results on cw electron spin MOKE microscopy. We demonstrate that at low lattice temperatures the influence of hot photocarriers on these measurements is twofold. Optically excited hot carriers affect both the measurement technique, the magneto-optical spin detection, and the subject of investigation, the electron spin transport processes.

We first establish that a spatial temperature gradient in the electron system, a byproduct of the nonresonant optical spin injection by the pump laser, locally disturbs the magneto-optical coefficient which links the electron spin polarization to the experimental observable, the Kerr rotation. As a consequence and contrary to the common assumption, MOKE microscopy performed using a single arbitrary probe wavelength therefore in general does not correctly reveal the true electron spin polarization profile.

Instead, for bulk GaAs we determine the local excitonic spin splitting energy by analyzing the spatial dependence of the full excitonic Kerr rotation spectrum. From the local excitonic spin splitting we obtain the true lateral electron spin polarization profile. Moreover we demonstrate that our analysis additionally yields full information on the local electron temperature. For the examined sample we further find that the true electron spin profile is also observed by measuring the local Kerr rotation when the probe laser energy is tuned far below the excitonic resonance.

Having established reliable ways to correctly measure the the local electron spin polarization in bulk GaAs, we next consider the influence of hot carriers on the electron spin diffusion process. We here synthesize our previous work on hot electron spin diffusion [80, 101] and our newly gained insights on the elimination of hot carrier effects in the spatially resolved MOKE spin detection. Owing to the high kinetic energy of the photoexcited electrons, the spin transport properties observed in low-temperature optical spectroscopy strongly deviate from the intrinsic properties of the examined system. We present a modified spin diffusion model which includes this hot carrier effect. From a combination of Hanle-MOKE measurements of the spin relaxation time and cw MOKE microscopy of steady-state spin diffusion we determine the intrinsic temperature dependence of the electron spin diffusion coefficient of a bulk n-GaAs sample.

We last examine the steady-state MOKE electron spin detection in QW 2DEGs. Similar to the case of bulk GaAs, we find that at low T_L a strong local modification of

the Kerr rotation spectrum prevents reliable cw MOKE microscopy. Moreover, for the examined (110) QWs the significantly more complex energetic structure of the optical transitions impedes a quantitative analysis of the Kerr rotation spectrum. Instead, we propose to measure the electron spin diffusion coefficient by picosecond real space imaging of optically excited electron spin packets using a spectrally broad probe pulse. These time-resolved measurements are the subject of the following chapter.

7.1 Hot carrier effects on the magneto-optical electron spin detection in bulk GaAs

7.1.1 Statement of the problem

Pump-probe MOKE spectroscopy and the related spin noise spectroscopy both infer information on the electron spin system of semiconductors by measuring small changes in the polarization of a linearly polarized probe laser. In spin noise spectroscopy the influence of the choice of a specific probe wavelength on the experimental results has received significant attention in the past [39, 169–171]. A similar critical assessment of the influence of the probe energy on results obtained from spatially resolved two-color MOKE spectroscopy, however, has been neglected in the respective pioneering works. This is problematic for the following reasons.

In two-color MOKE microscopy optical spin injection is achieved by a circularly polarized pump laser whose photon energy is tuned above the fundamental band gap [15, 30, 65, 68]. It has been known for a long time that in semiconductors the electron temperature T_e can significantly exceed the lattice temperature T_L as a result of the deposition of excess energy in the electron system by such above-bandgap optical excitation [23–27]. As detailed in chapter 4, this effect is most pronounced at very low lattice temperatures for which the energetic coupling between the electrons and the lattice system is weak, and vanishes with increasing T_L.

At liquid helium temperatures an overheating of the electron system is observed at rather low power densities $< 1\,\mathrm{W\,cm^{-2}}$ for which no heating of the lattice system occurs [25, 126]. Such power densities easily fall by orders of magnitude below excitation intensities typically required in pump-probe MOKE microscopy as a result of the necessity to strongly focus the pump laser to achieve high spatial resolution while exciting a detectable electron spin polarization. At low lattice temperatures pump-induced carrier heating therefore is inherent to the nonresonant[9] optical spin excitation in two-color MOKE microscopy and virtually cannot be avoided.

[9] The practice of nonresonant excitation in two-color MOKE microscopy stems from the experimental requirement to detune the pump with respect to the probe laser to enable spectral filtering of the collinear pump and probe beams. This is necessary to prevent a saturation of the balanced photoreceiver by modulated pump light.

We have previously used spatially resolved photoluminescence (SRPL) spectroscopy to demonstrate that for excitation by a focused laser the thermal non-equilibrium between the electron and the lattice system can persist over length scales exceeding ten micrometers in bulk GaAs [126]. These thermal relaxation lengths are comparable to typical spin diffusion lengths in n-doped GaAs. In the following we will show that consideration of the presence of such electron temperature gradients is essential for the correct MOKE electron spin detection at low T_L.

In two-color MOKE microscopy the probe laser energy is commonly tuned to the E_0 excitonic resonance and λ_{probe} is chosen such that the observed Kerr rotation is maximized to facilitate the detection of the small polarization signals [15, 32, 68]. Assuming a linear relation $\theta_K = \alpha S_z$ between the small Kerr rotation and the electron spin polarization, $S_z(r)$ then is determined by varying the relative distance r between the focused pump and probe lasers and measuring $\theta_K(r)$ (compare section 3.4.1).

If the magneto-optical coefficient α does not depend on the distance r, MOKE microscopy correctly reveals the local electron spin polarization $S_z(r)$. The excitonic optical resonances in semiconductors, however, are known to be strongly influenced by changes in the local charge carrier and exciton concentration and (electron) temperature [28, 172–178]. These parameters, however, all may vary significantly with the distance to the pump spot, e.g. due to concurrent excess photocarrier recombination or energy relaxation of hot electrons and holes. The influence of this variation of spin-unrelated parameters on the local magneto-optical coefficient $\alpha = \alpha(r)$ then masks the spatial dependence of the local electron spin polarization. As a consequence, MOKE microscopy performed using an arbitrary probe wavelength in general does not correctly reveal the true electron spin diffusion profile. This insight is contrary to the common assumption which underlies the spatially resolved electron spin detection by magneto-optical pump-probe techniques.

In the following we present representative cw spectroscopy data for the bulk n-GaAs sample 11889. We have observed results qualitatively similar to the ones presented here for a wide range of n-doped GaAs samples with room temperature electron densities between $7 \times 10^{15}\,\text{cm}^{-3}$ and $5 \times 10^{16}\,\text{cm}^{-3}$ and layer thicknesses between 500 nm and 1 µm.

All measurements are performed with the probe laser power fixed at 50 µW. The pump laser wavelength is $\lambda_{\text{pump}} = 7800\,\text{Å}$ and the pump power is 10 µW if not stated otherwise. For the dominant HH transition the 7800 Å pump light excites conduction band electrons with a mean initial excess of $\langle E_c^{\text{ini}} \rangle \approx 60\,\text{meV}$. The excitation wavelength, the pump and probe intensities, and the sample properties are chosen to resemble the experimental conditions typically found in comparable spatially resolved MOKE microscopy studies [15, 32, 68].

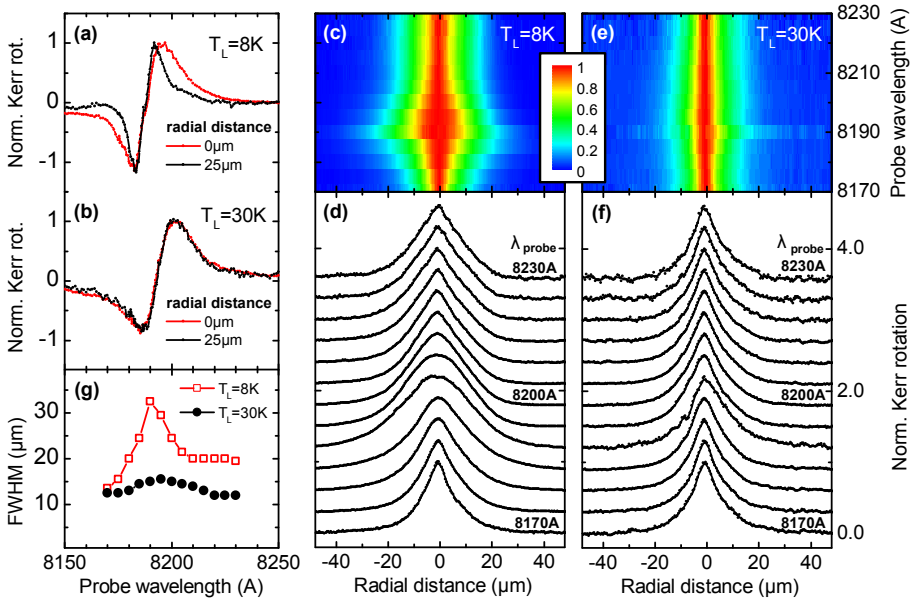

Figure 28: (a,b) Normalized local Kerr rotation spectra $\theta_K(\lambda_{\text{probe}})$ for different distances between the pump and probe spot at low (8 K) and high (30 K) lattice temperature. **(c,e)** Colormaps of the spatial dependence of the normalized local Kerr rotation $\theta_K(r)$ for different probe wavelengths measured between 8170 Å and 8230 Å in steps of 5 Å at low and high lattice temperature. Each $\theta_K(r)$ profile is normalized to the amplitude at the center of excitation. **(d,f)** Line cuts through the same data sets. **(g)** Full width at half maximum (FWHM) of the lateral Kerr rotation profile as a function of probe wavelength.

7.1.2 Local modification of the magneto-optical coefficient

To demonstrate the local modification of the magneto-optical coefficient $\alpha(r)$ by pump-induced electron heating we measure the E_0 excitonic Kerr rotation spectrum $\theta_K(\lambda_{\text{probe}})$ in the vicinity of the GaAs band gap as a function of radial distance r between the pump and probe spot. The spectra obtained at $T_L = 8\,\text{K}$ at the pump spot center and at $r = 25\,\mu\text{m}$ are shown in Fig. 28 (a). Both spectra are normalized to the maximum amplitude of the low-energy wing of the resonance for comparison. The Kerr spectrum exhibits an antisymmetric lineshape with a zero-crossing at 8189 Å (1.514 eV) which is characteristic for an energetic splitting of the $\sigma^{\pm}$ excitonic resonances [106, 179]. Moving away from the pump spot we find a strong change in the Kerr spectrum in which the resonance lineshape becomes significantly more narrow with increasing radial distance.

Thermal nonequilibrium between the lattice and electron system is only observed at low lattice temperatures. It results from the weak coupling between electrons and acoustic phonons. As detailed in chapter 4, for $T_e \gtrsim 30\,\text{K}$, energy relaxation of the electron system by LO phonon emission becomes efficient. For lattice temperatures exceeding $\approx 30\,\text{K}$ and cw photoexcitation, the electron and lattice system therefore

are in thermal equilibrium, i.e. $T_e = T_L$ [29, 126]. In this case all effects due to local carrier heating vanish and the spectral shape of the excitonic Kerr resonance should be spatially homogeneous and independent of the probe laser position. In Fig. 28 (b) we show that at $T_L = 30\,\mathrm{K}$ the Kerr rotation spectra measured at the center of excitation and at a distance of 25 µm from the pump spot indeed become identical within experimental resolution, i.e. the normalized $\theta_K(\lambda_{\mathrm{probe}})$ does not depend on the probe position.

We next demonstrate the consequence of the position dependence of the local magneto-optical coefficient $\alpha(r)$ for the spatially resolved MOKE electron spin detection. We therefore measure the lateral Kerr rotation profile $\theta_K(r)$ at $T_L = 8\,\mathrm{K}$ for different probe wavelengths which we vary between 8170 Å and 8230 Å in steps of 5 Å. The λ_{probe} dependence of the profiles, normalized to the peak value at the center of the pump spot for comparison, is shown in the colormap in Fig. 28 (c). The individual profiles are shown as line cuts through the same dataset in Fig. 28 (d). Starting from short probe wavelengths, the lateral Kerr rotation profiles $\theta_K(r)$ become much wider when approaching the zero-crossing of the excitonic Kerr resonance and become more narrow again when moving away from the central resonance wavelength [Fig. 28 (c)]. Moreover, the shape of the lateral Kerr rotation profile strongly changes for probe wavelengths close to 8190 Å, as depicted in Fig. 28 (d). The urging question which, if any, of the $\theta_K(r)$ profiles correctly maps the local spin polarization $S_z(r)$ will be answered in the following section.

To further quantify the above observations we plot the FWHM of the $\theta_K(r)$ profiles as a function of λ_{probe} in Fig. 28 (g). Starting from 14 µm at the shortest probe wavelength of 8170 Å, the FWHM more than doubles to values exceeding 30 µm at 8190 Å, then reduces, and finally stays constant at $\approx 20\,\mu\mathrm{m}$ for $\lambda_{\mathrm{probe}} \gtrsim 8210\,\text{Å}$. For these long probe wavelengths the normalized Kerr rotation profiles $\theta_K(r)$ are, within experimental resolution, identical and do not depend on λ_{probe} [compare Fig. 28 (d)].

The decay length on which the Kerr rotation decreases to its $(1/e)$ value, measured at a single λ_{probe} close to the Kerr rotation resonance maximum, has been used in the past to extract spin diffusion coefficients in bulk n-GaAs [32]. This $(1/e)$ decay length is closely related to the FWHM of the Kerr rotation profile. The strong variation of the FWHM with probe wavelength observed in our measurements raises doubts on the validity of this procedure.

For $T_L = 30\,\mathrm{K}$ we find no spatial variation in the local Kerr rotation spectrum and hence in the magneto-optical coefficient α. All Kerr rotation profiles therefore are now expected to reflect the actual local spin polarization $S_z(r)$ irrespective of the probe wavelength. In analogy to the previous measurements we present the λ_{probe} dependence of the $\theta_K(r)$ profiles for $T_L = 30\,\mathrm{K}$ in Figs. 28 (e,f). In contrast to the low lattice temperature case, the width and shape of the Kerr rotation profiles now only weakly depend on λ_{probe}. The FWHM of the $\theta_K(r)$ profiles only varies between $\approx$ 12-15 µm as shown in Fig. 28 (g).

We next confirm that the spatial dependence of the excitonic Kerr rotation spectrum $\theta_K(E_{\text{probe}})$ is quantitatively explained by considering thermal broadening of the excitonic resonance close to the pump spot. We therefore first characterize the intrinsic temperature dependence of the excitonic Kerr resonance linewidth, and subsequently analyze $\theta_K(E_{\text{probe}})$ in terms of a model which relates the Kerr rotation to spin-induced modifications of the dielectric function. This model is introduced in the following.

7.1.3 Excitonic Kerr rotation model

Following the concept of Refs. [151, 179] we model the dielectric functions $\tilde{\varepsilon}^{\pm}(\hbar\omega)$ for the energy range of interest in terms of a Lorentzian resonance representing the excitonic contribution and a static background $\varepsilon_b = 11.95$ [49] resulting from higher-energy transitions:

$$\tilde{\varepsilon}^{\pm}(\hbar\omega) = \varepsilon_b + \frac{A^{\pm}}{E_0^{\pm} - \hbar\omega + i\Gamma} \tag{7.1}$$

Here, E_0^+ (E_0^-) and A^+ (A^-) are the resonance energy and amplitude for the excitonic optical transition involving σ^+ (σ^-) photons. The parameter Γ describes the linewidth of the excitonic resonance.

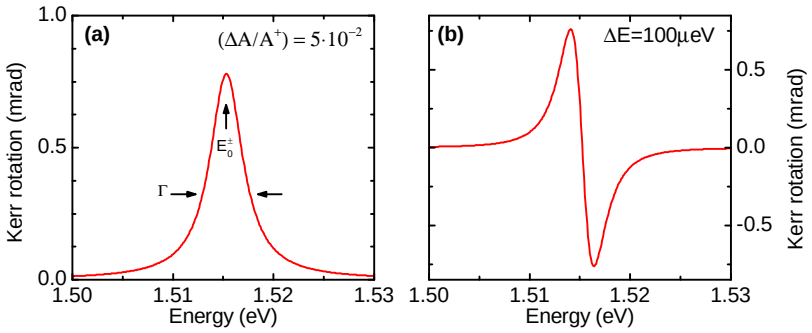

Figure 29: Excitonic Kerr rotation resonance model. **(a)** Excitonic Kerr rotation spectrum $\theta_K(E_{\text{probe}})$ calculated from Eqs. (3.42) - (3.44) and Eq. (7.1) assuming a relative reduction of the resonance amplitude $(A^- - A^+)/A^+ = 5 \times 10^{-2}$. The spectrum is symmetric with respect to the resonance energy $E_0^{\pm}$. The linewidth Γ of the excitonic resonance determines the width of the Kerr rotation spectrum. **(b)** Kerr rotation spectrum calculated for a spin splitting energy $\Delta E = (E_0^+ - E_0^-) = 100\,\mu\text{eV}$. The spectrum exhibits an antisymmetric lineshape with a zero-crossing at the excitonic resonance energy of the undisturbed system. Both spectra were calculated for $\Gamma = 2\,\text{meV}$, $(E_0^+ + E_0^-)/2 = 1.515\,\text{eV}$, and $A^- = 2.35\,\text{meV}$.

The influence of an imbalance in the resonance amplitudes $A^{\pm}$ and a splitting of the resonance energies $E_0^{\pm}$ on the spectral shape of the Kerr resonance is discussed in detail in Ref. [106] and is illustrated in Fig. 29. A difference in the resonance amplitudes

$\Delta A = (A^- - A^+)$ results in a contribution to the spectral dependence of the Kerr rotation which is symmetric with respect to the resonance energy and does not possess a sign change. In contrast, an energetic splitting of the excitonic resonances $\Delta E = (E_0^+ - E_0^-)$ leads to a spectral dependence of the Kerr rotation on the probe laser energy which is antisymmetric and exhibits a zero-crossing at the mean resonance energy as observed in our experiments. In both cases, the linewidth Γ determines the spectral region for which a non-zero Kerr rotation is observed. Moreover, an increase of Γ leads to an overall decrease of the resonance amplitude of $\theta_K(E_{\text{probe}})$ for a given ΔA or spin splitting energy ΔE.

7.1.4 Intrinsic temperature dependence of the Kerr rotation resonance linewidth

We first examine the intrinsic temperature dependence of $\theta_K(E_{\text{probe}})$. We achieve experimental conditions in which T_e is not modified by the optical excitation by strongly defocussing the pump and probe beams to a spot size $\gtrsim 100\,\mu\text{m}$ while keeping both laser powers fixed. We thus measure the Kerr spectrum for excitation densities well below $100\,\text{mW}\,\text{cm}^{-2}$. For these low excitation densities an upper bound of the excess photocarrier density is estimated to be of the order of $1 \times 10^{14}\,\text{cm}^{-3}$. Because of the high extrinsic electron concentration of $1.4 \times 10^{16}\,\text{cm}^{-3}$ of the sample under investigation, pump-induced carrier heating is negligible for such low excitation densities and $T_e = T_L$ for the temperature range of interest. We have additionally confirmed the absence of pump-induced carrier heating under defocussed excitation by further increasing the pump and probe spot size at fixed laser powers and comparing the normalized Kerr rotation spectra to the data presented here. We have found that a further decrease in pump intensity does not modify the linewidth of the Kerr spectrum and we thus measure the intrinsic excitonic resonance linewidth for the given lattice temperature.

For the low excitation density measurements, no calibration for the detection of absolute Kerr rotation angles is available and we therefore cannot determine the absolute value ΔE of the spin splitting. We are, however, able to extract the intrinsic temperature dependence of the linewidth $\Gamma(T)$ which is independent of the spin splitting and amplitude of the Kerr rotation spectrum. In Fig. 30 (a) we show normalized Kerr spectra $\theta_K(E_{\text{probe}})$ for lattice temperatures T_L ranging from 8 K to 25 K obtained under low excitation density conditions together with the best fits derived from the excitonic Lorentzian resonance model.

To obtain the best fits we have combined the macroscopic description of the Kerr rotation Eqs. (3.42) - (3.44) introduced in section 3.4.1 with Eq. (7.1) for the dielectric function in the vicinity of the E_0 excitonic resonances. For all examined temperatures we find that the Lorentzian resonance model provides a good description of the experimental data. This will in the following allow us to reliably extract information on both the local excitonic spin splitting $\Delta E(r)$ and resonance linewidth $\Gamma(r)$.

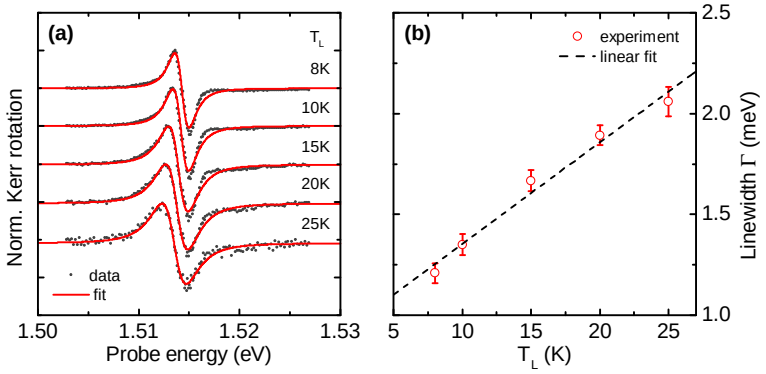

Figure 30: (a) Lattice temperature dependence of the normalized excitonic Kerr rotation spectrum $\theta_K(E_{\text{probe}})$ under low excitation density conditions (strongly defocussed pump and probe spots). Markers are experimental data, solid lines are fits to a Lorentzian excitonic resonance model (see text). **(b)** Temperature dependence of the linewidth $\Gamma(T_L)$ of the excitonic Kerr resonance. The dashed line is a linear fit.

The intrinsic temperature dependence of the excitonic linewidth obtained from these fits is shown in Fig. 30 (b). We find that $\Gamma(T)$ monotonically increases from a low temperature value of (1.2 ± 0.1) meV at $T_L = 8$ K to (2.1 ± 0.1) meV at $T_L = 25$ K, reflecting increased thermal broadening of the excitonic resonance at higher temperatures. The broadening of the excitonic resonance results from the interaction with acoustic and optical phonons and scattering from crystal impurities and imperfections [175,177,180]. For bulk semiconductors the temperature dependence of the excitonic linewidth is of the general form:

$$\Gamma(T) = \Gamma_0 + aT + bN_{\text{LO}}(T) \tag{7.2}$$

where the terms on the right hand side of the equation describe the contributions of scattering with impurities, acoustic, and longitudinal-optical phonons [175]. N_{LO} is the usual Bose-Einstein distribution function. For the low lattice temperatures examined in this work, scattering with LO phonons is negligible [181] and we expect a linear dependence of the linewidth on temperature as observed in Fig. 30 (b). From a linear fit to the remaining part of Eq. (7.2) we obtain $\Gamma_0 = (0.85\pm0.07)$ meV and a slope $a = (50\pm4)\,\mu\text{eV K}^{-1}$. This calibration measurement allows us in the following to deduce the electron temperature profile $T_e(r)$ from spatially resolved measurements of the local Kerr rotation spectrum.

7.1.5 Local measurement of the excitonic Kerr rotation spectrum

We now turn to the analysis of the spatial dependence of the local excitonic Kerr rotation spectrum. In Fig. 31 (a) we show $\theta_K(E_{\text{probe}})$ for distances of 0 µm to 25 µm to the pump spot measured in steps of 2.5 µm at $T_L = 8$ K together with the best fits from the

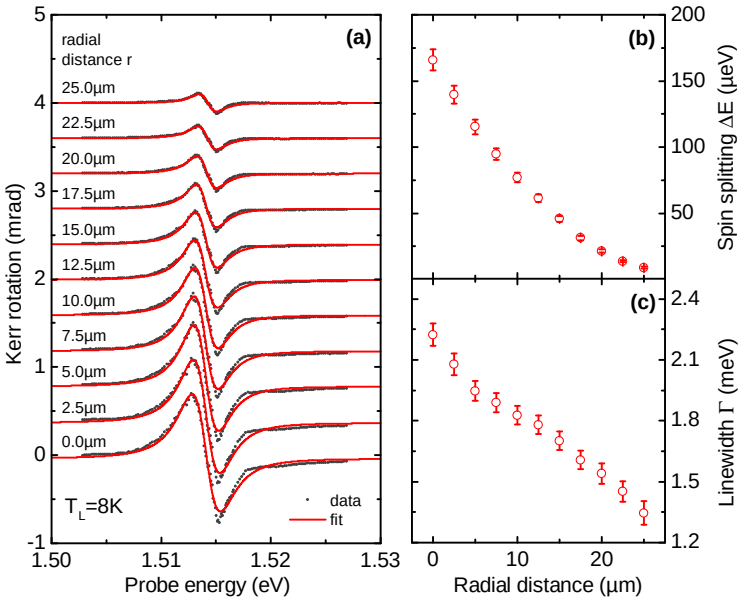

Figure 31: (a) Local Kerr spectrum $\theta_K(E_{\text{probe}})$ measured at increasing distances between the pump and probe spot at $T_L = 8\,\text{K}$. Solid lines are fits to a Lorentzian excitonic resonance model (see text). **(b)** Lateral profile of the excitonic spin splitting $\Delta E(r) \sim S_z(r)$ obtained from the model. **(c)** Local excitonic linewidth $\Gamma(r)$.

Lorentzian excitonic resonance model. For the resonance amplitude $A^{\pm}$ of the sample under investigation we assume a value of 2.35 meV which is found in Ref. [151] for bulk GaAs of comparable impurity concentration. We note that because of the dependence of the absolute value of the Kerr rotation on both the amplitude $A^{\pm}$ and ΔE this introduces an uncertainty in the absolute values obtained for the spin splitting. However, since an identical value for $A^{\pm}$ is used to fit all local Kerr spectra, relative changes in $\Delta E(r)$ and hence the general form of the spatial dependence of the spin splitting are not affected by this uncertainty.

To account for possible phase space filling effects due to spin-selective Pauli blockade of occupied electronic states [162, 182, 183] we further allow for a reduction of the resonance amplitude A^{+} for transitions involving the majority spin population as the final state in our fitting routine. We find that the relative reduction does never exceed 1 % and systematically decreases when moving away from the pump spot (not shown here). This rather small reduction of the excitonic absorption is expected in bulk semiconductors in which phase space filling is of minor importance compared to low-dimensional systems. We further note that the influence of the introduction of this additional degree of freedom to the fit on the results for ΔE and Γ is negligible.

In Figs. 31 (b) and (c) we show the spatial dependence of the local excitonic spin splitting $\Delta E(r)$ and the excitonic linewidth $\Gamma(r)$. We find that both quantities systemati-

cally decrease with increasing distance to the pump spot, reflecting lateral electron spin diffusion and hot carrier energy relaxation, respectively. In the following we describe how we extract information on the spatially resolved photocarrier energy relaxation and the local electron spin polarization from both parameters.

7.1.6 Kerr rotation resonance linewidth thermometry

We have reported previously on measurements of the local electron temperature by means of SRPL spectroscopy [101, 126]. Here we employ the spatially resolved measurement of the local excitonic resonance linewidth as a new technique for the determination of the lateral electron temperature profile. In Fig. 32 we plot $T_e(r)$ which we calculate from the spatial dependence of $\Gamma(r)$ shown in Fig. 31 (c) and the parameters obtained from the linear fit to the low excitation density calibration measurement of $\Gamma(T)$ shown in Fig. 30 (b). At the pump spot center we find a peak electron temperature $T_{e,\max} = (27 \pm 3)\,\mathrm{K}$. This result is in accordance with the expected limiting of T_e to $\lesssim 30\,\mathrm{K}$ by efficient LO phonon scattering. Moving away from the pump spot, $T_e(r)$ monotonically decreases and approaches $T_L = 8\,\mathrm{K}$ for $r \gtrsim 25\,\mu\mathrm{m}$. This thermal relaxation length significantly exceeds the pump spot size Δ_{pump} by more than a factor of 10. We attribute the macroscopic distance over which the thermal gradient in $T_e(r)$ persists to heat conduction (and possibly convection effects) in the electron system [126].

To check the validity of the determination of $T_e(r)$ profiles from the local excitonic linewidth we perform complementary SRPL spectroscopy measurements. In analogy to our experiments presented in Refs. [101, 126] we determine the local electron temperature from the lineshape analysis of the conduction band to neutral carbon acceptor $(\mathrm{e}, \mathrm{A}_\mathrm{C}^0)$ transition introduced in section 4.6. The experimental setup used for the SRPL measurements is described in section 5.2. Local photoexcitation is performed at 7850 Å excitation wavelength using a pump power of 10 µW, resulting in excitation conditions similar to our MOKE measurements and allowing for direct comparison of results obtained from both experiments.

In Fig. 32 (b) we show representative PL spectra measured at a distance of 0 µm, 6.5 µm, and 15 µm to the pump spot. Close to the pump spot the photoluminescence spectrum in the energy range of interest is dominated by the $(\mathrm{e}, \mathrm{A}_\mathrm{C}^0)$ transition occurring at 1.4931 eV [49]. Moving away from the pump spot, the $(\mathrm{e}, \mathrm{A}_\mathrm{C}^0)$ transition becomes increasingly disturbed by the nearby $(\mathrm{D}^0, \mathrm{A}_\mathrm{C}^0)$ donor acceptor pair transition at slightly lower photon energies (compare section 6.1).

To determine the local electron temperature we fit Eq. (4.13) to the measured PL spectra. For the fitting procedure we keep the acceptor binding energy fixed to the literature value $E_A = 26.0\,\mathrm{meV}$ [129] which corresponds to the observed $(\mathrm{e}, \mathrm{A}_\mathrm{C}^0)$ luminescence onset at 1.4931 eV. The remaining independent free parameters are the luminescence intensity amplitude and the searched T_e. Together with the experimental data we show in Fig. 32 (b) the $(\mathrm{e}, \mathrm{A}_\mathrm{C}^0)$ lineshape analysis from which we obtain the local electron

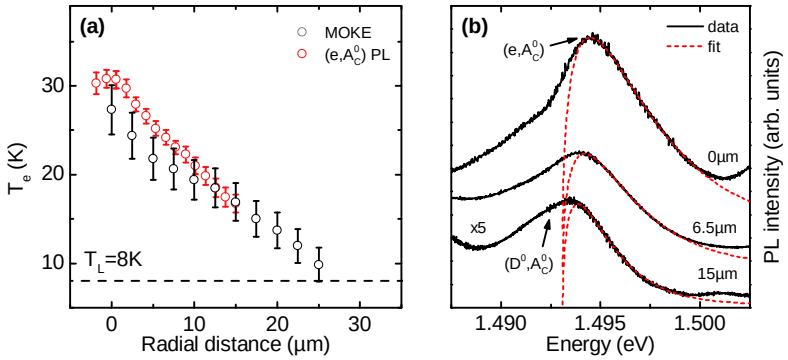

Figure 32: (a) Lateral electron temperature profile $T_e(r)$ obtained from spatially resolved measurements of the local excitonic resonance linewidth $\Gamma(r)$ (black circles) and spatially resolved $(\mathrm{e},\mathrm{A}_\mathrm{C}^0)$ PL spectroscopy (red circles). The dashed horizontal line indicates the lattice temperature $T_L = 8\,\mathrm{K}$. **(b)** Normalized PL spectra (black lines) obtained for a distance of 0 µm, 6.5 µm, and 15 µm to the pump spot. Red dashed lines are fits to the $(\mathrm{e},\mathrm{A}_\mathrm{C}^0)$ transition from which T_e is deduced.

temperature. In accordance with previous studies on the same sample [101] we find that for distances to the pump spot exceeding $\approx 15\,\mu\mathrm{m}$ the high energy tail of the $(\mathrm{e},\mathrm{A}_\mathrm{C}^0)$ transition becomes disturbed by the donor-acceptor pair transition. This prevents a reliable extraction of $T_e(r)$ from the $(\mathrm{e},\mathrm{A}_\mathrm{C}^0)$ PL for larger distances.

We now compare the results for the lateral $T_e(r)$ profile obtained from our MOKE microscopy and SRPL measurements in Fig. 32 (a). We find that the spatial dependence of $T_e(r)$ obtained from the local excitonic linewidth $\Gamma(r)$ is well reproduced by the SRPL results. Minor deviations between both datasets occur very close to the pump spot where the values obtained from the PL analysis exceed T_e as determined from the MOKE experiment. These deviations can possibly be attributed to a small difference in the respective pump spot sizes which results in slightly different excitation conditions. Moreover, the optical spin injection in the MOKE measurements using the slightly shorter pump wavelength of 7800 Å excites a fraction of the CB electrons with $E_c^{\mathrm{ini}} \gtrsim 2\hbar\omega_{\mathrm{LO}}$. The increased efficiency of the fast initial energy relaxation by LO phonon cascade emission therefore might lead to the slight reduction of T_e in the MOKE measurements as compared to the SRPL results obtained for excitation at 7850 Å for which $E_c^{\mathrm{ini}} < 2\hbar\omega_{\mathrm{LO}}$ (compare section 4.5).

Our above results demonstrate that spatially resolved information on the local charge carrier temperature can indeed be obtained from a lineshape analysis of the excitonic Kerr rotation resonance. Such an excitonic resonance linewidth thermometry technique has, to the best of our knowledge, not been reported previously. If experimentally feasible, a PL lineshape analysis of the $(\mathrm{e},\mathrm{A}^0)$ electron-acceptor or the $\mathrm{FX}-2\hbar\omega_{\mathrm{LO}}$ phonon assisted free exciton transition [184, 185] provides more direct access to the carrier distribution function and the carrier temperature. However, PL spectroscopy is limited

to the time and length scales of the photocarrier lifetime and the ambipolar or exciton diffusion length. Moreover, as observed above, PL thermometry is potentially prone to disturbances of the luminescence lineshape by spectrally nearby transitions. Two-color pump-probe MOKE microscopy therefore can be a valuable complementary technique which, provided sufficiently long spin relaxation time and diffusion lengths, potentially allows to access carrier temperatures on time and length scales for which SRPL spectroscopy is no longer viable.

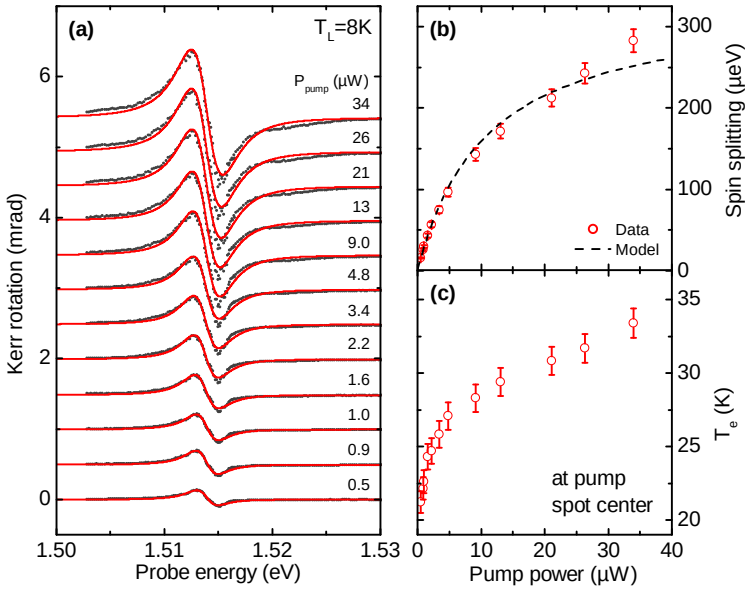

Figure 33: (a) Pump power dependence of the local Kerr rotation spectrum $\theta_K(E_{\text{probe}}, r = 0\,\mu\text{m})$ at the pump spot center for $T_L = 8\,\text{K}$. Solid lines are fits to a Lorentzian excitonic resonance model (see text). Curves are shifted vertically. **(b)** Pump power dependence of the local excitonic spin splitting $\Delta E(r=0) \sim S_z(r=0)$ obtained from the excitonic resonance model. The dashed black line is the best fit to the saturation model Eq. (7.4) **(c)** Local electron temperature $T_e(r=0)$ extracted from the excitonic resonance linewidth Γ.

We additionally investigate the pump power dependence of the excitonic spin splitting ΔE and resonance linewidth Γ at the pump spot center. The dependence of both parameters on P_{pump} reveals the saturation of the electron spin polarization and the electron temperature with increasing optical excitation density. We therefore measure at $T_L = 8\,\text{K}$ a series of of Kerr rotation spectra $\theta_K(E_{\text{probe}}, r = 0)$ for P_{pump} between $0.5\,\mu\text{W}$ and $34\,\mu\text{W}$. The experimental data together with the best fits from the Lorentzian resonance model are shown in Fig. 33 (a). Even for the highest excitation power the maximum observed Kerr rotation amplitude is below 0.85 mrad. This rather small value underlines the challenging requirements for the angular resolution necessary for a successful MOKE electron spin microscopy instrumentation.

In Fig. 33 (c) we show the electron temperature $T_e(P_{\text{pump}})$ at the pump spot center which we calculate from the measured resonance linewidth $\Gamma(P_{\text{pump}})$ and the calibration measurement of the intrinsic $\Gamma(T_e)$. The electron temperature exhibits the expected rapid saturation with increasing P_{pump} [compare our discussion in section 4.5 and Fig. 13 (a)]. Even at the lowest pump power of 0.5 µW the electron temperature $T_e = (21 \pm 1)\,\text{K}$ exceeds T_L by 13 K. This observation underlines that a mitigation of hot carrier effects in cw MOKE microscopy by reducing the excitation power is not feasible. When increasing P_{pump}, the electron temperature rapidly increases until energy relaxation by LO phonon emission and dissipation by electronic heat conduction away from the excitation site limits $T_e \lesssim 35\,\text{K}$.

7.1.7 Correct determination of the local electron spin polarization

We finally demonstrate how spatially resolved measurements of the full excitonic Kerr rotation spectrum can correctly determine the lateral electron spin polarization profile. In the preceding section we have found that the excitonic Kerr rotation stems from an energetic spin splitting ΔE of the exciton resonance energies for $\sigma^{\pm}$ photons. This energy splitting has been observed previously in transient pump-probe transmission spectroscopy [186] as well as in PL spectroscopy in GaAs QWs [187–189] and recently in bulk GaAs and $Al_xGa_{1-x}As$ samples [190].

From theory it is expected that the spin splitting energy is proportional to the density difference between spin-up and spin-down electrons, i.e. $\Delta E \sim (n_\uparrow - n_\downarrow)$ [191]. Owing to the high intrinsic carrier concentration of the examined sample, the pump-induced change in the total electron density $(n_\uparrow + n_\downarrow)$ is small. We therefore can directly determine the local electron spin polarization:

$$S_z(r) = \left[n_\uparrow(r) - n_\downarrow(r)\right] / \left[n_\uparrow(r) + n_\downarrow(r)\right] \sim \Delta E(r) \tag{7.3}$$

from the lateral profile of the local exciton spin splitting.[10]

Before addressing the local electron spin profile $S_z(r)$ we first briefly consider the dependence of the efficiency of optical orientation on the optical excitation density. In Fig. 33 (b) we observe the sublinear increase of the excitonic spin splitting $\Delta E(P_{\text{pump}}) \sim S_z(P_{\text{pump}})$ which is characteristic for the saturation of the electron spin polarization in n-type semiconductors with increasing optical excitation density [60]. The pump power dependence of the spin splitting is well described by the saturation equation [68, 91]:

$$\Delta E(P_{\text{pump}}) = \frac{\Delta E_{\text{sat}}}{1 + P_{\text{sat}}/P_{\text{pump}}} \tag{7.4}$$

Here ΔE_{sat} is the maximum attainable spin splitting and P_{sat} is a characteristic saturation power. From the fit of Eq. (7.4) to the experimentally observed power dependence of the spin splitting shown in Fig. 33 (b) we obtain $\Delta E_{\text{sat}} = (332 \pm 15)\,\mu\text{eV}$

[10] For QWs the equivalence of a measurement of ΔE and S_z has been demonstrated beautifully in Ref. [192] where the authors experimentally proof using picosecond PL spectroscopy that the time evolution of the spin splitting energy precisely follows the circular polarization degree of the luminescence.

and $P_{\mathrm{sat}} = (11 \pm 1)\,\mu\mathrm{W}$. This analysis a posterio demonstrates that we have carried out our measurements in a linear regime for which the electron spin density scales proportional to the optical excitation power.

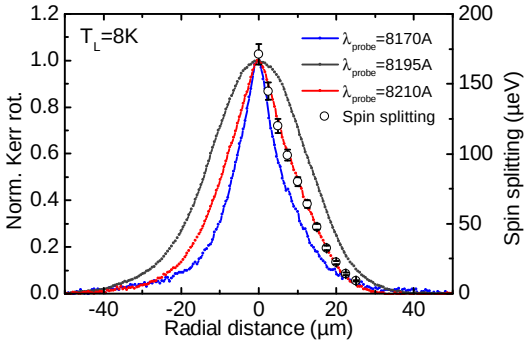

Figure 34: Comparison of the normalized lateral Kerr rotation profiles $\theta_K(r)$ obtained for different probe wavelengths and the lateral spin splitting profile $\Delta E(r) \sim S_z(r)$ (see text).

In Fig. 34 we finally show the lateral profile of the spin splitting $\Delta E(r)$ together with several representative normalized $\theta_K(r)$ profiles obtained at different probe wavelengths. Comparing both data sets we find a strong difference between the lateral Kerr rotation profile $\theta_K(r)$ measured at $\lambda_{\mathrm{probe}} = 8195\,\text{Å}$ and the spin splitting profile $\Delta E(r) \sim S_z(r)$. We therefore conclude that at low T_L the common practice [15, 32, 68] of probing the spin polarization with λ_{probe} tuned to the maximum amplitude of the Kerr rotation spectrum is detrimental to a correct determination of the spin polarization profile. The Kerr rotation profile measured at $\lambda_{\mathrm{probe}} = 8210\,\text{Å}$, however, perfectly coincides with the excitonic spin splitting $\Delta E(r)$. Comparing this result and Fig. 34 we find that for the examined sample 11889 the Kerr rotation profiles $\theta_K(r)$ measured with long probe wavelengths $\lambda_{\mathrm{probe}} \gtrsim 8210\,\text{Å}$, i.e. strongly detuned from the Kerr rotation resonance energy, correctly reflect the true local electron spin polarization.

7.1.8 Summary and conclusions

We have presented a systematic investigation of hot carrier effects on the magneto-optical electron spin detection in bulk GaAs. We have found that at low lattice temperatures the local optical excitation of spin polarized electrons also results in a lateral gradient of the electron temperature. This temperature gradient introduces a spatially varying linewidth of the local Kerr rotation spectrum by local thermal broadening of the excitonic resonance. This variation of the local magneto-optical coefficient $\alpha(r)$ is superimposed on the electron spin-related spatial dependence of the Kerr rotation. It prevents a reliable extraction of the lateral electron spin profile from measurements of the lateral Kerr rotation profile at fixed arbitrary probe wavelengths. Previous optical studies of electron spin diffusion in semiconductors have not taken such local heating effects on the magneto-optical spin detection into account, possibly leading to incorrect

quantitative results for electron spin diffusion coefficients. In particular, the oversight of hot carrier effects in the cw MOKE spin detection leads to a systematic overestimation of the spin diffusion length [compare e.g. Fig. 28 (g)]. Therefore previous observations of anomalous enhancements of the electron spin diffusivity and apparent violations of the classical Einstein relation [15, 32] and their theoretical interpretation by the influence of degeneracy [193] may be in question.

To correctly determine the local electron spin polarization we have quantitatively analyzed the full excitonic Kerr rotation spectrum in terms of a model from which we extract the local excitonic spin splitting energy. For the examined sample we have further found that the lateral spin polarization profile is also correctly obtained from fixed-wavelength measurements of the lateral Kerr rotation profile using long probe wavelengths well below the excitonic resonance energy. This insight will be used in the following section to determine the intrinsic temperature dependence of the electron spin diffusion coefficient of the bulk n-doped GaAs sample 11889.

7.2 Hot carrier effects on steady-state electron spin diffusion in n-type GaAs

In the preceding section we have shown that in MOKE microscopy experiments the optically induced temperature gradient in the electron system potentially disturbs the magneto-optical electron spin detection. Hot carriers, however, not only affect the optical spin detection, but also the subject of investigation, the electron spin diffusion process. The significance of pump-induced electron heating for the diffusion of photoexcited carriers has been understood for a long time in the context of exciton transport in QWs [103, 194–196]. However, such hot electron effects have been neglected in the interpretation of early results on low-temperature electron spin diffusion obtained from MOKE microscopy and TSG spectroscopy. Carter et al. were among the first to experimentally address such hot carrier effects on electron spin diffusion [95]. Their survey of spin and charge gratings in doped GaAs QWs strongly suggests the influence of hot photocarriers as the reason for an enhancement of the spin diffusion coefficient D_s observed under nonresonant optical excitation.

From the Einstein relation for non-degenerate semiconductors [197]:

$$eD_s = k_B T_e \mu_s \tag{7.5}$$

we expect that a local increase of $T_e(r)$, together with the (a priori unknown) temperature dependence $\mu_s(T_e)$, will introduce a spatial variation of the electron spin diffusion coefficient $D_s[T_e(r)]$. In this case conventional spin diffusion models [15, 31, 33] which assume a constant value for D_s do not provide a correct description of the spin polarization profile. Such a spatial variation of the spin diffusivity indeed has recently been demonstrated by us using low-temperature MOKE microscopy in bulk n-GaAs [80, 101]. We have shown that a careful consideration of the influence of hot carriers is crucial for a reliable extraction of spin propagation parameters from optical experiments. We have

conceived a modified diffusion model which allows to extract undisturbed values D_s^0 for the spin diffusivity which are not influenced by photocarrier heating.

In the following we synthesize this previous work and our newly gained insights on the elimination of hot carrier effects on the spatially resolved pump-probe spin detection. We combine cw Hanle-MOKE measurements of the electron spin relaxation time and steady-state MOKE microscopy to determine the intrinsic temperature dependence of the electron spin diffusion coefficient $D_s^0(T_L)$ of the bulk n-GaAs sample 11889. We then use additional cw MOKE microscopy measurements of electron spin diffusion in transverse magnetic fields to independently validate our results. The obtained temperature dependence of the spin diffusivity is used later in this work for the quantitative analysis of our time-resolved MOKE microscopy experiments.

7.2.1 Modified electron spin diffusion model

To determine the intrinsic electron spin diffusion coefficient $D_s^0(T_L)$ we measure line cuts of the steady state spin polarization profile $S_z(r)$ for T_L between 8 K and 35 K. The experimental data, acquired using $\lambda_{\text{pump}} = 7800\,\text{Å}$ and $P_{\text{pump}} = 10\,\mu\text{W}$, are shown in Fig. 35 (a). For the electron spin detection we chose $P_{\text{probe}} = 50\,\mu\text{W}$ and $\lambda_{\text{probe}} = 8210\,\text{Å}$, the parameter set which yields the correct spin profile (compare section 7.1.7). We next employ our modified spin diffusion model to extract the intrinsic temperature dependence $D_s^0(T_L)$ from these line cuts.

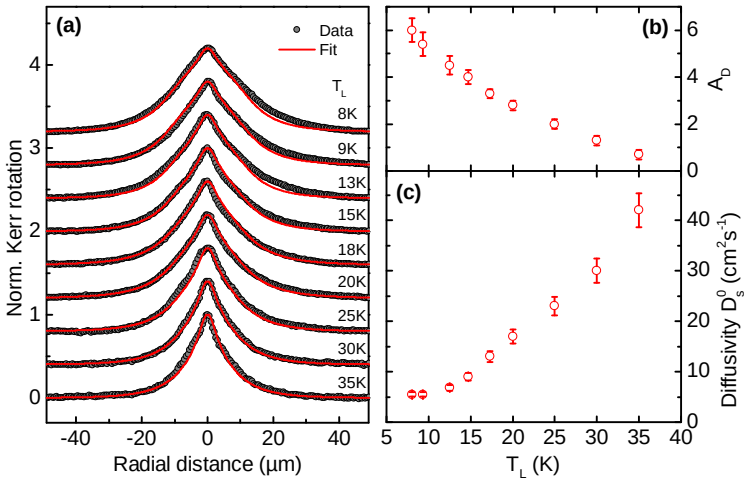

Figure 35: (a) Lateral steady-state electron spin polarization profiles measured for different lattice temperatures T_L between 8 K and 35 K (gray markers). Solid red lines are best fits from a modified diffusion model (see text). **(b)** Vanishing of the diffusion coefficient enhancement amplitude A_D with increasing lattice temperature. **(c)** Intrinsic temperature dependence of the spin diffusivity $D_s^0(T_L)$ extracted from the modified diffusion model.

The modified diffusion model is discussed in great detail in Ref. [101]. As stated earlier, optically induced spin diffusion is strongly influenced by pump-induced carrier heating. In principle it is possible to directly account for the measured local electron heating on the spin diffusion in terms of a local spin diffusivity $D_s[T_e(r)]$. However, the explicit analytical relationship $D_s(T_e)$ is not known a priori. To facilitate further analysis we instead approximate the spatial dependence of the spin diffusivity by a Gaussian. In the framework of the modified diffusion model the local enhancement of the electron spin diffusivity close to the pump spot by hot photocarriers therefore is considered by a spatially varying diffusion coefficient:

$$D_s(r,T_L) = D_s^0(T_L)\left[1 + A_D(T_L)\exp\left(-r^2/\sigma_D^2\right)\right] \tag{7.6}$$

The strength of the local diffusion enhancement by carrier heating is characterized by the amplitude A_D. This enhancement amplitude is a measure for the temperature difference between the electron system and the lattice. The local enhancement of $D_s(r)$ decays on a length scale described by σ_D. The spin diffusivity $D_s(r)$ reaches the intrinsic value $D_s^0(T_L)$ for distances far away from the pump spot for which the electron system and the lattice are in thermal equilibrium [compare Fig. 32 (a)].

We use a finite element method (FEM) solver to numerically solve the modified steady-state electron spin diffusion equation Eq. (3.30) for the spatially varying diffusion coefficient $D_s(r)$ Eq. (7.6). Optical spin excitation is modeled by the Gaussian source term Eq. (3.33) with an $(1/e)$ half width $\sigma_0 = 1.4\,\mu\text{m}$ (our optical resolution for cw excitation). Two boundary conditions are chosen to reflect the geometry of the sample. First, the spin polarization must vanish ($S_z = 0$) for large distances ($r \to \infty$). Second, the spin flux $\nabla_z S_z$ through the surface and backside of the epilayer must be zero. To determine D_s^0, a line cut at the surface of the computational domain is fitted to the experimental data. The only free parameter in this procedure other than the quantities which characterize $D_s(r)$ is $g_{z,0}$ which in this case serves as a scaling factor describing the ratio θ_K/S_z.

The spin relaxation time $\tau_s(T_L)$ in the spin diffusion equation Eq. (3.30) has been determined previously by us [80, 101] by standard cw Hanle-MOKE spectroscopy. The experimental procedure described in section 3.2.3 which we have used to measure τ_s is illustrated exemplarily for $T_L = 13\,\text{K}$ in Fig. 36 (a). For each temperature a series of Hanle curves for decreasing excitation densities was measured using strongly defocused pump and probe spots ($> 100\,\mu\text{m}$). The spin relaxation time τ_s was determined from an extrapolation of the half width at half maximum (HWHM) of Lorentzian fits of the Hanle curves to zero pump power assuming a constant[11] effective g-factor $g^* = -0.44$. At $T_L = 8.6\,\text{K}$ we have found $\tau_S = 170\,\text{ns}$, which decreases monotonically to 21 ns at 35 K [see Fig. 36 (b)]. These numbers are in excellent agreement with the established

[11] A review of experimental results on the temperature dependence of the electron g-factor in GaAs is given in Ref. [198]. We conclude that for the limited temperature range examined in this work the influence of the temperature dependence of the g-factor on the determination of τ_s from our Hanle-MOKE measurements is negligible.

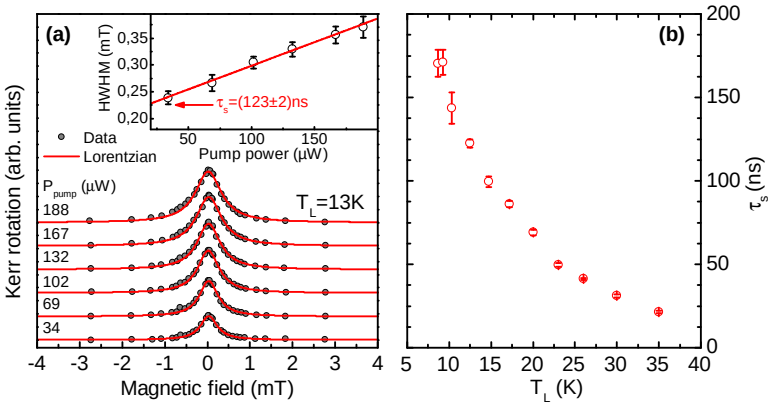

Figure 36: Continuous-wave Hanle-MOKE measurements of the electron spin relaxation time in the bulk n-GaAs sample 11889. **(a)** Hanle curves $S_z(B)$ measured at $T_L = 13\,\mathrm{K}$ for increasing excitation power (bottom to top). The inset shows the half width at half maximum (HWHM) of the Lorentzian Hanle curves as a function of P_{pump}. Extrapolation to zero pump power yields the spin relaxation time τ_s. **(b)** Lattice temperature dependence of the spin relaxation time.

literature [32, 67, 141].

The best fits obtained from the modified diffusion model are shown in Fig. 35 (a). In accordance with Ref. [101] we find good agreement with the experimental data over the whole examined temperature range for a constant enhancement decay length $\sigma_D \approx 7\,\mu\mathrm{m}$. The enhancement amplitude shown in Fig. 35 (b) systematically decreases from $A_D \approx 6$ at $T_L = 8\,\mathrm{K}$ to $A_D \approx 0.7$ at 35 K. This decrease demonstrates the vanishing influence of pump-induced electron heating at high lattice temperatures, for which the electron system and the lattice approach thermal equilibrium.

We last show in Fig. 35 (c) the intrinsic temperature dependence of the electron spin diffusion coefficient. For the examined temperature range we find that $D_s^0(T_L)$ monotonically increases from a low-temperature value of $(5.5 \pm 0.4)\,\mathrm{cm^2\,s^{-1}}$ at $T_L = 8\,\mathrm{K}$ up to $(42 \pm 3)\,\mathrm{cm^2\,s^{-1}}$ at the highest $T_L = 35\,\mathrm{K}$.

Comparison of our results $D_s^0(T_L)$ with the established literature is complicated by the fact that systematic investigations of the temperature dependence of electron spin diffusion in bulk n-GaAs are, to the best of our knowledge, not available. Moreover, numerical values for D_s in bulk GaAs samples with comparable impurity concentrations are scarce even for fixed low lattice temperatures. Ref. [15] reports for $T_L = 4\,\mathrm{K}$ spin diffusion coefficients of 3 and $15\,\mathrm{cm^2\,s^{-1}}$ for 1 μm thick bulk GaAs samples with electron concentrations of 1×10^{16} and $5 \times 10^{16}\,\mathrm{cm^{-3}}$, respectively[12]. These values are in reasonable agreement with our results. For elevated $T_L > 10\,\mathrm{K}$, no information on D_s in bulk n-GaAs is available. Instead of relying on previous literature we therefore next

[12] The same authors, however, report for the same T_L a conflicting value of $10\,\mathrm{cm^2\,s^{-1}}$ for a similar $n = 1 \times 10^{16}\,\mathrm{cm^{-3}}$ sample [32].

validate the internal consistency of our $D_s^0(T_L)$ and $\tau_s(T_L)$ results by complementary magneto-diffusion measurements.

7.2.2 Steady-state electron spin diffusion in magnetic fields

We last introduce magneto-diffusion spectroscopy, the spatially resolved observation of the depolarization of locally injected electron spins by transverse magnetic fields, as a valuable tool for the investigation of the interplay of spin relaxation and diffusion. For defocused cw excitation the depolarization $S_z(B_{xy})$ is intimately related to the spin relaxation time (compare section 3.2.3). Similar to this conventional Hanle effect, for focused excitation small in-plane magnetic fields B_{xy} lead to a quench of the local spin polarization. The decrease of $S_z(B_{xy}, r)$ with increasing B_{xy} here, however, not only depends on τ_s but is also limited by out-diffusion of electron spins from the excitation site. The efficiency of this process sensitively depends on $D_s(r)$ [71]. Magneto-diffusion measurements in particular are valuable to exclude an overestimation of the spin diffusivity caused e.g. by accidentally neglecting hot carrier effects [80]. Therefore a complimentary measurement of $S_z(r, B_{xy})$ can be used to independently confirm spin propagation and relaxation parameters obtained from zero-field MOKE microscopy.

In Fig. 37 we show color maps of the spin polarization $S_z(B_{xy}, r)$ which we measure for increasing magnetic fields between 0 and 6 mT at $T_L = 8$ K, 20 K, and 30 K. We observe the expected decrease of S_z with rising magnetic fields. For higher lattice temperatures the depolarization efficiency of B_{xy} decreases both due to the decrease of $\tau_s(T_L)$ and the increase of $D_s^0(T_L)$. The quantitative correctness of our previous results for the spin relaxation time and diffusion coefficient is confirmed by comparison with a parameter-free FEM simulation. For each T_L we numerically calculate $S_z(r, B_{xy})$ from Eq. (3.30) using the τ_s, A_D, and D_s^0 obtained in the previous section 7.2.1. For all temperatures we find good agreement between the experimental data and the FEM solution. This self-consistency of our cw MOKE microscopy data indeed demonstrates that we have successfully accounted for all hot carrier effects both in the spatially resolved electron spin detection as well as the electron spin diffusion.

7.2.3 Summary and conclusions

We have synthesized our insights on hot electron effects on both the magneto-optical electron spin detection and the electron spin diffusion process. Using probe energies which correctly yield $S_z(r)$ we have investigated the lattice temperature dependence of the electron spin diffusion coefficient. We have employed a modified spin diffusion model which accounts for the influence of hot electrons by introducing a spatially varying spin diffusivity. Our model yields excellent agreement with the experimental data for all experimental conditions. The temperature dependence of the parameters which describe the spatial variation of D_s is fully consistent with the cooling behavior of conduction band electrons in GaAs. Our analysis demonstrates that at low T_L the spin diffusivity D_s is massively enhanced close to the pump spot by hot photocarri-

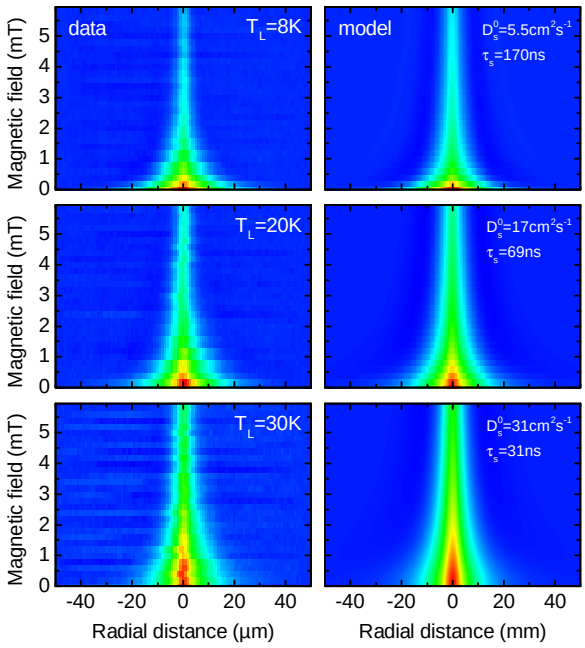

Figure 37: Steady-state electron spin diffusion in external transverse magnetic fields. The figure compares magneto-diffusion profiles $S_z(B_{xy}, r)$ measured at $T_L = 8$ K, 20 K, and 30 K (left) with parameter-free finite element method (FEM) solutions of the modified diffusion model (right, compare text). The color map represents the normalized spin polarization $S_z(r, B_{xy})$ ranging from high (red) to low (dark blue). The spin diffusion coefficients and spin relaxation times used in the FEM simulation have been determined independently from the Hanle-MOKE and Kerr microscopy measurements shown in Figs. 36 and 35 and are indicated in the respective panels.

ers. Moreover, the model is capable of separating the intrinsic spin diffusivity from the hot electron contribution, and allows us to obtain spin transport parameters of the undisturbed system. These parameters have been verified by complementary magneto-diffusion measurements.

7.3 Continuous-wave MOKE microscopy of electron spins in (110) quantum wells

In section 7.1 we have demonstrated how spin-unrelated changes in the local Kerr rotation spectrum potentially adulterate electron spin MOKE microscopy measurements in bulk semiconductors. For bulk GaAs we have demonstrated that the local modifications of the magneto-optical coefficient are due to temperature gradients in the electron system. Similar to bulk semiconductors, photocarrier heating is also routinely observed in QWs [27, 28]. Moreover, the spectral linewidth of excitonic optical resonances in

QWs are known to be strongly affected by changes in the carrier density [172–174]. It therefore stands to reason that the spatially resolved MOKE detection of electron spins in QW 2DEGs is similarly affected by local changes in the Kerr rotation spectrum as for the case of bulk semiconductors. In the following we will demonstrate for the (110) QW sample M4_2661 that this is indeed the case.

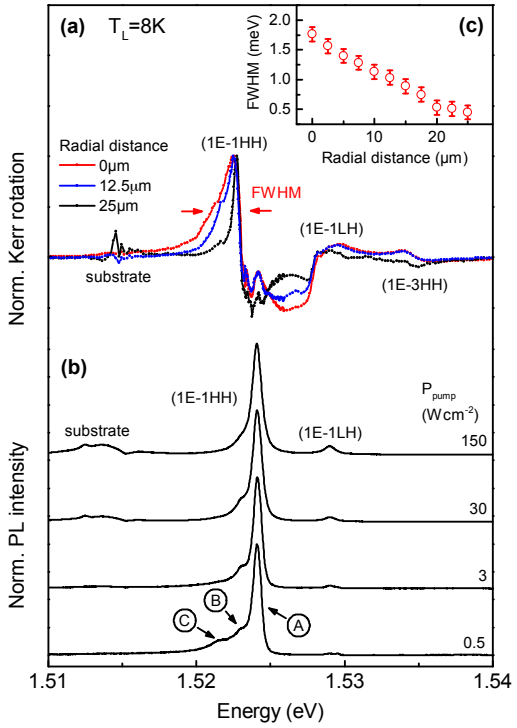

Figure 38: (a) Normalized local Kerr rotation spectra $\theta_K(E_{\text{probe}})$ of the (110) QW sample M4_2661 for different distances to the pump spot. Optical transitions contributing to the Kerr rotation are indicated by text labels. **(b)** Normalized PL spectra for increasing pump intensity ($\lambda_{\text{pump}} = 7850\,\text{Å}$). Labels A to C indicate different contributions to the fine structure of the (1E-1HH) transition which are resolved at low pump intensities (compare section 6.2). All spectra measured at $T_L = 8\,\text{K}$. Inset **(c)** Spectral FWHM of the low-energy wing of the (1E-1HH) Kerr rotation resonance (indicated in (a) by red arrows) as a function of distance to the pump spot.

In Fig. 38 (a) we compare local cw Kerr rotation spectra $\theta_K(E_{\text{probe}})$ measured at $T_L = 8\,\text{K}$ for different distances (0 µm, 12.5 µm, and 25 µm) to the pump spot. The pump wavelength is $\lambda_{\text{pump}} = 7800\,\text{Å}$ and $P_{\text{pump}} = 10\,\mu\text{W}$. The probe laser power is 50 µW. For comparison we also show PL spectra measured for different excitation densities. The PL transitions are identified in section 6.2.

In all Kerr rotation spectra we see strong contributions from the (1E-1HH) and (1E-1LH) transitions which are also present in the PL spectra. At $\approx 1.534\,\text{eV}$ we observe

an additional weak resonance in the Kerr rotation spectrum which we attribute to the (1E-3HH) transition. This transition is absent in PL since at low T_L the lower valence subbands are not populated by holes. It is, however, resolved in the Kerr rotation spectrum because of the spin-dependent Pauli blockade and an energetic splitting of the $\sigma^{\pm}$ transitions due to the spin polarized electrons in the lowest (1E) conduction subband [162, 182, 183]. Furthermore, the individual contributions of the transitions A to C of the (1E-1HH) resonance fine structure (compare section 6.2) are resolved in the Kerr rotation spectra. This underlines the significantly more complex structure of the Kerr rotation spectrum of the (110) QWs as compared to the bulk GaAs sample.

The position dependence of the Kerr rotation spectrum is qualitatively similar to our observations in bulk GaAs: At the pump spot center the resonances are spectrally very broad, but become significantly more narrow when moving away from the pump spot. For the (110) QWs, however, the mechanism leading this spatial variation of the magneto-optical coefficient is likely more complex than for the case of bulk GaAs. In addition to the carrier temperature $T_e(r)$, excitonic resonance linewidths in QWs are strongly influenced by scattering with other excitons and free carriers [174, 199, 200] whose density for the undoped QW sample strongly varies with the distance to the pump spot. These scattering processes are expected to be more important in QWs than in bulk samples because screening of the Coulomb interaction is weaker in low-dimensional systems [199].

In Fig. 38 (a) we observe that the position-dependence of the spectral width of the Kerr rotation resonances is most pronounced for the low-energy wing of the (1E-1HH) transition. This spectral region, however, is of most importance for MOKE microscopy where the probe laser energy is commonly tuned very slightly below the maximum of the lowest optical resonance in an attempt to minimize probe light absorption [15].

In Fig. 38 (b) we show that the spectral FWHM of the low-energy Kerr resonance peak strongly decreases from $\approx 1.8\,\mathrm{meV}$ at the center of excitation to $0.5\,\mathrm{meV}$ for $r \gtrsim 20\,\mu\mathrm{m}$. The implications for cw pump-probe MOKE microscopy are similar to the case of bulk GaAs: the spatial dependence of the Kerr rotation on $S_z(r)$ will be masked by the concurrent spin-unrelated spectral transfer of oscillator strength within the Kerr rotation spectrum. Therefore, again, the local spin polarization in general is not determined correctly from a measurement of the lateral Kerr rotation profile.

For the bulk GaAs sample 11889 we have determined $S_z(r)$ from a quantitative analysis of the local cw Kerr rotation spectrum using a single Lorentzian resonance model. For the (110) QW sample such an analysis is not feasible because of the significantly more complex structure of the electronic states involved in the Kerr rotation spectrum. In the following chapter we therefore present picosecond time-resolved Kerr microscopy with a broadband probe laser as an alternative approach for the measurement of electron spin diffusion coefficients.

Chapter 8

Time-resolved electron spin dynamics in quantum wells

The following chapter is a brief detour from our investigation of hot carrier effects which we use to demonstrate that our newly developed supercontinuum fiber-laser based MOKE microscope is operational for time-resolved spectroscopy. We present two different applications which illustrate the main capabilities of our instrument, the observation of the coherent spin transfer across a semiconductor heterointerface and picosecond real-space imaging of electron spin diffusion in (110) QWs. These examples demonstrate our instrument's unique coverage of an exceptionally broad energy range by a single laser source, and its high spatial and temporal resolution which allows for the time-resolved observation of electron spin transport in semiconductors.

8.1 Coherent spin transfer across a semiconductor heterointerface

We first demonstrate the two-color capabilities of our instrument. We therefore investigate the coherent spin transfer across a heterointerface between two semiconductors with strongly different band gaps. Such an investigation [201,202] requires pulsed pump and probe lasers which are independently tunable over a wide energy range and is therefore not possible using conventional degenerate pump-probe MOKE spectroscopy.

We examine the electron spin dynamics in the MDQW sample M4_2807. Here our long-term goal is the investigation of electron spin diffusion in degenerate ultrahigh-mobility 2DEGs using time-resolved MOKE microscopy. For low-dimensional degenerate electron systems the spin transport properties are expected to be strongly modified with respect to the charge transport by the spin Coulomb drag [96, 203, 204]. In high-mobility 2DEGs embedded in (110) QWs, non-conventional electron spin diffusion profiles have been repeatedly observed in cw MOKE microscopy studies [83, 168]. Moreover, for 2DEGs in GaAs QWs with charge mobilities comparable to our sample, Ref. [96] infers from aberrations from the usual decay characteristics of TSG amplitudes that at low T_L a crossover from diffusive to ballistic spin propagation takes place. Taken together, these observations make degenerate high-mobility MDQW 2DEGs promising systems for the observation of new spin transport physics.

8.1.1 Layer selective optical spin injection and detection

A crucial first step for picosecond MOKE microscopy studies is the verification of successful optical spin injection and spin detection. For single QWs containing a high density electron gas, nonresonant optical creation of an appreciable spin polarization can be challenging due to the small absorption coefficient of the QWs [168]. Such weak QW absorption is indeed observed in Fig 39 (a) where we compare low-temperature cw PL spectra of sample M4_2807 for two different excitation conditions. For $\lambda_{\text{pump}} = 7850\,\text{Å}$ (1.579 eV), the photon energy is below the GaAs/AlAs superlattice band gap and absorption of pump light is energetically possible only in the QW and the bulk GaAs layers (compare section 6.2). In this case, only PL which originates from bulk GaAs layers is observed and MDQW luminescence is virtually absent, i.e. below-barrier excitation only leads to negligible electron-hole pair creation in the QW.

The situation changes drastically for excitation with $\lambda_{\text{pump}} = 4440\,\text{Å}$ (2.793 eV) for which strong absorption in the GaAs/AlAs superlattice barriers occurs. Due to the gradual decrease of the relative Al fraction in the barriers, the average superlattice band gap decreases from $\approx 1.92\,\text{eV}$ to 1.67 eV (room temperature values) close to the QW interface. Photocreated carriers in the barrier therefore are guided into the QW where they recombine radiatively with resident electrons. This transfer of photocarriers from the barriers into the QW manifests as the strong MDQW PL observed in Fig. 39 (a) for above-barrier excitation.

From the above observation we anticipate for MOKE spectroscopy that below-barrier optical spin excitation will create spin polarized electrons only in the bulk GaAs layer, but will be inefficient in the QW. When the pump laser energy is tuned above the superlattice barrier band gap, however, optical spin excitation in the 2DEG is possible if the electrons retain their spin orientation while relaxing from the GaAs/AlAs barrier into the QW. To validate this conjecture and to establish the time scale on which the electron transfer from the barrier into the QW takes place we perform two-color TRKR spectroscopy using our supercontinuum MOKE instrumentation.

To selectively excite spin polarized electrons either in the QW or the superlattice barriers we use two different spectral slices of the pump laser supercontinuum. For below-barrier excitation we use a Thorlabs FBH780-10 dielectric bandpass filter which yields a central pump wavelength of 7800 Å (1.58 eV) with a spectral FWHM of 100 Å ($\approx 20\,\text{meV}$). Above-barrier excitation is achieved using a Thorlabs FBH-650-40 bandpass filter which yields a pump laser spectrum with a central wavelength of 6500 Å (1.91 eV) and a bandwidth of 400 Å ($\approx 120\,\text{meV}$). For all measurements presented below, $T_L = 8\,\text{K}$ and the time-averaged pump laser power is 6 µW. The probe laser power is 12 µW. The overlapping pump and probe spots are defocused to a spot size of $\approx 40\,\mu\text{m}$ to suppress lateral spin diffusion effects on the TRKR traces.

In Fig. 39 (b) we compare Kerr rotation spectra $\theta_K(\lambda_{\text{probe}})$ which we measure for both excitation conditions. We therefore tune the probe laser wavelength from 8000 to

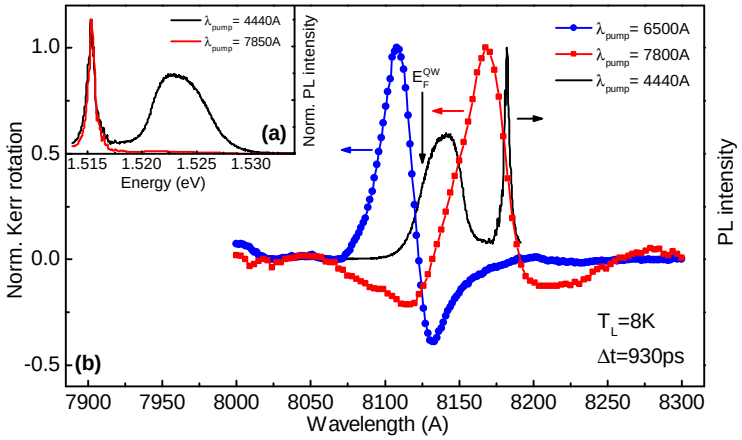

Figure 39: Two-color TRKR spectroscopy on the MDQW sample M4_2807. Inset **(a)** Normalized cw PL spectra for above (black) and below-barrier excitation (red). The excitation density is $< 0.1\,\mathrm{W\,cm^{-2}}$. Note the absence of QW luminescence for low-energy excitation. **(b)** Normalized Kerr rotation spectra $\theta_K(\lambda_{\mathrm{probe}})$ for excitation below (red) and above (blue) the GaAs/AlAs superlattice barrier band gap measured at a pump-probe delay $\Delta t = 930\,\mathrm{ps}$. The solid black line shows the cw PL for comparison. The vertical arrow indicates the spectral position of the 2DEG Fermi edge. All spectra for $T_L = 8\,\mathrm{K}$.

8300 Å by systematically varying the calibrated position of the focussing lens in our supercontinuum spectral slicing instrumentation (compare section 5.1.2). We choose a sufficiently long pump-probe delay $\Delta t = 930\,\mathrm{ps}$ to allow for the photoexcited electrons for above-barrier excitation to relax into the QW.

For low-energy excitation we observe a Kerr rotation resonance centered at $\approx 8180\,$Å which we assign to the 100 nm bulk n-GaAs layer. This assignment will be verified in the following by a measurement of the effective g-factor of the electron population associated with the resonance. When changing to above-barrier excitation the Kerr rotation spectrum undergoes a marked transition. A strong blueshift of the Kerr rotation resonance energy is observed. The zero-crossing of $\theta_K(\lambda_{\mathrm{probe}})$ now coincides with the Fermi edge E_F^{QW} of the MDQW 2DEG. In the spectral vicinity of 8180 Å no signatures of the bulk excitonic resonance is observed in the Kerr rotation spectrum, indicating that only a negligible spin polarization is excited in the bulk layers. This is expected from the high pump energy $1.91\,\mathrm{eV} > (E_0 + \Delta_{\mathrm{so}})$, for which the electrons excited from the LH and SO band compensate the spin polarization generated from the HH transition (compare section 2.3).

From the above observations we conclude that for high energy-excitation the Kerr rotation signal is exclusively due to the spin polarized 2DEG. Our measurements demonstrate that our two-color MOKE spectroscopy technique allows for the layer-selective optical spin injection and spin detection. The appropriate choice of the pump wavelength allows to selectively excite electron spin polarization in either the bulk GaAs layer or the MDQW 2DEG. The continuously tunable supercontinuum probe laser al-

lows us to selectively measure the electron spin dynamics of the spatially separated electron populations contained in different sample layers. The observed 11 meV energy difference of the peak amplitude position of $\theta_K(\lambda_{\text{probe}})$ for above- and below-barrier excitation is consistent with the 11.2 meV spectral separation of the bulk GaAs PL peak and the 2DEG Fermi edge which corroborates the above conclusion.

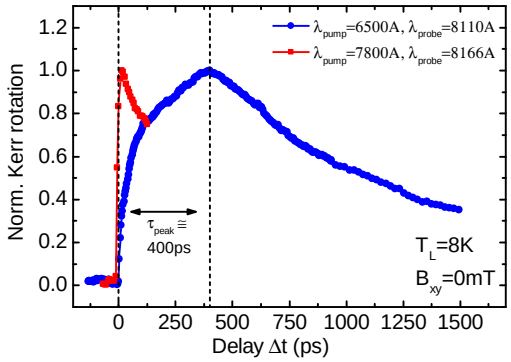

Figure 40: Transient Kerr rotation $\theta_K(\Delta t)$ for excitation below (red) and above (blue) the GaAs/AlAs superlattice barrier band gap at zero external magnetic field B_{xy}. For the measurement of the transients the probe laser wavelength is tuned to the maximum of the respective Kerr rotation spectrum (compare Fig. 39). The dashed vertical lines indicate our initial estimate $\tau_{\text{peak}} \approx 400\,\text{ps}$ for the transfer time of the spin polarized electrons from the barriers into the QW.

We next address the time scale on which the transfer of spin polarized electrons from the superlattice barrier into the QW takes place. We therefore compare in Fig. 40 time traces of the transient Kerr rotation $\theta_K(\Delta t)$ for above- and below-barrier excitation. For the measurement of the time traces we tune the probe laser to the maximum of the respective Kerr rotation resonance [compare Fig. 39 (b)], i.e. we probe $S_z(\Delta t)$ of the bulk GaAs electrons for below-barrier excitation and of the MDQW 2DEG for above-barrier excitation.

For below-barrier excitation, the peak electron spin polarization in the bulk layer is excited quasi-instantaneously and $\theta_K(\Delta t)$ reaches its maximum within the first 13 ps. In contrast, for above-barrier excitation we observe the comparatively slow build-up of $S_z(\Delta t)$ caused by the finite time required by the spin polarized electrons to relax into the QW. The transient $\theta_K(\Delta t)$ reaches its peak amplitude only after a characteristic time $\tau_{\text{peak}} \approx 400\,\text{ps}$. For $\Delta t > \tau_{\text{peak}}$ we observe a monotonic decrease of the 2DEG spin polarization. Here most of the photoexcited electrons have either relaxed from the superlattice into the QW or have lost their spin orientation, and the build-up of the 2DEG polarization by the spin transfer process is completed. Spin relaxation in the QW now dominates the dynamics and leads to the observed decay of the 2DEG polarization. To obtain further insights into the interplay of spin transfer and relaxation in both the barrier and the 2DEG we next turn to the hallmark experiment in TRKR spectroscopy, time-resolved spin quantum beat measurements.

8.1.2 Spin quantum beat spectroscopy

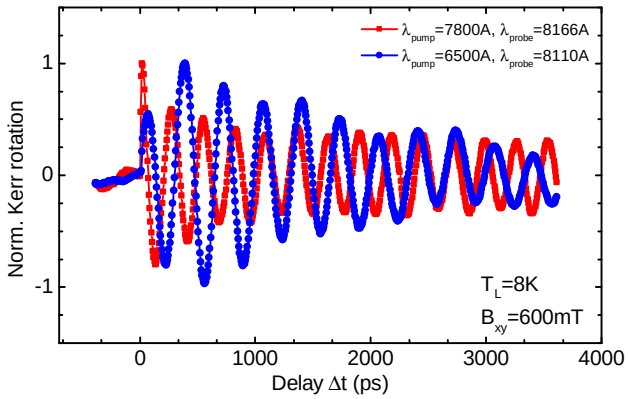

Figure 41: Spin quantum beats in the MDQW 2DEG (blue) and a bulk GaAs layer (red) at $T_L = 8\,\mathrm{K}$. The in-plane external magnetic field is $B_{xy} = 600\,\mathrm{mT}$. For the measurement of the transients the probe laser wavelength is tuned to the maximum of the respective Kerr rotation spectrum (compare Fig. 39). Note the non-monotonic time dependence of the amplitude envelope of the 2DEG trace.

In Fig. 41 we show TRKR traces $\theta_K(\Delta t)$ which we measure for the bulk GaAs layer for below-barrier excitation and for the MDQW 2DEG for above-barrier excitation with an external in-plane magnetic field $B_{xy} = 600\,\mathrm{mT}$. In the bulk GaAs layer, $S_z(\Delta t)$ exhibits a quasi-instantaneous rise to the peak polarization followed by the expected oscillatory decay (compare section 3.2.1). For the MDQW 2DEG, consistent with the zero-field trace of Fig. 40, the amplitude envelope of $S_z(\Delta t)$ rises within the first 400 ps before the decrease of the electron spin polarization sets in.

Comparing both datasets, we find that the Larmor frequency ω_L of the MDQW 2DEG is reduced with respect to the electron spin precession in the bulk GaAs layer. To quantify this observation we plot in Fig. 42 the spin precession angle:

$$\phi(\Delta t) = (|g^*|\,\mu_B B_{xy}/\hbar)\,\Delta t \tag{8.1}$$

which we extract from the maxima and minima (corresponding to precession angles equal to integer multiples of π) of the TRKR traces. From the slope of a linear fit of Eq. (8.1) to the experimental data we obtain an effective electron g-factor $|g^*| = (0.438 \pm 0.004)$ of the electron population observed for below-barrier excitation.[13] This value precisely coincides with the accepted literature value for the low-temperature electron g-factor of bulk GaAs [72]. We thereby confirm our previous assignment of electron spins in the bulk GaAs layer as the origin of the Kerr rotation resonance for below-barrier excitation.

[13] We note that our optical instrumentation allows for a more precise determination of relative changes in the g-factor. The uncertainty of the absolute value of $|g^*|$ is due to our measurement precision for the external magnetic field B_{xy} which we only know to $\approx (\pm 1\,\%)$ at the sample position.

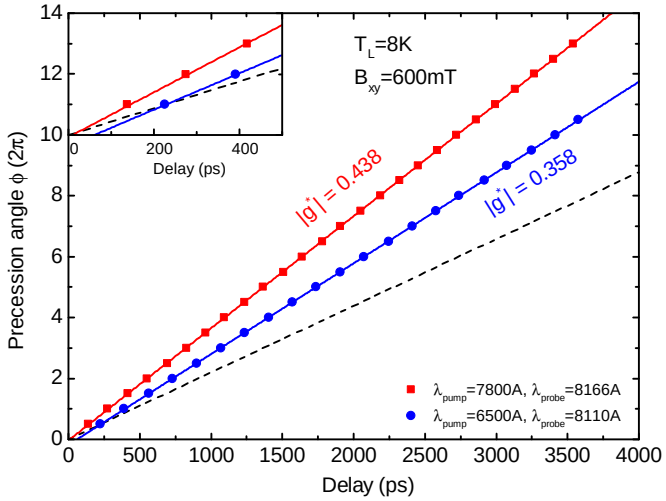

Figure 42: Spin precession angles $\phi(\Delta t)$ of the MDQG 2DEG (blue) and the bulk GaAs layer (red) extracted from the TRKR traces shown in Fig. 41. Solid lines are linear fits which yield the effective g-factors $|g^*| \sim (\partial\phi/\partial\Delta t)$. Note that for the 2DEG the extrapolation $\phi \to 0$ does yield a finite $\Delta t > 0$ (see inset). For comparison, the dashed line indicates the hypothetical spin precession angle for the 2DEG obtained when extrapolating $\phi(\Delta t)$ only from the origin at $\Delta t = 0$ ps to the first spin quantum beat resonance.

A linear fit of Eq. (8.1) to the MDQW 2DEG data measured for above-barrier excitation yields $|g^*_{\mathrm{QW}}| = (0.358 \pm 0.004)$. The observed decrease of $|g^*_{\mathrm{QW}}|$ with respect to the bulk value is likely caused by the increased average energy $\langle E_c \rangle$ of the electrons in the degenerate 2DEG. Ref. [205] reports for GaAs the expression

$$g^*(E_c) = g^*_0 + 6.3 \times E_c(\mathrm{eV}) \tag{8.2}$$

for the dependence of the effective g-factor on the electron kinetic energy. From the conduction band minimum value $g^*_0 = -0.44$ and the Fermi energy $E_F = 7.8$ meV of the 2DEG (compare section 6.2), we obtain a coarse estimate $g^*(E_F) \approx -0.39$ for the electrons at the Fermi edge. This value is in reasonable agreement with our experimental observation. Moreover, our simplistic analysis has neglected the influence of the penetration of the QW electron wave function into the GaAs/AlAs barriers which is expected to lead to an additional decrease of $|g^*_{\mathrm{QW}}|$ [206].

A peculiarity is observed in the inset of Fig. 42 where we show that for the 2DEG a linear extrapolation of the precession angle $\phi(\Delta t) \to 0$ does not yield the expected value $\Delta t = 0$, but a finite time $t_0 \approx 60$ ps. This indicates that for short delays after the optical excitation the electron spins initially precess with a significantly slower Larmor frequency in the barrier before relaxing into the QW (compare the reduced slope of the dashed line in the inset of Fig. 42 which shows the hypothetical 2DEG spin precession

angle obtained when extrapolating $\phi(\Delta t)$ from the origin at $\Delta t = 0\,\mathrm{ps}$ to the first spin quantum beat resonance). To quantify this observation we next use a two population spin transfer model to analyze $S_z(\Delta t)$ of the MDQW 2DEG.

8.1.3 Two population spin transfer model

Following the concept of Ref. [207] we model $S_z(\Delta t)$ by a system of coupled differential equations which describe the time evolution of the in-plane and out of plane components S'_x and S'_z of the electron spin polarization in the GaAs/AlAs superlattice barriers and their respective counterparts S_x and S_z of the MDQW 2DEG. The equations of motion for the spins in the barrier are obtained by including an additional spin transfer term in the usual Bloch equations Eqs. (3.9) - (3.11) as:

$$\frac{d}{dt}S'_x = -\frac{S'_x}{\tau_{\mathrm{tr}}} - \frac{S'_x}{T^*_{\mathrm{b}}} + \omega'_L S'_z \tag{8.3}$$

$$\frac{d}{dt}S'_z = -\frac{S'_z}{\tau_{\mathrm{tr}}} - \frac{S'_z}{T^*_{\mathrm{b}}} - \omega'_L S'_x \tag{8.4}$$

Here $\omega'_L = (g^*_b \mu_B B_{xy}/\hbar)$ is the Larmor frequency associated with the effective g-factor g^*_b of the barrier and T^*_b is the electron spin lifetime in the barrier. The spin transfer terms $-(S'_{x,z}/\tau_{\mathrm{tr}})$ account for the additional decay of the spin polarization in the barrier due to the relaxation of electrons into the QW. The solutions for Eqs. (8.3) and (8.4) are:

$$S'_x(\Delta t) = S'_0 \exp\left(-\frac{\Delta t}{\tau_{\mathrm{eff}}}\right) \sin\left(\omega'_L \Delta t\right) \tag{8.5}$$

$$S'_z(\Delta t) = S'_0 \exp\left(-\frac{\Delta t}{\tau_{\mathrm{eff}}}\right) \cos\left(\omega'_L \Delta t\right) \tag{8.6}$$

where we have introduced the effective spin lifetime $\tau_{\mathrm{eff}} = (1/T^*_b + 1/\tau_{\mathrm{tr}})^{-1}$.

Similar to Eqs. (8.3) and (8.4), the time evolution of the MDQW 2DEG spin polarization components is governed by:

$$\frac{d}{dt}S_x = +\frac{S'_x}{\tau_{\mathrm{tr}}} - \frac{S_x}{T^*_{\mathrm{QW}}} + \omega_L S_z \tag{8.7}$$

$$\frac{d}{dt}S_z = +\frac{S'_z}{\tau_{\mathrm{tr}}} - \frac{S_z}{T^*_{\mathrm{QW}}} - \omega_L S_x \tag{8.8}$$

with the Larmor frequency $\omega_L = (g^*_{\mathrm{QW}} \mu_B B_{xy}/\hbar)$ and the 2DEG spin lifetime T^*_{QW}. The first term on the right-hand side of Eqs. (8.7) and (8.8) describes the coherent spin transfer from the barrier into the QW which leads to the observed slow rise of $S_z(\Delta t)$. Using the initial condition $S_{z,x}(\Delta t = 0) = 0$ (i.e. spin polarized electrons are exclusively created in the barrier), the solution of the coupled Bloch equations for the out-of-plane

component of the MDQW 2DEG which we observe in our measurement is [207]:

$$S_z(\Delta t) = A\left[\exp\left(-\frac{\Delta t}{T_{QW}^*}\right)\cos\left(\omega_L \Delta t + \varphi\right) - \exp\left(-\frac{\Delta t}{\tau_{\text{eff}}}\right)\cos\left(\omega \Delta t + \varphi\right)\right] \tag{8.9}$$

with $A = S_0'/\left(\tau_{\text{tr}}\sqrt{a^2+b^2}\right)$, $a = 1/\tau_{\text{eff}} - 1/T_{\text{QW}}^*$, $b = \omega_L' - \omega_L$, and $\varphi = \tan^{-1}(b/a)$.

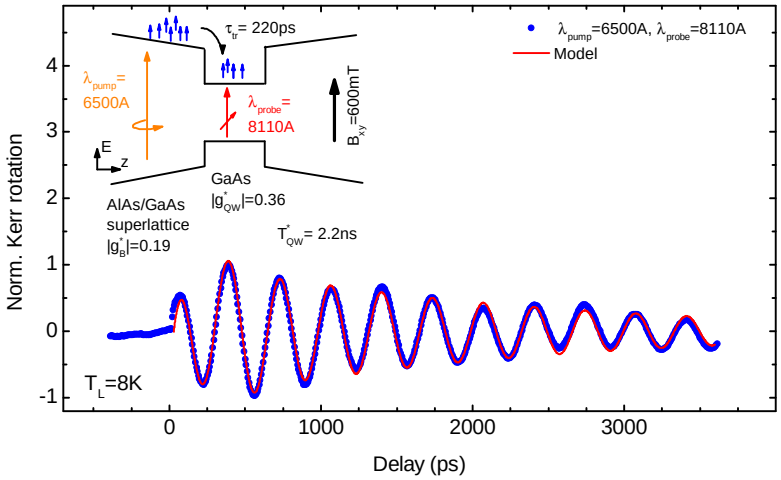

Figure 43: Two population model for $S_z(\Delta t)$ of the MDQW 2DEG. The inset shows a coarse schematic of the band structure of the graded GaAs/AlAs barriers and the GaAs QW. Text labels indicate the parameters (effective g-factors, spin transfer time, and 2DEG spin dephasing time) extracted from the fit of the model (red solid line, compare text) to the experimental data (blue markers).

In Fig. 43 we show the best fit of the $S_z(\Delta t)$ solution Eq. (8.9) to the experimental data. We find excellent agreement over the whole examined delay Δt. From the fit we obtain for the GaAs/AlAs barriers an average g-factor $g_b^* = (0.19 \pm 0.03)$. The MDQG 2DEG g-factor is $|g_{\text{QW}}^*| = (0.359 \pm 0.004)$ which agrees with the value obtained previously from the linear fit of the $\phi(\Delta t)$ data (compare Fig. 42). The spin transfer time is $\tau_{\text{tr}} = (220 \pm 30)\,\text{ps}$. Because of this short transfer time, the decrease of $S_{x,z}'$ in the barrier is dominated by the transfer into the QW. Therefore, only a lower bound $T_b^* \gtrsim 1\,\text{ns}$ for the spin lifetime in the barrier can be extracted from the model. For the electron spin lifetime of the MDQW 2DEG, the two-population model yields $T_{\text{QW}}^* = (2.2 \pm 0.2)\,\text{ns}$.

In Fig. 44 we show an independent confirmation of our T_{QW}^* result which we derive from cw Hanle-MOKE spectroscopy. We therefore measure, using strongly defocused pump and probe spots ($> 150\,\mu\text{m}$), the depolarization $S_z(B_{xy})$ for cw above-barrier excitation ($\lambda_{\text{pump}} = 6350\,\text{Å}$, $P_{\text{pump}} = 50\,\mu\text{W}$).[14] For the electron spin detection we tune the

[14] Continuous-wave above-barrier excitation is provided by a Coherent Cube diode laser.

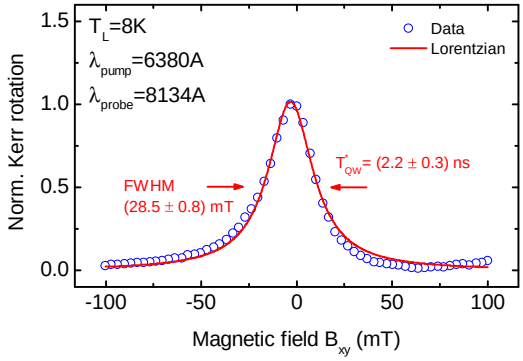

Figure 44: Continuous-wave Hanle-MOKE measurement on the MDQW 2DEG for above-barrier excitation with $\lambda_{\text{pump}} = 6350\,\text{Å}$ at $T_L = 8\,\text{K}$. The excitation density is $< 0.1\,\text{W}\,\text{cm}^{-2}$. The FWHM $B_{1/2} = (25.8 \pm 0.8)\,\text{mT}$ of the Lorentzian fit (red solid line) corresponds to a spin dephasing time $T^*_{\text{QW}} = (2.2 \pm 0.3)\,\text{ns}$.

Ti:Sa probe laser energy slightly below the 2DEG Fermi edge ($\lambda_{\text{probe}} = 8134\,\text{Å}$, $P_{\text{probe}} = 10\,\mu\text{W}$). A Lorentzian fit to the measured Hanle curve yields $B_{1/2} = (25.8 \pm 0.8)\,\text{mT}$. Because of the very low excitation densities used in this measurement ($< 0.1\,\text{W}\,\text{cm}^{-2}$) and the high MDQW 2DEG concentration, the width of the Hanle curve directly yields the electron spin lifetime. Using the effective g-factor g^*_{QW} obtained from TRKR spectroscopy, the spin lifetime is determined as $T^*_{\text{QW}} = (2.2 \pm 0.3)\,\text{ns}$. This value is in excellent agreement with the two population spin transfer model and provides an independent confirmation of the validity of our theoretical approach.

8.1.4 Summary and conclusions

We have demonstrated the operation of our time-resolved supercontinuum MOKE spectroscopy instrumentation. We have chosen an exemplary application which illustrates our instrument's capability to provide independently tunable pulsed pump and probe lasers. We therefore have studied the coherent transfer of electron spin polarization across a GaAs/AlAs interface in a MBE-grown heterostructure. Our measurements demonstrate that our two-color technique allows us to selectively excite and probe the electron spin polarization in a bulk GaAs layer and a MDQW 2DEG using an appropriate choice of pump and probe wavelengths.

We have quantitatively analyzed the transient Kerr rotation of the MDQW 2DEG for above-barrier spin excitation using a two population spin transfer model. Our analysis shows that the transfer of electron spins from the barrier into the QW takes place on a timescale of 230 ps and yields additional information on the QW and superlattice barrier effective g-factors and spin lifetimes. An independent cw Hanle-MOKE measurement of the MDQW 2DEG spin relaxation time has shown quantitative agreement with the result obtained from the spin transfer model.

8.2 Time-resolved electron spin dynamics in (110) quantum wells

We next turn to the investigation of the time-resolved electron spin dynamics in the GaAs (110) QW sample M4_2661. We have previously shown for this sample that local modifications of the magneto-optical coefficient prevent the correct spatially resolved electron spin detection by cw MOKE spectroscopy with a specially narrow Ti:Sa probe laser (compare section 7.3). We here take advantage of the broad spectral width of our tunable supercontinuum probe laser which allows us to circumvent the detrimental influence of local changes in the Kerr rotation spectrum in our time-resolved electron spin microscopy measurements.

8.2.1 Broadband supercontinuum electron spin detection

For pulsed optical spin excitation we spectrally filter the supercontinuum pump laser using a Thorlabs FBH780-10 dielectric bandpass filter (central wavelength 7800 Å, spectral FWHM 100 Å). The absorption of below-barrier pump light in the five identical (110) QWs in sample M4_2661 is sufficiently strong to excite an appreciable electron spin polarization. For the time-resolved electron spin detection we tune the central supercontinuum probe laser wavelength to the (1E-1HH) resonance at 8140 Å (compare section 7.3). In Fig. 45 we show the resulting pump and probe laser spectra together with a representative cw Kerr rotation spectrum $\theta_K(\lambda_{\text{probe}})$ of the (110) QW sample. Comparing both datasets we find that the $\approx 5\,\text{meV}$ spectral FWHM of the pulsed probe laser allows us to simultaneously probe the entire low-energy wing of the (1E-1HH) Kerr rotation resonance. The broadband Kerr rotation detection is therefore much less affected by a spectral transfer of oscillator strength within this observation window. In contrast to cw MOKE microscopy with the spectrally narrow Ti:Sa laser, we thereby suppress the detrimental effects of the spatially varying magneto-optical coefficient on the electron spin detection.

We have verified that the time-resolved Kerr microscopy results presented below do not change within experimental resolution under variation of the probe laser wavelength. For all measurements the time-averaged probe laser power is 12 µW. The pump power is varied between 1.5 µW and 5 µW as indicated in the text.

8.2.2 Spin quantum beats, resonant spin amplification, and anisotropic spin relaxation

Before addressing electron spin diffusion we briefly detour and examine the electron spin relaxation in the (110) QWs. In Fig. 46 (a) we show $\theta_K(\Delta t, r = 0)$ traces which we measure, using focused pump and probe lasers, at $T_L = 8\,\text{K}$ and $P_{\text{pump}} = 5\,\mu\text{W}$ for different in-plane magnetic fields B_{xy}. The spin precession angle $\phi(\Delta t)$ which we extract from these TRKR transients is shown in Fig. 46 (b). We observe the expected dependence $(\partial\phi/\partial\Delta t) \sim B_{xy}$ of the Larmor frequency on the magnetic field strength. From a linear fit to the $\phi(\Delta t)$ data obtained for the strongest magnetic field $B_{xy} = 600\,\text{mT}$,

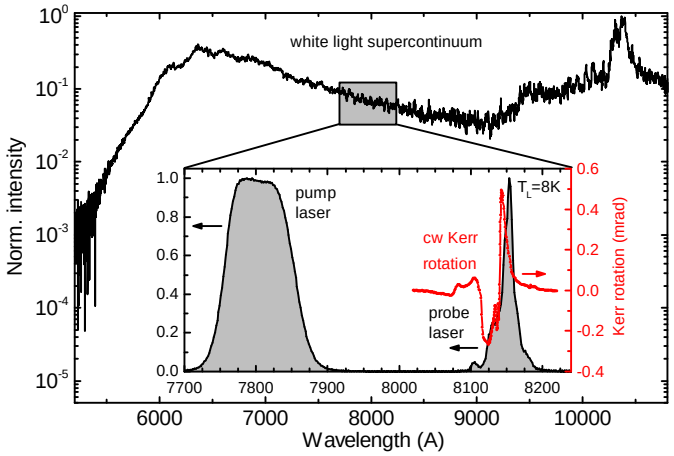

Figure 45: Spectral slicing of the "white light" supercontinuum for time-resolved MOKE microscopy on the (110) QW sample M4_2661. Inset: Normalized intensity spectra of the pulsed pump and probe lasers after spectral filtering (left axis, black). The spectral range of the inset is indicated by the gray box. The cw Kerr rotation $\theta_K(\lambda_{\text{probe}})$ measured at $T_L = 8\,\text{K}$ is shown on the right axis (red).

which allows for the most precise determination of the in-plane effective g-factor, we obtain $|g^*| = (0.402 \pm 0.004)$. The measured g^* significantly deviates from the bulk GaAs value of –0.44. Moreover, no signatures of a second precession frequency are observed in the Fourier transform power spectrum of the $\theta_K(\Delta t)$ traces (not shown here). Taken together these observations confirm that the broadband-detected Kerr rotation is only due to electron spins in the QW and does not contain relevant contributions from the bulk sample substrate.

For focused excitation $S_z(\Delta t, r = 0)$ decays due to the combined action of electron spin relaxation, out-diffusion away from the pump spot center, and concurrent photocarrier recombination. The radiative lifetime of photoexcited electron-hole pairs in the nominally undoped (110) QWs is $\tau_{\text{rad}} \lesssim 700\,\text{ps}$.[15] This radiative lifetime constitutes an upper bound for the electron spin lifetime in an intrinsic (i.e. undoped) system. Pronounced Larmor spin precession is, however, still observed in the $\theta_K(\Delta t, r = 0)$ transients up to the maximum experimentally accessible delay of 3.6 ns. For such sufficiently long delays $\Delta t \gg \tau_{\text{rad}}$ all excess photocarriers have recombined and the QW 2DEG density has returned to the equilibrium value. The $\theta_K(\Delta t)$ transients therefore strongly suggest, consistent with the previous observation of X^- negative trion PL (compare section 6.2), the presence of a dilute electron gas in the intentionally undoped

[15] We determine the radiative lifetime for below-barrier excitation using standard time-correlated single photon counting (TCSPC) spectroscopy [208]. Following the usual approach, we analyze the measured TCSPC traces by fitting the convolution of the measured instrument response function (IRF) and the solution of a rate equation model from which τ_{rad} is obtained. For $T_L = 5$-$30\,\text{K}$ the measurements yield an upper bound $\tau_{\text{rad}} \lesssim 700\,\text{ps}$.

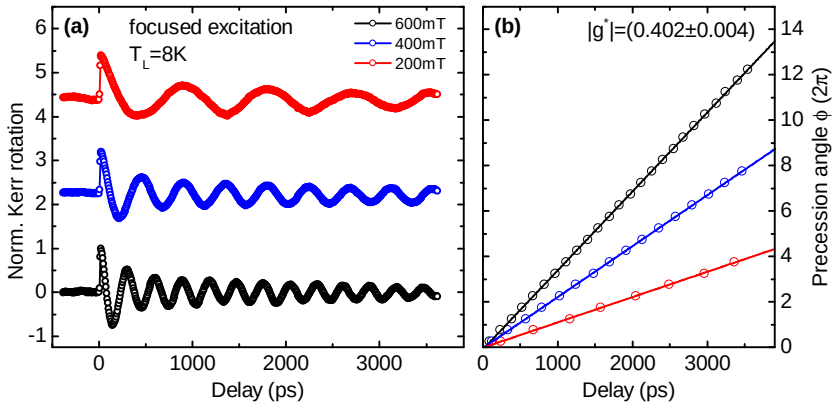

Figure 46: Spin quantum beats in the (110) QW 2DEG. **(a)** Normalized transient Kerr rotation $\theta_K(\Delta t, r=0)$ measured for increasing external in-plane magnetic fields (top to bottom). The lattice temperature is $T_L = 8\,\mathrm{K}$ and $P_{\mathrm{pump}} = 5\,\mu\mathrm{W}$. **(b)** Spin precession angles $\phi(\Delta t)$ of the QW 2DEG extracted from the TRKR traces shown in (a). Solid lines are linear fits which yield the effective in-plane g-factor $|g^*| \sim (\partial\phi/\partial\Delta t)$.

QWs in which the spin polarization is preserved for long times.

Exceptionally long spin lifetimes in this dilute electron gas and signatures of the anisotropic spin relaxation in the (110) QW 2DEGs are indeed observed in the cw Hanle-MOKE traces shown in Fig. 47 (a). For the Hanle measurements below-barrier optical excitation is provided at $\lambda_{\mathrm{pump}} = 7800\,\text{Å}$. For the steady-state spin detection the cw probe laser energy is tuned below the (1E-1HH) resonance ($\lambda_{\mathrm{probe}} = 8143\,\text{Å}$, $P_{\mathrm{probe}} = 50\,\mu\mathrm{W}$) to minimize probe laser absorption. At $T_L = 8\,\mathrm{K}$ we measure, using strongly defocused pump and probe lasers ($> 100\,\mu\mathrm{m}$), the depolarization $S_z(B_{xy})$ for increasing excitation densities. In Fig. 47 (b) we show the HWHM $B_{1/2}$ of Lorentzian fits to the resulting Hanle curves. Contrary to the isotropic spin relaxation in bulk n-GaAs where $B_{1/2} \sim \Gamma_s$ increases linearly with P_{pump} (compare Fig. 36), we here find a sublinear dependence of the spin relaxation rate $\Gamma_s \equiv 1/\tau_s$ on the pump power. This sublinear increase of Γ_s with optical excitation density is characteristic for the spin relaxation anisotropy in (110) QWs as detailed below.

Using the effective g-factor $|g^*| = 0.402$ obtained from the TRKR measurements, we calculate the excitation density dependence of the effective spin relaxation time $\tau_s(P_{\mathrm{pump}})$ which is shown in the inset of Fig. 47 (b). In the limit of vanishing optical excitation we observe an exceptionally long $\tau_s \gtrsim 100\,\mathrm{ns}$. This value is close to the highest 2DEG spin dephasing times reported in the literature [45, 46], demonstrating that, due to the symmetry-based suppression of the DP relaxation mechanism, electron spin polarization can be stored in dilute electron gases in symmetric (110) QWs for remarkably long times. With increasing pump power the spin lifetime decreases to $\tau_s \approx 20\,\mathrm{ns}$.

A qualitative model for the pump power dependence of the electron spin relaxation in

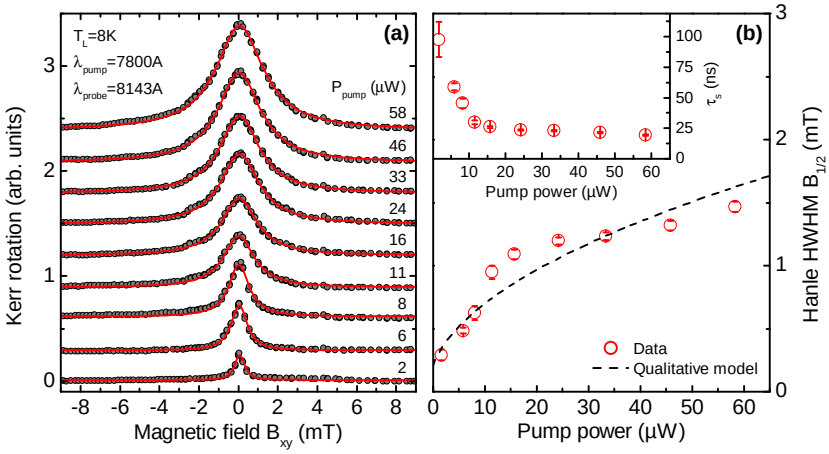

Figure 47: Continuous-wave Hanle-MOKE measurements on the (110) QW 2DEGs. **(a)** Hanle curves $S_z(B_{xy})$ (gray markers) for increasing excitation power (bottom to top) together with Lorentzian fits (red solid lines). **(b)** Half width at half maximum (HWHM) $B_{1/2}$ of the Lorentzian Hanle curves as a function of P_{pump}. The sublinear pump power dependence $B_{1/2}(P_{\text{pump}})$ is characteristic for the anisotropic spin relaxation in (110) QWs. The black dashed line is a fit of the qualitative model Eq. (8.12) for the anisotropic spin relaxation in (110) QWs (see text). The inset shows the effective spin relaxation time $\tau_s(P_{\text{pump}})$. All measurements are performed at $T_L = 8\,\text{K}$.

modulation-doped (110) QWs has been proposed in Refs. [83, 168]. The suppression of the Dyakonov-Perel relaxation for the out-of-plane spin component S_z results in a strong anisotropy of the electron spin relaxation rates in (110) QWs (compare section 3.1.2). As a result, the effective electron spin lifetime:

$$\tau_s = \sqrt{\tau_z \tau_\parallel} \tag{8.10}$$

extracted from the HWHM of cw Hanle-MOKE traces $S_z(B_{xy})$ is the geometric mean of the out-of-plane and in-plane spin dephasing times τ_z and $\tau_\parallel$. For the out-of-plane spin polarization S_z, the decay rate [168]:

$$1/\tau_z = 1/\tau_z^{\text{lim}} + \gamma_z^{\text{BAP}} n_h + \gamma^r n_h \tag{8.11}$$

is due to three different contributions. Here τ_z^{lim} is the intrinsic spin dephasing time in the limit of zero optical excitation. At high temperatures τ_z^{lim} is typically believed to be limited by intersubband electron scattering induced spin relaxation [38, 39]. At low T_L, out-of-plane spin dephasing is attributed to DP relaxation in the random Rashba fields of ionized impurities in the QW barriers [168]. The spin relaxation rate $\gamma_z^{\text{BAP}} n_h$ due to the BAP mechanism and the radiative recombination rate $\gamma^r n_h$ are both proportional to the optically excited hole density n_h, and $\Gamma_z = (1/\tau_z)$ therefore strongly increases with P_{pump}. In contrast, for the in-plane spin components S_{xy}, DP relaxation is dominant and $\Gamma_\parallel = (1/\tau_\parallel)$, to a first approximation, does not depend on $n_h \sim P_{\text{pump}}$. Therefore, from

Eqs. (8.10) and (8.11) the effective spin relaxation rate:

$$1/\tau_s \approx 1/\tau_s(0)\sqrt{1+P_{\mathrm{pump}}/P_{\mathrm{sat}}} \tag{8.12}$$

is expected to increase sublinearly with the optical pump power. Indeed, a best fit of Eq. (8.12) to the experimental data shown in Fig. 47 (b) is in qualitative agreement with our measurement. The model therefore provides a useful basic description for the physics underlying the anisotropic steady-state spin relaxation dynamics in (110) QWs. For low pump powers, however, Eq. (8.12) underestimates the increase of $\Gamma_s(P_{\mathrm{pump}})$. This is likely caused by neglecting the influence of radiative recombination on the in-plane spin lifetime $\tau_\parallel$ which is more significant in the very dilute 2DEG in our sample as compared to the strongly n-doped QWs of Refs. [83, 168].

We next return to time-resolved spectroscopy. When probing S_z for short negative delays $\Delta t < 0$, i.e. before the arrival of the corresponding pump pulse, we measure a remanent spin polarization. Because the long spin lifetimes $\tau_z \gtrsim t_{\mathrm{rep}}$ of the (110) QWs are comparable to the $t_{\mathrm{rep}} = 27.5\,\mathrm{ns}$ pulse-to-pulse interval of the supercontinuum source, $S_z(\Delta t)$ results from a superposition of the contributions of several previous pump pulses. The rather long spin lifetimes of the (110) QWs therefore allow for an investigation of the relaxation dynamics by the RSA technique (compare section 3.2.2).

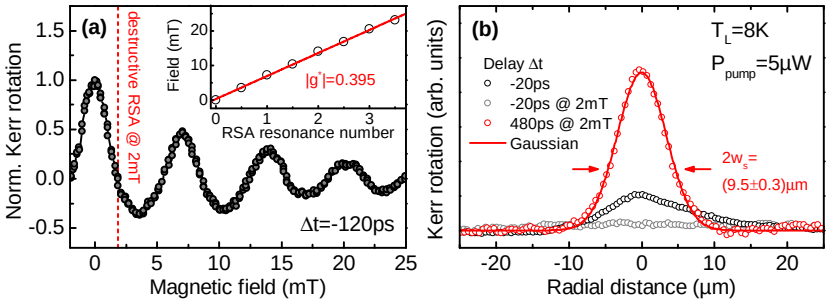

Figure 48: **(a)** RSA trace measured with defocused pump and probe spots. The first destructive interference is observed at $B^*_{xy} = 2\,\mathrm{mT}$. Inset: Magnetic field dependence of the RSA resonance number. The solid line is a linear fit from which the effective g-factor $|g^*| = 0.395$ is deduced. **(b)** Kerr rotation profiles $\theta_K(\Delta t, r)$ measured at short negative and positive delays. Application of $B^*_{xy} = 2\,\mathrm{mT}$ suppresses previous-pulse contributions by destructive RSA (compare gray and black profiles). Solid red line is a Gaussian fit. All data measured at $T_L = 8\,\mathrm{K}$.

In Fig. 48 (a) we show a representative RSA trace which we measure at $T_L = 8\,\mathrm{K}$ for a negative delay $\Delta t = -120\,\mathrm{ns}$. We minimize the influence of diffusion on the measurement by strongly defocusing the pump and probe spots ($> 50\,\mu\mathrm{m}$). This results in a time-averaged excitation density of $\approx 0.25\,\mathrm{W\,cm^{-2}}$. When sweeping the external magnetic field we observe the characteristic RSA oscillations in $S_z(B_{xy})$. From the slope of a linear fit of the constructive RSA resonance fields shown in the inset of Fig. 48 (a)

we determine, in agreement with the earlier spin quantum beat spectroscopy, the in-plane effective g-factor $|g^*| = (0.395 \pm 0.004)$. Most important for the following spin diffusion measurements, however, for specific field amplitudes B^*_{xy} the superposition of the single-pulse contributions precisely cancel each other and $S_z(\Delta t < 0) = 0$. The controlled application of such destructive RSA fields B^*_{xy} therefore allows us to suppress repetition-rate artifacts in our time-resolved spin diffusion microscopy measurements.

8.2.3 Picosecond real-space imaging of electron spin diffusion in (110) quantum wells

We now turn to the measurement of electron spin diffusion coefficients by time-resolved MOKE microscopy. To facilitate the following analysis, we limit our experiment to the contribution of the spin polarization resulting from the excitation by a single pump pulse. The previous-pulse suppression scheme therefore employed is exemplarily shown in Fig. 48 (b) where we compare spin polarization profiles $S_z(r)$ measured at $\Delta t = -20\,\mathrm{ps}$ for zero external magnetic field and $B^*_{xy} = 2\,\mathrm{mT}$. The field is chosen such that $S_z(\Delta t < 0)$ vanishes because of destructive spin interference [compare Fig. 48 (a)].[16] Without magnetic field the previous-pulse spin profile is clearly observed. Application of B^*_{xy} suppresses $S_z(\Delta t < 0, r)$ for all r and $\theta_K(\Delta t > 0)$ is then only due to the newly excited spins.

In Fig. 48 (b) we additionally show a single-pulse profile measured for $\Delta t = 480\,\mathrm{ps}$ and a Gaussian fit from which we determine the width w_s of the spin packet. The amplitude of the previous-pulse spin profile (black markers) is $\approx 25\,\%$ of the peak amplitude of this single-pulse spin profile (red markers). Moreover, since the initial expansion rate of the newly excited spin packet is significantly higher (compare section 3.3.1), the relative amplitude fraction of the previous-pulse profile even increases for longer delays. The reliable suppression of the previous-pulse S_z by applying B^*_{xy} is therefore crucial for the following analysis of our MOKE microscopy data.

To obtain the spin diffusion coefficient D_s of the (110) QW 2DEG we measure time traces of single-pulse spin polarization profiles $S_z(\Delta t, r)$ for increasing pump-probe delays Δt between $-20\,\mathrm{ps}$ and $814\,\mathrm{ps}$. A typical dataset resulting from this procedure, measured for $P_{\mathrm{pump}} = 3\,\mu\mathrm{W}$ at $T_L = 8\,\mathrm{K}$ by scanning r along the $[001]$ crystal direction, is shown in Fig. 49. In contrast to TSG spectroscopy, which only yields incomplete information on the overall amplitude decay of the spin grating, our picosecond imaging technique allows us to directly observe the time evolution of the optically excited electron spin packet in real-space. The diffusive spreading of the spin packet is clearly seen in the dataset from the increasing width of the $S_z(r)$ profiles for longer delays. The decay of the spin packet amplitude results from the combined influence of out-diffusion and spin relaxation.

[16] The external field B^*_{xy} leads to a coherent precession of the spin packet. However, for the weak field amplitude and the short observation window $t_{\mathrm{max}} = 814\,\mathrm{ps}$ of the measurements presented below, this precession only leads to a negligible relative reduction of the out-of-plane component of the spin polarization to a factor of $\cos(g^* \mu_B B_{xy}/t_{\mathrm{max}}/\hbar) = 0.998$ and therefore does not affect our MOKE microscopy measurements.

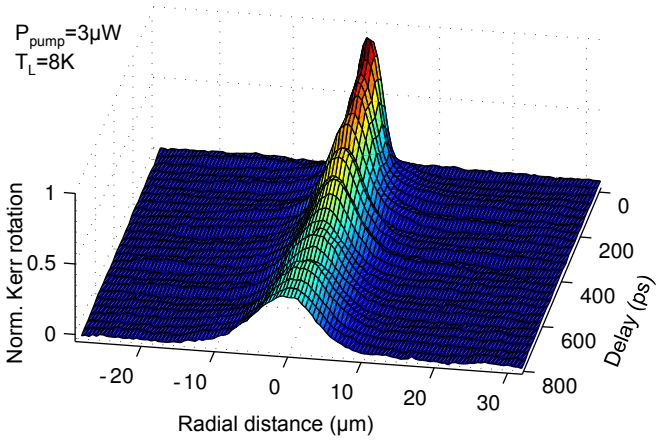

Figure 49: Time-resolved observation of the expansion of an optically excited electron spin packet in a (110) QW 2DEG. The colormap shows line-cuts through the radial-symmetric electron spin polarization profile $S_z(r)$ for increasing delays Δt measured for $P_{\text{pump}} = 3\,\mu\text{W}$ at $T_L = 8\,\text{K}$.

Contrary to cw spectroscopy, picosecond MOKE microscopy unambiguously yields the electron spin diffusion coefficient without relying on auxiliary spin relaxation time measurements. In Fig. 50 (a) we show a series of normalized line cuts of the electron spin polarization profile obtained from the dataset of Fig. 49 together with Gaussian fits. Comparison with these fits confirms that the shape of the spin packet remains Gaussian for all examined times.

In Fig. 50 (b) we plot $w_s^2(\Delta t)$ extracted from the Gaussian fits. For the shortest delay of 13 ps the squared spin packet width coincides with our optical resolution $\sigma_0^2 = 3.8\,\mu\text{m}^2$ indicated by the dashed line. The linear increase of $w_s^2(\Delta t)$ expected from Eq. (3.35) is clearly observed. From the slope of a linear fit we determine the spin diffusion coefficient $D_s = (100 \pm 3)\,\text{cm}^2\,\text{s}^{-1}$. This comparatively high value of D_s and the long time scales $\Delta t \gg \tau_{\text{rad}}$ for which the spin packet is observed (compare Fig. 46) suggests that the electron spin propagation is detached from the ambipolar diffusion of the photocreated holes and takes place in the dilute background QW 2DEG. This is an example of spin-charge-separation in optically induced bipolar transport of spin polarized carriers which has started to attract theoretical interest in the recent past [209].

Previous studies of spin propagation driven by surface acoustic waves (SAW) have indicated anisotropic spin transport along the [001] and [$\bar{1}$10] crystal directions in GaAs (110) QWs in the presence of small external magnetic fields [210]. We have verified that a similar dependence of the spin diffusion on crystal direction is not present in our measurements, i.e. we observe isotropic diffusion in the QW plane. This absence of anisotropies in the diffusion coefficient along the main crystal axis is demonstrated in

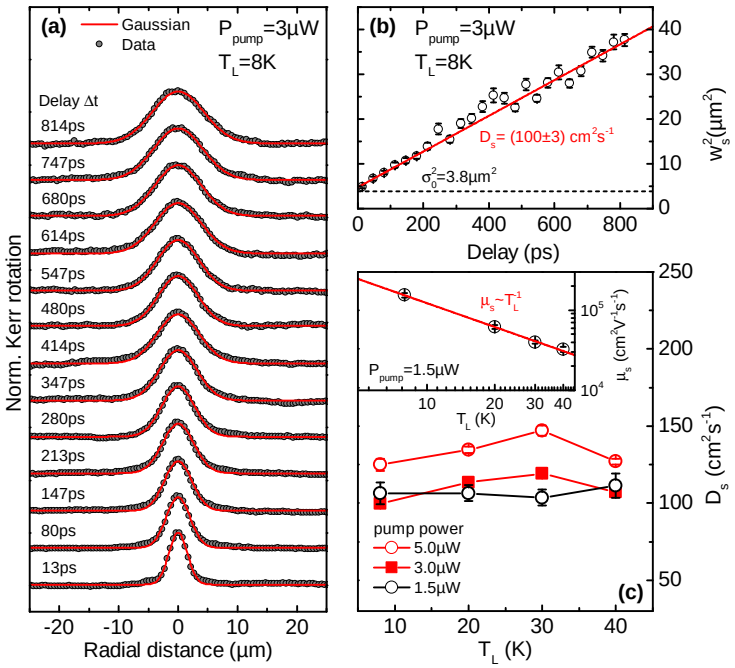

Figure 50: (a) Normalized spin polarization profiles (gray markers) for increasing delays (bottom to top) and Gaussian fits (red lines) measured for $T_L = 8\,\mathrm{K}$ and $P_{\mathrm{pump}} = 3\,\mu\mathrm{W}$. The delay Δt is indicated above the respective curve. **(b)** Time evolution of the squared Gaussian width $w_s^2(\Delta t)$ of the spin packet shown in (a). The red solid line is a linear fit from which the spin diffusion coefficient is determined. The optical resolution of the setup is indicated by the dashed black line. **(c)** Lattice temperature dependence of the spin diffusion coefficient D_s for different pump powers. Inset: Spin mobility $\mu_s(T_L)$ calculated via the Einstein relation from $D_s(T_L)$ measured for the lowest pump power.

Fig. 51 where we exemplarily show for $T_L = 8\,\mathrm{K}$ and $P_{\mathrm{pump}} = 5\,\mu\mathrm{W}$ that, within experimental resolution, identical expansions $w_s^2(\Delta t)$ of the spin packet width are observed along the main crystal axis. We therefore limit our following presentation to results obtained for measurements along the $[001]$ direction.

The dependence of the electron spin diffusion coefficient of the (110) QWs on pump power and lattice temperature is summarized in Fig. 50 (c). For T_L between 8 K and 40 K we measure the spin diffusivity for very low excitation powers $P_{\mathrm{pump}} = 1.5$, 3, and $5\,\mu\mathrm{W}$.[17] For all examined excitation densities we observe that D_s only varies weakly with the lattice temperature. We find that a reduction of the pump power from $5\,\mu\mathrm{W}$ to $3\,\mu\mathrm{W}$ leads to a systematic decrease of the spin diffusivity. A qualitatively similar decrease of D_s with excitation density has been observed previously for a (110) QW at

[17] Due to the very small Kerr rotation signals observed for the lowest pump power, for $P_{\mathrm{pump}} = 1.5\,\mu\mathrm{W}$ time traces are only be measured for delays $\Delta t \leq 414\,\mathrm{ps}$.

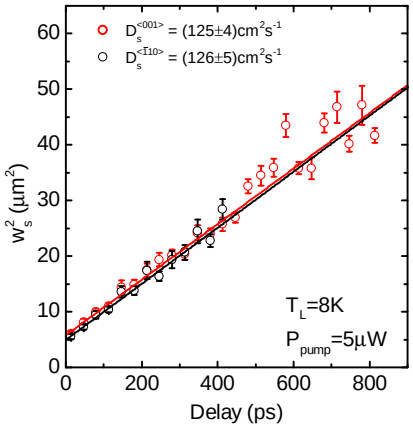

Figure 51: Comparison of the time-resolved observation of the optically excited spin packet width $w_s^2(\Delta t)$ along the main <001> (red markers) and <$\bar{1}$10> (black markers) crystal axis for $T_L = 8\,\mathrm{K}$ and $P_{\mathrm{pump}} = 5\,\mu\mathrm{W}$. The diffusion coefficients extracted from the slopes of the linear fits (solid lines) agree within experimental resolution, indicating the absence of anisotropic spin diffusion in the (110) QW sample.

room temperature [98]. At present, the physical origin of this pump power dependence is not known. However, a significant decrease of the diffusion coefficient when further lowering the pump power to 1.5 µW is not observed. This suggests that we have reduced pump-induced influences on D_s sufficiently to observe the intrinsic temperature dependence of the spin diffusivity.

We focus on $D_s(T_L)$ obtained for the lowest pump power of 1.5 µW for which we are closest to measuring the intrinsic spin diffusion coefficient of the dilute (110) QW 2DEG. In contrast to the case of bulk GaAs, where the spin diffusivity strongly depends on T_L (compare Fig. 35), we here find a constant value $D_s \approx 100\,\mathrm{cm}^2\,\mathrm{s}^{-1}$ for all examined lattice temperatures. A similar temperature-independent spin diffusivity has been observed previously for a GaAs (110) MQW sample up to room temperature [211].

We use the Einstein relation $\mu_s = (eD_s/k_BT_L)$ to calculate the temperature dependence of the spin mobility. Following Ref. [211] we infer the dominant scattering mechanism which limits the spin diffusivity in the (110) QW sample from $\mu_s(T_L)$. For the observed constant D_s, which is insensitive to changes of the lattice temperature, we find $\mu_s \sim T_L^{-1}$ as demonstrated in the inset of Fig. 48 (c). This temperature dependence is characteristic for a non-degenerate two-dimensional electron system where the mobility is limited by acoustic deformation potential scattering with a rate which increases proportional to the lattice temperature [211, 212].

8.2.4 Summary and conclusions

We have investigated the time-resolved electron spin dynamics in a (110) MQW sample. We have used TRKR spin quantum beat measurements to deduce the 2DEG effective

g-factor and to infer the time scales on which an optically excited QW electron spin packet persists. Comparison with the radiative carrier lifetime obtained from TCSPC spectroscopy allowed us to establish the presence of a dilute electron gas in the nominally undoped QWs in which the spin polarization is retained for long times. We have used cw Hanle-MOKE spectroscopy to demonstrate anisotropic spin relaxation in the (110) QWs. In the limit of vanishing optical excitation we have found exceptionally long electron spin relaxation times in excess of 100 ns.

We have presented a first application of our picosecond real-space imaging technique which allows us to directly observe the time-evolution of the diffusive expansion of optically excited spin packets. Using this technique we have investigated the dependence of the (110) QW electron spin diffusion coefficient on optical excitation density and lattice temperature. Having established the viability of our time-resolved supercontinuum MOKE microscopy instrumentation, we next turn to the investigation of transient hot electron effects on the spin diffusion in bulk GaAs.

Chapter 9

Picosecond real-space imaging of hot electron spin diffusion in bulk GaAs

We finally turn to the investigation of hot carrier effects on the time-resolved electron spin diffusion. In the following chapter we present picosecond real-space imaging of low-temperature electron spin diffusion in bulk GaAs. We directly measure the time-dependence of the electron spin diffusion coefficient from the momentary expansion rate of the spin packet. We observe a high initial expansion rate of the spin packet. For low lattice temperatures this expansion rate is strongly reduced with increasing time, reflecting a transient decrease of the spin diffusion coefficient. We show that this decrease of D_s is caused by the influence of the cooling of hot photocarriers on the electron spin diffusion coefficient.

9.1 Time-resolved spin diffusion microscopy

We study the time-resolved electron spin diffusion in the bulk n-GaAs sample 11889 for temperatures $T_L = 8\,\mathrm{K}$, 20 K, and 30 K. Optical excitation with a central wavelength $\lambda_{\mathrm{pump}} = 7800\,\text{Å}$ is again performed using a Thorlabs FBH780-10 dielectric bandpass filter. For the following measurements the time-averaged pump and probe power are 6 µW and 12 µW, respectively. The $\lambda_{\mathrm{probe}} \approx 8210\,\text{Å}$ central wavelength of the pulsed probe laser is tuned to the E_0 excitonic Kerr resonance and chosen such that the observed Kerr rotation is maximal. Again, our probe laser spectrum covers the entire low-energy wing of the Kerr rotation resonance (see Fig. 1 (b) in Ref. [213]) and we thereby suppress hot-carrier artifacts on the magneto-optical spin detection.

To observe the time-resolved electron spin diffusion process we measure for each T_L line cuts of the electron spin polarization profile $S_z(r)$ through the pump spot center for increasing pump-probe delays Δt between −100 ps and 1350 ps. A typical time trace of the local spin polarization $S_z(\Delta t, r = 0)$ additionally measured at $T_L = 8\,\mathrm{K}$ for delays up to 3000 ps is shown in Fig. 52 (a) on a logarithmic scale. The strong influence of diffusion on $S_z(\Delta t, r = 0)$, which according to Eq. (3.34) leads to a non-exponential decay of the spin polarization, is evident from the deviation of the experimental data from a straight line.

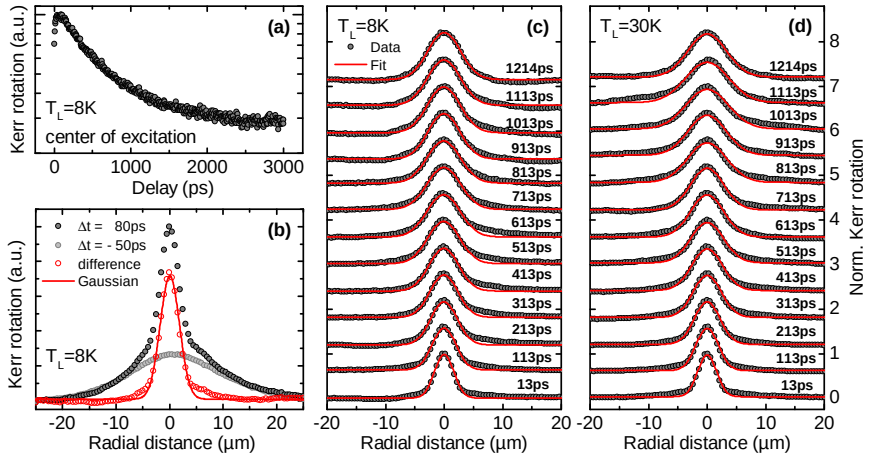

Figure 52: (a) Transient Kerr rotation $\theta_K(\Delta t, r = 0)$ of sample 11889 plotted on a logarithmic scale. The non-exponential decay reflects the influence of diffusion on the spin dynamics (see text). **(b)** Normalized lateral Kerr rotation profiles for delays $\Delta t = -50\,\mathrm{ps}$ (light gray markers) and $\Delta t = 80\,\mathrm{ps}$ (dark gray markers) at $T_L = 8\,\mathrm{K}$. The non-Gaussian spin profile observed at positive delay times is a superposition of the currently injected spin packet with previous-pulse contributions. The profile resulting from subtraction of the previous-pulse contributions (red markers) is shown together with a Gaussian fit (solid red line). **(c,d)** Single-pulse spin polarization profiles at $T_L = 8\,\mathrm{K}$ and 30 K (gray markers) for increasing delays (bottom to top) and Gaussian fits (solid lines). The delay Δt is indicated above the respective curve.

In Fig. 52 (b) we show the spin polarization profile $S_z(r)$ measured at $T_L = 8\,\mathrm{K}$ for a short delay $\Delta t = 80\,\mathrm{ps}$. The profile of the spin packet clearly is non-Gaussian. This is a result of the long spin relaxation time $\tau_s \approx 170\,\mathrm{ns}$ at low temperatures and the comparatively low spin diffusivity of the sample. Similar to the case of our (110) QW studies (compare section 8.2.3), the spin polarization excited by the previous pump pulses does not completely decay within the 27.5 ns pulse-to-pulse interval of our supercontinuum source. This is evidenced by the second $S_z(r)$ profile shown in Fig. 52 (b) measured at a short negative delay $\Delta t = -50\,\mathrm{ps}$ before the arrival of the corresponding pump pulse. We observe a substantial remanent spin polarization excited by previous pump pulses which strongly decreases for rising lattice temperatures and completely vanishes at $T_L = 30\,\mathrm{K}$. This reflects enhanced diffusion and the strong decrease of τ_s with increasing temperature [compare Figs. 35 (c) and 36 (b)].

We limit our analysis to the contribution of the spin polarization resulting from the excitation by a single pump pulse. Because of the linearity of the diffusion Eq. (3.30), the momentary spin polarization is a superposition of the contributions of all previous excitation pulses. On the short time scale of our observation window $\Delta t \leq 1350\,\mathrm{ps}$ and for the comparatively long pulse-to-pulse interval of our experiment, the spin profile resulting from the previous excitation pulses is virtually stationary. Following Ref. [14]

we therefore subtract the previous-pulse contribution profile measured at short negative delay of −50 ps from each spin polarization profile $S_z(\Delta t, r)$. The resulting single-pulse profiles are then Gaussians as shown in Fig. 52 (b) where we exemplarily compare the experimental data for $\Delta t = 80$ ps with a Gaussian fit. The alternative technique of reducing repetition-rate artifacts by suppression of previous-pulse contributions by destructive spin interference by application of a small in-plane magnetic field of ≈ 1 mT has been introduced in section 8.2.3. We have verified that, within experimental resolution, both methods yield identical results for the following analysis.

Time traces of single-pulse spin polarization profiles $S_z(\Delta t, r)$ obtained from the above procedure are shown in Figs. 52 (c) and (d) together with Gaussian fits for $T_L = 8$ K and 30 K. The shape of the spin packets remains Gaussian for all examined times. For the shortest delay of 13 ps, the $(1/e)$ half width of the spin packet coincides with our optical resolution. The diffusive spreading of the spin packet with increasing delay is clearly observed for both lattice temperatures. Careful inspection of Figs. 52 (c) and (d) for long delays further reveals a stronger increase of the Gaussian width at high lattice temperature. This reflects the expected increase of the spin diffusivity with rising temperature.

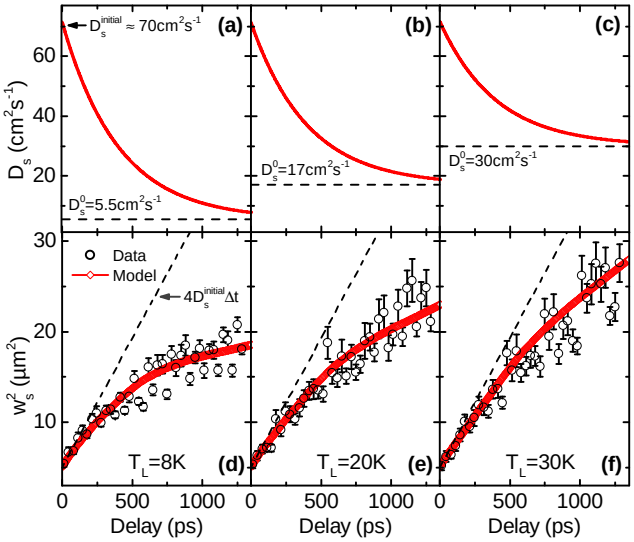

Figure 53: Time-resolved electron spin diffusion in sample 11889. **(a-c)** Time-dependent spin diffusion coefficient $D_s(\Delta t)$ used in our model (see text). The dashed lines indicate the intrinsic spin diffusivity D_s^0 which was obtained for the respective T_L from independent cw measurements. **(d-f)** Time evolution of the squared Gaussian width $w_s^2(\Delta t)$ of the electron spin packet (black markers) for $T_L = 8$ K, 20 K and 30 K. The dashed lines indicate the expansion of a spin packet for a constant diffusion coefficient $D_s^{\text{initial}} \approx 70\,\text{cm}^2\,\text{s}^{-1}$. Also shown is a fit of the analytical model Eq. (9.3) (red lines, see text).

In Figs. 53 (d-f) we plot $w_s^2(\Delta t)$ for increasing T_L which we obtain from the Gaussian fits of the single-pulse spin polarization profiles. For a constant spin diffusivity independent of the pump-probe delay we expect from Eq. (3.35) a linear dependence of w_s^2 on Δt with a slope of $4D_s$. For all examined lattice temperatures we observe, however, a strong deviation of $w_s^2(\Delta t)$ from this expected linear dependence on Δt. Instead, with increasing time the $w_s^2(\Delta t)$ curves are sublinear, reflecting a transient decrease of the spin diffusivity $D_s(\Delta t)$. This transient decrease is strongest for $T_L = 8\,\mathrm{K}$ and becomes less pronounced with increasing lattice temperature.

In contrast, we find for all examined lattice temperatures T_L that the initial spin packet expansion during the first $\approx 100\,\mathrm{ps}$ is well described by the same diffusion coefficient $D_s^{\mathrm{initial}} \approx 70\,\mathrm{cm^2\,s^{-1}}$ as indicated by black dashed lines. For long delays $\Delta t \gtrsim 800\,\mathrm{ps}$ the expansion is quasi-linear with Δt, indicating that $D_s(\Delta t)$ has approached a respective equilibrium value which is found to increase with T_L.

In the remaining part of this chapter we will demonstrate that the observed decrease of $D_s(\Delta t)$ is consistently explained by considering the influence of the transient cooling of hot photocarriers on the spin diffusion coefficient. The $\lambda_{\mathrm{pump}} \approx 7800\,\mathrm{Å}$ pump pulse excites electrons with an average excess energy $\langle E_{\mathrm{c,i}} \rangle \approx 60\,\mathrm{meV}$. This deposition of excess energy in the electron system leads to a strong heating of the electrons and results in an initial electron temperature T_e which significantly exceeds the lattice temperature. Owing to the high initial kinetic energy of the spin polarized electrons, the spin diffusion coefficient will be strongly enhanced for short delays. With increasing Δt, energy relaxation of the hot carriers takes place. This leads to the observed decrease of $D_s(\Delta t)$ down to the intrinsic value $D_s^0(T_L)$ for the respective lattice temperature.

9.2 Transient hot carrier effects on the electron spin diffusion coefficient

We next use the intrinsic temperature dependence of the spin diffusion coefficient which we have determined in section 7.2.1 from cw MOKE microscopy for the analysis of our time-resolved spectroscopy results. In Fig. 54 (a) we therefore reprint the temperature dependence $D_s^0(T_L)$. As discussed earlier, we find that $D_s^0(T_L)$ monotonically increases with rising temperature. For $T_L \geq 12\,\mathrm{K}$ we observe that this increase of the spin diffusivity is approximately proportional to the lattice temperature, i.e. $D_s^0 \sim T_L$.

We now use this $D_s^0(T_L)$ dependence for the interpretation of our time-resolved measurements. We first consider the very fast initial expansion of the electron spin packet. For $\Delta t \lesssim 100\,\mathrm{ps}$ we have found that the expansion rate is independent of the lattice temperature and corresponds to a spin diffusivity $D_s^{\mathrm{initial}} \approx 70\,\mathrm{cm^2\,s^{-1}}$.

Comparison with the intrinsic temperature dependence of the spin diffusivity $D_s^0(T_L)$ allows for an estimation of the initial photocarrier temperature: From the linear extrapolation of $D_s^0(T_L)$ for $T_L \geq 12\,\mathrm{K}$ shown in Fig. 54 (a) we can estimate an initial electron temperature $T_e^{\mathrm{initial}} \approx 60\,\mathrm{K}$ for very short delays $\Delta t \lesssim 100\,\mathrm{ps}$ after the pump

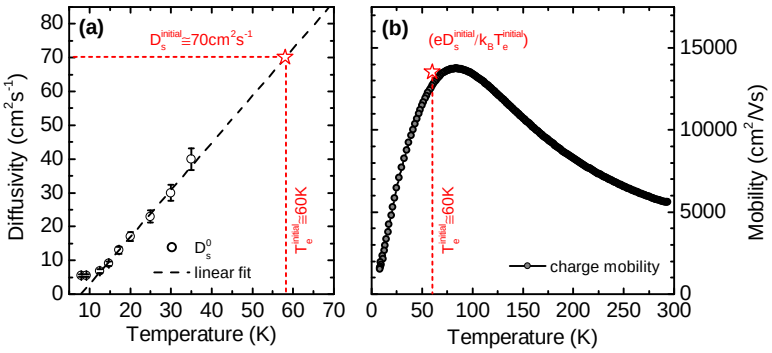

Figure 54: (a) Intrinsic spin diffusivity $D_s^0(T_L)$ (black markers) of sample 11889. The dashed line is a linear fit for $T_L \geq 12\,\mathrm{K}$. Red dashed lines and the red marker indicate the initial diffusivity and effective temperature of the spin packet at $\Delta t \approx 0\,\mathrm{ps}$ (see text). **(b)** Charge mobility obtained from a van der Pauw measurement (gray markers). The red marker is the spin mobility calculated from the Einstein relation $\mu_s = (eD_s/k_BT_e)$ for the initial electron temperature and spin diffusivity of (a).

pulse.[18] Our estimate for T_e is in good agreement with previous picosecond TRPL spectroscopy [118] and transient absorption spectroscopy [214, 215] studies of photocarrier cooling in bulk GaAs. The observed initial spin diffusivity D_s^{initial} is constant for all examined T_L because the initial kinetic energy of the electrons (and hence the initial electron temperature) is solely determined by the large excitation excess energy $\langle E_{\mathrm{c,i}} \rangle$ and does not depend on the lattice temperature.

The observed values for the initial spin diffusivity D_s^{initial} and electron temperature T_e^{initial} are consistent with independent charge transport measurements. In Fig. 54 (b) we show the temperature dependence of the electron charge mobility $\mu_c(T_L)$ determined from a standard van der Pauw characterization [101]. Using the Einstein relation Eq. (7.5), we calculate the expected spin mobility $\mu_s(T_e^{\mathrm{initial}}) \approx 13\,500\,\mathrm{cm^2\,V^{-1}\,s^{-1}}$ (red marker). This value agrees within 6 % with the charge mobility $\mu_c(T_e^{\mathrm{initial}})$ obtained from the transport measurement. This excellent agreement proves the validity of our extrapolation for $D_s^0(T_L)$ and the internal consistency of our cw and time-resolved spectroscopy data and substantiates our following analysis of the transient spin diffusion microscopy results.

The temporal evolution of the electron temperature $T_e(\Delta t, r)$ following the short localized excitation by the pump pulse is governed by energy relaxation by emission

[18] For the 6 µW pump power and the 36.4 MHz repetition rate employed in our experiment we estimate an initial photocarrier-density of $\approx 1.5 \times 10^{17}\,\mathrm{cm^{-3}}$ after the excitation pulse which significantly exceeds the doping density of our sample. Time-resolved PL studies [118] on bulk GaAs have established that the photocarrier thermalization by electron-electron scattering takes place on timescales well below 15 ps even for excitation densities two orders of magnitude lower than employed in our work (compare section 4.3). We therefore conclude that the electron ensemble is thermalized even for the shortest delays of 13 ps examined in our measurements and can be characterized by a well-defined electron temperature.

of phonons, heat conduction in the electron system, and possibly impact ionization of donor-bound electrons [24]. At the present time an exact quantitative treatment of this problem is not feasibly due to the limited understanding of the interplay of the transient heat conduction and impact ionization processes. To facilitate the following analysis, we instead characterize the entire electron spin packet by an effective temperature T_{eff}. In a first approximation we model the thermal relaxation of the electrons constituting the spin packet by Newtonian cooling with a rate:

$$\frac{\partial T_{\text{eff}}}{\partial \Delta t} \propto (T_{\text{eff}} - T_L) \tag{9.1}$$

for which T_{eff} will approach T_L exponentially for long delays.

Motivated by the linear dependence of D_s^0 on temperature observed in Fig. 54 (c) we then approximate the transient spin diffusion coefficient by:

$$D_s(\Delta t, T_L) = D_s^0(T_L)\left[1 + A_t(T_L)\exp\left(-\Delta t/\tau_c\right)\right] \tag{9.2}$$

The cooling constant τ_c characterizes the time scale on which the effective temperature T_{eff} of the spin packet decays to the respective lattice temperature T_L. Following the cooling of the spin packet, for increasing delay the spin diffusivity $D_s(\Delta t)$ approaches the equilibrium value D_s^0 for the respective lattice temperature T_L. We have determined this $D_s^0(T_L)$ independently from cw spectroscopy [compare Fig. 35 (c)]. The transient enhancement amplitude A_t is a measure for the influence of the high initial kinetic energy of the photocarriers on the spin diffusivity. It is determined by the boundary condition $D_s(\Delta t = 0) = D_s^{\text{initial}}$, leaving the cooling time constant τ_c as the only free parameter.

To relate the transient diffusion coefficient Eq. (9.2) to the $(1/e)$ half width $w_s(\Delta t)$ which we extract from our experiment we integrate Eq. (3.36). The time-evolution of the squared $(1/e)$ half width is obtained as:[19]

$$w_s^2(\Delta t, T_L) = \sigma_0^2 + 4D_s^0(T_L)\left(\Delta t + A_t\tau_c\left[1 - \exp\left(-\Delta t/\tau_c\right)\right]\right) \tag{9.3}$$

Variation of τ_c and comparison of the analytical solution Eq. (9.3) with the experimental data allows us to determine the unknown cooling time. Following this procedure, best agreement is found for $\tau_c = 400\,\text{ps}$. In Figs. 53 (d-f) we show the resulting $w_s^2(\Delta t)$ curves obtained from our model Eq. (9.3) for this τ_c together with the experimental data. Very similar cooling times have been observed previously in time-resolved exciton diffusion experiments for GaAs QWs [103].

[19] We additionally use a transient FEM solver to verify that Eq. (9.3) correctly describes the time evolution of a Gaussian spin packet for the time-dependent spin diffusivity $D_s(\Delta t, T_L)$ Eq. (9.2). Excitation by the short pump pulse is modeled by a Gaussian source term $g_z(\Delta t, r) = g_{z,0}\exp\left(-r^2/\sigma_0^2\right)\exp\left(-(\Delta t^2/\tau_g^2\right)$. The spatial extent of the source term is determined by our optical resolution σ_0. A pulse length $\tau_g = 3\,\text{ps}$ (our instrument's time resolution) is used in the simulations. For the spin relaxation time $\tau_s(T_L)$ we use the values shown in Fig. 36 (b). From the FEM solution of our model we extract the squared Gaussian $(1/e)$ half width $w_s^2(\Delta t)$ which agrees within computational uncertainty with the analytical model Eq. (9.3).

Comparing $\tau_c = 400\,\text{ps}$ with typical cooling times expected from the electron-phonon energy loss rates Eqs. (4.7) - (4.9) [Fig. 12 (b)] we find that the experimentally observed electron cooling is substantially faster than predicted by the simple scattering theory. This result suggests that the fast dilution of the excess energy by heat conduction in the electron system [126] is the dominant decay channel for the energy relaxation of the carrier system. For all examined lattice temperatures T_L we find excellent quantitative agreement between the experimental data and the model for the same value of τ_c. The resulting time-dependent spin diffusion coefficient $D_s(\Delta t)$ used for the respective calculation is shown in Figs. 53 (a-c). For comparison we also show by dashed lines the intrinsic spin diffusivity D_s^0 for the respective lattice temperature which is approached for long delays.

9.3 Transient spin diffusion in external magnetic fields

We next consider the time-resolved electron spin diffusion in transverse magnetic fields. From our above analysis of our cw and time-resolved MOKE microscopy data we have determined all relevant parameters which govern the electron cooling, spin relaxation, and transient changes in the spin transport properties. We additionally validate this parameter set by observing the transient decay $S_z(\Delta t, r = 0)$ at the pump spot center which must be consistently explained by our results for $D_s(T_L, \Delta t)$ and $\tau_s(T_L)$.

In Fig. 55 we show time traces $\theta_K(\Delta t, r = 0)$ which we measure at $T_L = 8\,\text{K}, 20\,\text{K}$, and $30\,\text{K}$ for an external in-plane magnetic field $B_{xy} = 600\,\text{mT}$. To describe the oscillatory decay of S_z we insert $w_s^2(T_L, \Delta t)$ in the spin diffusion equation solution Eq. (3.34). The precession in the external field is considered by an additional Larmor precession term $\cos(\omega_L t)$. Moreover, for all examined bulk n-GaAs samples we observe that the build-up of the Kerr rotation signal happens on a time scale of $\approx$ 50-100 ps [compare Fig. 52 (a)]. Following Ref. [190] we consider this finite rise time of the Kerr rotation signal by an additional amplitude factor $[1 - \exp(-\Delta t / t_{\text{rise}})]$. For $r = 0$, we obtain the experimentally observed Kerr rotation transient at the pump spot center:

$$\theta_K(\Delta t) = \frac{\theta_{K,\text{max}}}{w_s^2(T_L, \Delta t)} [1 - \exp(-\Delta t / t_{\text{rise}})] \exp\left(\frac{-\Delta t}{\tau_s(T_L)}\right) \cos(\omega_L t) \qquad (9.4)$$

We stress that, except for $t_{\text{rise}} = (80 \pm 20)\,\text{ps}$, which only affects the initial Kerr rotation rise, all parameters entering Eq. (9.4) have been completely determined by our previous analysis, i.e. our model does not include additional adjustable parameters. In Fig. 55 we show that our model Eq. (9.4) accurately describes the time evolution $S_z(\Delta t, r = 0)$ by the combined action of spin diffusion and relaxation. The overall agreement between our data, obtained from a range of different cw and time-resolved spectroscopy experiments, and our quantitative modeling for all experimental situations demonstrates that we have arrived at a coherent understanding of the intricate interplay of hot carrier relaxation and photoinduced electron spin dynamics.

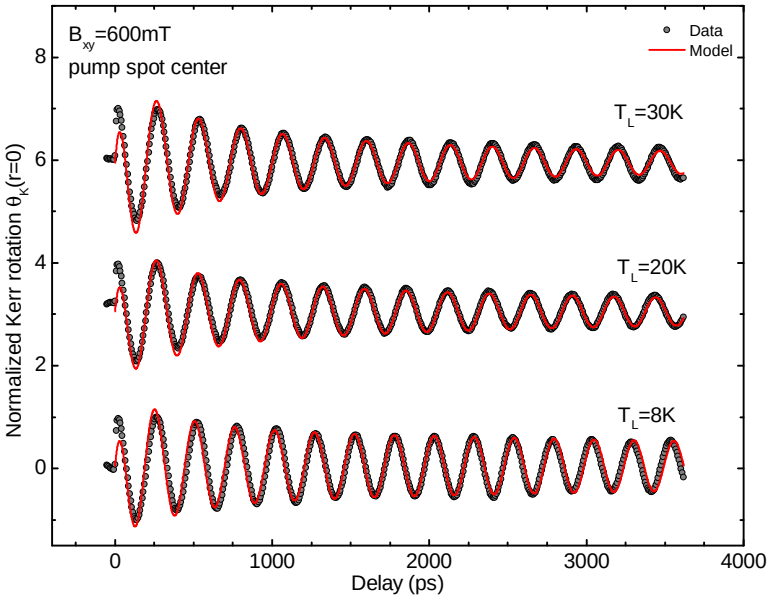

Figure 55: Transient decay of the electron spin polarization in sample 11889 at the pump spot center in an external magnetic field. Gray markers are $\theta_K(\Delta t, r=0)$ transients measured for $T_L = 8$, 20, and 30 K. Red solid lines are solutions of the analytical model Eq. (9.4). The model parameters have been determined independently from zero-field time-resolved spin diffusion measurements and cw spectroscopy (see text).

9.4 Comparison with an additional sample

To further corroborate our modelling we additionally study the time-resolved electron spin diffusion in the second bulk n-GaAs sample 12464. We therefore again measure, using a slightly reduced pump power $P_{\text{pump}} = 5\,\mu\text{W}$, time-traces of single-pulse[20] spin polarization profiles $S_z(\Delta t, r)$ for $T_L = 8\,\text{K}$, 20 K, and 40 K.

In Figs. 56 (d-f) we show the diffusive expansion $w_s^2(\Delta t)$ extracted from Gaussian fits to the $S_z(\Delta t, r)$ profiles. We observe for $\Delta t \lesssim 100\,\text{ps}$ the expected fast initial expansion of the spin packet, corresponding here to an initial diffusivity $D_s^{\text{initial}} \approx 60\,\text{K}$ independent of T_L, which gradually slows down to the intrinsic diffusion coefficient for increasing delays. To obtain information on $D_s^0(T_L)$ of sample 12464 we fit the $w_s^2(\Delta t)$ traces with the model Eq. (9.3). Because of the very similar donor concentrations of both samples we assume the identical cooling time constant $\tau_c = 400\,\text{ps}$ of sample 11889. From the fits of Eq. (9.3) with $D_s^0(T_L)$ as the only adjustable parameter we determine the unknown intrinsic spin diffusion coefficient for the examined T_L shown in Figs. 56 (a-c).

Comparing the intrinsic spin diffusion coefficients, we find that at $T_L = 8\,\text{K}$ the dif-

[20] We here suppress previous-pulse contributions $S_z(\Delta t < 0)$ by destructive RSA with an in-plane magnetic field $B_{xy} = 1\,\text{mT}$ (compare section 8.2.3).

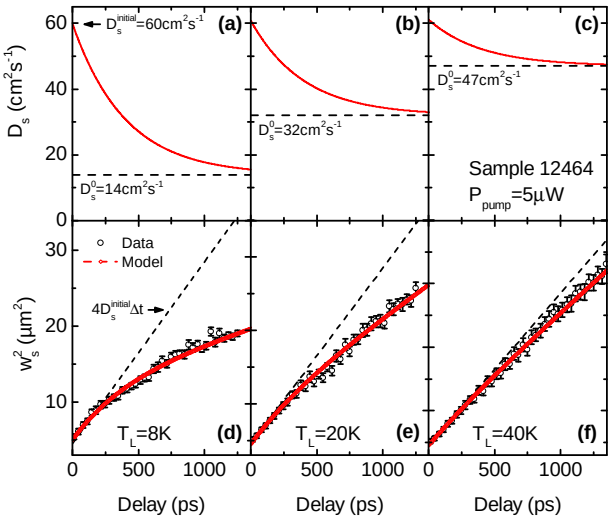

Figure 56: Time-resolved electron spin diffusion in sample 12464. **(a-c)** Time-dependent spin diffusion coefficient $D_s(\Delta t)$ obtained from the fits in (d-f). The dashed lines indicate the intrinsic spin diffusivity D_s^0 approached for long delays. **(d-f)** Time evolution of the squared Gaussian width $w_s^2(\Delta t)$ of the electron spin packet (black circles) for $T_L = 8\,\mathrm{K}$, 20 K, and 40 K. The dashed lines indicate the initial spin packet expansion with $D_s^{\mathrm{initial}} \approx 60\,\mathrm{cm^2\,s^{-1}}$. Also shown is a fit of the analytical model Eq. (9.3) (red, see text). All data measured for $P_{\mathrm{pump}} = 5\,\mu\mathrm{W}$.

fusivity of sample 12464 exceeds the respective value of sample 11889 by a factor of ≈ 2.5. The same relative enhancement by a factor of 2.5 is also observed in the low-temperature charge mobilities μ_c of both samples (1050 vs. 2600 $\mathrm{cm\,V^{-2}\,s^{-1}}$ at 4.2 K). In contrast, for sample 12464 the initial diffusivity after the excitation pulse D_s^{initial} is slightly reduced with respect to the value measured on sample 11889. Moreover, for sample 12464 at the highest examined lattice temperature only a weak decrease of $D_s(\Delta t)$ is observed for long delays, indicating that T_e^{initial} here only slightly exceeds $T_L = 40\,\mathrm{K}$. Taken together both observations suggest that the initial electron temperature following the excitation pulse in sample 12464 is lower than in sample 11889. This is likely the result of the reduced excitation power employed in our MOKE microscopy measurements on sample 12464.

This reduction of D_s^{initial} for lower excitation density is demonstrated for sample 12464 in Fig. 57 (b) where we show $w_s^2(\Delta t)$ measured at $T_L = 8\,\mathrm{K}$ for high (5 μW) and low (3 μW) pump power. Our analysis in Fig. 57 (a) demonstrates that the reduction of P_{pump} leads to a decrease of D_s^{initial} from 60 to 50 $\mathrm{cm^2\,s^{-1}}$, while both traces converge to the same intrinsic value D_s^0 for $\Delta t \gg \tau_c$.

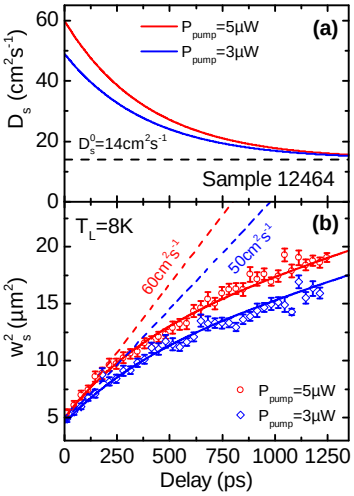

Figure 57: Pump power dependence of the time-resolved electron spin diffusion in sample 12464. **(a)** Time-dependent spin diffusion coefficient $D_s(\Delta t)$ for high (5 µW, red) and low (3 µW, blue) excitation power obtained from the fits in (b). Note that both traces converge to the same intrinsic diffusivity $D_s^0 = 14\,\mathrm{cm}^2\,\mathrm{s}^{-1}$. **(b)** Time evolution of the squared Gaussian width $w_s^2(\Delta t)$ of the electron spin packet for high (red markers) and low (blue markers) power excitation together with fits of the model Eq. (9.3). Dashed lines indicate the initial spin packet expansion rates.

9.5 Summary and conclusions

We have used picosecond Kerr microscopy to image the expansion of optically excited electron spin packets by spin diffusion in bulk GaAs. The time-resolved measurement of the Gaussian width of the spin packet allows us for the first time to directly observe the influence of pump-induced photocarrier heating on the electron spin diffusion coefficient. By comparison with our cw MOKE microscopy measurements we are able to draw the following physical picture: For very short delays after the pump pulse, spin diffusion is very fast and the high initial diffusivity is only governed by the initial kinetic energy of the photoexcited electrons. With increasing delay, thermal relaxation of the hot photocarriers takes places. The cooling of the electron population down to the lattice temperature by phonon emission, donor impact ionization, and heat conduction in the electron system is found to happen on a time scale $\tau_c \approx 400\,\mathrm{ps}$. This transient reduction of the kinetic energy of the electrons is reflected by a strong decrease of the spin diffusion coefficient with increasing time. For long delays $\Delta t \gg \tau_c$ the influence of photocarrier heating vanishes. The expansion of the spin packet is then observed to take place with the rate expected from the intrinsic spin diffusion coefficient which we have independently determined from cw Kerr microscopy.

Chapter 10

Summary

In the present thesis *Hot spin carriers in cold semiconductors* we have investigated hot carrier effects in low-temperature photoinduced MOKE microscopy of electron spins in semiconductor heterostructures. Our studies have revealed that the influence of hot photocarriers in magneto-optical pump-probe experiments is twofold.

First, it is commonly assumed that a measurement of the local Kerr rotation using an arbitrary probe wavelength maps the local electron spin polarization. This is the fundamental assumption underlying the widely used two-color MOKE microscopy technique. Our cw spectroscopy experiments have demonstrated that, in general, this assumption is not correct.

At low lattice temperatures the nonresonant spin excitation by the focused pump laser inevitably leads to a significant heating of the electron system. This heating, in turn, locally modifies the magneto-optical coefficient which links the experimentally observed Kerr rotation to the electron spin polarization. As a consequence, the spin-induced local Kerr rotation is augmented by spin-unrelated changes in the magneto-optical coefficient. A spatially resolved measurement of the Kerr rotation then does not correctly map the electron spin polarization profile.

We have demonstrated different ways to overcome this limitation and to correctly measure the electron spin profile. For cw spectroscopy we have demonstrated how the true local electron spin polarization can be obtained from a quantitative analysis of the full excitonic Kerr rotation spectrum. Alternatively, picosecond MOKE microscopy using a spectrally broad probe laser pulse mitigates hot-carrier effects on the magneto-optical spin detection and allows to directly observe the time-resolved expansion of an optically excited electron spin packet in real-space.

Second, we have shown that hot photocarriers strongly modify the spin diffusion process. Owing to their high kinetic energy, hot carriers greatly enhance the electron spin diffusion coefficient with respect to the intrinsic value of the undisturbed system. Therefore, for steady-state excitation the spin diffusivity is strongly enhanced close to the pump spot center where hot electrons are present. Similarly, for short delays following pulsed excitation the high initial temperature of the electrons leads to a very fast initial expansion of the spin packet which gradually slows as the electrons cool down to the lattice temperature.

While few previous publications have recognized the possible influence of hot car-

riers on the electron spin transport properties, the present work is the first to directly observe and quantify such hot carrier contributions. We have developed models which for steady-state and pulsed excitation quantitatively describe the experimentally observed electron spin diffusion. These models are capable of separating the intrinsic spin diffusivity from the hot electron contribution, and allow to obtain spin transport parameters of the undisturbed system.

We have performed extensive cw and time-resolved spectroscopy studies of the lattice temperature dependence of the electron spin diffusion in bulk GaAs. Using our models we have obtained a consistent set of parameters for the intrinsic temperature dependence of the electron spin diffusion coefficient and spin relaxation time and the hot carrier contributions which quantitatively describes all experimental observations. Our analysis unequivocally demonstrates that we have, as we believe for the first time, arrived at a coherent understanding of photoinduced low-temperature electron spin diffusion in bulk semiconductors.

Chapter 11

Bibliography

[1] G. E. Moore. Cramming more components onto integrated circuits. *Electronics*, 38(8):114, 1965.

[2] R. H. Dennard, F. H. Gaensslen, V. L. Rideout, E. Bassous, and A. R. LeBlanc. Design of ion-implanted MOSFET's with very small physical dimensions. *IEEE Journal of Solid-State Circuits*, 9(5):256, 1974.

[3] H. Esmaeilzadeh, E. Blem, R. St Amant, K. Sankaralingam, and D. Burger. Dark silicon and the end of multicore scaling. *Computer Architecture (ISCA), 2011 38th Annual International Symposium on*, page 365, 2011.

[4] H. Esmaeilzadeh, E. Blem, R. St. Amant, K. Sankaralingam, and D. Burger. Power challenges may end the multicore era. *Communications of the ACM*, 56(2):93, 2013.

[5] D. D. Awschalom and J. M. Kikkawa. Electron Spin and Optical Coherence in Semiconductors. *Physics Today*, 52(6):33, 1999.

[6] G. A. Prinz. Magnetoelectronics. *Science*, 282(5394):1660, 1998.

[7] S. A. Wolf and D. M. Treger. Spintronics: A new paradigm for electronics for the new millennium. *IEEE Transactions on Magnetics*, 36(5):2748, 2000.

[8] S. A. Wolf, D. D. Awschalom, R. A. Buhrman, J. M. Daughton, S. von Molnar, M. L. Roukes, A. Y. Chtchelkanova, and D. M. Treger. Spintronics: A spin-based electronics vision for the future. *Science*, 294(5546):1488, 2001.

[9] D. D. Awschalom, D. Loss, and N. Samarth, editors. *Semiconductor Spintronics and Quantum Computation*. NanoScience and Technology. Springer, Berlin, 2002.

[10] D. D. Awschalom and M. E. Flatté. Challenges for semiconductor spintronics. *Nature Physics*, 3(3):153, 2007.

[11] J. M. Kikkawa, I. P. Smorchkova, N. Samarth, and D. D. Awschalom. Room-temperature spin memory in two-dimensional electron gases. *Science*, 277(5330):1284, 1997.

[12] J. J. Baumberg, S. A. Crooker, D. D. Awschalom, N. Samarth, H. Luo, and J. K. Furdyna. Ultrafast Faraday spectroscopy in magnetic semiconductor quantum structures. *Phys. Rev. B*, 50(11):7689, 1994.

[13] J. M. Kikkawa and D. D. Awschalom. Resonant spin amplification in n-type GaAs. *Phys. Rev. Lett.*, 80(19):4313, 1998.

[14] J. M. Kikkawa and D. D. Awschalom. Lateral drag of spin coherence in gallium arsenide. *Nature*, 397(6715):139, 1999.

[15] S. A. Crooker and D. L. Smith. Imaging Spin Flows in Semiconductors Subject to Electric, Magnetic, and Strain Fields. *Phys. Rev. Lett.*, 94(23):236601, 2005.

[16] S. A. Crooker, M. Furis, X. Lou, C. Adelmann, D. L. Smith, C. J. Palmstrom, and P. A. Crowell. Imaging spin transport in lateral ferromagnet/semiconductor structures. *Science*, 309(5744):2191, 2005.

[17] Y. K. Kato, R. C. Myers, A. C. Gossard, and D. D. Awschalom. Current-Induced Spin Polarization in Strained Semiconductors. *Phys. Rev. Lett.*, 93(17):176601, 2004.

[18] Y. K. Kato, R. C. Myers, A. C. Gossard, and D. D. Awschalom. Observation of the spin Hall effect in semiconductors. *Science*, 306(5703):1910, 2004.

[19] V. Sih, R. C. Myers, Y. K. Kato, W. H. Lau, A. C. Gossard, and D. D. Awschalom. Spatial imaging of the spin Hall effect and current-induced polarization in two-dimensional electron gases. *Nature Physics*, 1(1):31, 2005.

[20] J. Berezovsky, M. H. Mikkelsen, O. Gywat, N. G. Stoltz, L. A. Coldren, and D. D. Awschalom. Nondestructive Optical Measurements of a Single Electron Spin in a Quantum Dot. *Science*, 314(5807):1916, 2006.

[21] J. Berezovsky, M. H. Mikkelsen, N. G. Stoltz, L. A. Coldren, and D. D. Awschalom. Picosecond Coherent Optical Manipulation of a Single Electron Spin in a Quantum Dot. *Science*, 320(5874):349, 2008.

[22] M. P. Walser, C. Reichl, W. Wegscheider, and G. Salis. Direct mapping of the formation of a persistent spin helix. *Nature Physics*, 8(10):757, 2012.

[23] J. Shah and R. C. C. Leite. Radiative Recombination from Photoexcited Hot Carriers in GaAs. *Phys. Rev. Lett.*, 22(24):1304, 1969.

[24] R. Ulbrich. Energy Relaxation of Photoexcited Hot Electrons in GaAs. *Phys. Rev. B*, 8(12):5719, December 1973.

[25] R. G. Ulbrich. Low density photoexcitation phenomena in semiconductors: Aspects of theory and experiment. *Solid-State Electronics*, 21(1):51, 1978.

[26] J. Shah. Hot electrons and phonons under high intensity photoexcitation of semiconductors. *Solid-State Electronics*, 21(1):43, 1978.

[27] S. A. Lyon. Spectroscopy of hot carriers in semiconductors. *J. Lumin.*, 35(3):121, 1986.

[28] J. Shah. *Ultrafast Spectroscopy of Semiconductors and Semiconductor Nanostructures*. Springer Series in Solid-State Sciences. Springer, Berlin, 2nd edition, 1999.

[29] H. Münzel, A. Steckenborn, and D. Bimberg. Hot electrons in cold semiconductors: GaAs, InP and CdTe. *J. Lumin.*, 24/25:569, 1981.

[30] M. Furis, D. L. Smith, and S. A. Crooker. Bias-dependent electron spin lifetimes in *n*-GaAs and the role of donor impact ionization. *Appl. Phys. Lett.*, 89:102102, 2006.

[31] M. Hruška, Š. Kos, S. A. Crooker, A. Saxena, and D. L. Smith. Effects of strain, electric, and magnetic fields on lateral electron-spin transport in semiconductor epilayers. *Phys. Rev. B*, 73(7):075306, 2006.

[32] M. Furis, D. L. Smith, S. Kos, E. S. Garlid, K. S. M. Reddy, C. J. Palmstrom, P. A. Crowell, and S. A. Crooker. Local Hanle-effect studies of spin drift and diffusion in n:GaAs epilayers and spin-transport devices. *New. J. Phys.*, 9:347, 2007.

[33] S. A. Crooker, M. Furis, X. Lou, P. A. Crowell, D. L. Smith, C. Adelmann, and C. J. Palmstrom. Optical and electrical spin injection and spin transport in hybrid Fe/GaAs devices. *J. Appl. Phys*, 101(8):081716, 2007.

[34] J. M. Kikkawa, J. A. Gupta, I. Malajovich, and D. D. Awschalom. Spin coherence in semiconductors: storage, transport and reduced dimensionality. *Physica E*, 9(1):194, 2001.

[35] Y. Ohno, R. Terauchi, T. Adachi, F. Matsukura, and H. Ohno. Spin relaxation in GaAs (110) quantum wells. *Phys. Rev. Lett.*, 83(20):4196, 1999.

[36] K. C. Hall, K. Gündoğdu, J. L. Hicks, A. N. Kocbay, M. E. Flatté, T. F. Boggess, K. Holabird, A. Hunter, D. H. Chow, and J. J. Zinck. Room-temperature electric-field controlled spin dynamics in (110) InAs quantum wells. *Appl. Phys. Lett.*, 86(20):202114, 2005.

[37] T. Korn. Time-resolved studies of electron and hole spin dynamics in modulation-doped GaAs/AlGaAs quantum wells. *Phys. Reports*, 494(5):415, 2010.

[38] S. Döhrmann, D. Hägele, J. Rudolph, M. Bichler, D. Schuh, and M. Oestreich. Anomalous Spin Dephasing in (110) GaAs Quantum Wells: Anisotropy and Intersubband Effects. *Phys. Rev. Lett.*, 93(14):147405, 2004.

[39] G. M. Müller, M. Römer, D. Schuh, W. Wegscheider, J. Hübner, and M. Oestreich. Spin Noise Spectroscopy in GaAs (110) Quantum Wells: Access to Intrinsic Spin Lifetimes and Equilibrium Electron Dynamics. *Phys. Rev. Lett.*, 101(20):206601, 2008.

[40] V. V. Bel'kov, P. Olbrich, S. A. Tarasenko, D. Schuh, W. Wegscheider, T. Korn, C. Schüller, D. Weiss, W. Prettl, and S. D. Ganichev. Symmetry and Spin Dephasing in (110)-Grown Quantum Wells. *Phys. Rev. Lett.*, 100(17):176806, 2008.

[41] S. A. Tarasenko. Spin relaxation of conduction electrons in (110)-grown quantum wells: A microscopic theory. *Phys. Rev. B*, 80(16):165317, 2009.

[42] M. M. Glazov, M. A. Semina, and E. Ya. Sherman. Spin relaxation in multiple (110) quantum wells. *Phys. Rev. B*, 81(11):115332, 2010.

[43] J. Hübner, S. Kunz, S. Oertel, D. Schuh, M. Pochwała, H. Duc, J. Förstner, T. Meier, and M. Oestreich. Electron g-factor anisotropy in symmetric (110)-oriented GaAs quantum wells. *Phys. Rev. B*, 84(4):041301, 2011.

[44] S. Oertel, S. Kunz, D. Schuh, W. Wegscheider, J. Hübner, and M. Oestreich. Electron spin relaxation as tracer of excitons in a two-dimensional electron-hole plasma inside a (110)-GaAs quantum well. *Eur. Phys Lett.*, 96(6):67010, 2011.

[45] M. Griesbeck, M. Glazov, E. Ya. Sherman, D. Schuh, W. Wegscheider, C. Schüller, and T. Korn. Strongly anisotropic spin relaxation revealed by resonant spin amplification in (110) GaAs quantum wells. *Phys. Rev. B*, 85(8):085313, 2012.

[46] A. Hernández-Mínguez, K. Biermann, R. Hey, and P. V. Santos. Spin transport and spin manipulation in GaAs (110) and (111) quantum wells. *Phys. Status Solidi B (DOI:10.1002/pssb.201350202)*, 2014.

[47] P. Y. Yu and M. Cardona. *Fundamentals of Semiconductors: Physics and Materials Properties*. Springer, Berlin, 2010.

[48] G. Bastard. *Wave Mechanics Applied to Semiconductor Heterostructures*. Les Editions de Physique. Les Ulis Cedex, France, 1988.

[49] M. R. Brozel and G. E. Stillmann, editors. *Properties of Gallium Arsenide*. INSPEC, The Institution of Electrical Engineers, London, 3rd edition, 1996.

[50] C. Kittel. *Introduction to Solid State Physics*. John Wiley and Sons, New York, 8th edition, 2005.

[51] J. S. Blakemore. Semiconducting and other major properties of gallium arsenide. *J. Appl. Phys*, 53(10):R123, 1982.

[52] I. Vurgaftman, J. R. Meyer, and L. R. Ram-Mohan. Band parameters for III–V compound semiconductors and their alloys. *J. Appl. Phys*, 89(11):5815, 2001.

[53] W. Zawadzki and P. Pfeffer. Spin splitting of subband energies due to inversion asymmetry in semiconductor heterostructures. *Semiconductor Science and Technology*, 19(1):R1, 2004.

[54] M. Fox. *Optical Properties of Solids*. Oxford Master Series in Condensed Matter Physics. Oxford University Press, Oxford, 2001.

[55] M. S. Dresselhaus, G. Dresselhaus, and A. Jorio. *Group Theory: Application to the Physics of Condensed Matter*. Springer, Berlin, 2008.

[56] J. J. Sakurai. *Advanced Quantum Mechanics*. Addison-Wesley, Redwood City, 1987.

[57] C. Cohen-Tannoudji, L. Diu, and F. Laloë. *Quantum Mechanics*, volume one. Hermann, Paris, 1977.

[58] J. M. Luttinger and W. Kohn. Motion of Electrons and Holes in Perturbed Periodic Fields. *Phys. Rev.*, 97:869, 1955.

[59] L. A. Coldren and S. W. Corzine. *Diode Lasers and Photonic Integrated Circuits*. Wiley Series in Microwave and Optical Engineering. John Wiley and Sons, New York, 1995.

[60] I. Žutić and S. das Sarma. Spintronics: Fundamentals and applications. *Rev. Mod. Phys.*, 76(2):323, 2004.

[61] J. Batey and S. L. Wright. Energy band alignment in GaAs:(Al,Ga)As heterostructures: The dependence on alloy composition. *J. Appl. Phys*, 59(1):200–209, 1986.

[62] N. W. Ashcroft and N. D. Mermin. *Solid State Physics*. Harcourt College Publishers, Orlando, 8th edition, 1976.

[63] H. Haug and S. W. Koch. *Quantum Theory of the Optical and Electronic Properties of Semicondcutors*. World Scientific Publishing, Hong Kong, 2nd edition, 1993.

[64] J. D. Jackson. *Classical Electrodynamics*. John Wiley and Sons, New York, 3rd edition, 1999.

[65] F. Meier and B. P. Zakharchenya, editors. *Optical Orientation*, volume 8 of *Modern Problems in Condensed Matter Sciences*. North-Holland, Amsterdam, 1984.

[66] S. Pfalz, R. Winkler, T. Nowitzki, D. Reuter, A. D. Wieck, D. Hägele, and M. Oestreich. Optical orientation of electron spins in GaAs quantum wells. *Phys. Rev. B*, 71(16):165305, 2005.

[67] R. I. Dzhioev, K. V. Kavokin, V. L. Korenev, M. V. Lazarev, B. Y. Meltser, M. N. Stepanova, B. P. Zakharchenya, D. Gammon, and D. S. Katzer. Low-temperature spin relaxation in n-type GaAs. *Phys. Rev. B*, 66(24):245204, 2002.

[68] J.-H. Quast, G. V. Astakhov, W. Ossau, L. W. Molenkamp, J. Heinrich, S. Höfling, and A. Forchel. Influence of light on spin diffusion in weak magnetic fields. *Phys. Rev. B*, 79(24):245207, 2009.

[69] M. Kohl, M. Freeman, D. D. Awschalom, and J. Hong. Femtosecond spectroscopy of carrier-spin relaxation in GaAs-$Al_xGa_{1-x}As$ quantum wells. *Phys. Rev. B*, 44(11):5923, 1991.

[70] J. Hübner and M. Oestreich. Optical orientation in quantum wells. *Semiconductor Science and Technology*, 23(11):114006, 2008.

[71] J. Fabian, A. Matos-Abiague, C. Ertler, P. Stano, and I. Žutić. Semiconductor spintronics. *Acta Phys. Slov.*, 57(4 and 5):565, 2007.

[72] C. Weisbuch and C. Hermann. Optical detection of conduction-electron spin resonance in GaAs, $Ga_{1-x}In_xAs$, and $Ga_{1-x}Al_xAs$. *Phys. Rev. B*, 15(2):816, 1977.

[73] A. Heberle, W. W. Rühle, and K. Ploog. Quantum beats of electron Larmor precession in GaAs wells. *Phys. Rev. Lett.*, 72(24):3887, 1994.

[74] D.J. Griffiths. *Introduction to Quantum Mechanics*. Pearson Education, 2005.

[75] M. I. Dyakonov, editor. *Spin Physics in Semiconductors*. Springer Series in Solid-State Sciences. Springer, Berlin, 2008.

[76] F. Bloch. Nuclear induction. *Phys. Rev.*, 70:460, 1949.

[77] G. Fishman and G. Lampel. Spin relaxation of photoelectrons in p-type gallium arsenide. *Phys. Rev. B*, 16(2):820, 1977.

[78] M. W. Wu, J. H. Jiang, and M. Q. Weng. Spin dynamics in semiconductors. *Physics Reports*, 493(2-4):61, 2010.

[79] J. Fabian and S. das Sarma. Spin relaxation of conduction electrons. *J. Vac. Sci. Technology*, 17(4):1708, 1999.

[80] T. Henn. *Lateral Spin Diffusion in n-Type Gallium Arsenide*. Physikalisches Institut der Bayerischen Julius-Maximilians-Universität Würzburg, 2011.

[81] D. Hilton and C. Tang. Optical Orientation and Femtosecond Relaxation of Spin-Polarized Holes in GaAs. *Phys. Rev. Lett.*, 89(14):146601, 2002.

[82] K. Zerrouati, F. Fabre, G. Bacquet, J. Bandet, J. Frandon, G. Lampel, and D. Paget. Spin-lattice relaxation in p-type gallium arsenide single crystals. *Phys. Rev. B*, 37(3):1334, 1988.

[83] R. Völkl, M. Griesbeck, S. Tarasenko, D. Schuh, W. Wegscheider, C. Schüller, and T. Korn. Spin dephasing and photoinduced spin diffusion in a high-mobility two-dimensional electron system embedded in a GaAs-(Al,Ga)As quantum well grown in the [110] direction. *Phys. Rev. B*, 83(24):241306, June 2011.

[84] R. I. Dzhioev, V. L. Korenev, I. Merkulov, B. P. Zakharchenya, D. Gammon, A. Efros, and D. S. Katzer. Manipulation of the Spin Memory of Electrons in n-GaAs. *Phys. Rev. Lett.*, 88(25):256801, 2002.

[85] L. Meier, G. Salis, I. Shorubalko, E. Gini, S. Schön, and K. Ensslin. Measurement of Rashba and Dresselhaus spin–orbit magnetic fields. *Nature Physics*, 3(9):650, 2007.

[86] G. Dresselhaus. Spin-orbit coupling effects in zinc blende structures. *Phys. Rev.*, 100(2):580, 1955.

[87] M. Brand, A. Malinowski, O. Karimov, P. Marsden, R. Harley, A. Shields, D. Sanvitto, D. Ritchie, and M. Simmons. Precession and Motional Slowing of Spin Evolution in a High Mobility Two-Dimensional Electron Gas. *Phys. Rev. Lett.*, 89(23):236601, 2002.

[88] W. Leyland, R. Harley, M. Henini, A. Shields, I. Farrer, and D. Ritchie. Oscillatory Dyakonov-Perel spin dynamics in two-dimensional electron gases. *Phys. Rev. B*, 76(19):195305, 2007.

[89] R. Winkler. Spin orientation and spin precession in inversion-asymmetric quasi-two-dimensional electron systems. *Phys. Rev. B*, 69(4):045317, 2004.

[90] M. Glazov and E. L. Ivchenko. Resonant spin amplification in nanostructures with anisotropic spin relaxation and spread of the electronic g factor. *Semiconductors*, 42(8):951, 2008.

[91] G. V. Astakhov, M. M. Glazov, D. R. Yakovlev, E. A. Zhukov, W. Ossau, L. W. Molenkamp, and M. Bayer. Time-resolved and continuous-wave optical spin pumping of semiconductor quantum wells. *Semiconductor Science and Technology*, 23(11):114001, 2008.

[92] H. Hoffmann, G. V. Astakhov, T. Kiessling, W. Ossau, G. Karczewski, T. Wojtowicz, J. Kossut, and L. W. Molenkamp. Optical spin pumping of modulation-doped electrons probed by a two-color Kerr rotation technique. *Phys. Rev. B*, 74(7):073407, 2006.

[93] K. V. Kavokin. Spin relaxation of localized electrons in n-type semiconductors. *Semiconductor Science and Technology*, 23:114009, 2008.

[94] A. R. Cameron, P. Riblet, and A. Miller. Spin gratings and the measurement of electron drift mobility in multiple quantum well semiconductors. *Phys. Rev. Lett.*, 76(25):4793, 1996.

[95] S. G. Carter, Z. Chen, and S. T. Cundiff. Optical Measurement and Control of Spin Diffusion in n-Doped GaAs Quantum Wells. *Phys. Rev. Lett.*, 97(13), 2006.

[96] C. P. Weber, N. Gedik, J. E. Moore, J. Orenstein, J. Stephens, and D. D. Awschalom. Observation of spin Coulomb drag in a two-dimensional electron gas. *Nature*, 437(7063):1330, October 2005.

[97] C. P. Weber, J. Orenstein, B. Bernevig, S.-C. Zhang, J. Stephens, and D. D. Awschalom. Nondiffusive Spin Dynamics in a Two-Dimensional Electron Gas. *Phys. Rev. Lett.*, 98(7):076604, 2007.

[98] K. Chen, W. Wang, J. Wu, D. Schuh, W. Wegscheider, T. Korn, and T. Lai. Transmission-grating-photomasked transient spin grating and its application to measurement of electron-spin ambipolar diffusion in (110) GaAs quantum wells. *Opt. Express*, 20(7):8192, 2012.

[99] H. Zhao, M. Mower, and G. Vignale. Ambipolar spin diffusion and D'yakonov-Perel' spin relaxation in GaAs quantum wells. *Phys. Rev. B*, 79(11):115321, 2009.

[100] G. Wang, B. L. Liu, A. Balocchi, P. Renucci, C. R. Zhu, T. Amand, C. Fontaine, and X. Marie. Gate control of the electron spin-diffusion length in semiconductor quantum wells. *Nature Communications*, 4:2372, 2013.

[101] J.-H. Quast, T. Henn, T. Kiessling, W. Ossau, L. W. Molenkamp, D. Reuter, and A. D. Wieck. Hot carrier effects on lateral electron spin diffusion in n-type GaAs. *Phys. Rev. B*, 87(20):205203, 2013.

[102] J. Crank. *The mathematics of diffusion*. Oxford University Press, Oxford, 2nd edition, 1975.

[103] H. W. Yoon, D. R. Wake, J. P. Wolfe, and H. Morkoç. In-plane transport of photoexcited carriers in GaAs quantum wells. *Phys. Rev. B*, 46(20):13461, 1992.

[104] L. M. Smith, D. R. Wake, J. P. Wolfe, D. Levi, M. V. Klein, J. Klem, T. Henderson, and H. Morkoç. Picosecond imaging of photoexcited carriers in quantum wells: Anomalous lateral confinement at high densities. *Phys. Rev. B*, 38(8):5788, 1988.

[105] N. Kumar, Q. Cui, F. Ceballos, D. He, Y. Wang, and H. Zhao. Exciton diffusion in monolayer and bulk $MoSe_2$. *Nanoscale*, 6:4915, 2014.

[106] A. V. Kimel, V. V. Pavlov, R. V. Pisarev, V. N. Gridnev, F. Bentivegna, and T. Rasing. Ultrafast dynamics of the photo-induced magneto-optical Kerr effect in CdTe at room temperature. *Phys. Rev. B*, 62(16):R10610, 2000.

[107] A. V. Kimel, F. Bentivegna, V. N. Gridnev, V. V. Pavlov, R. V. Pisarev, and T. Rasing. Room-temperature ultrafast carrier and spin dynamics in GaAs probed by the photoinduced magneto-optical Kerr effect. *Phys. Rev. B*, 63(23):235201, 2001.

[108] K. Shinagawa. Faraday and Kerr Efects in Ferromagnets. In S. Sugano and N. Kojima, editors, *Magneto-Optics*, Springer Series in Solid-State Sciences. Springer, Berlin, 2000.

[109] W. Reim and J. Schoenes. Magneto-optical spectroscopy of f-electron systems. In K. H. J. Buschow and E. P. Wohlfahrt, editors, *Ferromagnetic materials. A handbook on the properties of magnetically ordered substances.*, volume 5, book 2, page 133. North-Holland, Amsterdam, 1990.

[110] M. Born and E. Wolf. *Principles of optics. Electromagnetic theory of propagation, interference and diffraction of light*. Cambridge University Press, Cambridge, 7th (expanded) edition, 2006.

[111] A. D. Fried. Relationship of time-reversal symmetry breaking to optical Kerr rotation. *Phys. Rev. B*, 90:121112, 2014.

[112] S. Permogorov. Hot excitons in semiconductors. *Phys. Status Solidi B*, 68(1):9, 1975.

[113] H. Münzel, D. Bimberg, and A. Steckenborn. Direct evidence for screening of carrier-acoustic phonon interaction at low to medium carrier densities in GaAs. *Physics Letters A*, 117-118:214, 1983.

[114] G. Fasol and H. Hughes. Band-structure determination of GaAs from hot-electron luminescence. *Phys. Rev. B*, 33(4):2953, 1986.

[115] D. W. Snoke, W. W. Rühle, Y. C. Lu, and E. Bauser. Evolution of a nonthermal electron energy distribution in GaAs. *Phys. Rev. B*, 45(19):10979, 1992.

[116] D. W. Snoke. Density-Dependence of Electron-Scattering at Low-Density. *Phys. Rev. B*, 50(16):11583, 1994.

[117] D. W. Snoke. Theory of electron-electron scattering at low density. *Phys. Rev. B*, 47(20):13346, 1993.

[118] D. W. Snoke, W. W. Rühle, Y. C. Lu, and E. Bauser. Nonthermalized distribution of electrons on picosecond time scale in GaAs. *Phys. Rev. Lett.*, 68(7):990, 1992.

[119] J. Kash. Carrier-carrier scattering: An experimental comparison of bulk GaAs and GaAs/$Al_xGa_{1-x}As$ quantum wells. *Phys. Rev. B*, 48(24):18336, 1993.

[120] T. Elsaesser, J. Shah, L. Rota, and P. Lugli. Initial thermalization of photoexcited carriers in GaAs studied by femtosecond luminescence spectroscopy. *Phys. Rev. Lett.*, 66(13):1757, 1991.

[121] F. Reif. *Fundamentals of statistical and thermal physics*. McGraw-Hill Book Company, New York, international student edition edition, 1965.

[122] J. M. Ziman. *Electrons and Phonons*. Oxford Classic Texts in the Physical Sciences. Oxford University Press, Oxford, 2001.

[123] C. Weisbuch. Photocarrier thermalization by laser excitation spectroscopy. *Phys. Lett. A*, 21(1):179, 1978.

[124] J. Kash. Carrier-carrier scattering in GaAs: Quantitative measurements from hot (e,A^0) luminescence. *Phys. Rev. B*, 40(5):3455, 1989.

[125] E. O. Göbel and O. Hildebrand. Thermalization of the Electron-Hole Plasma in GaAs. *Phys. Status Solidi B*, 88(2):645, 1978.

[126] T. Kiessling, J.-H. Quast, A. Kreisel, T. Henn, W. Ossau, and L. W. Molenkamp. Spatially resolved photocarrier energy relaxation in low-doped bulk GaAs. *Phys. Rev. B*, 86(16):161201, 2012.

[127] M. Beck. *Time and spatially resolved photoluminescence studies of hot electrons in bulk GaAs*. Physikalisches Institut der Bayerischen Julius-Maximilians-Universität Würzburg, 2013.

[128] J. I. Pankove. *Optical Processes in semiconductors*. Dover Publications, Inc., New York, 1975.

[129] D. J. Ashen, P. J. Dean, D. T. J. Hurle, and J. B. Mullin. The incorporation and characterisation of acceptors in epitaxial GaAs. *J. Phys. Chem. Solids*, 1975.

[130] D. M. Eagles. Optical absorption and recombination radiation in semiconductors due to transitions between hydrogen-like acceptor impurity levels and the conduction band. *J. Phys. Chem. Solids*, 16(1-2):76, 1960.

[131] W. Dumke. Optical Transitions Involving Impurities in Semiconductors. *Phys. Rev.*, 132(5):1998, 1963.

[132] W. Vassen, C. Zimmermann, R. Kallenbach, and T. W. Hänsch. A frequency-stabilized titanium sapphire laser for high-resolution spectroscopy. *Optics Commun.*, 75(5-6):435, 1990.

[133] T. L. Boyd H. J. Kimble. Frequency stabilization of a continuous-wave Ti:sapphire laser. *Optics Letters*, 16(11):808, 1991.

[134] K. C. Harvey C. J. Myatt. External-cavity diode laser using a grazing-incidence diffraction grating. *Optics Letters*, 16(12):910, 1991.

[135] S. A. Crooker, F. D. Betz, J. Levy, and D. D. Awschalom. Femtosecond synchronization of two passively mode-locked Ti:sapphire lasers. *Rev. Scient. Instr.*, 67(6):2068, 1996.

[136] E. Zhukov, D. Yakovlev, M. Bayer, M. Glazov, E. L. Ivchenko, G. Karczewski, T. Wojtowicz, and J. Kossut. Spin coherence of a two-dimensional electron gas induced by resonant excitation of trions and excitons in CdTe/(Cd,Mg)Te quantum wells. *Phys. Rev. B*, 76(20):205310, 2007.

[137] H. Kano and H. Hamaguchi. Femtosecond coherent anti-Stokes Raman scattering spectroscopy using supercontinuum generated from a photonic crystal fiber. *Appl. Phys. Lett.*, 85(19):4298, 2004.

[138] R. Holzwarth, T. Udem, T. W. Hänsch, J. Knight, W. Wadsworth, and P. Russell. Optical Frequency Synthesizer for Precision Spectroscopy. *Phys. Rev. Lett.*, 85(11):2264, 2000.

[139] E. Auksorius, B. R. Boruah, C. Dunsby, P. M. P. Lanigan, G. Kennedy, M. A. A. Neil, and P. M. W. French. Stimulated emission depletion microscopy with a supercontinuum source and fluorescence lifetime imaging. *Optics Letters*, 33(2):113, 2008.

[140] I. Hartl, X. D. Li, C. Chudoba, R. K. Ghanta, T. H. Ko, J. G. Fujimoto, J. K. Ranka, and R. S. Windeler. Ultrahigh-resolution optical coherence tomography using continuum generation in an air–silica microstructure optical fiber. *Optics Letters*, 26(9):608, 2001.

[141] M. Römer, H. Bernien, G. M. Müller, D. Schuh, J. Hübner, and M. Oestreich. Electron-spin relaxation in bulk GaAs for doping densities close to the metal-to-insulator transition. *Phys. Rev. B*, 81(7):075216, 2010.

[142] T. Damen, L. Via, J. Cunningham, J. Shah, and L. Sham. Subpicosecond spin relaxation dynamics of excitons and free carriers in GaAs quantum wells. *Phys. Rev. Lett.*, 67(24):3432, 1991.

[143] J. M. Dudley and S. Coen. Supercontinuum generation in photonic crystal fiber. *Rev. Mod. Phys.*, 78(4):1135, 2006.

[144] J. Teipel, K. Franke, D. Türke, F. Warken, D. Meiser, M. Leuschner, and H. Giessen. Characteristics of supercontinuum generation in tapered fibers using femtosecond laser pulses. *Appl. Phys. B*, 77(2-3):245, 2003.

[145] J. Teipel, D. Türke, H. Giessen, A. Killi, U. Morgner, M. Lederer, D. Kopf, and M. Kolesik. Diode-pumped, ultrafast, multi-octave supercontinuum source at repetition rates between 500 kHz and 20 MHz using Yb:glass lasers and tapered fibers. *Optics Express*, 13(5):1477, 2005.

[146] K. F. Mak, K. He, J. Shan, and T. F. Heinz. Control of valley polarization in monolayer MoS2 by optical helicity. *Nature Nanotech.*, 7(8):494, 2012.

[147] J. C. Kemp. Piezo-optical birefringence modulators: new use for a long-known effect. *J. Opt. Soc. Am.*, 59(8):950, 1969.

[148] S. A. Crooker, J. Baumberg, F. Flack, N. Samarth, and D. D. Awschalom. Terahertz Spin Precession and Coherent Transfer of Angular Momenta in Magnetic Quantum Wells. *Phys. Rev. Lett.*, 77(13):2814, 1996.

[149] R. M. A. Azzam and N. M. Bashara. *Ellipsometry and polarized light*. North-Holland, Amsterdam, 1987.

[150] M. Abramowitz and I. A. Stegun, editors. *Handbook of mathematical functions with formulas, graphs, and mathematical tables.* Dover Publications, Inc., New York, 1965.

[151] S. Adachi. Excitonic effects in the optical spectrum of GaAs. *Phys. Rev. B*, 41(2):1003, 1990.

[152] S. Linden, H. Giessen, and J. Kuhl. XFROG - A New Method for Amplitude and Phase Characterization of Weak Ultrashort Pulses. *Phys. Status Solidi B*, 206(1):119, 1998.

[153] B. Metzger, A. Steinmann, F. Hoos, S. Pricking, and H. Giessen. Compact laser source for high-power white-light and widely tunable sub 65 fs laser pulses. *Optics Letters*, 35(23):3961, 2010.

[154] E. Bogardus and H. Bebb. Bound-Exciton, Free-Exciton, Band-Acceptor, Donor-Acceptor, and Auger Recombination in GaAs. *Phys. Rev.*, 176(3):993, 1968.

[155] K. Kheng, R. Cox, M. d'Aubigné, F. Bassani, K. Saminadayar, and S. Tatarenko. Observation of negatively charged excitons X- in semiconductor quantum wells. *Phys. Rev. Lett.*, 71(11):1752, 1993.

[156] G. V. Astakhov, D. R. Yakovlev, V. Kochereshko, W. Ossau, J. Nürnberger, W. Faschinger, and G. Landwehr. Charged excitons in ZnSe-based quantum wells. *Phys. Rev. B*, 60(12):R8485, 1999.

[157] G. V. Astakhov and W. Ossau. Magneto-optics of modulation doped quantum wells based on II-VI semiconductor compounds. *Phys. Status Solidi C*, 4(9):3310, 2007.

[158] A. Manassen, E. Cohen, A. Ron, E. Linder, and L. Pfeiffer. Exciton and trion spectral line shape in the presence of an electron gas in GaAs/AlAs quantum wells. *Phys. Rev. B*, 54(15):10609, 1996.

[159] A. Ron, H. W. Yoon, M. D. Sturge, A. Manassen, E. Cohen, and L. N. Pfeiffer. Thermodynamics of free trions in mixed type quantum wells. *Solid State Commun.*, 97(9):741–745, 1996.

[160] A. Esser, E. Runge, R. Zimmermann, and W. Langbein. Photoluminescence and radiative lifetime of trions in GaAs quantum wells. *Phys. Rev. B*, 62(12):8232, 2000.

[161] A. Esser, E. Runge, R. Zimmermann, and W. Langbein. Trions in GaAs Quantum Wells: Photoluminescence Lineshape Analysis. *Phys. Status Solidi A*, 178(1):489, 2000.

[162] S. Schmitt-Rink, D. S. Chemla, and D. A. B. Miller. Theory of transient excitonic optical nonlinearities in semiconductor quantum-well structures. *Phys. Rev. B*, 32(10):6601, 1985.

[163] S. Schmitt-Rink, D. S. Chemla, and D. A. B. Miller. Linear and nonlinear optical properties of semiconductor quantum wells. *Adv. in Phys.*, 38(2):89, 1989.

[164] G. Livescu, D. A. B. Miller, D. S. Chemla, M. Ramaswamy, T.-Y. Chang, N. Sauer, A. C. Gossard, and J. H. English. Free carrier and many-body effects in absorption spectra of modulation-doped quantum wells. *Quantum Electronics*, 24(8):1677, 1988.

[165] D. Keller, D. R. Yakovlev, G. V. Astakhov, W. Ossau, S. A. Crooker, T. Slobodskyy, A. Waag, G. Schmidt, and L. W. Molenkamp. Magneto-optics of two-dimensional electron gases modified by strong Coulomb interactions in ZnSe quantum wells. *Phys. Rev. B*, 72(23):235306, 2005.

[166] A. Tredicucci, Y. Chen, F. Bassani, J. Massies, C. Deparis, and G. Neu. Center-of-mass quantization of excitons and polariton interference in GaAs thin layers. *Phys. Rev. B*, 47(16):10348, 1993.

[167] A. S. Chaves, A. F. S. Penna, J. M. Worlock, G. Weimann, and W. Schlapp. Optical control of two-dimensional electron density in a single asymmetric quantum well. *Surface Science*, 170(1-2):618, 1986.

[168] R. Völkl, M. Schwemmer, M. Griesbeck, S. A. Tarasenko, D. Schuh, W. Wegscheider, C. Schüller, and T. Korn. Spin polarization, dephasing, and photoinduced spin diffusion in (110)-grown two-dimensional electron systems. *Phys. Rev. B*, 89(7):075424, 2014.

[169] M. Römer, J. Hübner, and M. Oestreich. Spin noise spectroscopy in semiconductors. *Rev. Scient. Instr.*, 78(10):103903, 2007.

[170] S. A. Crooker, L. Cheng, and D. L. Smith. Spin noise of conduction electrons in n-type bulk GaAs. *Phys. Rev. B*, 79(3):035208, 2009.

[171] G. M. Müller, M. Oestreich, M. Römer, and J. Hübner. Semiconductor spin noise spectroscopy: Fundamentals, accomplishments, and challenges. *Physica E*, 43(2):569, 2010.

[172] R. Leite, J. Shah, and J. Gordon. Effect of Electron-Exciton Collisions on the Free-Exciton Linewidth in Epitaxial GaAs. *Phys. Rev. Lett.*, 23(23):1332, 1969.

[173] L. Schultheis, A. Honold, J. Kuhl, K. Köhler, and C. Tu. Optical dephasing of homogeneously broadened two-dimensional exciton transitions in GaAs quantum wells. *Phys. Rev. B*, 34(12):9027, 1986.

[174] A. Honold, L. Schultheis, J. Kuhl, and C. Tu. Collision broadening of two-dimensional excitons in a GaAs single quantum well. *Phys. Rev. B*, 40(9):6442, 1989.

[175] S. Rudin, T. L. Reinecke, and B. Segall. Temperature-dependent exciton linewidths in semiconductors. *Phys. Rev. B*, 42(17):11218, 1990.

[176] D.-S. Kim, J. Shah, J. Cunningham, T. Damen, W. Schäfer, M. Hartmann, and S. Schmitt-Rink. Giant excitonic resonance in time-resolved four-wave mixing in quantum wells. *Phys. Rev. Lett.*, 68(7):1006, 1992.

[177] H. Qiang, F. H. Pollak, C. M. Sotomayor Torres, W. Leitch, A. H. Kean, M. A. Stroscio, G. J. Iafrate, and K. W. Kim. Size dependence of the thermal broadening of the exciton linewidth in $GaAs/Ga_{0.7}Al_{0.3}As$ single quantum wells. *Appl. Phys. Lett.*, 61(12):1411, 1992.

[178] R. Hellmann, M. Koch, J. Feldmann, S. T. Cundiff, E. O. Göbel, D. R. Yakovlev, A. Waag, and G. Landwehr. Homogeneous linewidth of excitons in semimagnetic $CdTe/Cd_{1-x}Mn_xTe$ multiple quantum wells. *Phys. Rev. B*, 48(4):2847, 1993.

[179] W. Maślana, W. Mac, J. A. Gaj, P. Kossacki, A. Golnik, J. Cibert, S. Tatarenko, T. Wojtowicz, G. Karczewski, and J. Kossut. Faraday rotation in a study of charged excitons in $Cd_{1-x}Mn_xTe$. *Phys. Rev. B*, 63(16):165318, 2001.

[180] V. L. Alperovich, V. M. Zaletin, A. F. Kravchenko, and A. S. Terekhov. The influence of phonons and impurities on the broadening of excitonic spectra in gallium arsenide. *Phys. Status Solidi B*, 77(2):465, 1976.

[181] D. Gammon, S. Rudin, T. L. Reinecke, D. S. Katzer, and C. S. Kyono. Phonon broadening of excitons in $GaAs/Al_xGa_{1-x}As$ quantum wells. *Phys. Rev. B*, 51(23):16785, 1995.

[182] S. Hunsche, K. Leo, H. Kurz, and K. Köhler. Exciton absorption saturation by phase-space filling: influence of carrier temperature and density. *Phys. Rev. B*, 49(23):16565, 1994.

[183] A. Thilagam. Dimensionality dependence of Pauli blocking effects in semiconductor quantum wells. *J. Phys. Chem. Solids*, 60(4):497, 1999.

[184] E. Gross, S. Permogorov, and B. Razbirin. Free exciton motion in crystals and exciton-phonon interaction. *J. Phys. Chem. Solids*, 27(10):1647, 1966.

[185] B. Segall and G. Mahan. Phonon-assisted recombination of free excitons in compound semiconductors. *Phys. Rev.*, 171(3):935, 1968.

[186] J. B. Stark, W. H. Knox, and D. S. Chemla. Spin-resolved femtosecond magnetoexciton interactions in GaAs quantum wells. *Phys. Rev. B*, 46(12):7919, 1992.

[187] T. Amand, X. Marie, B. Baylac, B. Dareys, J. Barrau, M. Brousseau, R. Planel, and D. J. Dunstan. Enhanced exciton blue shift in spin polarized dense exciton system in quantum wells. *Phys. Lett. A*, 193(1):105, 1994.

[188] L. Viña, L. Muñoz, E. Pérez, J. Fernández-Rossier, C. Tejedor, and K. Ploog. Spin splitting in a polarized quasi-two-dimensional exciton gas. *Phys. Rev. B*, 54(12):R8317, 1996.

[189] G. Aichmayr, L. Viña, S. P. Kennedy, R. T. Phillips, and E. E. Mendez. The role of spin in interacting excitonic gases. *Phys. Status Solidi A*, 190(3):615, 2002.

[190] E. V. Kozhemyakina, K. S. Zhuravlev, A. Amo, D. Ballarini, and L. Viña. Observation of the zero-magnetic-field exciton spin splitting in high quality bulk GaAs and AlGaAs. *Appl. Phys. Lett.*, 95(18):182107, 2009.

[191] J. Fernández-Rossier, C. Tejedor, L. Muñoz, and L. Viña. Polarized interacting exciton gas in quantum wells and bulk semiconductors. *Phys. Rev. B*, 54(16):11582, 1996.

[192] L. Muñoz, E. Pérez, L. Viña, J. Fernández-Rossier, C. Tejedor, and K. Ploog. Spin splitting of excitons in GaAs quantum wells at zero magnetic field. *Solid-State Electronics*, 40(1):755, 1996.

[193] M. E. Flatte and J. M. Byers. Spin diffusion in semiconductors. *Phys. Rev. Lett.*, 84(18):4220, 2000.

[194] J. P. Wolfe, H. W. Yoon, D. R. Wake, and H. Morkoç. 'Diffusion' of carriers in a semiconductor quantum well. *Semicond. Sci. Technol*, 7(3B):B240, 1992.

[195] H. Zhao, S. Moehl, S. Wachter, and H. Kalt. Hot exciton transport in ZnSe quantum wells. *Appl. Phys. Lett.*, 80(8):1391, 2002.

[196] H. Zhao, B. Dal Don, S. Moehl, H. Kalt, K. Ohkawa, and D. Hommel. Spatiotemporal dynamics of quantum-well excitons. *Phys. Rev. B*, 67(3):035306, 2003.

[197] R. A. Smith. *Semiconductors*. Cambridge University Press, Cambridge, 2nd edition, 1987.

[198] W. Zawadzki, P. Pfeffer, R. Bratschitsch, Z. Chen, S. T. Cundiff, B. N. Murdin, and C. R. Pidgeon. Temperature dependence of the electron spin g factor in GaAs. *Phys. Rev. B*, 78(24):245203, 2008.

[199] M. Koch, G. Bastian, R. Hellmann, J. Feldmann, E. O. Göbel, and P. Dawson. Exciton scattering with bare electrons. *Phys. Status Solidi B*, 188(1):485, 1995.

[200] W. Liu, D. Jiang, K. Luo, Y. Zhang, and X. Yang. Broadening of the excitonic linewidth due to scattering of two-dimensional free carriers. *Appl. Phys. Lett.*, 67(5):679, 1995.

[201] I. Malajovich, J. M. Kikkawa, D. D. Awschalom, J. Berry, and N. Samarth. Coherent Transfer of Spin through a Semiconductor Heterointerface. *Phys. Rev. Lett.*, 84(5):1015, 2000.

[202] I. Malajovich, J. J. Berry, N. Samarth, and D. D. Awschalom. Persistent sourcing of coherent spins for multifunctional semiconductor spintronics. *Nature*, 411(6839):770, 2001.

[203] I. D'Amico and G. Vignale. Spin diffusion in doped semiconductors: The role of Coulomb interactions. *Europhys. Lett.*, 55:566, 2001.

[204] I. D'Amico and C. A. Ullrich. Coulomb interactions and spin transport in semiconductors: The spin Coulomb drag effect. *Phys. Status Solidi B*, 247(2):235, 2010.

[205] M. Yang, R. Wagner, B. Shanabrook, J. Waterman, and W. Moore. Spin-resolved cyclotron resonance in InAs quantum wells: A study of the energy-dependent g factor. *Phys. Rev. B*, 47(11):6807, 1993.

[206] G. Salis, Y. K. Kato, K. Ensslin, D. C. Driscoll, A. C. Gossard, and D. D. Awschalom. Electrical control of spin coherence in semiconductor nanostructures. *Nature*, 414(6864):619, 2001.

[207] X. Z. Ruan, B. Q. Sun, Y. Ji, W. Yang, J. H. Zhao, and Z. Y. Xu. Direct observation of coherent spin transfer processes in an InGaAs/GaAs quantum well via two-color time-resolved Kerr rotation measurements. *Semicond. Sci. Technol*, 23(7):075021, 2008.

[208] W. Becker. *Advanced time-correlated single photon counting techniques*. Springer Series in Chemical Physics. Springer, Berlin, 2005.

[209] M. Q. Weng and M. W. Wu. Spin-charge separation in bipolar spin transport in (111) GaAs quantum wells. *Phys. Rev. B*, 88(19):195310, 2013.

[210] O. Couto, F. Iikawa, J. Rudolph, R. Hey, and P. Santos. Anisotropic Spin Transport in (110) GaAs Quantum Wells. *Phys. Rev. Lett.*, 98(3):036603, 2007.

[211] P. Eldridge, W. Leyland, P. Lagoudakis, O. Karimov, M. Henini, D. Taylor, R. T. Phillips, and R. Harley. All-optical measurement of Rashba coefficient in quantum wells. *Phys. Rev. B*, 77(12):125344, 2008.

[212] V. Arora and A. Naeem. Phonon-scattering-limited mobility in a quantum-well heterostructure. *Phys. Rev. B*, 31(6):3887, 1985.

[213] T. Henn, T. Kiessling, W. Ossau, L. W. Molenkamp, D. Reuter, and A. D. Wieck. Picosecond real-space imaging of electron spin diffusion in GaAs. *Phys. Rev. B*, 88:195202, 2013.

[214] D. von der Linde and R. Lambrich. Direct Measurement of Hot-Electron Relaxation by Picosecond Spectroscopy. *Phys. Rev. Lett.*, 42(16):1090, 1979.

[215] R. F. Leheny, J. Shah, R. L. Fork, C. V. Shank, and A. Migus. Dynamics of hot carrier cooling in photo-excited GaAs. *Solid State Commun.*, 31(11):809, 1979.

Zusammenfassung

Die vorliegende Arbeit *Hot spin carriers in cold semiconductors* untersuchte den Einfluss heißer Ladungsträger in pump-probe magneto-optischer Kerr-Effekt (MOKE) Tieftemperatur-Mikroskopie-Messungen der optisch induzierten Elektronenspin-Dynamik in Galliumarsenid-basierten Halbleiterheterostrukturen. Unsere Untersuchungen zeigten, dass dieser Einfluss von zweierlei Art ist.

Der erste Aspekt betrifft die magneto-optische Elektronenspin-Detektion. Es wird gewöhnlich angenommen, dass eine Messung der lokalen Kerr-Rotation unter Verwendung einer beliebigen Probelaser-Wellenlänge korrekt die lokale Elektronenspinpolarisation abbildet. Diese Prämisse ist die fundamentale Grundlage der MOKE Elektronenspin-Mikroskopie. Unsere Dauerstrich-Spektroskopie-Ergebnisse belegen, dass diese Annahme im Allgemeinen nicht korrekt ist.

Bei tiefen Gittertemperaturen führt die nichtresonante optische Anregung spinpolarisierter Elektronen zu einer signifikanten Heizung des Elektronensystems. Diese Heizung modifiziert lokal den magneto-optischen Koeffizienten, der die im Experiment beobachtete Kerr-Rotation mit der zu messenden Elektronenspinpolarisation verknüpft. Als Konsequenz ist die spininduzierte lokale Kerr-Rotation von spinunabhängigen Änderungen des magneto-optischen Koeffizienten überlagert. Eine ortsaufgelöste Messung der Kerr-Rotation bildet dann im Allgemeinen nicht korrekt die lokale Elektronenspinpolarisation ab.

Wir haben verschiedene Möglichkeiten demonstriert, diese Einschränkung zu überwinden und das korrekte Elektronenspin-Profil zu bestimmen. Für Dauerstrich-Anregung haben wir gezeigt, dass das Elektronenspin-Profil korrekt durch eine quantitative Analyse des lokalen exzitonischen Kerr-Rotations-Spektrums ermittelt werden kann. Alternativ minimiert Pikosekunden-zeitaufgelöste MOKE Mikroskopie unter Verwendung eines spektral breiten gepulsten Probelasers den Einfluss heißer Elektronen auf die magneto-optische Spin-Detektion und erlaubt die direkte Beobachtung der diffusiven Ausbreitung optisch erzeugter Elektronenspin-Pakete im Realraum.

Als zweites Hauptergebnis haben wir gezeigt, dass optische angeregte heiße Ladungsträger auch signifikant den eigentlichen Spindiffusions-Prozess beeinflussen. Aufgrund ihrer hohen kinetischen Energie erhöht die Anwesenheit heißer Photoladungsträger stark den Elektronenspin-Diffusionskoeffizienten im Vergleich zum intrinsischen Wert des ungestörten Systems. Aus diesem Grund ist bei tiefen Gittertemperaturen für lokale Dauerstrich-Anregung der Spin-Diffusionskoeffizient in der Nähe des fokussierten Pumplaserstrahls, in der heiße Elektronen vorhanden sind, stark erhöht. Analog führt für kurze Zeiten nach gepulster optischer Anregung die hohe anfängliche Elektronen-

temperatur zu einer sehr schnellen initialen Ausbreitung des Spin-Paktes, welche sich allmählich verlangsamt, während die Elektronen auf die Gittertemperatur abkühlen.

Während einzelne frühere Arbeiten bereits den möglichen Einfluss heißer Ladungsträger auf den Elektronenspin-Transport erkannten, ist die vorliegende Arbeit die erste, die die Wirkung heißer Träger auf die Elektronenspin-Diffusion direkt beobachtet und quantifiziert. Wir haben verschiedene Modelle entwickelt, die für gepulste und Dauerstrich-Anregung quantitativ die experimentell beobachtete Elektronenspin-Diffusion beschreiben. Diese Modelle sind in der Lage, die intrinsische Spindiffusivität von den Beiträgen heißer Ladungsträger zu trennen und erlauben, die Spintransport-Eigenschaften des ungestörten Systems zu bestimmen.

Wir haben durch zeitaufgelöste und Dauerstrich-Anregungs-Experimente die Gittertemperatur-Abhängigkeit der Spindiffusion in n-dotiertem Volumen-GaAs untersucht. Mit Hilfe unserer Modelle haben wir einen konsistenten Parameter-Satz für die intrinsische Temperaturabhängigkeit der Spinrelaxationszeit und des Elektronenspin-Diffusionskoeffizienten sowie der Beiträge heißer Ladungsträger ermittelt, der quantitativ alle experimentellen Beobachtungen beschreibt. Unsere Analyse zeigt, dass wir damit erstmals ein kohärentes Verständnis der optisch induzierten Tieftemperatur-Elektronenspin-Diffusion in Halbleitern entwickelt haben.

Acknowledgements

This work has been made possible by of the support and help of many people. I am particularly indebted to:

Prof. Dr. Wolfgang Ossau and Dr. Tobias Kießling for the supervision of my thesis,

Prof. Dr. Laurens W. Molenkamp for providing access to the infrastructure of his chair Experimentelle Physik III,

Prof. Dirk Reuter (Universität Paderborn) and Prof. Andreas. D. Wieck (Universität Bochum) as well as Dr. Klaus Biermann and Dr. Paulo V. Santos (Paul-Drude-Institut für Festkörperelektronik Berlin) for providing the high quality MBE samples,

Jan-Henrik Quast for introducing me to MOKE microscopy,

Michael Beck for cooperation on the spatially resolved electron temperature PL spectroscopy,

Franz Münzhuber and Steffen Bieker for sharing the pursuit of the perfect optical spectroscopy setup,

my family, and Saskia, the greatest person in the world!